AFRL-RQ-ED-TR-2021-0018

High Fidelity Modeling of Field-Reversed Configuration (FRC) Thrusters

Robert Martin

Éder M. Sousa (ERC)
Richard Abrantes (NRC Post-Doctoral Fellow)
Michael Kapper (ERC)
Robert Lilly (Jacobs)

Air Force Research Laboratory (AFMC)
In-Space Propulsion Branch
AFRL/RQRS
1 Ara Drive
Edwards AFB, CA 93524

December 2021

In-House Final Report

DISTRIBUTION STATEMENT A: Approved for Public Release; Distribution is Unlimited.

AIR FORCE RESEARCH LABORATORY
AEROSPACE SYSTEMS DIRECTORATE

■ Air Force Materiel Command ■ United States Air Force ■ Edwards Air Force Base, CA 93524

NOTICE PAGE

Using Government drawings, specifications, or other data included in this document for any purpose other than Government procurement does not in any way obligate the U.S. Government. The fact that the Government formulated or supplied the drawings, specifications, or other data does not license the holder or any other person or corporation; or convey any rights or permission to manufacture, use, or sell any patented invention that may relate to them.

This report was cleared for public release by the Air Force Research Laboratory Public Affairs Office (AFRL/PA) and is available to the general public, including foreign nationals.

AFRL-RQ-ED-TR-2021-0018 HAS BEEN REVIEWED AND IS APPROVED FOR PUBLICATION IN ACCORDANCE WITH ASSIGNED DISTRIBUTION STATEMENT.

This report is published in the interest of scientific and technical information exchange, and its publication does not constitute the Government's approval or disapproval of its ideas or findings.

REPORT DOCUMENTATION PAGE

Form Approved
OMB No. 0704-0188

Public reporting burden for this collection of information is estimated to average 1 hour per response, including the time for reviewing instructions, searching existing data sources, gathering and maintaining the data needed, and completing and reviewing this collection of information. Send comments regarding this burden estimate or any other aspect of this collection of information, including suggestions for reducing this burden to Department of Defense, Washington Headquarters Services, Directorate for Information Operations and Reports (0704-0188), 1215 Jefferson Davis Highway, Suite 1204, Arlington, VA 22202-4302. Respondents should be aware that notwithstanding any other provision of law, no person shall be subject to any penalty for failing to comply with a collection of information if it does not display a currently valid OMB control number. **PLEASE DO NOT RETURN YOUR FORM TO THE ABOVE ADDRESS.**

1. REPORT DATE *(MM/DD/YYYY)*	**2. REPORT TYPE**	**3. DATES COVERED** *(From - To)*
12/01/2021	Final Report	04/26/2018 – 09/02/2021

4. TITLE AND SUBTITLE
High Fidelity Modeling of Field-Reversed Configuration (FRC) Thrusters

5a. CONTRACT NUMBER
In-House

5b. GRANT NUMBER

5c. PROGRAM ELEMENT NUMBER
61102F

6. AUTHOR(S)
Robert Martin (AFRL), Éder M. Sousa (ERC), Richard Abrantes (NRC), Michael Kapper (ERC), Robert Lilly (Jacobs)

5d. PROJECT NUMBER

5e. TASK NUMBER

5f. WORK UNIT NUMBER
Q200

7. PERFORMING ORGANIZATION NAME(S) AND ADDRESS(ES)

AFRL/RQRS
In-Space Propulsion Branch
1 Ara Road
Edwards AFB, CA 93524

8. PERFORMING ORGANIZATION REPORT NO.

9. SPONSORING / MONITORING AGENCY NAME(S) AND ADDRESS(ES)
Air Force Research Laboratory
Rocket Propulsion Division
AFRL/RQR
5 Pollux Drive
Edwards AFB, CA 93524

10. SPONSOR/MONITOR'S ACRONYM(S)

11. SPONSOR/MONITOR'S REPORT NUMBER(S)
AFRL-RQ-ED-TR-2021-0018

12. DISTRIBUTION / AVAILABILITY STATEMENT
DISTRIBUTION STATEMENT A. Approved for public release; distribution is unlimited

13. SUPPLEMENTARY NOTES
PA Clearance No. AFRL-2021-4182 Cleared: 23 Nov 2021

14. ABSTRACT

This work continues development of an advanced multiscale and multifidelity Modeling & Simulation (M&S) capability targeted at the fundamental studies of the physical characteristics of Field-Reversed Configuration (FRC) plasma for advanced space propulsion. This work consists of numerical method development, physical model development, and systematic studies of the non-linear plasma dynamics and finite rate chemical processes governing FRC formation, acceleration, stability and interaction with the environment. While the use of FRCs as a high efficiency/high thrust successor to the current generation of Electric Propulsion devices (Hall Effect Thrusters and Ion thrusters) holds great promise, especially as the foundation of a true hybrid chemical/electric propulsion capability, the need to optimize these devices for relatively low (5-30 kW) power levels to make them relevant to modern satellites requires a much more comprehensive understanding of the fundamental physics of these devices. The foundation of this understanding is being built through the development of a consistent hierarchy of plasma models describing the complex behavior of magnetized partially ionized plasmas coupled with sufficient ancillary physics models (coil models for accurate evaluation of mutual inductance and Collisional-Radiative models for spectroscopic validation) to effectively study real FRC devices. By leveraging recent and on-going research efforts in fundamental algorithms for multiscale plasma simulations as well as the development of advanced physical models, the state-of-the-art in M&S capability for realistic FRC simulation is enhanced. Detailed studies will be performed to elucidate the underlying physics of FRC operation and guide existing experimental FRC thruster investigations currently underway at AFRL In-Space Propulsion Branch.

15. SUBJECT TERMS

16. SECURITY CLASSIFICATION OF:			**17. LIMITATION OF ABSTRACT**	**18. NUMBER OF PAGES**	**19a. NAME OF RESPONSIBLE PERSON**
					David Bilyeu
a. REPORT	**b. ABSTRACT**	**c. THIS PAGE**			**19b. TELEPHONE NO** *(include area code)*
Unclassified	**Unclassified**	**Unclassified**	SAR	281	N/A

Standard Form 298 (Rev. 8-98)
Prescribed by ANSI Std. 239.18

Final Report
LRIR No. 17RQCOR465

High Fidelity Modeling of Field-Reversed Configuration (FRC) Thrusters

AFOSR Program Officer: Dr. M. Birkan, AFOSR/RTA
Laboratory Task Manager: Dr. Robert Martin, AFRL/RQRS

Abstract

This work continues development of an advanced multiscale and multifidelity Modeling & Simulation (M&S) capability targeted at the fundamental studies of the physical characteristics of Field-Reversed Configuration (FRC) plasma for advanced space propulsion. This work consists of numerical method development, physical model development, and systematic studies of the non-linear plasma dynamics and finite rate chemical processes governing FRC formation, acceleration, stability and interaction with the environment. While the use of FRCs as a high efficiency/high thrust successor to the current generation of Electric Propulsion (EP) devices (Hall Effect Thrusters (HETs) and Ion thrusters) holds great promise, especially as the foundation of a true hybrid chemical/electric propulsion capability, the need to optimize these devices for relatively low (5-30 kW) power levels to make them relevant to modern satellites requires a much more comprehensive understanding of the fundamental physics of these devices. The foundation of this understanding is being built through the development of a consistent hierarchy of plasma models describing the complex behavior of magnetized partially ionized plasmas coupled with sufficient ancillary physics models (coil models for accurate evaluation of mutual inductance and Collisional-Radiative (C-R) models for spectroscopic validation) to effectively study real FRC devices. By leveraging recent and on-going research efforts in fundamental algorithms for multiscale plasma simulations as well as the development of advanced physical models, the state-of-the-art in M&S capability for realistic FRC simulation is enhanced. Detailed studies will be performed to elucidate the underlying physics of FRC operation and guide existing experimental FRC thruster investigations currently underway at Air Force Research Laboratory (AFRL) In-Space Propulsion Branch (AFRL/RQRS). In addition, this new toolset holds promise for investigating fundamental physics behavior such as magnetic reconnection, plasma turbulence, and plasma instabilities. This research has been directly transferred into in-house 6.2 R&D programs via Thermophysics Universal Research Framework (TURF) to pave the way towards a predictive FRC capability and provide a solid cornerstone for future fundamental research into other applications of interest for the United States Air Force (USAF) and future United States Space Force (USSF).

Distribution Statement A: Approved for Public Release; Distribution is Unlimited. AFRL-2021-4182

Contents

1 Introduction and Program Description **1**

1.1 Review of FRC Technology 1

1.2 Technical Challenges 3

2 Objectives and Recent Progress **5**

3 Conclusions and Recommended Future Work **9**

4 References **10**

A Enhanced Fluid Plasma Models **A-1**

A.1 Improved Models and Understanding for Field-Reversed Configuration (FRC) Thrusters (1/2): Introduction and Models A-2

A.2 Multifluid Simulations Incorporating Braginskii Transport Applied To RMF Driven Field Reversed Configuration Formation A-53

A.3 Development and implementation of a new linearized Riemann solver in TURF for the Euler equations including development of MHD solvers A-54

B Enhanced Non-Equilibrium Plasma Models **B-1**

B.1 Effects of Collisional-Radiative Processes with Relative Drift in Electric Propulsion Devices B-2

B.2 Potential Energy and Angular Momentum Conservation in Particle Merging and Collision Models B-13

C Machine Learning for FRC Formation Dynamics **C-1**

C.1 Towards Predictive M&S in the Age of Big Data and Overfitting C-2

C.2 Analyzing the Field Reversed Configuration Formation Stage using Machine Learning Algorithms C-31

C.3 Using Neural Networks to Understand Field Reversed Configuration Formation Stage C-45

C.4 Improved Models and Understanding for Field-Reversed Configuration (FRC) Thrusters (2/2): Learning and Conclusion C-46

Distribution Statement A: Approved for Public Release; Distribution is Unlimited. AFRL-2021-4182

List of Symbols and Acronyms

AFRL	Air Force Research Laboratory
AFRL/RQRS	AFRL In-Space Propulsion Branch
CEX	Charge Exchange
cFAC	C++ Variant of the Flexible Atomic Code
CFP	Closed-Field Plasmoid
C-R	Collisional-Radiative
DNN	Deep Neural Network
PINN	Physics Informed Neural Network
DSMC	Direct Simulation Monte Carlo
EEDF	Electron Energy Distribution Function
ELF	Electrodeless Lorentz Force
EMPT	Electromagnetic Plasmoid Thruster
EP	Electric Propulsion
FRC	Field-Reversed Configuration
HET	Hall Effect Thruster
Isp	Specific Impulse
LPI	Laser Plasma Interaction
LRIR	Laboratory Research Initiation Request
M&S	Modeling & Simulation
MFP	Multi-Fluid Plasma
MHD	Magnetohydrodynamics
PDE	Partial Differential Equation
PI	Preionization
PIC	Particle-In-Cell
RMF	Rotating Magnetic Field
TURF	Thermophysics Universal Research Framework
USAF	United States Air Force
USSF	United States Space Force

Related Research Grants

Grant Number

14RQCOR13 "High Fidelity Modeling of Field-Reversed Configuration (FRC) Thrusters" (PO:Birkan) [1].

17RQCOR463 "A Hybrid Model for Multiscale Laser Plasma Simulations with Detailed Collisional Physics" (PO:Marshall) [2].

20RQCOR088 "Tightly Coupled Multiphysics Modeling of High Power Electric Propulsion for Very Low Earth Orbit." (PO:Birkan).

20RQCOR098 "V&V and Optimization Using Nonlinear Dynamical Systems Theory in Electric Propulsion Devices" (PO:Leve).

Distribution Statement A: Approved for Public Release; Distribution is Unlimited. AFRL-2021-4182

High Fidelity Modeling of Field-Reversed Configuration (FRC) Thrusters

Robert Martin*, Éder M. Sousa†, Richard Abrantes‡, Michael Kapper§, Robert Lilly¶

September 8, 2021

1 Introduction and Program Description

The project continued development of the required tools for accurately simulating FRC thruster operation. This work began with the Laboratory Research Initiation Request (LRIR) "High Fidelity Modeling of Field-Reversed Configuration (FRC) Thrusters" (PO:Birkan) [1] (14RQCOR13) aimed to develop enhanced M&S tools for transient magnetized plasmas in propulsion relevant conditions. As explained in that report, this thruster concept was chosen as it is representative of many of the ubiquitous modeling challenges in the domain of dynamic low-temperature magnetized plasma. While high power FRC formation is relatively straightforward in fusion energy applications, FRC formation is considerably more challenging for anticipated levels of solar-electric spacecraft power. To overcome this challenge, a deep understanding of this lower temperature plasma regime is critical to advance plasma propulsion technology beyond the current generation of electrostatic propulsion devices such as the Hall thrusters and ion thrusters.

In this report, FRC technology is first reviewed as it was in the final report of the prior LRIR. An overview of the challenges the technology poses is also recapped. The objectives and progress that has been made since the first phase of the project is then reviewed in Section 2 broken down into subsections on physical model enhancement and efforts to extract distilled knowledge from detailed simulation results. Section 3 then provides conclusions drawn from this work and recommendations for future efforts. Finally, the appendices provide detailed reference material on work presented and published in pursuit of these objectives for reference from the main text.

1.1 Review of FRC Technology

The FRC, a type of Closed-Field Plasmoid (CFP), is a self-organized, magnetized plasma configuration in the shape of a highly compact toroid characterized by the presence of closed magnetic field lines and a high ratio of toroidal to poloidal current. The ratio of plasma pressure to magnetic pressure (β) is close to unity, i.e. the highest plasma density that can be attained for given external magnets. A small poloidal field also contributes to the particle confinement. Since FRCs are magnetically insulated from the external field - the plasma is not tied to an external field line - they can readily detach from the confining external field. Furthermore, most of the current in FRCs is

*corresponding author: robert.martin.101@us.af.mil, AFRL, Edwards AFB
†ERC Inc., Edwards AFB
‡NRC Post-Doctoral Fellow
§ERC Inc., Edwards AFB
¶Jacobs Inc., Edwards AFB

Distribution Statement A: Approved for Public Release; Distribution is Unlimited. AFRL-2021-4182

in a layer near the surface of the plasmoid so they can be efficiently translated and accelerated by applied magnetic fields. Due to a number of ancillary benefits for this configuration such as having no external electrodes (the plasma being quasi-neutral, there is no need for beam neutralization), wide propellant compatibility, high power efficiency, and low specific weight, FRCs are attractive candidates for next-generation Space Force in-space propulsion needs.

The interest in using FRCs for space propulsion involves much lower power levels (in the tens-hundreds of kW) compared to fusion energy applications which have been the focus of prior interest in the configuration. This leads to the biggest challenge in designing FRC thrusters - the difficulty in efficiently producing and accelerating plasmoids within the constraints of a limited on-orbit power budget.[1] A fundamental constraint on any fixed-power EP system is the tradeoff between propellant mass efficiency (known as Specific Impulse (Isp)) and total thrust. Given the very disparate range of potential Space Force mission requirements - high Isp/low thrust for on-orbit operations and low Isp/high thrust for rapid orbit transfer - it is critical to optimize a FRC system over a very wide trade-space. Spanning this space requires an innovative approach to thruster design for which high-fidelity simulations play a very important role. Therefore, developing this fundamental capability to study the plasma physics, especially associated with FRC thrusters, is at the heart of this project.

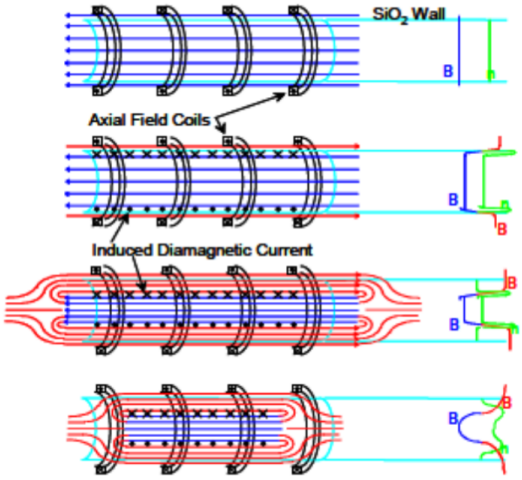

Figure 1: Schematic of θ-pinch FRC formation

To date, a limited number of laboratory thrusters have demonstrated the feasibility of using FRCs for propulsion application. Two of the most advanced designs are the Electromagnetic Plasmoid Thruster (EMPT), which uses a θ-pinch formation, and the Electrodeless Lorentz Force (ELF) thruster [3].In the θ-pinch formation, the pulse is initiated with a background uniform plasma at a constant axial (bias) field, the FRC is formed by pulsing external coils reversing the applied field. This induces currents at the plasma boundary and "pinching" of the plasma at both ends (see Fig. 1). The initial bias field is trapped inside the plasma and forced to reconnect at the end points (X-points of the "separatrix") creating an elongated toroidal shape. In the second approach, a Rotating Magnetic Field (RMF), produced by two AC antennas typically phased at 90 degrees, creates an electron plasma current large enough to reverse the axially applied bias magnetic field (see Fig. 2).

[1] In addition, design of any flight-like system must necessarily have a high power efficiency otherwise the challenges due to heat rejection become insurmountable.

Distribution Statement A: Approved for Public Release; Distribution is Unlimited. AFRL-2021-4182

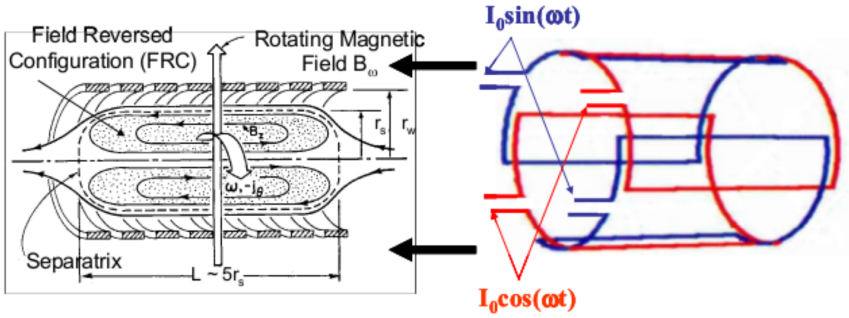

Figure 2: Schematic of RMF FRC thruster (left) and typical saddle coil geometry (right)

Though prior efforts to assess the feasibility of neutral entrainment and peristaltic dynamic acceleration [4, 5] (capture of ambient gas) for higher thruster performance have suggested additional potential options in the engineering design of FRC thrusters, significant gaps remain in the scientific understanding of the critical plasma processes involved in basic FRC formation, acceleration, and interaction with ambient gases. Computationally, the primary challenge lies in the multiscale (a typical FRC thruster spans over 5 orders of magnitude in space and 6 orders in time[2]) and multiphysics (approximate models are known to miss important physics while fully detailed kinetic simulations are computationally prohibitive) aspects of the problem. Furthermore, as progress has been made computationally, the need for highly resolved validation data have increased rapidly. To this end, AFRL/RQRS has previously had both 6.1 and 6.2 experimental efforts to develop diagnostics and FRC testbeds specifically to support better understanding of critical FRC plasma processes. While these experimental campaigns are critical to developing general design philosophies for low-power plasmoid formation, the complexity of non-linear plasma processes rapidly reduces the utility of approximate design tools as the design traverses the theoretical design envelope. While numerical simulations are an essential component for robust predictive design and optimization capability for FRC thrusters, these efforts are most productive when performed in conjunction with robust experimental capabilities.

1.2 Technical Challenges

The overall goals of the project remain the same as in LRIR 14RQ13COR. The goal is development and application of high-fidelity modeling tools to study the most important physical processes in FRC operation. The aim is improving thruster design and developing a predictive design capability. It is important to describe briefly the operational phases of the FRC thruster in order to better identify the technical challenges associated with each of them. These phases are:

1. **Preionization** - A FRC pulse begins with neutral propellant flow into the thruster. In all but the highest power FRCs, it is necessary to create a low level ($\approx 1\%$) of background plasma through some sort of Preionization (PI) process. The energetic requirements for this PI stage are low; however, the spatial distribution defines critical ionization initial conditions [6] for the formation of the first plasmoid. Recent results by Kirtley indicate that for multi-pulse plasmoid operation, the second and subsequent FRC formation processes are inherently facilitated by the final conditions of the previous pulse. The implication of this is that the residual species distribution from the first pulse must be modeled correctly. Modeling preionization

[2]Temporal scales range from inertial effects of electron motion (i.e. plasma frequency, ω_{pe}) to the transit time of neutral flows - from O(1 ns) to O(100 ms) - and spatial length scales range from the electron Debye length (λ_{De}) to the device size - from O(1 μm) to O(10 cm).

Distribution Statement A: Approved for Public Release; Distribution is Unlimited. AFRL-2021-4182

in general is extremely difficult since injected propellant could be preionized by a number of different mechanisms - indeed, besides various gas injection strategies, propellants as diverse as ionic liquids requiring separate vaporization stages are already being tested as potential FRC propellants. Since even the shortest of FRC firings consists of hundreds of individual plasmoid ejections, the high-fidelity modeling effort focused on weakly ionized, rarefied, chemically reacting flow for the accurate evaluation of the residual state of the neutral gas for the 10s of milliseconds after FRC expulsion until the subsequent formation pulse.

2. **Formation** - The plasmoid formation sequence contains the most complex series of physical processes needed for accurately modeling the operation of FRC thrusters. During this phase, the critical details of ionization kinetics drive the flow from a weakly ionized rarefied state to a fully ionized continuum state. Given the very weak collisionality at the beginning of this process, it is strongly suspected that non-equilibrium aspects of the Electron Energy Distribution Functions (EEDFs) play a critical role in the beginning of FRC formation. As the degree of ionization of the plasma increases, the EEDF should relax toward local thermodynamic equilibrium and the spatio-temporal interaction between the electron current and the applied magnetic field becomes more and more critical in defining the final envelope of the FRC.
3. **Translation** - After formation, the typical plasmoid residence time in the thruster is on the order of 10 μs. During this time, the plasma remains essentially fully ionized and the strong toroidal current interacts with the external field to produce the Lorentz force which accelerates the plasmoid. As the plasmoid translates downstream, it interacts with slow neutrals in its path through elastic and inelastic collisions. Predicting the degree to which these interactions remove/add[3] momentum from the plasmoid dictates the ultimate performance of the FRC. While the electrons may be sufficiently collisional to maintain a Maxwellian EEDF, the ions and neutrals, especially those external to the FRC, are unlikely to reach such an equilibrium and therefore may require additional kinetic treatment to accurately model their interactions with the FRC and trajectories in the near-spacecraft environment.

Each phase of FRC operation is associated with a set of technical challenges which, in turn translate into several areas of focus for this research program. The technical challenges are the following:

1. **Field/plasma model** - Plasmas are extremely rich in physics largely because of the coupling between the phase space configuration and self-induced electromagnetic forces; furthermore, in a sharp break from neutral flows, plasma responds to non-local effects (such as external magnetic fields) at the timescales of the speed-of-light. In FRCs, given the relatively slow frequency of the RMF driving field and the diffusion of neutral gases relative to the electron plasma frequency, there is an enormous range of timescales which the field/plasma model must resolve. Different plasma models attempt to circumvent this multi-scale problem through fundamental assumptions which restrict the limit to which the model is valid. For instance, Magnetohydrodynamics (MHD) has been frequently used for FRC simulation but makes the very strict assumption that the plasma is a single quasi-neutral fluid. While the quasi-neutrality assumption most likely is not the case as multi-fluid modeling indicates coherent charge separation structures, these models still provide good qualitative insight and are relatively computationally inexpensive. Moving through the hierarchy of fluid models gradually relaxes these assumptions and permits more fundamental physics of the FRC device to emerge. Kinetic models, such as a Particle-In-Cell (PIC) approach, free the simulation to explore the full range of plasma even when non-local thermal equilibrium is required.

[3]The neutral entrainment concept actually relies on the elastic Charge Exchange (CEX) mechanism to recover momentum from the flow between pulses of additional downstream coils

Distribution Statement A: Approved for Public Release; Distribution is Unlimited. AFRL-2021-4182

2. **Collisional physics** - The kinetics of ionization are critical to the efficiency (and ultimate success) of FRC formation at low power levels. This process can best be simulated through the use of a sufficiently detailed C-R model. Furthermore, since the electrons are likely to be non-Maxwellian to some degree during the formation process (especially since the PI stage generates such a small number of electrons), the potential need for non-Maxwellian C-R should also be considered. Inelastic particle collisions, particularly dealing with momentum and energy exchange between charged and neutral species in the multi-fluid plasma model, must also be consistently derived from underlying excitation, recombination and ionization cross sections to ensure that comparison/hybridization between continuum (which use rate based terms) and kinetic (which use cross-sections) codes are consistent.
3. **Multi-scale effects** - FRC simulation is particularly challenging because of the dramatic differences in plasma behavior inside and outside the separatrix. In the interior, continuum approaches can generally be used effectively to average the small scale features (such as the Debye length and Larmor radius); however, it is the kinetic effects which at the boundary of the separatrix, such as magnetic reconnection at the X-points, which drive critical physics of FRC formation. Developing numerical techniques to extend kinetic simulation to larger time and length-scales without losing numerical stability and accuracy, as well as developing hybridization techniques to couple with continuum models, is critical to resolution of the full spectrum of scales necessary to correctly predict FRC physics.
4. **System complexity** - Any realistic FRC simulation toolkit requires at least a certain level of accuracy in the representation of geometric and materials complexities. For instance, the driving coil for the RMF requires an antenna with a complex shape ("saddle coil", see Fig. 2) which results in an applied field that is neither truly uniform nor conveniently symmetric. While previous experimental validation programs at AFRL/RQRS attempted to reduce the geometric complexity as much as possible, progress in model validation is slow without the ability to run parallel numerical and experimental studies. While gaseous monatomic propellants are the first choice for study of FRC thrusters, the potential for operation on alternative propellant materials such as ionic liquid decomposition products or even high altitude earth or martian atmospheric gasses provides interesting potential paths towards significantly enhanced propulsion capabilities. However, the added complexity of molecular mixture collisional processes and their interactions with the plasmadynamics further complicates the development and integration of the numerical and physical models required for design of these potential systems.

Though necessary for understanding FRC thrusters, the technical challenges listed above have application to a broad range of plasma conditions beyond FRCs. For instance, the same challenges addressed with the field/plasma model are immediately applicable to problems such as theoretical as astrophysics and applied as plasma processing. Similarly, the same collisional physical models needed to study FRC plasma evolution are critical for developing reliable spectral thruster diagnostics. Similarly, the same multi-scale effects which characterize FRC thrusters also challenge our existing generation of HET simulation tools [7]. Any advancements made in bridging the scale gap will contribute directly to further investigation of the plasma turbulence characterizing virtually all magnetized plasma environments, both for propulsion and power generation.

2 Objectives and Recent Progress

The overall goal of this program is the development of a coherent hierarchy of computational models from kinetic to continuum regimes capable of modeling complex multi-scale plasma encountered in USSF propulsion applications like those specifically encountered in the FRC thruster. Though

Distribution Statement A: Approved for Public Release; Distribution is Unlimited. AFRL-2021-4182

understanding the details of every phase of FRC operation is a lofty challenge, enormous progress can be made through the appropriate development and implementation of fundamental physics models.

In addition, gains in algorithmic acceleration, hardware acceleration, and the recent development of our modern, flexible object-oriented simulation framework, TURF [8, 9], offered promising opportunities to apply and couple these disparate models. However, validation of these computational developments slowed with the discontinuation of in-house 6.2 experimental validation campaigns and preionization studies. While collaboration with MSNW LLC briefly alleviated this data deficit, the ability to design high-efficiency, low-power FRC thrusters critically depends on close interaction between numerical and experimental efforts.

In this phase of the project, progress has been made in the following areas:

1. **Enhanced Fluid Plasma Models** - In the prior effort, a multi-fluid plasma framework which includes electron momentum was developed to explore breakdown of standard magnetohydrodynamic physics in the FRC. This effort has been previously described in detail in Reference [1]. The current effort, overviewed in the presentation attached in Appendix A.1, aimed to extend the range of validity for these models to produce predictions in relevant plasma conditions for the existing low power FRC experiments.

   The major model extensions explored for expanding the range of applicability in this work were the incorporation of electron fluid (Braginskii) transport and enhancing numerical stability through the hybridization of standard energy conserving Riemann solvers with an entropy conserving Riemann solver. These efforts were aimed at overcoming stability challenges with the original fluid model when applied to strong rarefaction as when the plasmoid leaves the thruster wall during formation when the electron temperature is low. Strong rarefaction violates the fluid assumptions upon which the Multi-Fluid Plasma (MFP) model was derived. Strong rarefactions generally challenge energy conserving fluid equations requiring the incorporation of sufficiently aggressive limiters that induce numerical diffusion that artificially heats the flow in order to avoid negative pressure solver numerical failures.

   A first attempt to mitigate the impacts of this strong rarefaction, shown in Appendix A.2, is a poster describing efforts to incorporate Braginskii transport within the Apollo framework. The idea was that sufficient physical diffusion could potentially alleviate the need for aggressive limiters to stabilize the numerical solution in the rarefaction region. A reference Couette flow validation configuration was tested with moderate success. However, the amount of physical transport provided proved insufficient to fully stabilize the MFP solver for low temperature electrons.

   In a subsequent effort described in detail in Appendix A.3, Dr. Kapper attempted to directly mitigate the challenges invoked by strong rarefactions by developing a novel hybrid fluid solver that transitions from energy to entropy conserving formulations adaptively based off the local fluid conditions. This handoff is required for flows that include both shocks and strong rarefactions. The entropy conserving formulation is ideal for strong rarefactions as it mitigates the need for entropy conservation violating limiters. However, entropy increases within shocks in Euler flows and therefore the energy conserving formulation is required in regions near shocks to provide accurate jump conditions. In anticipation of more general utility, these solvers were incorporated into the TURF framework for use in future projects, though the hybridization

Distribution Statement A: Approved for Public Release; Distribution is Unlimited. AFRL-2021-4182

has not yet been fully ported to the framework. In the case of the FRC formation problem, the entropy preserving formulation may be sufficient to preserve electron pressure positivity in the strong rarefaction region. As long as the electron fluid remains subsonic and are not expected to form shockwaves, this is a reasonable model for non-neutral FRC formation studies and recommended for further evaluation in future work.

2. **Enhanced Non-Equilibrium Models** - In the prior phase of the program, inelastic rates resulting from inelastic C-R mechanisms were derived as described in References [10, 11]. The work used inelastic cross-sections leveraging a detailed C-R model developed through a parallel Laser Plasma Interaction (LPI) LRIR to generate mass, momentum and energy exchange terms for the MFP closure model in the method suggested. This ensures that the plasma hierarchy is consistent with respect to collisional transport. In the prior work, only detailed multi-fluid rates for hydrogen were obtained due to the simplicity of accessing the necessary cross sections. In the current phase of the project, this method has been applied to detailed multistage xenon C-R ionization based on the C++ Variant of the Flexible Atomic Code (cFAC) [12, 13] described in Appendix B.1. Rather than attempting to run the rate calculations in-line, the rate data is tabulated as in the case of the output of other C-R models like the IONMIX code[14]. However, in the multi-fluid version of these rate tables, an additional axis is included to account for the relative drift/streaming velocity of the electron fluid to account for the variation of collisional interactions as a function of electron current in the ion fluid center of mass reference frame. This allows for tabulation of necessary closure rates. Since the conclusion of this phase of the project, this work has been extended further in Reference [15] as part of the new LRIR project, "Tightly Coupled Multiphysics Modeling of High Power Electric Propulsion for Very Low Earth Orbit." (PO:Birkan) (20RQCOR088).

   Long term goals for the program included extending to the application of non-Maxwellian C-R models to account for electron non-equilibrium kinetic behavior of the plasma during the initial phases of ionization. While the majority of this work has shifted to the companion LRIR project, "A Hybrid Model for Multiscale Laser Plasma Simulations with Detailed Collisional Physics" (PO:Marshall) [2] (17RQCOR463), one contribution stemming from this project is a suggested modification to the elastic Coulomb collision mechanism for particle plasma codes described in Appendix B.2. It was found that the Direct Simulation Monte Carlo (DSMC) method for processing elastic Coulomb collisions pioneered by Nanbu (References [16, 17]) could be modified slightly to ensure that the collisions were processed in a plane conserving angular momentum. In the traditional DSMC methods, this collision plane was selected randomly and is a reasonable choice for unmagnetized Coulomb collisions. While the DSMC method has long ago been shown to conserve angular momentum in the asymptotic limit of infinitesimal collision partner distance, in the finite particle count limit, this results in random walks in angular momentum. By replacing the random orientation of the collision plane with a plane defined by the relative physical location of collision partner pairs, the angular momentum conservation is guaranteed. Further work is required to determine if this choice non-physically impacts correlations for plasma with density gradients, but at the very least, this method should inhibit non-physical numerical diffusion of gyro-centers resulting in numerical inaccuracies when elastic collisions are activated. This work should further be extended to both short-range elastic and inelastic collisions for transitionally collisional magnetized plasma flows.

Distribution Statement A: Approved for Public Release; Distribution is Unlimited. AFRL-2021-4182

3. **Machine Learning for FRC Formation Dynamics** - While physical fidelity of FRC simulations have continued to be advanced, a major outstanding issue remains in validation of these simplified models in the context of non-idealized experimental complexities. Rather than examining point solutions that are certain to diverge from even the most carefully controlled experiments due to the inherent idealizations used in the models, extracting actionable insights from the simulations requires identification of non-trivial trends present in ensembles of simulations. While the nonlinear complexity of the very high degree of freedom simulations provides no guarantee that there is a smooth behavioral response from input conditions to final output observations, the dynamics connecting initial and final state for Partial Differential Equation (PDE) solutions of autonomous physical dynamics implies the existence of smooth nonlinear maps from input to output observable. This philosophy is described in the presentation material attached in Appendix C.1.

   The existence of this nonlinear input-output dependence suggest that a sufficiently powerful universal nonlinear approximator could potentially exploit any inherent physical regularity in the output space to more rapidly extract and predict interpolative trends in the observed outputs of interest. This motivated the work described in Appendices C.2 & C.3. In this work, the problem of formation for the RMF FRC is explored by analyzing the sort of estimates for the boundary between formation and failure that exist by building various machine learned classifiers on an ensemble of numerical test cases. In particular, the trend extracted from a Deep Neural Network (DNN) classifier attained a 92% accuracy in predicting field reversal from the simulations and most interestingly identified a need for slightly higher applied RMF amplitude for a given RMF frequency to obtain reversal than is predicted by the estimates of Milroy in Reference [18]. While true for the multi-fluid numerical implementation studied, a corresponding experimental campaign should be explored in the future to confirm these predictions.

   Even for relatively simple binary classification, i.e. does field reversal exits for a given input condition, data for learning this input-output map may be quite large for complex systems. While this can potentially be mitigated via adaptive sampling coupled within the numerical or experimental learning loop, this unconstrained learning process remains fundamentally an interpolative one with few guarantees for extrapolative power to configurations not previously encountered. This is generally a concern for complex engineering systems where the number of experimental test cases possible for validation may be quite low. However, an assumption that physical processes are fundamentally invariant in space and time enables recasting this learning process to one of learning an input-output map for unresolved model closures rather than attempting to extract an input-output map from experimental condition all the way to observed quantity of interest. It is therefore conjectured that machine learned closures for unresolved/modeled physical phenomena may offer both a better constrained learning process and potentially more experimental observations per experiment than is possible for prediction of final quantities of interest. This alternative approach, initially proposed in Appendix C.1 suggests an alternate route towards predictive modeling by using the model calibration process to infer invariant unresolved physical mechanism. This approach, paralleling the recent push towards Physics Informed Neural Network (PINN) architectures such as Reference [19], shifts some of the prediction burden back onto the numerically resolvable physics with the learning constrained to invariant closure relationships that are potentially less data intensive. This learning is best constrained by attempting to close a feed-back loop between model parameters and experimental observation. This approach helped spawn a follow on LRIR project, "V&V

Distribution Statement A: Approved for Public Release; Distribution is Unlimited. AFRL-2021-4182

and Optimization Using Nonlinear Dynamical Systems Theory in Electric Propulsion Devices" (PO:Leve) (20RQCOR098), where some of these ideas may be explored more fully in the future. It also provides a major recommendation that future efforts should involve tight coupling between experimental and modeling efforts focused at synchronizing model with observed experimental plasma closure relationships to help learn generalized relationships useful for constructing the physically constrained surrogate models needed for rapid design optimization in the future.

3 Conclusions and Recommended Future Work

The overall project enhanced AFRL capabilities for modeling MFP models for simulating magnetized pulsed thruster configurations. However, significantly more work is required to extend these capabilities to more realistic three-dimensional boundary conditions. The suspension of both AFRL and external (MSNW LLC) experimental campaigns further inhibited progress towards a validation of these modeling capabilities. While progress continued advancing model capabilites, without a steady supply of validation data, it is hard to confirm whether the enhancements address the near term model insufficiencies. Further, while the machine learning effort produced interesting new trends in the prediction of field reversal for the FRC formation progress, it is challenging to determine whether this observed discrepancy from prior efforts to estimate this boundary result from numerical inadequacies or if the observed trend is physically present in experimental attempts to form FRC plasmoids. It is therefore highly recommended that future resumption of FRC model development is closely integrated with a parallel experimental campaign. Due to the complex dynamical response of FRC formation to input pulse, timing, and physical geometry, making significant progress towards FRC thruster designs with sufficient efficiency for practical low-power operation remains elusive. It is therefore highly encouraged that future research efforts incorporate significant data fusion and model synchronization in building the physics informed surrogate models necessary for efficient exploration of the FRC design space. Within AFRL, this motivates taking a step back to determine the steps necessary for plasma model experimental synchronization in relatively simpler HET configurations where relatively simpler quasi steady-state operation is sought before attempting to tackle the full complexity of pulsed transient plasma.

Distribution Statement A: Approved for Public Release; Distribution is Unlimited. AFRL-2021-4182

4 References

References

[1] J. Koo, Eder Sousa, and Robert Martin. "Final Report: High Fidelity Modeling of Field-Reversed Configuration (FRC) Thrusters". In: *AFRL Technical Report*. AFRL-RQ-ED-TR-2017-0002. Edwards AFB, CA, May 2017.

[2] David Bilyeu. "Final Report: A Hybrid Model for Multiscale Laser Plasma Simulations with Detailed Collisional Physics". In: *AFRL Technical Report*. AFRL-RQ-ED-TR-2017-0012. Edwards AFB, CA, June 2017.

[3] John T Slough, David E Kirtley, and Thomas Weber. "Pulsed Plasmoid Propulsion: The ELF Thruster". In: *31st Int. Electr. Propuls. Conf.* Ann Arbor, Michigan, 2009, pp. 1–24. URL: http://erps.spacegrant.org/uploads/images/images/iepc_articledownload_1988-2007/2009index/IEPC-2009-265.pdf.

[4] David Kirtley et al. *Neutral Entrainment Demonstation in a Xenon FRC Thruster Experiment*. Tech. rep. ADA596806. PA#13192. DTIC, Mar. 2013.

[5] Jeremiah Brackbill et al. "Ionization and Charge Exchange Reactions in a Neutral Entrainment of a Field Reversed Configuration Thruster". In: *AIAA-2012-4102*. 48th AIAA Joint Propulsion Conference. Atlanta, GA, 2012.

[6] M. Tuszewski. "Field reversed configurations". In: *Nuclear Fusion* 28 (1988), pp. 2033–2092.

[7] S. J. Araki et al. "SM/MURF: Current Capabilities and Verification as a Replacement of AFRL Plume Simulation Tool COLISEUM". In: *52nd AIAA/SAE/ASEE Joint Propulsion Conference*. AIAA 2016-4939. Salt Lake City, Utah, 2016, pp. 1–29.

[8] Robert Martin and Justin Koo. Thermophysics Universal Research Framework - Infrastructure Release. Version 1.0.0. Air Force Research Laboratory (AFRL/RQRS). Apr. 2015.

[9] Samuel Araki et al. Tutorial for the Thermophysics Universal Research Framework. TURF-IR 2017a, PA#17441. AFRL-RQ-ED-OT-2017-186. Air Force Research Laboratory (AFRL/RQRS). May 2017.

[10] Hai P. Le and Jean-Luc Cambier. "Modeling of inelastic collisions in a multifluid plasma: Excitation and deexcitation". In: *Physics of Plasmas* 22.9 (2015), p. 093512. DOI: 10.1063/1.4931170. eprint: https://doi.org/10.1063/1.4931170. URL: https://doi.org/10.1063/1.4931170.

[11] Hai P. Le and Jean-Luc Cambier. "Modeling of inelastic collisions in a multifluid plasma: Ionization and recombination". In: *Physics of Plasmas* 23.6 (2016), p. 063505. DOI: 10.1063/1.4953050. eprint: https://doi.org/10.1063/1.4953050. URL: https://doi.org/10.1063/1.4953050.

[12] M.F. Gu. "The flexible atomic code". In: *Canadian Journal of Physics* 86.5 (2008), pp. 675–689. DOI: 10.1139/P07-197.

[13] E. Stambulchik. *cFAC*. https://github.com/fnevgeny/cfac.

[14] J.J. Macfarlane. "IONMIX - a code for computing the equation of state and radiative properties of LTE and non-LTE plasmas". In: *Computer Physics Communications* 56.2 (1989), pp. 259–278. ISSN: 0010-4655. DOI: https://doi.org/10.1016/0010-4655(89)90023-4. URL: http://www.sciencedirect.com/science/article/pii/0010465589900234.

Distribution Statement A: Approved for Public Release; Distribution is Unlimited. AFRL-2021-4182

[15] Richard J. E. Abrantes and Robert S. Martin. "Reduced-order modeling of plasma ionization due to multifluid, collisional-radiative effects". In: *Physics of Plasmas* 28.2 (2021), p. 022104. DOI: 10.1063/5.0029881. eprint: https://doi.org/10.1063/5.0029881. URL: https://doi.org/10.1063/5.0029881.

[16] K. Nanbu. In: *Phys. Rev. E* 55 (1997), pp. 4642–4652.

[17] K. Nanbu. "Probability Theory of Electron-Molecule, Ion-Molecule, Molecule-Molecule, and Coulomb Collisions for Particle Modeling of Materials Processing Plasmas and Gases". In: *Trans. Plasma Science* 28 (3 2000), pp. 971–989.

[18] Richard D. Milroy. "A numerical study of rotating magnetic fields as a current drive for field reversed configurations". In: *Phys. Plasmas* 6.7 (1999), p. 2771. ISSN: 1070664X. DOI: 10.1063/1.873234. URL: http://link.aip.org/link/PHPAEN/v6/i7/p2771/s1%7B%5C&%7DAgg=doi.

[19] Maziar Raissi, Alireza Yazdani, and George Em Karniadakis. "Hidden fluid mechanics: Learning velocity and pressure fields from flow visualizations". In: 367.6481 (2020), pp. 1026–1030. DOI: 10.1126/science.aaw4741.

Distribution Statement A: Approved for Public Release; Distribution is Unlimited. AFRL-2021-4182

A Enhanced Fluid Plasma Models **A-1**

A.1 Improved Models and Understanding for Field-Reversed Configuration (FRC) Thrusters (1/2): Introduction and Models A-2

A.2 Multifluid Simulations Incorporating Braginskii Transport Applied To RMF Driven Field Reversed Configuration Formation A-53

A.3 Development and implementation of a new linearized Riemann solver in TURF for the Euler equations including development of MHD solvers A-54

Distribution Statement A: Approved for Public Release; Distribution is Unlimited. AFRL-2021-4182

Improved Models and Understanding for Field-Reversed Configuration (FRC) Thrusters

Robert Martin[1], Eder Sousa[2], Robert Lilly[2], Michael Kapper[2]

[1]Air Force Research Laboratory,
[2]ERC Inc.,
Edwards Air Force Base, CA USA

AFOSR Space Propulsion and Power Review, 2018
Distribution A - Approved for public release;
Distribution unlimited.
PA clearance No. 18476

Distribution Statement A: Approved for Public Release; Distribution is Unlimited. AFRL-2021-4182

Outline

1. Introduction & Challenges
2. Model Enhancements
3. Learning in Parameter Space
4. Conclusion & Future Directions

Distribution Statement A: Approved for Public Release; Distribution is Unlimited. AFRL-2021-4182

Introduction to Air Force FRC Interest

Field-Reversed Configuration:

- Concept from Fusion Energy
  - Challenge Scaling Down for Propulsion

RP3X FRC Thruster

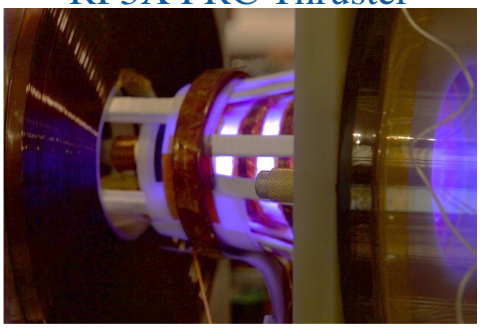

Distribution Statement A: Approved for Public Release; Distribution is Unlimited. AFRL-2021-4182

Introduction to Air Force FRC Interest

Field-Reversed Configuration:

- Concept from Fusion Energy
  - Challenge Scaling Down for Propulsion
- Electrodeless (+ Limits Erosion)

RP3X FRC Thruster

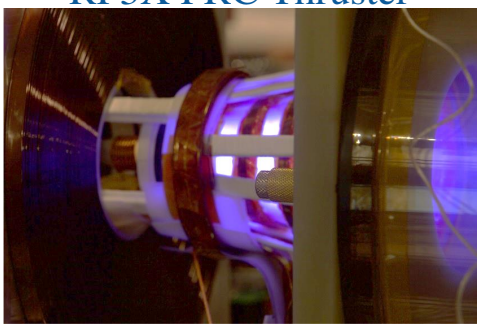

Distribution Statement A: Approved for Public Release; Distribution is Unlimited. AFRL-2021-4182

Introduction to Air Force FRC Interest

Field-Reversed Configuration:

- Concept from Fusion Energy
  - Challenge Scaling Down for Propulsion
- Electrodeless (+ Limits Erosion)
- Acceleration Mechanism $J \times B$
  + Enables Flexible Fuels

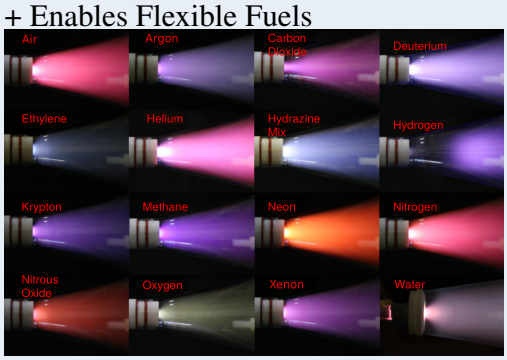

Pancotti, et al, "Adaptive Electric Propulsion for ISRU Missions", 20th Adv. Space Prop., 11/2014

RP3X FRC Thruster

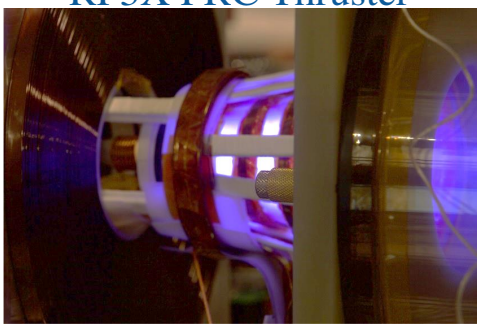

Distribution Statement A: Approved for Public Release; Distribution is Unlimited. AFRL-2021-4182

Introduction to Air Force FRC Interest

Field-Reversed Configuration:

- Concept from Fusion Energy
  - Challenge Scaling Down for Propulsion
- Electrodeless (+ Limits Erosion)
- Acceleration Mechanism $J \times B$
  + Enables Flexible Fuels
- Pulsed Operation
  +Tunable Thrust/ISP
  - Complex Coupled Dynamics
  - High Dimensional Parameter Space

RP3X FRC Thruster

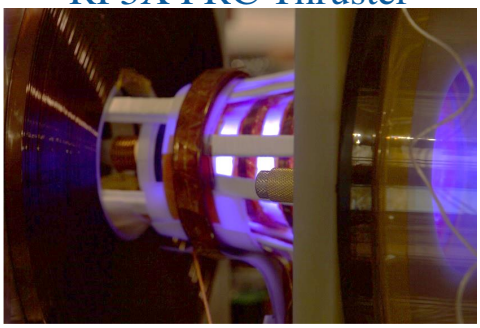

Distribution Statement A: Approved for Public Release; Distribution is Unlimited. AFRL-2021-4182

Introduction to Air Force FRC Interest

Field-Reversed Configuration:

- Concept from Fusion Energy
  - Challenge Scaling Down for Propulsion
- Electrodeless (+ Limits Erosion)
- Acceleration Mechanism $J \times B$
  + Enables Flexible Fuels
- Pulsed Operation
  +Tunable Thrust/ISP
  - Complex Coupled Dynamics
  - High Dimensional Parameter Space
- Common Challenges/Benefits for EM
  + MPD/PIT/PPT

Complex Devices to Design

RP3X FRC Thruster

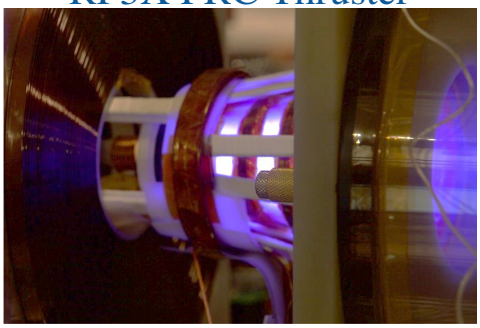

Distribution Statement A: Approved for Public Release; Distribution is Unlimited. AFRL-2021-4182

Introduction to Air Force FRC Interest

Field-Reversed Configuration:

- Concept from Fusion Energy
  - Challenge Scaling Down for Propulsion
- Electrodeless (+ Limits Erosion)
- Acceleration Mechanism $J \times B$
  + Enables Flexible Fuels
- Pulsed Operation
  +Tunable Thrust/ISP
  - Complex Coupled Dynamics
  - High Dimensional Parameter Space
- Common Challenges/Benefits for EM
  + MPD/PIT/PPT
  + Similar Tools Required

Complex Devices to Design
Pose Significant Modeling Challenge

RP3X FRC Thruster

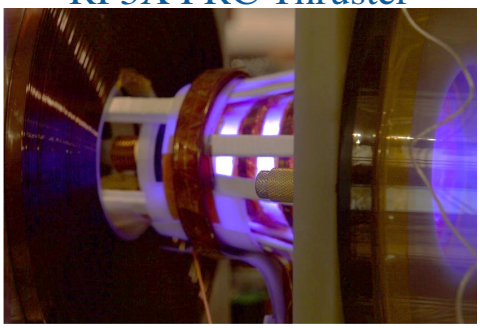

Distribution Statement A: Approved for Public Release; Distribution is Unlimited. AFRL-2021-4182

Tool Development Spanning Regimes

The Boltzmann Equation for $f(\mathbf{x}, \mathbf{v}; t)$:

$$\frac{\partial f_s}{\partial t} + \mathbf{v} \cdot \frac{\partial f_s}{\partial \mathbf{x}} + \frac{q_s}{m_s}(\mathbf{E} + \mathbf{v} \times \mathbf{B}) \frac{\partial f_s}{\partial \mathbf{v}} = \left(\frac{\partial f_s}{\partial t} \right)_{coll}$$

Range of Validity

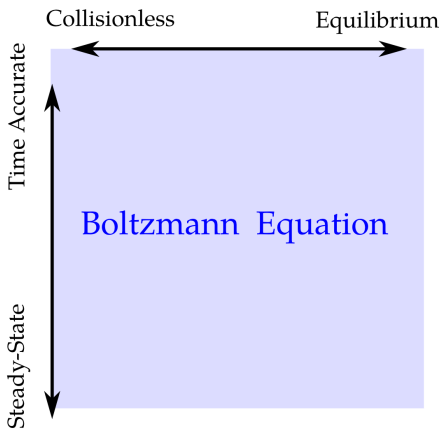

Distribution Statement A: Approved for Public Release; Distribution is Unlimited. AFRL-2021-4182

Tool Development Spanning Regimes

The Boltzmann Equation for $f(\mathbf{x}, \mathbf{v}; t)$:

$$\frac{\partial f_s}{\partial t} + \mathbf{v} \cdot \frac{\partial f_s}{\partial \mathbf{x}} + \frac{q_s}{m_s}(\mathbf{E} + \mathbf{v} \times \mathbf{B}) \frac{\partial f_s}{\partial \mathbf{v}} = \left(\frac{\partial f_s}{\partial t} \right)_{coll}$$

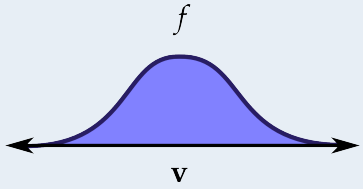

Range of Validity

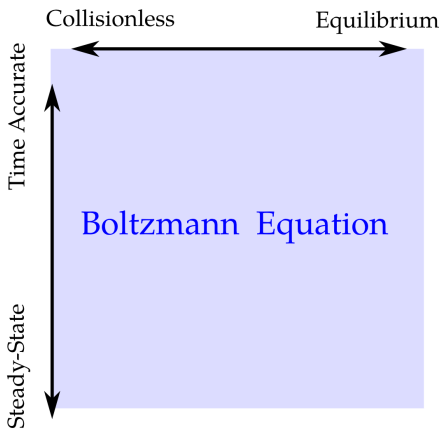

Distribution Statement A: Approved for Public Release; Distribution is Unlimited. AFRL-2021-4182

Tool Development Spanning Regimes

The Boltzmann Equation for $f(\mathbf{x}, \mathbf{v}; t)$:

$$\frac{\partial f_s}{\partial t} + \mathbf{v} \cdot \frac{\partial f_s}{\partial \mathbf{x}} + \frac{q_s}{m_s}(\mathbf{E} + \mathbf{v} \times \mathbf{B}) \frac{\partial f_s}{\partial \mathbf{v}} = \left(\frac{\partial f_s}{\partial t} \right)_{coll}$$

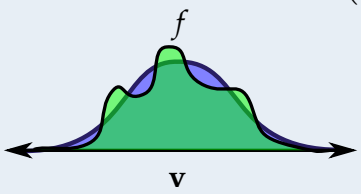

Range of Validity

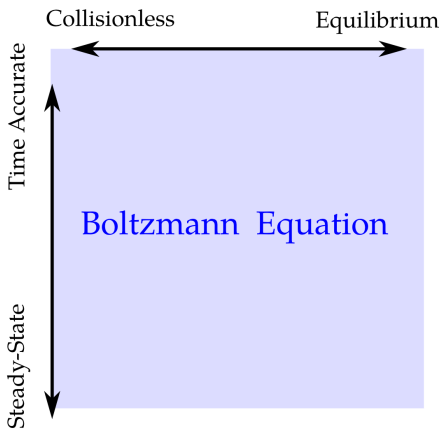

Distribution Statement A: Approved for Public Release; Distribution is Unlimited. AFRL-2021-4182

Tool Development Spanning Regimes

The Boltzmann Equation for $f(\mathbf{x}, \mathbf{v}; t)$:

$$\frac{\partial f_s}{\partial t} + \mathbf{v} \cdot \frac{\partial f_s}{\partial \mathbf{x}} + \frac{q_s}{m_s}(\mathbf{E} + \mathbf{v} \times \mathbf{B}) \frac{\partial f_s}{\partial \mathbf{v}} = \left(\frac{\partial f_s}{\partial t} \right)_{coll}$$

- Collisionality Limits:
  (Vlasov) $0 \leftarrow \left(\frac{\partial f_s}{\partial t} \right)_{coll} \rightarrow \infty$ (Euler)

Range of Validity

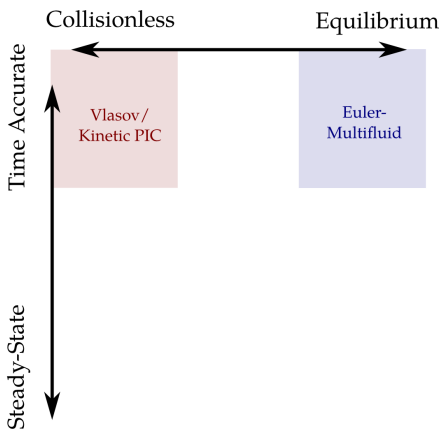

Distribution Statement A: Approved for Public Release; Distribution is Unlimited. AFRL-2021-4182

Tool Development Spanning Regimes

The Boltzmann Equation for $f(\mathbf{x}, \mathbf{v}; t)$:

$$\frac{\partial f_s}{\partial t} + \mathbf{v} \cdot \frac{\partial f_s}{\partial \mathbf{x}} + \frac{q_s}{m_s}(\mathbf{E} + \mathbf{v} \times \mathbf{B}) \frac{\partial f_s}{\partial \mathbf{v}} = \left(\frac{\partial f_s}{\partial t} \right)_{coll}$$

- Collisionality Limits:
  $$\text{(Vlasov) } 0 \leftarrow \left(\frac{\partial f_s}{\partial t} \right)_{coll} \rightarrow \infty \text{ (Euler)}$$
- Ohm's Law:
  $$(m_e \ll m_i) \rightarrow \frac{\partial f_e}{\partial t} \equiv 0$$

Range of Validity

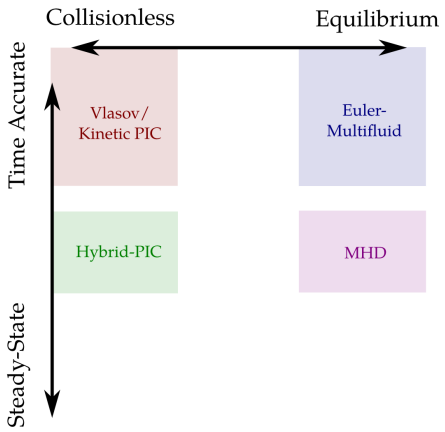

Distribution Statement A: Approved for Public Release; Distribution is Unlimited. AFRL-2021-4182

Tool Development Spanning Regimes

The Boltzmann Equation for $f(\mathbf{x}, \mathbf{v}; t)$:

$$\frac{\partial f_s}{\partial t} + \mathbf{v} \cdot \frac{\partial f_s}{\partial \mathbf{x}} + \frac{q_s}{m_s}(\mathbf{E} + \mathbf{v} \times \mathbf{B}) \frac{\partial f_s}{\partial \mathbf{v}} = \left(\frac{\partial f_s}{\partial t} \right)_{coll}$$

- Collisionality Limits:
  $$\text{(Vlasov) } 0 \leftarrow \left(\frac{\partial f_s}{\partial t} \right)_{coll} \rightarrow \infty \text{ (Euler)}$$
- Ohm's Law:
  $$(m_e \ll m_i) \rightarrow \frac{\partial f_e}{\partial t} \equiv 0$$
- Steady-State Solutions:
  $$\frac{\partial}{\partial t} \equiv 0$$

Range of Validity

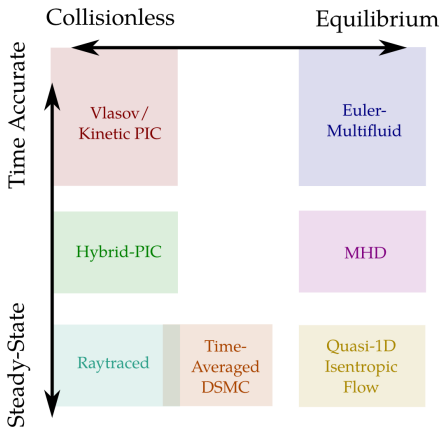

Distribution Statement A: Approved for Public Release; Distribution is Unlimited. AFRL-2021-4182

Tool Development Spanning Regimes

The Boltzmann Equation for $f(\mathbf{x}, \mathbf{v}; t)$:

$$\frac{\partial f_s}{\partial t} + \mathbf{v} \cdot \frac{\partial f_s}{\partial \mathbf{x}} + \frac{q_s}{m_s}(\mathbf{E} + \mathbf{v} \times \mathbf{B}) \frac{\partial f_s}{\partial \mathbf{v}} = \left(\frac{\partial f_s}{\partial t} \right)_{coll}$$

- Collisionality Limits:
  $$\text{(Vlasov) } 0 \leftarrow \left(\frac{\partial f_s}{\partial t} \right)_{coll} \rightarrow \infty \text{ (Euler)}$$
- Ohm's Law:
  $$(m_e \ll m_i) \rightarrow \frac{\partial f_e}{\partial t} \equiv 0$$
- Steady-State Solutions:
  $$\frac{\partial}{\partial t} \equiv 0$$

Limits Exchange Accuracy for Cost

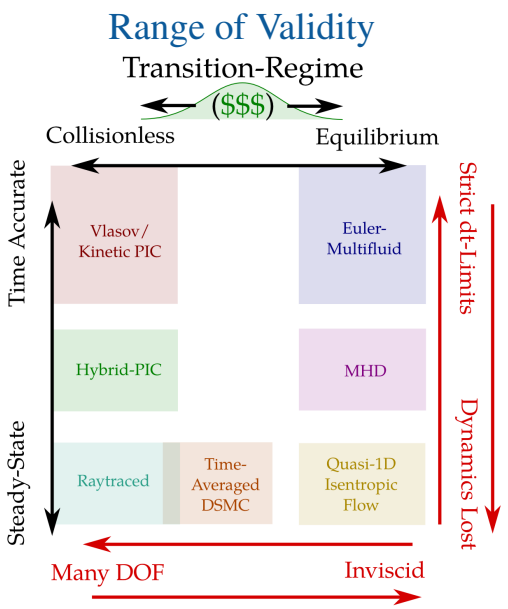

Distribution Statement A: Approved for Public Release; Distribution is Unlimited. AFRL-2021-4182

Tool Development Spanning Regimes

The Boltzmann Equation for $f(\mathbf{x}, \mathbf{v}; t)$:

$$\frac{\partial f_s}{\partial t} + \mathbf{v} \cdot \frac{\partial f_s}{\partial \mathbf{x}} + \frac{q_s}{m_s}(\mathbf{E} + \mathbf{v} \times \mathbf{B}) \frac{\partial f_s}{\partial \mathbf{v}} = \left(\frac{\partial f_s}{\partial t} \right)_{coll}$$

- Collisionality Limits:
  $$\text{(Vlasov) } 0 \leftarrow \left(\frac{\partial f_s}{\partial t} \right)_{coll} \rightarrow \infty \text{ (Euler)}$$
- Ohm's Law:
  $$(m_e \ll m_i) \rightarrow \frac{\partial f_e}{\partial t} \equiv 0$$
- Steady-State Solutions:
  $$\frac{\partial}{\partial t} \equiv 0$$

Limits Exchange Accuracy for Cost

Transition Incurs Costs to Limit

Range of Validity

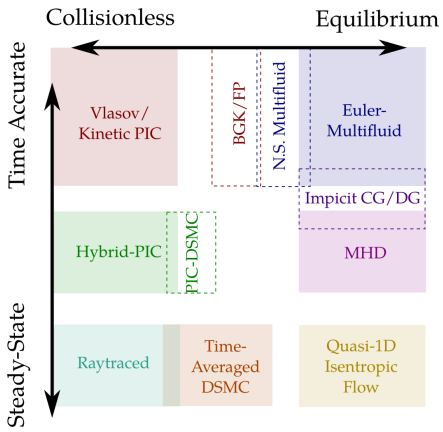

Distribution Statement A: Approved for Public Release; Distribution is Unlimited. AFRL-2021-4182

Tool Development Spanning Regimes

The Boltzmann Equation for $f(\mathbf{x}, \mathbf{v}; t)$:

$$\frac{\partial f_s}{\partial t} + \mathbf{v} \cdot \frac{\partial f_s}{\partial \mathbf{x}} + \frac{q_s}{m_s}(\mathbf{E} + \mathbf{v} \times \mathbf{B}) \frac{\partial f_s}{\partial \mathbf{v}} = \left(\frac{\partial f_s}{\partial t} \right)_{coll}$$

- Collisionality Limits:
  $$\text{(Vlasov) } 0 \leftarrow \left(\frac{\partial f_s}{\partial t} \right)_{coll} \rightarrow \infty \text{ (Euler)}$$
- Ohm's Law:
  $$(m_e \ll m_i) \rightarrow \frac{\partial f_e}{\partial t} \equiv 0$$
- Steady-State Solutions:
  $$\frac{\partial}{\partial t} \equiv 0$$

Limits Exchange Accuracy for Cost
Transition Incurs Costs to Limit
$(\nu = 0 \neq \nu \rightarrow 0)$
But Relaxes/Removes Assumptions

Range of Validity

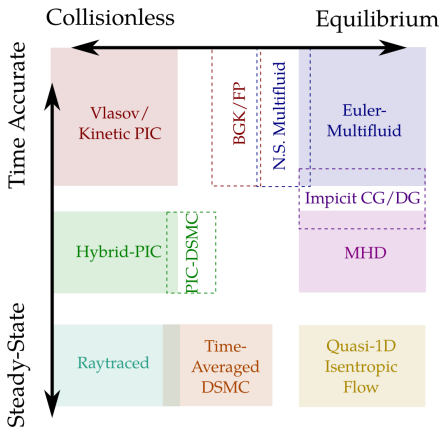

Distribution Statement A: Approved for Public Release; Distribution is Unlimited. AFRL-2021-4182

Tool Development Spanning Regimes

The Boltzmann Equation for $f(\mathbf{x}, \mathbf{v}; t)$:

$$\frac{\partial f_s}{\partial t} + \mathbf{v} \cdot \frac{\partial f_s}{\partial \mathbf{x}} + \frac{q_s}{m_s}(\mathbf{E} + \mathbf{v} \times \mathbf{B}) \frac{\partial f_s}{\partial \mathbf{v}} = \left(\frac{\partial f_s}{\partial t} \right)_{coll}$$

- Collisionality Limits:
  $(\text{Vlasov}) \; 0 \leftarrow \left(\frac{\partial f_s}{\partial t} \right)_{coll} \rightarrow \infty \; (\text{Euler})$
- Ohm's Law:
  $(m_e \ll m_i) \rightarrow \frac{\partial f_e}{\partial t} \equiv 0$
- Steady-State Solutions:
  $\frac{\partial}{\partial t} \equiv 0$

Limits Exchange Accuracy for Cost
Transition Incurs Costs to Limit

TURF: For Exploring Efficient Methods
Minimizing Cost/Accuracy & Redundancy

Range of Validity

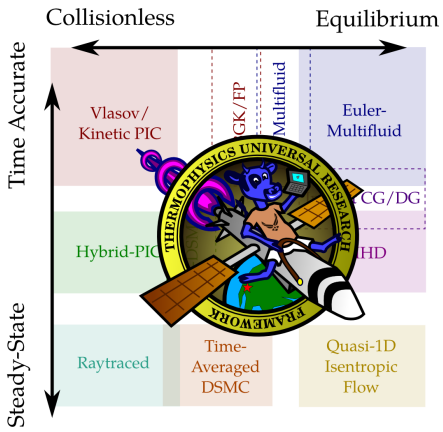

Distribution Statement A: Approved for Public Release; Distribution is Unlimited. AFRL-2021-4182

Progress on MF Formation/Reversal

Apollo Formation Simulations:

- RMF $\rightarrow j_\theta \rightarrow B_z$-Reversal

DG FRC-Formation

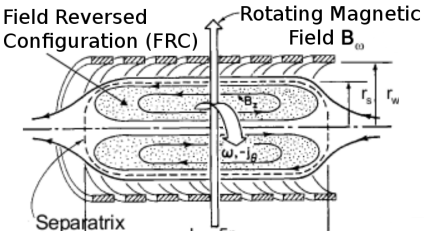

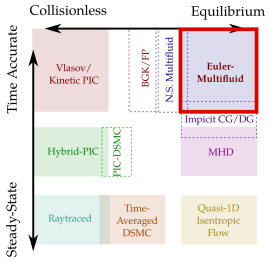

Distribution Statement A: Approved for Public Release; Distribution is Unlimited. AFRL-2021-4182

Progress on MF Formation/Reversal

Apollo Formation Simulations:

- RMF $\rightarrow j_\theta \rightarrow B_z$-Reversal
- Initially Conditions:
  Fully Ionized Xe Gas
  n_i=n_e=$10^{20}/m^3$
  60G Bias (Z) + 60G RMF @ 1MHz

DG FRC-Formation

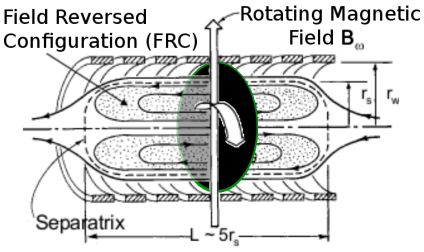

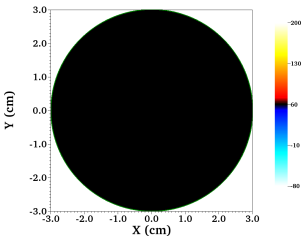

t=0ω

Distribution Statement A: Approved for Public Release; Distribution is Unlimited. AFRL-2021-4182

Progress on MF Formation/Reversal

Apollo Formation Simulations:

- RMF $\rightarrow j_\theta \rightarrow B_z$-Reversal
- Initially Conditions:
  Fully Ionized Xe Gas
  n_i=n_e=$10^{20}/m^3$
  60G Bias (Z) + 60G RMF @ 1MHz
- Strong Reversal B_z Reversal by 180°

DG FRC-Formation

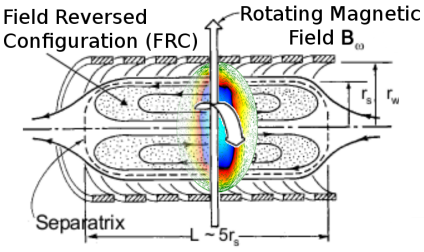

t=0-0.5ω

Distribution Statement A: Approved for Public Release; Distribution is Unlimited. AFRL-2021-4182

Progress on MF Formation/Reversal

Apollo Formation Simulations:

- RMF $\rightarrow j_\theta \rightarrow B_z$-Reversal
- Initially Conditions:
  Fully Ionized Xe Gas
  n_i=n_e=$10^{20}/m^3$
  60G Bias (Z) + 60G RMF @ 1MHz
- Strong Reversal B_z Reversal by 180°
- Reversal Weakens, 180°-360°

DG FRC-Formation

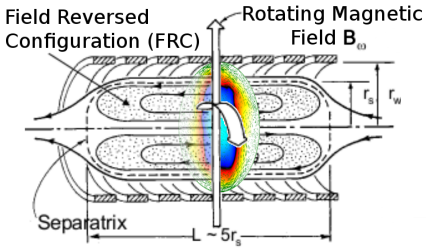

t=0.5-1.0ω

Distribution Statement A: Approved for Public Release; Distribution is Unlimited. AFRL-2021-4182

Progress on MF Formation/Reversal

Apollo Formation Simulations:

- RMF $\rightarrow j_\theta \rightarrow B_z$-Reversal
- Initially Conditions:
  Fully Ionized Xe Gas
  n_i=n_e=$10^{20}/m^3$
  60G Bias (Z) + 60G RMF @ 1MHz
- Strong Reversal B_z Reversal by 180°
- Reversal Weakens, 180°-360°
- Cycle Repeats
  (But Lower Amplitude)

DG FRC-Formation

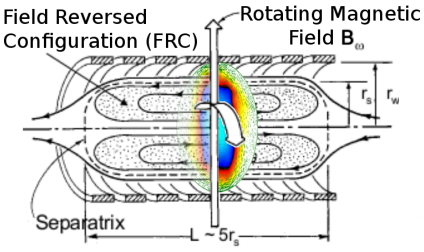

t=1.0-2.0ω

Distribution Statement A: Approved for Public Release; Distribution is Unlimited. AFRL-2021-4182

Progress on MF Formation/Reversal

Apollo Formation Simulations:

- RMF $\rightarrow j_\theta \rightarrow B_z$-Reversal
- Initially Conditions:
  Fully Ionized Xe Gas
  n_i=n_e=$10^{20}/m^3$
  60G Bias (Z) + 60G RMF @ 1MHz
- Strong Reversal B_z Reversal by 180°
- Reversal Weakens, 180°-360°
- Cycle Repeats
  (But Lower Amplitude)
- Parameter Space is being Explored

DG FRC-Formation

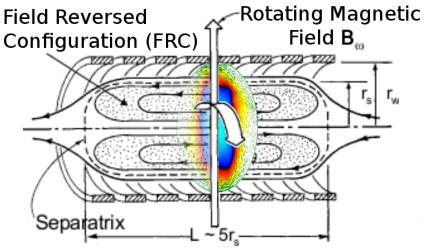

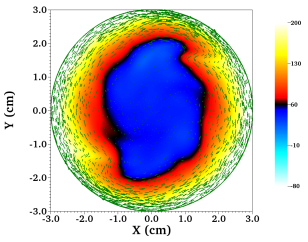

t=1.0-2.0ω

Distribution Statement A: Approved for Public Release; Distribution is Unlimited. AFRL-2021-4182

Progress on MF Formation/Reversal

Apollo Formation Simulations:

- RMF $\rightarrow j_\theta \rightarrow B_z$-Reversal
- Initially Conditions:
  Fully Ionized Xe Gas
  n_i=n_e=$10^{20}/m^3$
  60G Bias (Z) + 60G RMF @ 1MHz
- Strong Reversal B_z Reversal by 180°
- Reversal Weakens, 180°-360°
- Cycle Repeats
  (But Lower Amplitude)
- Parameter Space is being Explored

Also Needs Experimental Validation!

DG FRC-Formation

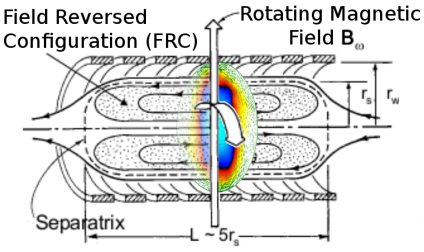

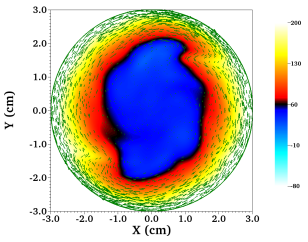

t=1.0-2.0ω

Distribution Statement A: Approved for Public Release; Distribution is Unlimited. AFRL-2021-4182

Radiative Emission Validation

High Fidelity Validation:

- FRCs are Dynamic Pulsed Devices

DG FRC-Formation

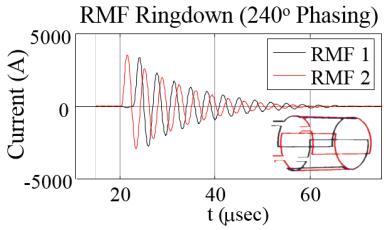

MSNW Ar FRC Formation

Distribution Statement A: Approved for Public Release; Distribution is Unlimited. AFRL-2021-4182

Radiative Emission Validation

High Fidelity Validation:

- FRCs are Dynamic Pulsed Devices
- Ext. Probes Probes avoid Disruption
  ...but Mostly Limited View

DG FRC-Formation

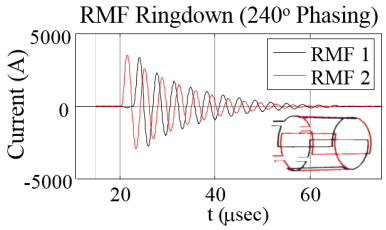

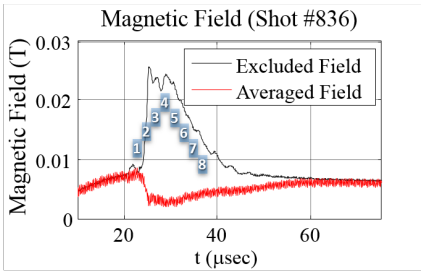

MSNW Ar FRC Formation

Distribution Statement A: Approved for Public Release; Distribution is Unlimited. AFRL-2021-4182

Radiative Emission Validation

High Fidelity Validation:

- FRCs are Dynamic Pulsed Devices
- Ext. Probes Probes avoid Disruption
  ...but Mostly Limited View
- Fast Camera:
  Absolute Magnitudes Difficult
  Relatively High Dimensional

DG FRC-Formation

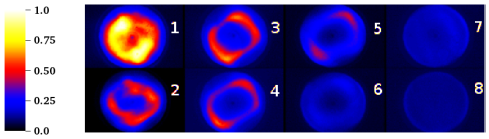

(False Color Intensity - MSNW Fast Camera Studies)

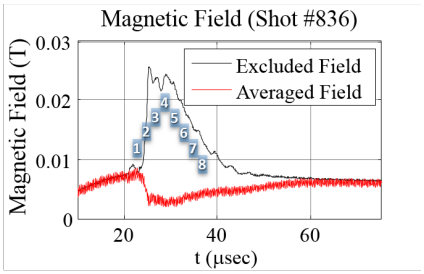

MSNW Ar FRC Formation

Distribution Statement A: Approved for Public Release; Distribution is Unlimited. AFRL-2021-4182

Radiative Emission Validation

High Fidelity Validation:

- FRCs are Dynamic Pulsed Devices
- Ext. Probes Probes avoid Disruption
  ...but Mostly Limited View
- Fast Camera:
  Absolute Magnitudes Difficult
  Relatively High Dimensional
- Emission from IonMix (n_e, T_e) Table
- Plotted at Equivalent ω

DG FRC-Formation

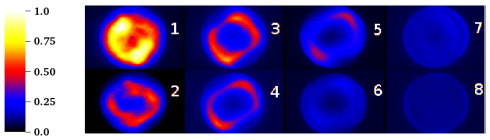

(False Color Intensity - MSNW Fast Camera Studies)

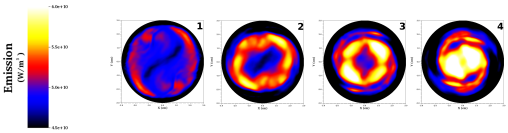

(Apollo Multifluid Simulation Emission Intensity)

Distribution Statement A: Approved for Public Release; Distribution is Unlimited. AFRL-2021-4182

Radiative Emission Validation

High Fidelity Validation:

- FRCs are Dynamic Pulsed Devices
- Ext. Probes Probes avoid Disruption
  ...but Mostly Limited View
- Fast Camera:
  Absolute Magnitudes Difficult
  Relatively High Dimensional
- Emission from IonMix (n_e, T_e) Table
- Plotted at Equivalent ω
- Similar Structures in **2** & **3**
  Despite Different Conditions

DG FRC-Formation

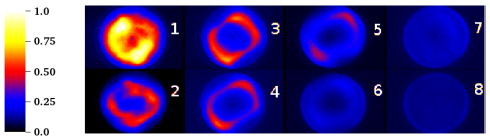

(False Color Intensity - MSNW Fast Camera Studies)

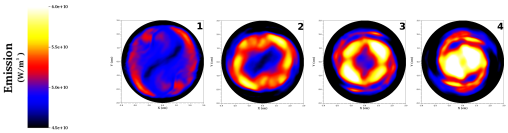

(Apollo Multifluid Simulation Emission Intensity)

Distribution Statement A: Approved for Public Release; Distribution is Unlimited. AFRL-2021-4182

Radiative Emission Validation

High Fidelity Validation:

- FRCs are Dynamic Pulsed Devices
- Ext. Probes Probes avoid Disruption
  ...but Mostly Limited View
- Fast Camera:
  Absolute Magnitudes Difficult
  Relatively High Dimensional
- Emission from IonMix (n_e, T_e) Table
- Plotted at Equivalent ω
- Similar Structures in **2** & **3**
  Despite Different Conditions
- Experiment Relaxes but
  Simulation Intensifies in **4+**

DG FRC-Formation

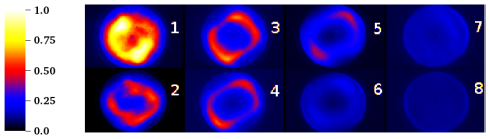

(False Color Intensity - MSNW Fast Camera Studies)

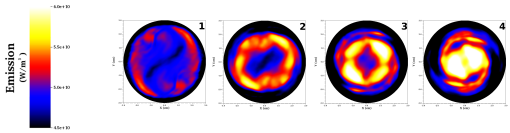

(Apollo Multifluid Simulation Emission Intensity)

Distribution Statement A: Approved for Public Release; Distribution is Unlimited. AFRL-2021-4182

Radiative Emission Validation

High Fidelity Validation:

- FRCs are Dynamic Pulsed Devices
- Ext. Probes Probes avoid Disruption
  ...but Mostly Limited View
- Fast Camera:
  Absolute Magnitudes Difficult
  Relatively High Dimensional
- Emission from IonMix (n_e, T_e) Table
- Plotted at Equivalent ω
- Similar Structures in **2** & **3**
  Despite Different Conditions
- Experiment Relaxes but
  Simulation Intensifies in **4+**

Model Needs Additional Physics

DG FRC-Formation

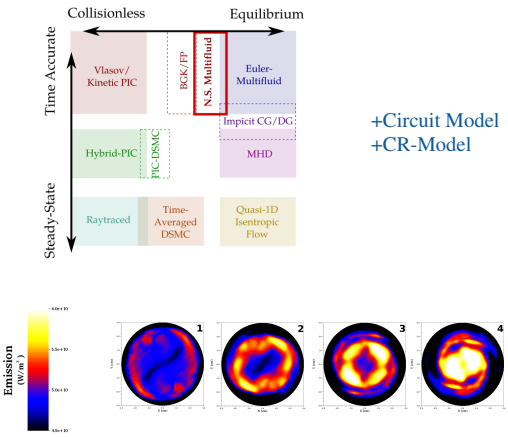

(Apollo Multifluid Simulation Emission Intensity)

Distribution Statement A: Approved for Public Release; Distribution is Unlimited. AFRL-2021-4182

AFRL Model Development/Project Synergies:

Model	Need	Platform	Project	Progress	Demo
Circuit	BC/Energy Cons.	TURF	1 & 2	Runtime Arbitrary ODE B.C.s	Lorenz DSMC Inflow
Radiative	Physics/Energy Cons.	R&D	3	Full Level-Grouped Ar Model	Abrantes PhD (UCLA 2018)
Multi-Fluid	Physics/Stability	Apollo	4	N.S./Braginskii	Poiselle/Taylor Couette
Multi-Fluid	Physics/Stability	TURF/R&D	4	Hybrid Entropy/Energy Cons.	Einfeldt/Step/Cylinder/Jet
Kinetic	Charge Separation	TURF	1 & 4	Boltzmann-n_e vs. $\langle n_e \rangle$	Quasi-1D HET

Projects:

1. In-House AFRL 6.2 Research
2. AFOSR Comp Math Lab-Task (New), PO: Fahroo
3. AFOSR Plasma/Electro-energetics Lab-Task, PO: Marshall
4. AFOSR Space Propulsion & Power, PO: Birkan

Distribution Statement A: Approved for Public Release; Distribution is Unlimited. AFRL-2021-4182

AFRL Model Development/Project Synergies:

Model	Need	Platform	Project	Progress	Demo
Circuit	BC/Energy Cons.	TURF	1 & 2	Runtime Arbitrary ODE B.C.s	Lorenz DSMC Inflow
Radiative	Physics/Energy Cons.	R&D	3	Full Level-Grouped Ar Model	Abrantes PhD (UCLA 2018)
Multi-Fluid	Physics/Stability	Apollo	4	N.S./Braginskii	Poiselle/Taylor Couette
Multi-Fluid	Physics/Stability	TURF/R&D	4	Hybrid Entropy/Energy Cons.	Einfeldt/Step/Cylinder/Jet
Kinetic	Charge Separation	TURF	1 & 4	Boltzmann-n_e vs. $\langle n_e \rangle$	Quasi-1D HET

Projects:

1. In-House AFRL 6.2 Research
2. AFOSR Comp Math Lab-Task (New), PO: Fahroo
3. AFOSR Plasma/Electro-energetics Lab-Task, PO: Marshall
4. AFOSR Space Propulsion & Power, PO: Birkan

Distribution Statement A: Approved for Public Release; Distribution is Unlimited. AFRL-2021-4182

N.S. Multifluid Definitions

$$\partial_t \mathbf{Q} + \nabla \cdot \mathbf{F}^{Hyp} + \nabla \cdot \mathbf{F}^{Para} = \mathbf{S}^{EM} + \mathbf{S}^{ie}$$

$$\mathbf{Q} = \begin{bmatrix} \rho_e \\ \rho_e \mathbf{u_e} \\ \mathscr{E}_e \\ \rho_i \\ \rho_i \mathbf{u_i} \\ \mathscr{E}_i \end{bmatrix} \quad \mathbf{F}^{Hyp} = \begin{bmatrix} \rho_e \mathbf{u_e} \\ \rho_e \mathbf{u_e}\mathbf{u_e} + p_e \mathbf{I} \\ \mathbf{u_e} \cdot (\mathscr{E}_e + p_e)\mathbf{I} \\ \rho_i \mathbf{u_i} \\ \rho_i \mathbf{u_i}\mathbf{u_i} + p_i \mathbf{I} \\ \mathbf{u_i} \cdot (\mathscr{E}_i + p_i)\mathbf{I} \end{bmatrix} \quad \mathbf{F}^{Para} = \begin{bmatrix} 0 \\ \mathbf{\Pi}_e \\ \mathbf{u_e} \cdot \mathbf{\Pi}_e + \mathbf{q_e} \\ 0 \\ \mathbf{\Pi}_i \\ \mathbf{u_i} \cdot \mathbf{\Pi}_i + \mathbf{q_i} \end{bmatrix}$$

$$\mathbf{S}^{EM} = \begin{bmatrix} 0 \\ q_e n_e (\mathbf{E} + \mathbf{u_e} \times \mathbf{B}) \\ q_e n_e \mathbf{u_e} \mathbf{E} \\ 0 \\ q_i n_i (\mathbf{E} + \mathbf{u_i} \times \mathbf{B}) \\ q_i n_i \mathbf{u_i} \mathbf{E} \end{bmatrix} \quad \mathbf{S}^{ie} = \begin{bmatrix} 0 \\ -\mathbf{R}_{ie} \\ \mathbf{u}_e \cdot \mathbf{R}_{ie} + \mathbf{Q}^e_{ie} \\ 0 \\ -\mathbf{R}_{ei} \\ \mathbf{u}_i \cdot \mathbf{R}_{ei} + \mathbf{Q}^i_{ei} \end{bmatrix}$$

The EOS used here: $p = nk_BT$. Energy $\mathscr{E} = \frac{p}{\gamma - 1} + \frac{1}{2}\rho \mathbf{u} \cdot \mathbf{u}$.

Distribution Statement A: Approved for Public Release; Distribution is Unlimited. AFRL-2021-4182

N.S. Multifluid Definitions

$$\partial_t \mathbf{Q} + \nabla \cdot \mathbf{F}^{Hyp} + \nabla \cdot \mathbf{F}^{Para} = \mathbf{S}^{EM} + \mathbf{S}^{ie}$$

$$\mathbf{Q} \quad \mathbf{F}^{Hyp} \quad \mathbf{F}^{Para} \quad \mathbf{S}^{EM} \quad \mathbf{S}^{ie}$$

$$\begin{bmatrix} \rho_e \\ \rho_e \mathbf{u_e} \\ \mathscr{E}_e \\ \rho_i \\ \rho_i \mathbf{u_i} \\ \mathscr{E}_i \end{bmatrix} \quad \begin{bmatrix} \rho_e \mathbf{u_e} \\ \rho_e \mathbf{u_e} \mathbf{u_e} + p_e \mathbf{I} \\ \mathbf{u_e} \cdot (\mathscr{E}_e + p_e) \mathbf{I} \\ \rho_i \mathbf{u_i} \\ \rho_i \mathbf{u_i} \mathbf{u_i} + p_i \mathbf{I} \\ \mathbf{u_i} \cdot (\mathscr{E}_i + p_i) \mathbf{I} \end{bmatrix} \quad \begin{bmatrix} 0 \\ \mathbf{\Pi}_e \\ \mathbf{u_e} \cdot \mathbf{\Pi}_e + \mathbf{q_e} \\ 0 \\ \mathbf{\Pi}_i \\ \mathbf{u_i} \cdot \mathbf{\Pi}_i + \mathbf{q_i} \end{bmatrix} \quad \begin{bmatrix} 0 \\ q_e n_e (\mathbf{E} + \mathbf{u_e} \times \mathbf{B}) \\ q_e n_e \mathbf{u_e} \mathbf{E} \\ 0 \\ q_i n_i (\mathbf{E} + \mathbf{u_i} \times \mathbf{B}) \\ q_i n_i \mathbf{u_i} \mathbf{E} \end{bmatrix} \quad \begin{bmatrix} 0 \\ -\mathbf{R}_{ie} \\ \mathbf{u}_e \cdot \mathbf{R}_{ie} + \mathbf{Q}^e_{ie} \\ 0 \\ -\mathbf{R}_{ei} \\ \mathbf{u}_i \cdot \mathbf{R}_{ei} + \mathbf{Q}^i_{ei} \end{bmatrix}$$

The EOS used here: $p = nk_BT$. Energy $\mathscr{E} = \frac{p}{\gamma - 1} + \frac{1}{2}\rho \mathbf{u} \cdot \mathbf{u}$.

Distribution Statement A: Approved for Public Release; Distribution is Unlimited. AFRL-2021-4182

N.S. Multifluid Definitions

$$\partial_t \mathbf{Q} + \nabla \cdot \mathbf{F}^{Hyp} + \nabla \cdot \mathbf{F}^{Para} = \mathbf{S}^{EM} + \mathbf{S}^{ie}$$

$$\mathbf{Q} = \begin{bmatrix} \rho_e \\ \rho_e \mathbf{u_e} \\ \mathscr{E}_e \\ \rho_i \\ \rho_i \mathbf{u_i} \\ \mathscr{E}_i \end{bmatrix} \quad \mathbf{F}^{Hyp} = \begin{bmatrix} \rho_e \mathbf{u_e} \\ \rho_e \mathbf{u_e}\mathbf{u_e} + p_e \mathbf{I} \\ \mathbf{u_e} \cdot (\mathscr{E}_e + p_e)\mathbf{I} \\ \rho_i \mathbf{u_i} \\ \rho_i \mathbf{u_i}\mathbf{u_i} + p_i \mathbf{I} \\ \mathbf{u_i} \cdot (\mathscr{E}_i + p_i)\mathbf{I} \end{bmatrix} \quad \mathbf{F}^{Para} = \begin{bmatrix} 0 \\ \mathbf{\Pi}_e \\ \mathbf{u_e} \cdot \mathbf{\Pi}_e + \mathbf{q_e} \\ 0 \\ \mathbf{\Pi}_i \\ \mathbf{u_i} \cdot \mathbf{\Pi}_i + \mathbf{q_i} \end{bmatrix}$$

$$\mathbf{S}^{EM} = \begin{bmatrix} 0 \\ q_e n_e (\mathbf{E} + \mathbf{u_e} \times \mathbf{B}) \\ q_e n_e \mathbf{u_e} \mathbf{E} \\ 0 \\ q_i n_i (\mathbf{E} + \mathbf{u_i} \times \mathbf{B}) \\ q_i n_i \mathbf{u_i} \mathbf{E} \end{bmatrix} \quad \mathbf{S}^{ie} = \begin{bmatrix} 0 \\ -\mathbf{R}_{ie} \\ \mathbf{u}_e \cdot \mathbf{R}_{ie} + \mathbf{Q}^e_{ie} \\ 0 \\ -\mathbf{R}_{ei} \\ \mathbf{u}_i \cdot \mathbf{R}_{ei} + \mathbf{Q}^i_{ei} \end{bmatrix}$$

The EOS used here: $p = nk_BT$. Energy $\mathscr{E} = \frac{p}{\gamma - 1} + \frac{1}{2}\rho \mathbf{u} \cdot \mathbf{u}$.

Progress:

Classic (Newtonian) and Braginskii Formulations Implemented

Distribution Statement A: Approved for Public Release; Distribution is Unlimited. AFRL-2021-4182

N.S. Multifluid Definitions

$$\partial_t \mathbf{Q} + \nabla \cdot \mathbf{F}^{Hyp} + \nabla \cdot \mathbf{F}^{Para} = \mathbf{S}^{EM} + \mathbf{S}^{ie}$$

$$\mathbf{Q} = \begin{bmatrix} \rho_e \\ \rho_e \mathbf{u_e} \\ \mathscr{E}_e \\ \rho_i \\ \rho_i \mathbf{u_i} \\ \mathscr{E}_i \end{bmatrix} \quad \mathbf{F}^{Hyp} = \begin{bmatrix} \rho_e \mathbf{u_e} \\ \rho_e \mathbf{u_e}\mathbf{u_e} + p_e \mathbf{I} \\ \mathbf{u_e} \cdot (\mathscr{E}_e + p_e)\mathbf{I} \\ \rho_i \mathbf{u_i} \\ \rho_i \mathbf{u_i}\mathbf{u_i} + p_i \mathbf{I} \\ \mathbf{u_i} \cdot (\mathscr{E}_i + p_i)\mathbf{I} \end{bmatrix} \quad \mathbf{F}^{Para} = \begin{bmatrix} 0 \\ \mathbf{\Pi}_e \\ \mathbf{u_e} \cdot \mathbf{\Pi}_e + \mathbf{q_e} \\ 0 \\ \mathbf{\Pi}_i \\ \mathbf{u_i} \cdot \mathbf{\Pi}_i + \mathbf{q_i} \end{bmatrix}$$

$$\mathbf{S}^{EM} = \begin{bmatrix} 0 \\ q_e n_e (\mathbf{E} + \mathbf{u_e} \times \mathbf{B}) \\ q_e n_e \mathbf{u_e} \mathbf{E} \\ 0 \\ q_i n_i (\mathbf{E} + \mathbf{u_i} \times \mathbf{B}) \\ q_i n_i \mathbf{u_i} \mathbf{E} \end{bmatrix} \quad \mathbf{S}^{ie} = \begin{bmatrix} 0 \\ -\mathbf{R}_{ie} \\ \mathbf{u}_e \cdot \mathbf{R}_{ie} + \mathbf{Q}^e_{ie} \\ 0 \\ -\mathbf{R}_{ei} \\ \mathbf{u}_i \cdot \mathbf{R}_{ei} + \mathbf{Q}^i_{ei} \end{bmatrix}$$

The EOS used here: $p = nk_BT$. Energy $\mathscr{E} = \frac{p}{\gamma - 1} + \frac{1}{2}\rho \mathbf{u} \cdot \mathbf{u}$.

Progress:

Classic (Newtonian) and Braginskii Formulations Implemented

Validation Cases:

Newtonian	Braginskii
Channel Flow: ✓	Hartman: (Pending)
Cylindrical Couette: ✓	Magneto-Rotational Instability: (Pending)

Distribution Statement A: Approved for Public Release; Distribution is Unlimited. AFRL-2021-4182

Channel Flow Results

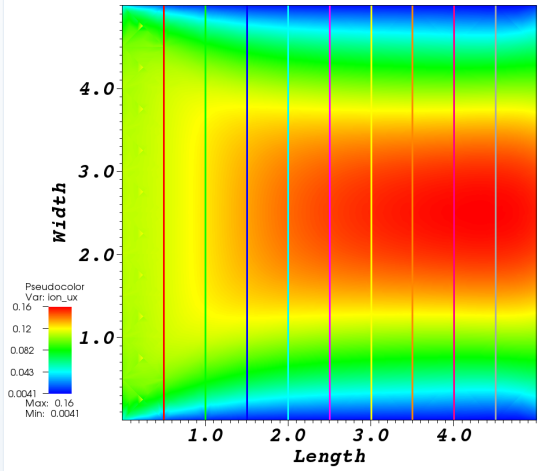

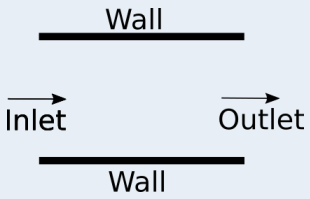

- A solid, no slip, boundary is enforced at the walls
- The input boundary uses a fixed Dirichlet condition. The flow is low subsonic (0.10 Mach).
- The exit using a von Neumann boundary condition on all variables except for pressure, which is set to the inlet condition.
- The chosen Reynolds number is approximately 30.

Distribution Statement A: Approved for Public Release; Distribution is Unlimited. AFRL-2021-4182

Channel Flow Results

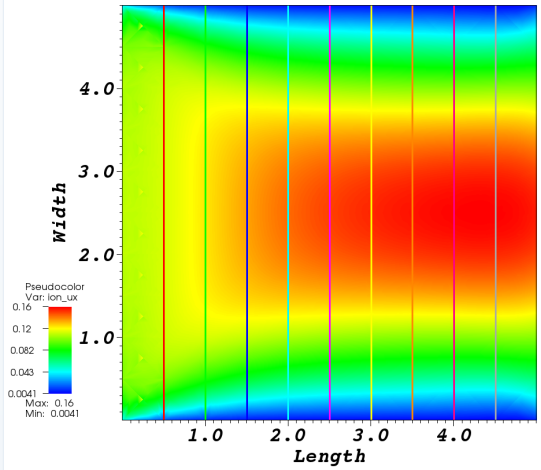

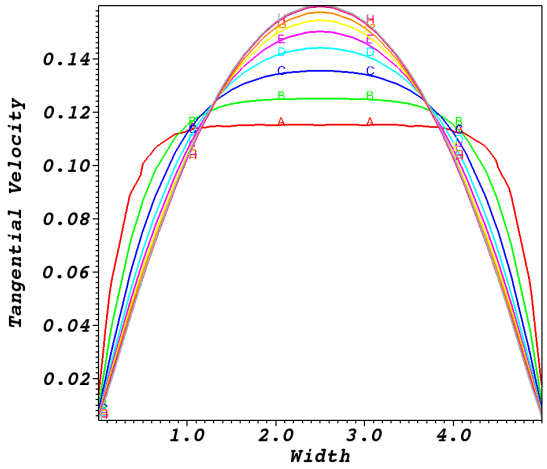

- A solid, no slip, boundary is enforced at the walls
- The input boundary uses a fixed Dirichlet condition. The flow is low subsonic (0.10 Mach).
- The exit using a von Neumann boundary condition on all variables except for pressure, which is set to the inlet condition.
- The chosen Reynolds number is approximately 30.

Distribution Statement A: Approved for Public Release; Distribution is Unlimited. AFRL-2021-4182

Taylor Couette Results

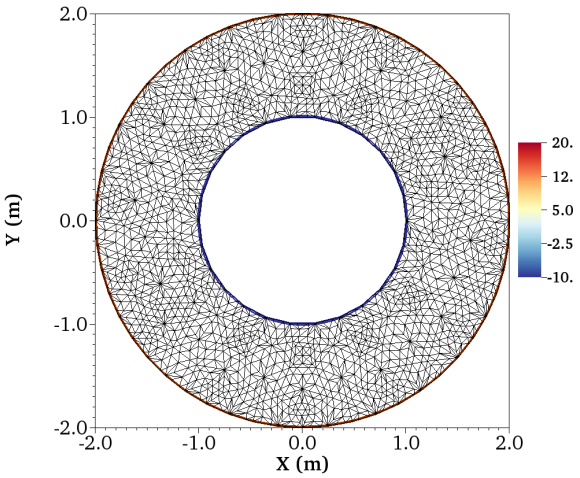

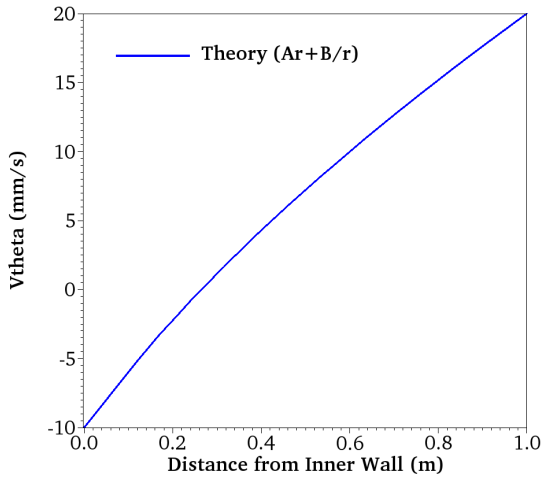

- Counter rotating solid, no slip, boundary is enforced at the inner/outer walls
- Reynolds number independent solution is rapidly established
- Good Agreement with Analytic Solution Attained

Distribution Statement A: Approved for Public Release; Distribution is Unlimited. AFRL-2021-4182

Taylor Couette Results

- Counter rotating solid, no slip, boundary is enforced at the inner/outer walls
- Reynolds number independent solution is rapidly established
- Good Agreement with Analytic Solution Attained

Distribution Statement A: Approved for Public Release; Distribution is Unlimited. AFRL-2021-4182

Entropy Conservation and Hybridization

Entropy Formulation:

- Strong Rarefactions often break Fluid Codes (i.e. Negative Pressures/Artificial Heating)
- Low-β Numerical Instabilities in Apollo (Low-T_e)

Einfeldt 1-2-3 : Energy

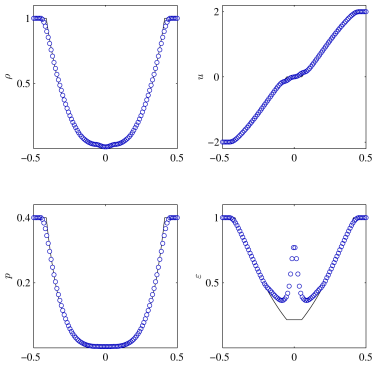

Solution to Einfeldt's 1-2-3 problem as obtained with conservation of energy. (Kapper PhD, OSU, '09)

Distribution Statement A: Approved for Public Release; Distribution is Unlimited. AFRL-2021-4182

Entropy Conservation and Hybridization

Entropy Formulation:

- Strong Rarefactions often break Fluid Codes (i.e. Negative Pressures/Artificial Heating)
- Low-β Numerical Instabilities in Apollo (Low-T_e)
- Low-Power Lab Experiments are Low-T_e ($\approx$10eV)
- Relevant Regime Numerically Inaccessible (i.e. T_e<20eV)

Einfeldt 1-2-3 : Energy

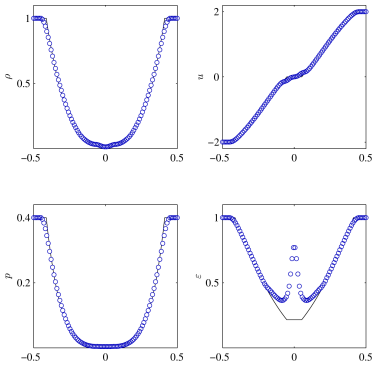

Solution to Einfeldt's 1-2-3 problem as obtained with conservation of energy. (Kapper PhD, OSU, '09)

Distribution Statement A: Approved for Public Release; Distribution is Unlimited. AFRL-2021-4182

Entropy Conservation and Hybridization

Entropy Formulation:

- Strong Rarefactions often break Fluid Codes (i.e. Negative Pressures/Artificial Heating)
- Low-β Numerical Instabilities in Apollo (Low-T_e)
- Low-Power Lab Experiments are Low-T_e ($\approx$10eV)
- Relevant Regime Numerically Inaccessible (i.e. T_e<20eV)
- Entropy Cons. Helps for Strong Expansions (Ch.8, Kapper PhD, OSU '09)

Einfeldt 1-2-3 : Entropy

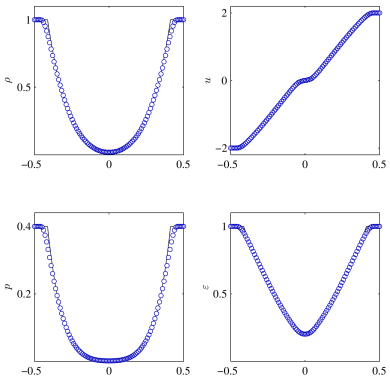

Solution to Einfeldt's 1-2-3 problem as obtained with conservation of entropy. (Kapper PhD, OSU, '09)

Distribution Statement A: Approved for Public Release; Distribution is Unlimited. AFRL-2021-4182

Entropy Conservation and Hybridization

Entropy Formulation:

- Strong Rarefactions often break Fluid Codes (i.e. Negative Pressures/Artificial Heating)
- Low-β Numerical Instabilities in Apollo (Low-T_e)
- Low-Power Lab Experiments are Low-T_e ($\approx$10eV)
- Relevant Regime Numerically Inaccessible (i.e. T_e<20eV)
- Entropy Cons. Helps for Strong Expansions (Ch.8, Kapper PhD, OSU '09)
- Updated Method Enables Extreme Pressure Ratios (Kapper, 2018)

Einfeldt Vacuum Limit : Entropy

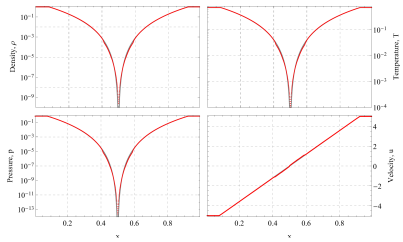

Solution to Einfeldt's Vacuum Limit (Mach 5, γ=7/5) problem as obtained with conservation of entropy and new linearization. (Kapper 18)

$$T/T_0=10^{-4}$$
$$\rho/\rho_0=10^{-9}$$
$$P/P_0=10^{-13}$$

Distribution Statement A: Approved for Public Release; Distribution is Unlimited. AFRL-2021-4182

Entropy Conservation and Hybridization

Entropy Formulation:

- Strong Rarefactions often break Fluid Codes (i.e. Negative Pressures/Artificial Heating)
- Low-β Numerical Instabilities in Apollo (Low-T_e)
- Low-Power Lab Experiments are Low-T_e ($\approx$10eV)
- Relevant Regime Numerically Inaccessible (i.e. T_e<20eV)
- Entropy Cons. Helps for Strong Expansions (Ch.8, Kapper PhD, OSU '09)
- Updated Method Enables Extreme Pressure Ratios (Kapper, 2018)
- Apollo $Q \rightarrow$ Electron Entropy Cons. (Sousa, TBD)

$$\begin{bmatrix} \mathbf{Q} \\ \rho_e \\ \rho_e \mathbf{u_e} \\ \mathscr{E}_e \\ \rho_i \\ \rho_i \mathbf{u_i} \\ \mathscr{E}_i \end{bmatrix} \rightarrow \begin{bmatrix} \mathbf{Q} \\ \rho_e \\ \rho_e \mathbf{u_e} \\ \rho_e s_e \\ \rho_i \\ \rho_i \mathbf{u_i} \\ \mathscr{E}_i \end{bmatrix}$$

$$s_e = P_e / \rho_e^{\gamma}$$

Distribution Statement A: Approved for Public Release; Distribution is Unlimited. AFRL-2021-4182

Entropy Conservation and Hybridization

Entropy Formulation:

- Strong Rarefactions often break Fluid Codes (i.e. Negative Pressures/Artificial Heating)
- Low-β Numerical Instabilities in Apollo (Low-T_e)
- Low-Power Lab Experiments are Low-T_e ($\approx$10eV)
- Relevant Regime Numerically Inaccessible (i.e. T_e<20eV)
- Entropy Cons. Helps for Strong Expansions (Ch.8, Kapper PhD, OSU '09)
- Updated Method Enables Extreme Pressure Ratios (Kapper, 2018)
- Apollo $Q \rightarrow$ Electron Entropy Cons. (Sousa, TBD)
- Extending to Hybrid Energy/Entropy Cons. (Kapper, 2018)

Linde-Roe Corner Expansion

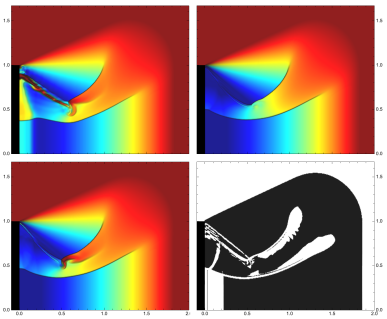

Top Left: Energy Conservation
Top Right: Entropy Conservation
Bottom Left: Hybrid Solution
Bottom Right: Hybrid Compression Flag

(Kapper '18)

Distribution Statement A: Approved for Public Release; Distribution is Unlimited. AFRL-2021-4182

Entropy Conservation and Hybridization

Entropy Formulation:

- Strong Rarefactions often break Fluid Codes (i.e. Negative Pressures/Artificial Heating)
- Low-β Numerical Instabilities in Apollo (Low-T_e)
- Low-Power Lab Experiments are Low-T_e ($\approx$10eV)
- Relevant Regime Numerically Inaccessible (i.e. T_e<20eV)
- Entropy Cons. Helps for Strong Expansions (Ch.8, Kapper PhD, OSU '09)
- Updated Method Enables Extreme Pressure Ratios (Kapper, 2018)
- Apollo $Q \rightarrow$ Electron Entropy Cons. (Sousa, TBD)
- Extending to Hybrid Energy/Entropy Cons. (Kapper, 2018)

Mach 10.2 Cylinder

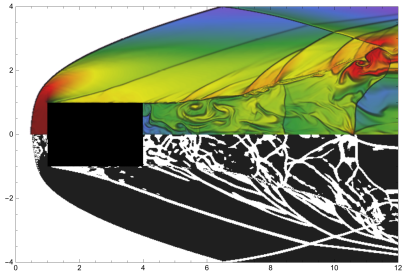

Plot of *logT* plus simulated Schlieren (top) and Hybrid Switch (bottom)

(Kapper '18)

Distribution Statement A: Approved for Public Release; Distribution is Unlimited. AFRL-2021-4182

Entropy Conservation and Hybridization

Entropy Formulation:

- Strong Rarefactions often break Fluid Codes (i.e. Negative Pressures/Artificial Heating)
- Low-β Numerical Instabilities in Apollo (Low-T_e)
- Low-Power Lab Experiments are Low-T_e ($\approx$10eV)
- Relevant Regime Numerically Inaccessible (i.e. T_e<20eV)
- Entropy Cons. Helps for Strong Expansions (Ch.8, Kapper PhD, OSU '09)
- Updated Method Enables Extreme Pressure Ratios (Kapper, 2018)
- Apollo $Q \rightarrow$ Electron Entropy Cons. (Sousa, TBD)
- Extending to Hybrid Energy/Entropy Cons. (Kapper, 2018)

Mach 1.5 Underexpanded Jet

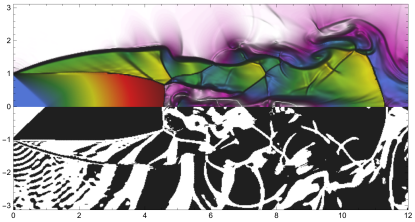

Plot of Mach plus simulated Schlieren (top) and Hybrid Switch (bottom)

(Kapper '18)

Distribution Statement A: Approved for Public Release; Distribution is Unlimited. AFRL-2021-4182

Viscosity Implementation

The Braginskii equations:

- Implementation of Parabolic Flux: $\mathbf{\Pi}_\alpha$, and $\mathbf{q}_\alpha$ (Viscosity & Heat Flux)
- The viscosity begins with the classic Newtonian tensor (1).

$$\overleftrightarrow{\mathbf{W}} = \nabla\mathbf{u} + \nabla\mathbf{u}^T - \left(\frac{2}{3}\nabla\cdot\mathbf{u}\right)\overleftrightarrow{\mathbf{I}} \tag{1}$$

- $\overleftrightarrow{\mathbf{W}}$ is rotated into the magnetic field coordinate frame.
- $\overleftrightarrow{\mathbf{W}}_r$ is then decomposed into parallel, perpendicular, and gyroviscous $\mathscr{W}_i$
- Each of $\mathscr{W}_i$ components is multiplied by a scalar η_i.

Finally,

$$\mathbf{\Pi}_\alpha = rot_{lab}\left(\sum_{i=0}^{N=4}\eta_i\mathscr{W}_i\right) \tag{2}$$

Distribution Statement A: Approved for Public Release; Distribution is Unlimited. AFRL-2021-4182

Multifluid Simulations Incorporating Braginskii Transport Applied To RMF Driven Field Reversed Configuration Formation

Robert C. Lilly[1], Éder M. Sousa[1], and Robert S. Martin[2]

Modeling & Simulation Group
In-Space propulsion Branch (RQRS)
[1]ERC Inc., [2]Air Force Research Lab
Edwards AFB, CA
*robert.lilly.3.ctr@us.af.mil

This work is supported by grant 17RQCOR465 from the United States Air Force Office of Scientific Research.
Distribution Statement A: Approved for Public Release; Distribution is Unlimited. PA# 18639.

Abstract

In order to realize the theoretical performance benefits of the Field Reversed Configuration (FRC) spacecraft propulsion concept, AFRL/RQRS is developing a high fidelity modeling and simulation capability. This work details recent progress in upgrading a multifluid simulation code from inviscid to viscous flow through the implementation of the Braginskii transport equations. Validation results for the Taylor-Couette problem are presented. This setup is first adapted to the 2D annular neutral fluid problem first for decoupled neutral nondimensional-ized gas (Navier-Stokes) and then for the coupled non-dimensionalized simulation with the multifluid plasma model. However, when applied to the FRC relevant dimensional parameter space, stable numerical solution remains an open challenge. These validation cases represent a critical increment towards accurate multifluid simulation of the viscous regieme of the FRC formation problem.

Field Reversed Configuration (FRC)

The FRC is a toroidal magnetic confinement system with little or no toroidal field, composed of nested toroidal magnetic surfaces.

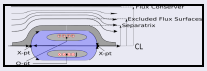

⇒ The separatrix forms the nominal boundary, separating closed from open magnetic surfaces.
⇒ The excluded flux surfaces support the translatable FRC, with high-β, and high power density

Application Motivation - Propulsion

As a propulsion system, the FRC offers considerable operational flexibility

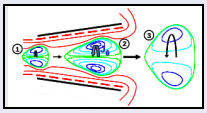

Slough et al., IEPC-2009-265 (2009)

⇒ Broad Isp range (1,000-10,000) seconds
⇒ High power throughput, propellant agnostic, and throttlable
⇒ Electrodeless implies Long Life
⇒ Pulsed operation permits alternative power supply designs

Parameter Space

⇒ Parameter space space indicates fluid approximation valid for ions, but only marginally so for electrons.

parameter	units	electrons	Xenon ions (Xe^+)	neutrals
n	$[m^{-3}]$	10^{20}	10^{20}	10^{20}
T	$[eV]$	49	16	0.03
D	$[A]$	-	-	5.6
λ_D	$[\mu m]$	5.204	2.974	-
Λ	-	177000	33040	-
$ln\Lambda$	-	12.1	10.4	-
ω_{pa}	$[GHz]$	564.1	1.15	-
$v_{th,a}$	$[\frac{km}{sec}]$	2935	3.419	14.1
$\nu_{ii,a}$	$[MHz]$	38.56	0.362	2.01
λ_{mfp}	$[mm]$	76.1	9.72	7.06
Kn	-	0.41	0.052	0.038
Re	-	0.34	4.4	*

Table: Parameters, Deflections. n (particle density), T (temperature), D (atomic diameter), λ_D (debye length), and Λ (plasma parameter). Kn (Knudsen number), Re (Reynolds number). Scale length is the circumference of the FRC flux conserver, which has a radius of 1 cm.

The Multi-Fluid Plasma Model

⇒ The electron and ions fluids are evolved using the following equations

$$\partial_t \mathbf{Q} + \nabla \cdot \mathbf{F}^{Hyp} + \nabla \cdot \mathbf{F}^{Para} = \mathbf{S}^{EM} + \mathbf{S}^{ie} \tag{1}$$

$$\begin{matrix}\mathbf{Q} & \mathbf{F}^{Hyp} & \mathbf{F}^{Para} & \mathbf{S}^{EM} & \mathbf{S}^{ie}\end{matrix}$$
$$\begin{bmatrix} \rho_n \\ \rho_n \mathbf{u}_n \\ \mathscr{E}_n \\ \rho_i \\ \rho_i \mathbf{u}_i \\ \mathscr{E}_i \end{bmatrix} \begin{bmatrix} \rho_n \mathbf{u}_n \\ \rho_n \mathbf{u}_n \mathbf{u}_n + p_n \mathbf{I} \\ \mathbf{u}_n (\mathscr{E}_n + p_n) \mathbf{I} \\ \rho_i \mathbf{u}_i \\ \rho_i \mathbf{u}_i \mathbf{u}_i + p_i \mathbf{I} \\ \mathbf{u}_i (\mathscr{E}_i + p_i) \mathbf{I} \end{bmatrix} \begin{bmatrix} 0 \\ \mathbf{\Pi}_n \\ \mathbf{u}_n \cdot \mathbf{\Pi}_n + \mathbf{q}_n \\ 0 \\ \mathbf{\Pi}_i \\ \mathbf{u}_i \cdot \mathbf{\Pi}_i + \mathbf{q}_i \end{bmatrix} \begin{bmatrix} 0 \\ q_n n_n (\mathbf{E} + \mathbf{u}_n \times \mathbf{B}) \\ q_n n_n \mathbf{u}_n \mathbf{E} \\ 0 \\ q_i n_i (\mathbf{E} + \mathbf{u}_i \times \mathbf{B}) \\ q_i n_i \mathbf{u}_i \mathbf{E} \end{bmatrix} \begin{bmatrix} 0 \\ -\mathbf{R}_n \\ \mathbf{u}_n \cdot \mathbf{R}_n + \mathbf{Q}_n^e \\ 0 \\ -\mathbf{R}_n \\ \mathbf{u}_i \cdot \mathbf{R}_n + \mathbf{Q}_n^i \end{bmatrix} \tag{2}$$

- The viscosity begins with the classic Newtonian tensor:

$$\overleftrightarrow{\mathbf{W}} = \nabla \mathbf{u} + \nabla \mathbf{u}^T - \left(\frac{2}{3} \nabla \cdot \mathbf{u}\right) \overleftrightarrow{\mathbf{I}} \tag{3}$$

- $\overleftrightarrow{\mathbf{W}}$ is rotated into the magnetic field coordinate frame.
- The resulting $\widehat{\mathbf{W}}_i$ is then decomposed into parallel, perpendicular, and gyroviscous matrices $\mathscr{W}_i$. Each of $\mathscr{W}_i$ components is multiplied by the magnetized scalar η_i. Finally

$$\mathbf{\Pi}_n = rot_{bb} \left(\sum_{i=0}^{N=4} \eta_i \mathscr{W}_i \right) \tag{4}$$

⇒ Maxwell's equations describe the electric and magnetic fields

$$\partial_t \begin{bmatrix} \mathbf{E} \\ \mathbf{B} \\ \phi \\ \psi \end{bmatrix} + \begin{bmatrix} -c^2 \nabla \times \mathbf{B} \\ \nabla \times \mathbf{E} \\ \chi \nabla \cdot \mathbf{E} \\ \gamma c^2 \nabla \cdot \mathbf{B} \end{bmatrix} + \begin{bmatrix} \chi c^2 \nabla \phi \\ \gamma \nabla \psi \\ 0 \\ 0 \end{bmatrix} = \begin{bmatrix} \frac{1}{\mu} e \left(Z_i n_i \mathbf{u}_i - n_e \mathbf{u}_e \right) \\ 0 \\ \chi e \left(Z_i n_i - n_e \right) \\ 0 \end{bmatrix} \tag{5}$$

⇒ The electrons and ions are coupled through the source terms.
⇒ The scope of this work has been to extend Apollo, an AFRL fluids solver, from handling only inviscid fluids, but also viscous as well.
⇒ This has involved providing a discontinuous galerkin finite element gradient function and the subsequent incorporation of said functionality into Apollo's DG framework.

Braginskii Validation Problem

The Couette problem, a pair of counter rotating cylinders, serves as the validation problem.
⇒ Assuming the $\mathbf{j} \times \mathbf{B}$ forces are balanced by the viscous and resistance terms yields:

$$\nabla \cdot \mathbf{\Pi}_n = -\mathbf{R}_u^{\alpha\beta} + q_n n_n \left(\mathbf{u}_n \times \mathbf{B} \right) \tag{6}$$

where $\mathbf{u}_n = i u_n + j v_n + k w_n$ and α is the species subscript. This can be expanded and rewritten as a set of second order ODEs.

$$\partial_{r,r} \left[U_e^\Theta \right] + \frac{2}{r} \partial_r \left[U_e^\Theta \right] + \frac{\alpha}{\mu_e} \left[U_i^\Theta - U_e^\Theta \right] + \frac{q_e n_e U_e^z B_r}{\mu_e} = 0 \tag{7}$$

$$\partial_{r,r} \left[U_i^\Theta \right] + \frac{2}{r} \partial_r \left[U_i^\Theta \right] - \frac{\alpha}{\mu_i} \left[U_e^\Theta - U_i^\Theta \right] + \frac{q_e n_e U_i^z B_r}{\mu_i} = 0 \tag{8}$$

$$\partial_{r,r} \left[U_e^z \right] + \frac{1}{r} \partial_r \left[U_e^z \right] + \frac{\alpha}{\mu_e} \left[U_e^z - U_i^z \right] - \frac{q_e n_e U_e^\Theta B_r}{\mu_e} = 0 \tag{9}$$

$$\partial_{r,r} \left[U_i^z \right] + \frac{1}{r} \partial_r \left[U_i^z \right] - \frac{\alpha}{\mu_i} \left[U_e^z - U_i^z \right] - \frac{q_e n_e U_i^\Theta B_r}{\mu_i} = 0 \tag{10}$$

and numerically solved using Mathematica as shown in the column to the right.

⇒ Boundary conditions (for no slip conducting wall): For the flow and field variables: $\mathbf{U}_{BC}^\Theta = V_{wall}$, $\mathbf{E}_{BC} = \mathbf{E}_\Omega - \mathbf{E}_\Omega^\parallel$, $\mathbf{B}_{BC} = \mathbf{B}_\Omega - \mathbf{B}_\Omega^\perp$, and for gradients $\nabla \mathbf{E} = 0$, and $\nabla \mathbf{B} = 0$.

Braginskii Validation Problem

The Couette problem set up

⇒ Plasma initially quiescent, with an applied B_r. Walls are spun up in opposite directions. Mathematica result (NDSolve) provided below.

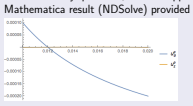

⇒ This sample Mathematica result for the case with $V_{inner} = 1e^{-4}$, $V_{outer} = 2e^{-4}$, $B_r = 5e^{-1}$, $\alpha = 0$, $n_e = n_i = 10^{22}$, $\mu_e = 1$, and $\mu_i = 1e^{-4}$ illustrates where the electron fluid is dominated by isotropic viscosity, whereas the ions are magnetically constrained.
⇒ Now in the decoupled neutral fluid pilot calculation below, all the physical constants and variables have been set to one. Comparison to theoretical provided.

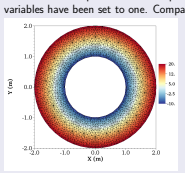

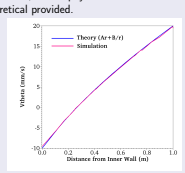

⇒ In the plasma calculation, for the same operating point, and the magnetic field is set at $B_r = 10$ (left) and $B_r = 1$ (right). with the interspecies collision operator set as $R = 1$. As B_r increases toward the axis, the electron fluid stiffens.

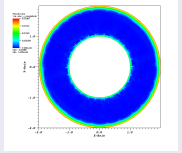

$v_{\theta,e}$, $B_r = 10$

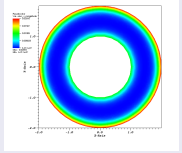

$v_{\theta,e}$, $B_r = 1$

Difficulties

⇒ With source terms turned on and proper values used for physical constants (mass, charge, dielectric, etc.), a non-physical current develops at the wall which eventually forces the electrons, and later, the ions, to violate the no slip boundary conditions.
⇒ The results below illustrate V_θ for electrons. As can be seen, the electric field overwhelms the imposed boundary conditions.

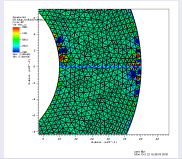

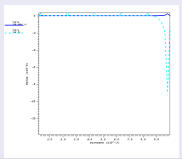

Distribution Statement A: Approved for Public Release; Distribution is Unlimited. AFRL-2021-4182

FINAL REPORT

Development and implementation of a new linearized Riemann solver in TURF for the Euler equations including development of MHD solvers

P.I.: Michael Kapper
20700 Tuxedo Ct, Castro Valley, CA 94552
Email: michael.kapper@gmail.com
Phone: (510) 209-3574

2020

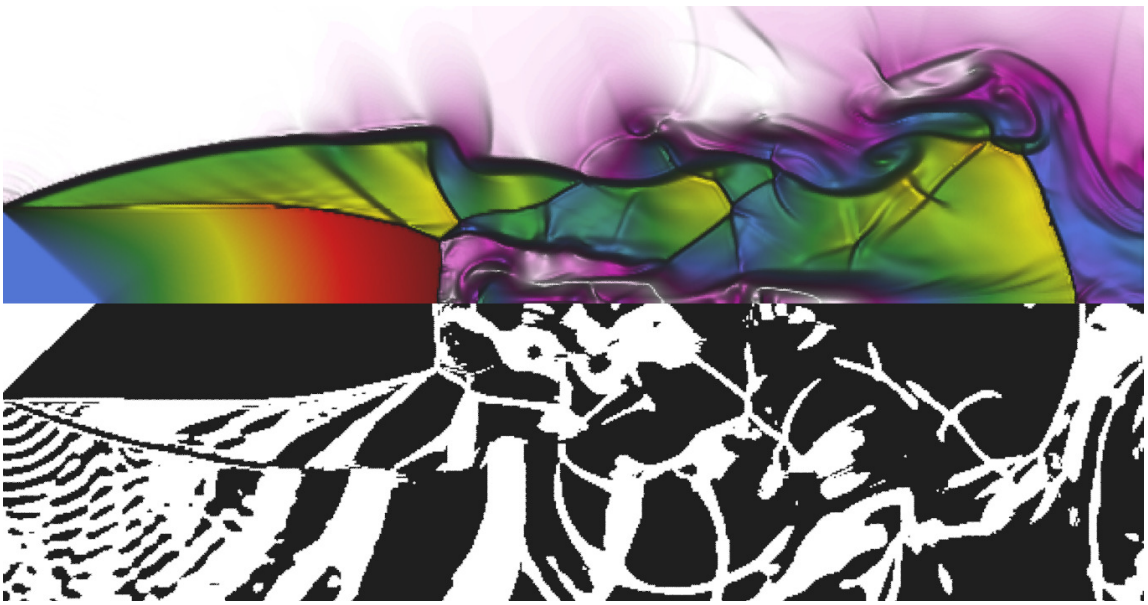

Distribution Statement A: Approved for Public Release; Distribution is Unlimited. AFRL-2021-4182

Chapter 1

A positively-conservative linearized Riemann solver for isentropic real-gas flow transport

Abstract

In this work, a positively-conservative, approximate Riemann solver for the Euler equations under isentropic conditions is developed. It is a flux-difference splitting scheme, based around a characteristic decomposition which is constructed to preserve specific entropy across the nonlinear waves. At its core is a linearization that is fully consistent with the Rankine-Hugoniot relations and is able to resolve contact discontinuities. The scheme is presented for both energy- as well as entropy-conserving formulations, resulting in a novel, hybridized scheme that combines both conservation types through the framework of the linearized Riemann problem. The scheme is also extended to higher order via reconstruction techniques which require a full characteristic decomposition. This is accomplished by introducing a novel set of left Eigenvectors that can be used to obtain a characteristic transformation even when Roe's linearization fails. The resulting scheme is highly accurate and robust in the presence of both kinetically-dominated flows and strong rarefactions. Also introduced are new Eigenvalues with a strong physical basis which are less diffusive than the standard HLLE numerical wave speeds while preserving positivity, which can be applied to other approximate Riemann solvers.

1.1 Introduction

In the simulation of high enthalpy flow, the case of strongly expanding rarefaction waves is a commonly encountered problem, whether it be the result of base flows or highly transient conditions such as rapid thermalization due to applied or generated heat sources. When considering such highly nonlinear flow transport, the role of the numerical scheme becomes crucial. As the strength of the

Distribution Statement A: Approved for Public Release; Distribution is Unlimited. AFRL-2021-4182

nonlinear waves increase, approaching and exceeding the sonic limit, the chosen signal velocities which linearize the rarefaction fan must be able to produce physical and accurate solutions.

Approximate Riemann solvers for the Euler equations generally have two difficulties to deal with when applied to strongly expanding flows. The first is to preserve positivity of pressure and density throughout the reconstructed Riemann fan, while the second is to extract an accurate pressure value from the total energy when the kinetic energy dominates. In regards to the first difficulty, Einfeldt *et al* [1991] showed that Roe's scheme fails to produce a physically-meaningful linearization for expanding flows above a critical Mach number and introduced the HLLE scheme which served as an improvement in this regard. The failure results from underpredicting the nonlinear wave speeds, resulting in nonphysical rarefaction shocks as well as negative densities and pressure in the star or intermediate region of the Riemann fan. In regards to rarefaction waves in particular, the nonlinear nature of the Euler equations increases with the strength of the expansion. Rarefaction waves consist of a diverging fan characteristics that is reduced to a single linear characteristic through linearization. The chosen linearization must be able to approximate the speed of the wave to recover as much of the physical advection as possible. Failure to do so can lead to smeared waves if the wave speed is overestimated or rarefaction shocks if it is underestimated, or even nonphysical states leading to a failure of the linearization, as in the case of Roe's linearization. This nonlinearity cannot be described in a linear advection sense and therefore better approximations must be made. In fact, we could say that an approximation can lead to a change in the physics and great care must therefore be taken in the process.

The second aforementioned difficulty lies in extracting an accurate pressure value from the total energy when the kinetic energy is dominant. This is not a deficiency of any scheme *per se* but rather a conditioning problem of the way fluxes are evaluated and the solution is updated. This problem is independent of whether a scheme is positively conservative or not and manifests itself as a nonphysical spike in temperature and entropy in expanding flows which are sufficiently strong. This overheating phenomenon arises because the truncation errors lead to an overestimate of pressure. This can also be observed in solutions of Roe's scheme for which a valid linearization is produced. This can be a problem not only for correctly capturing the flow properties but also for any kinetic processes which are temperature dependent. Cocchi *et al* [2000] introduced a technique in which the internal energy is linearly convected independently of the total energy for isentropic flows to avoid this loss of precision. This technique was shown to reduce anomolous temperature jumps in expanding base flows. The drawback to such a technique is that the introduced equation is in non-conservative form, introducing a source term which is nontrivial to compute. One possible solution to this is to consider the characteristic decomposition in entropy variables since one is able to explicitly conserve entropy across the nonlinear waves in the Riemann fan. This also helps in assessing the positively conservative nature of a scheme as only positive density in the star region is a necessary requisite to do so. By convecting the entropy, we can extract the pressure in a completely conservative context. By eliminating artificial entropy generation, accurate temperature values can be achieved.

Both of the aforementioned shortcomings would then seem be addressable by the governing equations cast in isentropic form. This has yet to be done in a practical and efficient manner and requires a thorough investigation. There are many challenges to constructing and implementing such a scheme which is the focus of this report which is organized in the following manner. The governing equations are presented for the Euler equations in energy conservation form which are transformed into isentropic form following previous work. The intended finite volume scheme for

Distribution Statement A: Approved for Public Release; Distribution is Unlimited. AFRL-2021-4182

solving the governing equations is then given which requires the approximate solution of the Riemann problem. Previous approximate linearizations are then discussed to give a background before presenting the approach taken here which is entirely specific to the isentropic form of the equations. Practical methods for extending the new linearization to general 3D coordinates as well as hybridization with Roe's scheme in particular and energy-conservation schemes in general are given. The scheme is then applied to selected benchmark problems to assess its capabilities.

1.2 Governing equations

The transport here is described by a continuum description of the gas. It begins with a statement of the Euler equations and which are further developed by adding a transport equation for internal energy and subsequently entropy. As the focus of the current work is isentropic flows, it is natural to work in terms of an entropy variable. The current analysis is restricted to polytropic gas transport in one spatial dimension. We consider here the inviscid compressible Euler equations in conservation form in one dimension:

$$\frac{\partial Q}{\partial t} + \frac{\partial F(Q)}{\partial x} = 0 \tag{1.1}$$

$$Q = \begin{pmatrix} \rho \\ \rho u \\ E \end{pmatrix}, \quad F = \begin{pmatrix} \rho u \\ \rho u^2 + p \\ u H_\circ \end{pmatrix}. \tag{1.2}$$

where ρ is the mass density, u is the velocity (or specific momentum m/ρ), p is the thermodynamic pressure, $H_\circ = E + p$ is stagnation enthalpy density, and the total energy density E is comprised of the internal and kinetic contributions,

$$E = \rho\varepsilon + \frac{1}{2}\rho u^2 \tag{1.3}$$

with ε being the specific internal energy of the gas. The gas is assumed to be calorically ideal such that

$$p = (\gamma - 1)\rho\varepsilon. \tag{1.4}$$

Since the internal energy of the system can only be obtained by subtracting the kinetic energy from the total energy, numerical approximations can lead to gross inaccuracies when the kinetic energy becomes very dominant. This issue was addressed by Cocchi *et al* [2000] and utilized by the FLASH code [2019] by convecting the internal energy separately in the form

$$\frac{\partial \rho\varepsilon}{\partial t} + \frac{\partial[(\rho\varepsilon + p)u]}{\partial x} = u\frac{\partial p}{\partial x} \tag{1.5}$$

This redundancy allows the pressure to be computed directly from internal energy, ε, providing a more accurate value where numerical errors would produce otherwise unacceptable results. The equation is activated when the ratio of internal to kinetic energies falls below a pre-determined

Distribution Statement A: Approved for Public Release; Distribution is Unlimited. AFRL-2021-4182

threshold. Although a positive pressure can now be guaranteed, it comes at the cost of introducing a nonconservative equation into the system. This is coincidentally a similar dilemma encoutered in two-temperature systems in which the thermalization between the electrons and heavy particles is not rapid enough, necessitating a separate temperature for the electrons. A solution to remove the nonconservative energy equation was introduced by Brassier & Gallice [1998] which was to write the electron energy equation in conservative form using entropy variables, leading to an isentropic description of the electrons.

As existing Riemann solvers were extended quite naturally with great success to the two-temperature system, Kapper [2009] took the same approach and applied it to the overall energy equation, showing that it could successfully solve Einfeldt's strong rarefaction problems with accurate pressures. This approach leads to the Euler equations in the isentropic form,

$$Q = \begin{pmatrix} \rho \\ \rho u \\ S \end{pmatrix}, \quad F = \begin{pmatrix} \rho u \\ \rho u^2 + p \\ uS \end{pmatrix}. \tag{1.6}$$

where S is the entropy density. For a polytropic gas, with constant adiabatic exponent γ, the specific entropy function takes the form

$$s = \frac{p}{\rho^\gamma}. \tag{1.7}$$

yielding differential forms for the pressure

$$dp = \rho^{\gamma-1} dS + (\gamma - 1) S \rho^{\gamma-2} d\rho \tag{1.8}$$

and entropy density

$$dS = \frac{dp}{\rho^{\gamma-1}} - (\gamma - 1)\frac{p}{\rho^\gamma} d\rho. \tag{1.9}$$

If, however, the specific heats are temperature dependent, the entropy funtion takes the form

$$s = \frac{p}{e^{s^\circ/R}} \tag{1.10}$$

where s° is the zero-point temperature-dependent component of entropy,

$$s^\circ = \int_0^{T_*} \frac{c_p}{T} dT, \tag{1.11}$$

R is the gas constant, and $p_r = e^{s^\circ/R}$ is the relative pressure. Differentiating the ideal gas law

$$dp = RT d\rho + \rho R dT \tag{1.12}$$

and combining with the Gibbs equation with $dh = c_p dT$

$$ds = c_p \frac{dT}{T} - \frac{dp}{\rho T} \tag{1.13}$$

the differential pressure is found as a function of the conserved quantities,

$$dp = \gamma RT d\rho - (\gamma - 1) T s d\rho + (\gamma - 1) T dS. \tag{1.14}$$

Distribution Statement A: Approved for Public Release; Distribution is Unlimited. AFRL-2021-4182

In practice, the relative pressure and its derivative are tabulated *a priori* and a Newton-Raphson method is used to obtain the temperature from the entropy function which is then used to compute the pressure from the ideal gas law, thus completing the equation of state. For most expanding flows, the temperature dependence for the given jump in variables will be fairly weak, making for a nearly linear dependence of s° on T and a fast convergence. The choice of the entropy function does not affect the derivation of the Riemann solver, and the pressure can be left in it's general form.

This form of the equations is highly desireable since both direct access to the pressure is available and it is fully conservative. Its validity is restricted to shock-free regions of flow which is entirely acceptable since we anticipate kinetic energy dominated flows to be in regions characterized by strong rarefaction, in which case the flow is isentropic. However, since it is in pure conservation for, it is valid in regions of isentropic discontinuities which is extremely valuable when considering contact discontinuities.

We require the entropy equation as it allows the capturing of contact discontinuities and other entropy waves. In the absence of such entropy jumps, the equation becomes redundant and must be handled accordingly.

1.3 The Riemann problem

In order to find numerical solutions of equation systems (1.2) and (1.6), a finite-volume method is employed with discrete cells i separated by interfaces $i+1/2$ spaced Δx apart. The cell average conservative quantites are given in the $x-$direction without any loss of generality by

$$Q_i^n = \frac{1}{\Delta x}\int_{x_{i-1/2}}^{x_{i+1/2}} Q(x,t^n)dx \tag{1.15}$$

at discrete time level t^n. The update after one time step of size Δt for the cell average reads as

$$Q_i^{n+1} = Q_i^n + \frac{\Delta t}{\Delta x}(F_{i-1/2}^{(\mathrm{num})} - F_{i+1/2}^{(\mathrm{num})}) \tag{1.16}$$

and contains a numerical flux function

$$F_{i+1/2}^{(\mathrm{num})} = \tilde{F}(Q_{L,i+1/2}, Q_{R,i+1/2}). \tag{1.17}$$

which requires the left and right limiting values of the variable vector Q at the interface $i+1/2$. The evaluation of the numerical flux function is accomplished by considering the Riemann problem

$$\mathbf{Q}(x,0) = \begin{cases} \mathbf{Q}_{\mathrm{L}} & \text{for} \quad x<0 \\ \mathbf{Q}_{\mathrm{R}} & \text{for} \quad x>0 \end{cases} \tag{1.18}$$

In this work the following general form for the numerical flux function given by

$$\tilde{F}(Q_{L,i+1/2}, Q_{R,i+1/2}) = \frac{1}{2}(F(\mathbf{Q}_{\mathrm{L}}) + F(\mathbf{Q}_{\mathrm{R}})) - \frac{1}{2}\tilde{A}(\mathbf{Q}_{\mathrm{L}}, \mathbf{Q}_{\mathrm{R}})(\mathbf{Q}_{\mathrm{R}} - \mathbf{Q}_{\mathrm{L}}) \tag{1.19}$$

known as flux difference splitting will be assumed where the Jacobian matrix $\tilde{A}$ is a linearization of the Riemann problem, acting as a dissipation mechanism to stabilize the scheme.

Distribution Statement A: Approved for Public Release; Distribution is Unlimited. AFRL-2021-4182

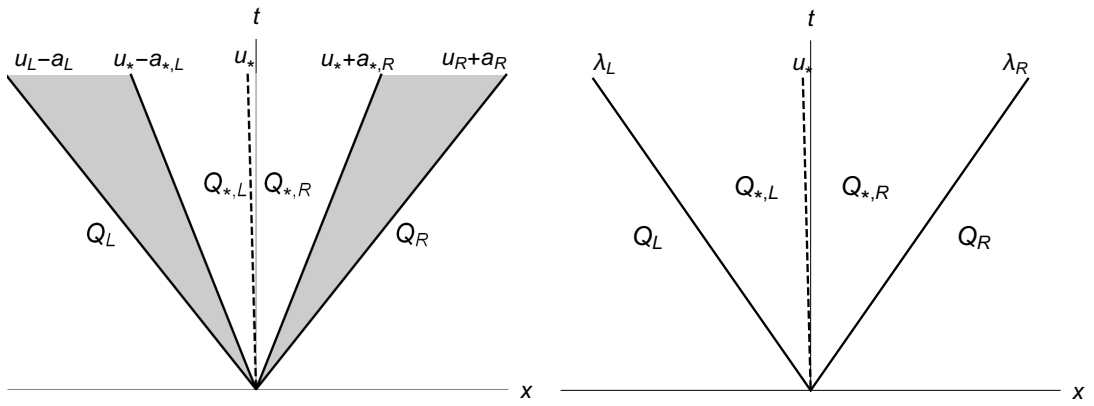

Figure 1.1: A Riemann fan for the case of two rarefaction waves with a central *star* region separated by a contact discontinuity *left*. An approximation produced by a linearization of the problem *right*.

1.4 Linearization of the rarefaction problem

An essential part of approximate Riemann solvers based on the flux difference splitting approach is the linearization of the exact Riemann problem. For system Eq. (1.6) rarefaction waves are the only nonlinear waves to be considered since the system is not applicable to shock waves. A linearization of the nonlinear waves results in a fan of single line characteristics of constant speed as shown in Fig. 1.1. The difficulty and therefore trick of linearizing the Riemann problem is developing a scheme that reults in a suitable wave speed which reproduces the physical nonlinear effects as best as possible. In the case of a rarefaction wave, the nonlinear diverging characterisitcs are collapsed onto a single linear characteristic. Although by definition a linearization cannot resolve the structure of the fan itself, a bit of control can be exercised over the wave speeds to influence the jump in conserved quantities across the rarefaction wave as well as their intermediate states. In the following sections, we briefly discuss Roe's, Einfeldt's, and the HLLC linearizations before detailing our current approach. In all three cases, the approach is to find a linear wave speed for the rarefaction wave by choosing an appropriate averaged state. Our new scheme retains the same linear fan structure as Roe's scheme, namely 2 intermediate states for the 1D Euler equations. The common requirements for the following flux-difference splitting schemes is that the Jacobian matrix $\mathbf{A}$ is required to:

- have real Eigenvalues $\lambda_i = \lambda_i(\mathbf{Q}_\mathrm{L}, \mathbf{Q}_\mathrm{R})$, which are defined to be increasing as $\lambda_1 \leq \lambda_2 \leq \cdots \leq \lambda_m$ and a complete set of linearly independent right eigenvectors, $\vec{r}^{(1)}, \vec{r}^{(2)}, \ldots, \vec{r}^{(m)}$
- be consistent with the exact Jacobian, $\hat{\mathbf{A}}(\mathbf{Q}_\mathrm{L}, \mathbf{Q}_\mathrm{R}) = \mathbf{A}(\hat{\mathbf{Q}})$
- and satisfies conservation across discontinuities, $\mathbf{F}(\mathbf{Q}_\mathrm{R}) - \mathbf{F}(\mathbf{Q}_\mathrm{L}) = \hat{\mathbf{A}}(\mathbf{Q}_\mathrm{R} - \mathbf{Q}_\mathrm{L})$

Distribution Statement A: Approved for Public Release; Distribution is Unlimited. AFRL-2021-4182

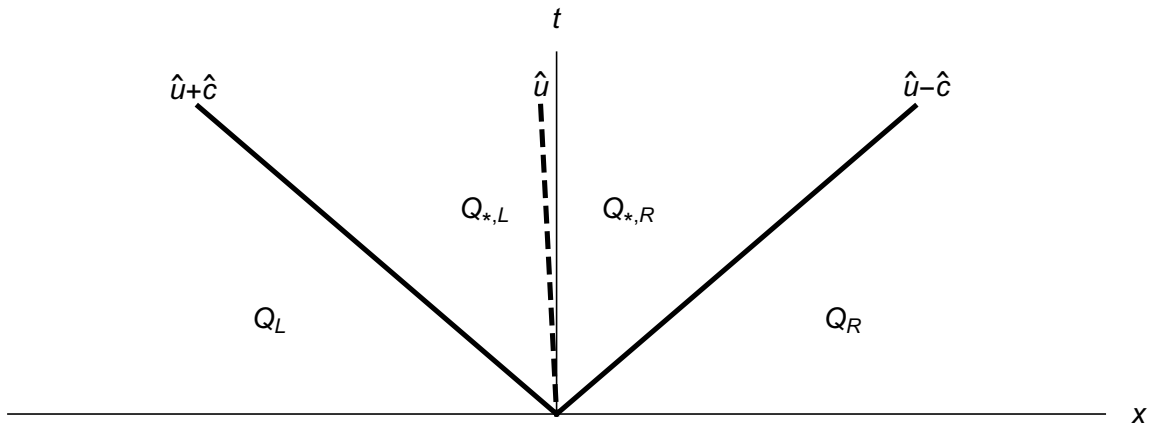

Figure 1.2: Roe's linearization for expansion problem with left- and right-traveling rarefaction waves.

1.4.1 Roe's linearization

Roe's linearization remains a staple of shock capturing schemes because it provides an approximation of all waves in the system by utilizing an intermediate state which is elegant yet simple to compute if the Eigensystem is known. With one linear contact and two nonlinear waves for the one-dimensional system, it allows for two intermediate star states in the solution of 1D Godunov's problem as illustrated in Fig. 1.2. However, Roe's scheme is well known to underestimate the wave speed of the linearized characteristic.

The well-known linearization for Eqs. (1.2) is given for a polytropic gas by

$$\mathbf{A} = \begin{pmatrix} 0 & 1 & 0 \\ (\gamma-3)\frac{1}{2}u^2 & -(\gamma-3)u & \gamma-1 \\ (\gamma-1)u^3 - \frac{\gamma u E}{\rho} & \frac{\gamma E}{\rho} - (\gamma-1)\frac{3}{2}u^2 & \gamma u \end{pmatrix} \tag{1.20}$$

and can be decomposed into real, independent Eigenvectors

$$\vec{r}_1 = \begin{pmatrix} 1 \\ \tilde{u} - \tilde{c} \\ \tilde{h}_\circ - \tilde{a}\tilde{u} \end{pmatrix}, \quad \vec{r}_2 = \begin{pmatrix} 1 \\ \tilde{u} \\ \frac{1}{2}\tilde{u}^2 \end{pmatrix}, \quad \vec{r}_3 = \begin{pmatrix} 1 \\ \tilde{u} + \tilde{c} \\ \tilde{h}_\circ + \tilde{a}\tilde{u} \end{pmatrix}. \tag{1.21}$$

with Roe averages defined by

$$\tilde{\rho} = \sqrt{\rho_{\text{L}}\rho_{\text{R}}}, \tag{1.22}$$

$$\tilde{u} = \beta_{\text{L}} u_{\text{L}} + \beta_{\text{R}} u_{\text{R}}, \tag{1.23}$$

and

$$\tilde{h}_\circ = \beta_{\text{L}} h_{\circ_{\text{L}}} + \beta_{\text{R}} h_{\circ_{\text{R}}} \tag{1.24}$$

with $\beta_{\text{L}} = \rho_{\text{L}}/(\rho_{\text{L}} + \rho)$ and $\beta_{\text{R}} = 1 - \beta_{\text{L}}$, which produce a Jacobian at the cell interface consistent with the exact Jacobian while also satisfying the Rankine-Hugoniot jump conditions. The left

Distribution Statement A: Approved for Public Release; Distribution is Unlimited. AFRL-2021-4182

Eigenvectors take the form

$$\vec{\ell}_1 = \frac{1}{|R|}\begin{pmatrix} -\tilde{u}(\frac{1}{2}\tilde{a}\tilde{u}+\tilde{h}) \\ \tilde{a}\tilde{u}+\tilde{h} \\ -\tilde{a} \end{pmatrix}^T, \quad \vec{\ell}_2 = \frac{1}{|R|}\begin{pmatrix} \tilde{a}(\tilde{u}^2-2\tilde{h}) \\ -2\tilde{a}\tilde{u} \\ -(\gamma-1)\tilde{s} \end{pmatrix}^T, \quad \vec{\ell}_3 = \frac{1}{|R|}\begin{pmatrix} -\tilde{u}(\frac{1}{2}\tilde{a}\tilde{u}+\tilde{h}) \\ \tilde{a}\tilde{u}+\tilde{h} \\ -\tilde{a} \end{pmatrix}^T. \tag{1.25}$$

where $|R| = -2\tilde{a}\tilde{h}$. The same approach for linearization can be applied to the Jacobian matrix from the energy conservation form of the equations, Eq. (1.6), which take the form for a polytropic gas

$$\mathbf{A} = \begin{pmatrix} 0 & 1 & 0 \\ (\gamma-1)s\rho^{\gamma-1} & 2u & \rho^{\gamma-1} \\ -us & s & u \end{pmatrix} \tag{1.26}$$

and can be decomposed into real, independent Eigenvectors

$$\vec{r}_1 = \begin{pmatrix} 1 \\ \tilde{u}-\tilde{c} \\ \tilde{s} \end{pmatrix}, \quad \vec{r}_2 = \begin{pmatrix} 1 \\ \tilde{u} \\ -(\gamma-1)\tilde{s} \end{pmatrix}, \quad \vec{r}_3 = \begin{pmatrix} 1 \\ \tilde{u}+\tilde{c} \\ \tilde{s} \end{pmatrix}. \tag{1.27}$$

with Roe averages defined by

$$\tilde{\rho} = \sqrt{\rho_{\text{L}}\rho_{\text{R}}}, \tag{1.28}$$

$$\tilde{u} = \beta_{\text{L}}u_{\text{L}} + \beta_{\text{R}}u_{\text{R}}, \tag{1.29}$$

and

$$\tilde{s} = \beta_{\text{L}}s_{\text{L}} + \beta_{\text{R}}s_{\text{R}}. \tag{1.30}$$

This produces a Jacobian at the cell interface consistent with the exact Jacobian while also satisfying the Rankine-Hugoniot jump conditions. In addition, the wave strengths $\alpha_i (i = 1, \ldots, 3)$ are defined as the coefficients of the projection of $\mathbf{Q}_{\text{R}} - \mathbf{Q}_{\text{L}}$ onto the right Eigenvector basis,

$$\mathbf{Q}_{\text{R}} - \mathbf{Q}_{\text{L}} = \alpha_1\vec{r}^{(1)} + \alpha_2\vec{r}^{(2)} + \alpha_3\vec{r}^{(3)}. \tag{1.31}$$

The states $\mathbf{Q}_{*,\text{L}}$ and $\mathbf{Q}_{*,\text{R}}$ are given by

$$\mathbf{Q}_{*,\text{L}} = \mathbf{Q}_{\text{L}} + \alpha_1\vec{r}^{(1)} \tag{1.32}$$

and

$$\mathbf{Q}_{*,\text{R}} = \mathbf{Q}_{\text{L}} + \alpha_1\vec{r}^{(1)} + \alpha_2\vec{r}^{(2)} + \alpha_3\vec{r}^{(3)} = \mathbf{Q}_{\text{R}} - \alpha_3\vec{r}^{(3)}. \tag{1.33}$$

From these relations, the values for the intermediate star region can be deduced for Roe's linearization. For the Riemann problem with the initial data $\mathbf{Q}_{\text{L}} = (\rho, -\rho u, E)^T$ and $\mathbf{Q}_{\text{R}} = (\rho, \rho u, E)^T$, the density and pressure in the star region are given by

$$\rho_* = \rho(1 - \text{Ma}) \quad \text{and} \quad p_* = s(\rho_*)^\gamma \tag{1.34}$$

respectively, leading to the necessary condition of $\text{Ma} \leq 1$ in order for the problem to be linearizable, and is independent of γ. This does not offer much advantage over Roe's linearization for the energy conservation scheme which was shown to have the very similar condition $\text{Ma} \leq \sqrt{2/(\gamma(3-\gamma))}$, or $\text{Ma} \leq 0.94$ for $\gamma = 7/5$.

Distribution Statement A: Approved for Public Release; Distribution is Unlimited. AFRL-2021-4182

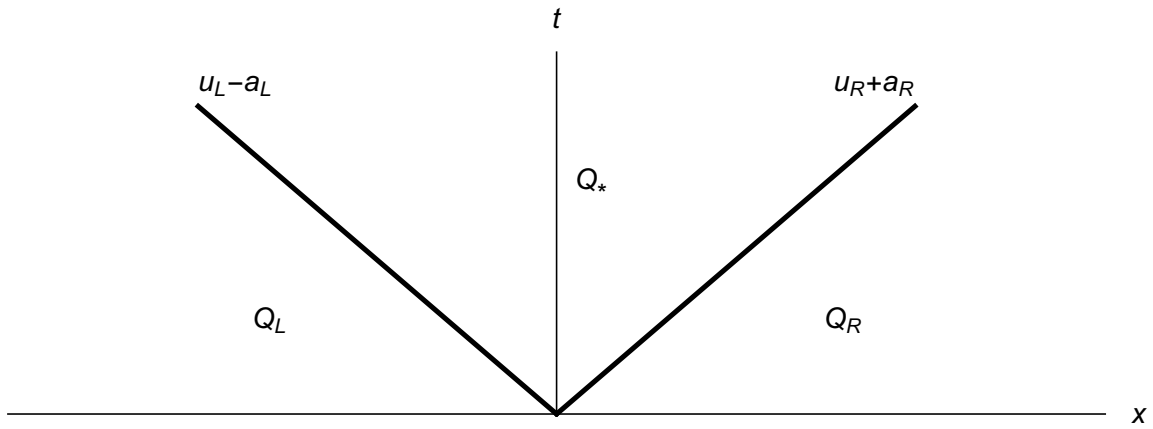

Figure 1.3: Characteristic fan for HLLE linearization of the expansion problem.

The shortcoming of Roe's linearization for both energy and entropy conservation forms is the restriction that the Roe averages place on the nonlinear numerical wave speeds. The linearized wave speeds $\tilde{u} \pm \tilde{c}$ grossly underpredicts the rarefaction wave speeds and thus to maintain conervation of the conservative variables across the fan, the mass density and pressure must take on unphysically negative values.

1.4.2 HLLE linearization

Because of the failure of Roe's linearization for relatively strong rarefactions, the HLLE linearization became a viable fix, with the two often hybridized together (Quirk 1991). In contrast to Roe's linearization, the HLLE Riemann solver does not explicitly resolve the linear contact wave and thus is limited by a single star intermediate region as can be seen in Fig. 1.3. This compromise of the linear wave resolution however allows much greater flexibility in choosing the nonlinear wave speeds. This in turn makes it trivial to ensure both positive density and pressure in the star region while maintaing conservation across the jumps

The intermediate star region produced by the HLLE-Riemann solver linearization is given by

$$\mathbf{Q}_*^{\text{HLLE}} = \frac{b_{\text{R}}\mathbf{Q}_{\text{R}} - b_{\text{L}}\mathbf{Q}_{\text{L}}}{b_{\text{R}} - b_{\text{L}}} - \frac{\mathbf{F}_{\text{R}} - \mathbf{F}_{\text{L}}}{b_{\text{R}} - b_{\text{L}}} \tag{1.35}$$

with the resulting mass density, velocity, and pressure in the intermediate state taking the forms

$$\rho_*^{\text{HLLE}} = \frac{\rho_{\text{R}}(b_{\text{R}} - u_{\text{R}}) + \rho_{\text{L}}(b_{\text{L}} - u_{\text{L}})}{b_{\text{R}} - b_{\text{L}}} \tag{1.36}$$

$$u_*^{\text{HLLE}} = \frac{(b_{\text{R}} - u_{\text{R}})\rho_{\text{R}}u_{\text{R}} + (b_{\text{L}} - u_{\text{L}})\rho_{\text{L}}u_{\text{L}} - \Delta p}{(b_{\text{R}} - u_{\text{R}})\rho_{\text{R}} - (b_{\text{L}} - u_{\text{L}})\rho_{\text{L}}} \tag{1.37}$$

$$p_*^{\text{HLLE}} = \frac{(b_{\text{R}} - u_{\text{R}})S_{\text{R}} + (b_{\text{L}} - u_{\text{L}})S_{\text{L}}}{b_{\text{R}} - b_{\text{L}}}(\rho_*^{\text{HLLE}})^{\gamma-1} \tag{1.38}$$

Distribution Statement A: Approved for Public Release; Distribution is Unlimited. AFRL-2021-4182

respectively. Einfeldt *et al* proposed taking the numerical signal velocities to be the head wave speed of the rarefaction wave, $b_{\text{R}} = u_{\text{R}} + a_{\text{R}}$ and $b_{\text{L}} = u_{\text{L}} - a_{\text{L}}$, which result in a positively conservative scheme. The chioce of wave speed is extremely robust but however extremely diffusive and as a result went on to provide the minimum allowed values which would result in a positive intermediate density:

$$a_{\text{L}} \geq \frac{\gamma - 1}{2\gamma} c_{\text{L}}^2 \quad \text{and} \quad a_{\text{R}} \geq \frac{\gamma - 1}{2\gamma} c_{\text{R}}^2 \tag{1.39}$$

where c is the speed of sound. Because the HLLE linearization is based on nonlinear wavespeeds of the head of the rarefaction wave, it is overly diffusive and results in an intermediate state with values which are too high. Furthermore, the merging of the intermediate states smears out any contacts which are generated from the initial conditions. To avoid the convergent case in which , the numerical speeds must be modified to allow for convergent flows as well, as in the case of shocks. The speeds are modified according to

$$\lambda_{\text{L}} = \min[u_{\text{L}} - a_{\text{L}}, \hat{u} - \hat{a}] \quad \text{and} \quad \lambda_{\text{R}} = \max[u_{\text{R}} + a_{\text{R}}, \hat{u} + \hat{a}] \tag{1.40}$$

The advantage over Roe's linearization is that the HLLE linearization is positively conservative such that ρ and E remain positive for all conditions. This contributes to the schemes robust nature and allows for solutions where Roe's scheme fails. However it does not provide a transformation to characteristic space and Roe's linearization is still relied upon for high-order reconstruction schemes.

1.4.3 A new linearization

It would present a great advantage if the flexibility of the HLLE method in selecting the nonlinear wave speeds could be combined with the power of Roe's scheme to resolve the contact wave while maintaining a flux-difference splitting formulation. For the Euler equations with conservation of energy, it is not possible to derive closed form linearizations due to the complexity of the energy jump across the rareaction waves. However, the entropy variables present a natural expression for the linearization since the specific entropy does not jump across the rarefaction waves.

Therefore, instead of abandoning the characteristic decomposition, a heuristic method is employed in which any jump in the specific entropy across the each nonlinear wave is strictly eliminated. This is uniquely obtained by letting $s = s_{\text{L}}$ for the left-running nonlinear Eigenvector and $s = s_{\text{R}}$ for the right-running nonlinear Eigenvector. Furthermore, it is desireable to allow the Eigenvalues to be as general as possible since the rarefaction shocks caused by Roe's scheme result from the spectral radius being too small. The numerical velocity for the contact is taken simply as the the velocity in the star region, to be determined by the jump relations. Also, since there is a jump in density across the contact wave, the term $\partial S/\partial \rho_*$ is left in its general form to be determined by the jump conditions. Since across the contact wave the derivative $\partial S/\partial \rho_*$ cannot be explicitly computed because of the jump in entropy, the quantity must follow from the jump conditions. This results in Eigenvectors of the form

$$\vec{r}^{(1)} = \begin{pmatrix} 1 \\ \lambda_{\text{L}} \\ s_{\text{L}} \end{pmatrix}, \quad \vec{r}^{(2)} = \begin{pmatrix} 1 \\ u_* \\ \frac{\partial S}{\partial \rho}_* \end{pmatrix}, \quad \vec{r}^{(3)} = \begin{pmatrix} 1 \\ \lambda_{\text{R}} \\ s_{\text{R}} \end{pmatrix}. \tag{1.41}$$

Distribution Statement A: Approved for Public Release; Distribution is Unlimited. AFRL-2021-4182

where the nonlinear wave speeds λ are of the form $u \pm a$. This leaves the middle Eigenvector to be a function of the speed of the contact wave and the partial derivative of the entropy with respect to density, $S_{\rho_*} = \partial S / \partial \rho_*$. The corresponding left Eigenvectors are found to be

$$\vec{l}^{(1)} = \frac{1}{|R|} \begin{pmatrix} \frac{\partial S}{\partial \rho}_* \lambda_{\mathrm{R}} - s_{\mathrm{R}} u_* \\ s_{\mathrm{R}} - \frac{\partial S}{\partial \rho}_* \\ u_* - \lambda_{\mathrm{R}} \end{pmatrix}^T, \quad \vec{l}^{(2)} = \frac{1}{|R|} \begin{pmatrix} s_{\mathrm{R}} \lambda_{\mathrm{L}} - s_{\mathrm{L}} \lambda_{\mathrm{R}} \\ s_{\mathrm{L}} - s_{\mathrm{R}} \\ \lambda_{\mathrm{R}} - \lambda_{\mathrm{L}} \end{pmatrix}^T, \quad \vec{l}^{(3)} = \frac{1}{|R|} \begin{pmatrix} s_{\mathrm{L}} u_* - \lambda_{\mathrm{L}} \frac{\partial S}{\partial \rho}_* \\ \frac{\partial S}{\partial \rho}_* - s_{\mathrm{L}} \\ \lambda_{\mathrm{L}} - u_* \end{pmatrix}^T. \tag{1.42}$$

by inverting the matrix R, the columns of which are the right Eigenvectors. Here, $|R|$ denotes the determinant of R

$$|R| = s_{\mathrm{R}}(\lambda_{\mathrm{L}} - u_*) - s_{\mathrm{L}}(\lambda_{\mathrm{R}} - u_*) + \frac{\partial S}{\partial \rho}_* (\lambda_{\mathrm{R}} - \lambda_{\mathrm{L}}) \tag{1.43}$$

The Jacobian at the cell interface is then determined by

$$A = R \Lambda L \tag{1.44}$$

where R is the column matrix of right Eigenvectors, L is the row matrix of left Eigenvalues, and Λ is the diagonal matrix of Eigenvalues.

$$A = \frac{1}{|R|} \begin{pmatrix} 0 & & \\ u_*(\lambda_{\mathrm{R}}(\lambda_{\mathrm{R}} - u_*)s_{\mathrm{L}} - \lambda_{\mathrm{L}}(\lambda_{\mathrm{L}} - u_*)s_{\mathrm{R}}) - \frac{\partial S}{\partial \rho}_* \lambda_{\mathrm{L}} \lambda_{\mathrm{R}} \Delta\lambda & \cdots & \\ \frac{\partial S}{\partial \rho}_* (s_{\mathrm{L}}(\lambda_{\mathrm{L}} - u_*)\lambda_{\mathrm{R}} - s_{\mathrm{R}}(\lambda_{\mathrm{R}} - u_*)\lambda_{\mathrm{L}}) + u_* s_{\mathrm{L}} s_{\mathrm{R}} \Delta\lambda & & \\ & |R| & \\ & s_{\mathrm{R}}(\lambda_{\mathrm{R}}^2 - u_*^2) - s_{\mathrm{L}}(\lambda_{\mathrm{L}}^2 - u_*^2) + \frac{\partial S}{\partial \rho}_* (\lambda_{\mathrm{R}}^2 - \lambda_{\mathrm{L}}^2) & \cdots \\ & \frac{\partial S}{\partial \rho}_* (s_{\mathrm{R}}(\lambda_{\mathrm{R}} - u_*) - s_{\mathrm{L}}(\lambda_{\mathrm{L}} - u_*)) - s_{\mathrm{L}} s_{\mathrm{R}} \Delta\lambda & \\ & & 0 \\ & & (\lambda_{\mathrm{L}} - u_*)(\lambda_{\mathrm{R}} - u_*)\Delta\lambda \\ & & s_{\mathrm{R}} \lambda_{\mathrm{R}}(\lambda_{\mathrm{L}} - u_*) - s_{\mathrm{L}} \lambda_{\mathrm{L}}(\lambda_{\mathrm{R}} - u_*) + u_* \frac{\partial S}{\partial \rho}_* \Delta\lambda \end{pmatrix} \tag{1.45}$$

As can be seen, the Jacobian is not defined by a single, well-defined state, but rather a complex combination of left and right states. This however does not take awway from the linearization. It is still valid that Eq. (1.45) is still consistent with the exact Jacobian. This Jacobian is then used to satisfy the Rankine-Hugoniot conditions via

$$\Delta F = A \Delta Q, \tag{1.46}$$

yielding an intermediate wave speed identical to that of the HLLE linearization,

$$u_* = \frac{\Delta(\mu u) - \Delta p}{\Delta \mu} \tag{1.47}$$

and the partial derivative,

$$\frac{\partial S}{\partial \rho}_* = \frac{\mathcal{P} \Delta(\mu s) + \mu_{\mathrm{L}} \mu_{\mathrm{R}} \Delta\lambda \Delta s}{\mathcal{P} \Delta \mu}, \tag{1.48}$$

Distribution Statement A: Approved for Public Release; Distribution is Unlimited. AFRL-2021-4182

both expressed in terms of the left and right nonlinear numerical signal speeds, where $\mu_{\text{L}} = \rho_{\text{L}}(\lambda_{\text{L}} - u_{\text{L}})$, $\mu_{\text{R}} = \rho_{\text{R}}(\lambda_{\text{R}} - u_{\text{R}})$, and $\mathcal{P} = \mu_{\text{R}}(\lambda_{\text{L}} - u_{\text{R}}) - \mu_{\text{L}}(\lambda_{\text{R}} - u_{\text{L}}) + \Delta p$ have been defined. The difference operator is defined as $\Delta(\cdot) = (\cdot)_{\text{R}} - (\cdot)_{\text{L}}$. The contact wave speed is equivalent to the HLL intermediate star state velocity. This is the unique result for satisfying the jump conditions. With these variables defined and using we have that the wave strengths $\alpha_i (i = 1, \ldots, 3)$ as the coefficients of the projection of $\mathbf{Q}_{\text{R}} - \mathbf{Q}_{\text{L}}$ onto the right Eigenvector basis,

$$\Delta \mathbf{Q} = \sum_{k=1}^{N} \alpha_k \vec{r}^{(k)} \tag{1.49}$$

where the jump across k-th wave is given by

$$\Delta Q^{(k)} = \alpha_k \vec{r}^{(k)} \tag{1.50}$$

and k-th wave strength,

$$\alpha_k = \vec{\ell}^{(k)} \Delta Q \tag{1.51}$$

the conserved quantities in the intermediate states are found to be

$$\rho_{*,\text{L}} = \rho_{\text{L}} + \alpha_1 \vec{r}_1^{(1)} \quad \text{and} \quad \rho_{*,\text{R}} = \rho_{\text{R}} - \alpha_3 \vec{r}_1^{(3)}, \tag{1.52}$$

$$(\rho u)_{*,\text{L}} = (\rho u)_{\text{L}} + \alpha_1 \vec{r}_2^{(1)} \quad \text{and} \quad (\rho u)_{*,\text{R}} = (\rho u)_{\text{R}} - \alpha_3 \vec{r}_2^{(3)}, \tag{1.53}$$

and

$$S_{*,\text{L}} = S_{\text{L}} + \alpha_1 \vec{r}_3^{(1)} \quad \text{and} \quad S_{*,\text{R}} = S_{\text{R}} - \alpha_3 \vec{r}_3^{(3)} \tag{1.54}$$

from which the primitive quantities can be derived

$$u_{*,\text{L}} = \frac{(\rho u)_{*,\text{L}}}{\rho_{*,\text{L}}} \quad \text{and} \quad u_{*,\text{R}} = \frac{(\rho u)_{*,\text{R}}}{\rho_{*,\text{R}}} \tag{1.55}$$

$$s_{*,\text{L}} = \frac{S_{*,\text{L}}}{\rho_{*,\text{L}}} = s_{\text{L}} \quad \text{and} \quad s_{*,\text{R}} = \frac{S_{*,\text{R}}}{\rho_{*,\text{R}}} = s_{\text{R}} \tag{1.56}$$

and

$$p_{*,\text{L}} = \rho_{*,\text{L}}^{\gamma} s_{\text{L}} \quad \text{yielding} \quad p_{*,\text{R}} = \rho_{*,\text{R}}^{\gamma} s_{\text{R}} \tag{1.57}$$

Solving Eq. (1.52), the mass density in the left star region is explicitly given by

$$\rho_{*,\text{L}} = \frac{\Delta \mu}{|R|} \left(\frac{\partial S}{\partial \rho}_{*} - s_{\text{R}} \right) \tag{1.58}$$

Inserting Eqs. (1.43) and (1.48) into Eq. (1.58), simplifying and inserting Eq. (1.47) into the numerator of the result, we find

$$\rho_{*,\text{L}} = \rho_{\text{L}} \left(\frac{\lambda_{\text{L}} - u_{\text{L}}}{\lambda_{\text{L}} - u_{*}} \right) \tag{1.59}$$

Similarly for right star region,

$$\rho_{*,\text{R}} = \rho_{\text{R}} \left(\frac{\lambda_{\text{R}} - u_{\text{R}}}{\lambda_{\text{R}} - u_{*}} \right). \tag{1.60}$$

Distribution Statement A: Approved for Public Release; Distribution is Unlimited. AFRL-2021-4182

With u_* and $\frac{\partial S}{\partial \rho}_*$ as defined above, it is easy to show that $u_* = u_{*,\mathrm{L}} = u_{*,\mathrm{R}}$ is automatically satisfied. Furthermore, $u_{*,\mathrm{L}} = u_{*,\mathrm{R}}$ can also be solved for $\frac{\partial S}{\partial \rho}_*$

$$\frac{\partial S}{\partial \rho}_* = \frac{(\lambda_\mathrm{R} - u_\mathrm{R})(\lambda_\mathrm{L} - u_*)S_\mathrm{L} - (\lambda_\mathrm{L} - u_\mathrm{L})(\lambda_\mathrm{R} - u_*)S_\mathrm{L}}{(\lambda_\mathrm{R} - u_\mathrm{R})(\lambda_\mathrm{L} - u_*) - (\lambda_\mathrm{L} - u_\mathrm{L})(\lambda_\mathrm{R} - u_*)} \tag{1.61}$$

which yields a nice compact form

$$\frac{\partial S}{\partial \rho}_* = \frac{\rho_{*,\mathrm{R}} s_\mathrm{R} - \rho_{*,\mathrm{L}} s_\mathrm{L}}{\rho_{*,\mathrm{R}} - \rho_{*,\mathrm{L}}} = \frac{\Delta S_*}{\Delta \rho_*} \tag{1.62}$$

Eq. (1.47) for the contact wave speed is equivalent to the HLL star state velocity (see Toro [1999] and Batten [1999]) although the derivations result from different approaches. Nothing has been guaranteed in the star state with these values other than that entropy is constant across the nonlinear waves. To complete the scheme without any further conditions, we must simply select a viable wave speed. For maximum robustness, we can select the HLLE signal velocities. In this case u_* satisfies the Rankine-Hugoniot jump conditions but does not guarantee a constant pressure across the contact, hence the signal speed for the contact discontinuity will differ from the exact solution as will the values in the star region.

Note that no restrictions have been put on the nonlinear wave speeds other than that they must produce positive density and pressure values in the star state. From Eqs. (1.59) and (1.60), the only restriction on the wave speeds are $\lambda_\mathrm{L} < u_\mathrm{L}$ and $\lambda_\mathrm{R} > u_\mathrm{R}$. The relatively unrestrictive nature of the condition is due to the fact that $p_{*,\mathrm{L}}$ and $p_{*,\mathrm{R}}$ are not held constant across the contact wave. Thus, they can vary quite differently from one another while satisfying the jump conditions. Constant pressure across the contact wave can be enforced by requiring $p_* = p_{*,\mathrm{L}} = p_{*,\mathrm{R}}$. Solving for $p_{*,\mathrm{L}} = p_{*,\mathrm{R}}$ yields both

$$\frac{\partial S}{\partial \rho}_* = \frac{s_\mathrm{R}^{1/\gamma} s_\mathrm{L} - s_\mathrm{L}^{1/\gamma} s_\mathrm{R}}{\Delta s^{1/\gamma}} \tag{1.63}$$

and

$$u_* = \frac{\mu_\mathrm{R} s_\mathrm{R}^{1/\gamma} \lambda_\mathrm{L} - \mu_\mathrm{L} s_\mathrm{L}^{1/\gamma} \lambda_\mathrm{R}}{\Delta(\mu s^{1/\gamma})}. \tag{1.64}$$

Now, by setting Eqs. (1.48) and (1.63) equal to each other,

$$\frac{s_\mathrm{R}^{1/\gamma} s_\mathrm{L} - s_\mathrm{L}^{1/\gamma} s_\mathrm{R}}{\Delta s^{1/\gamma}} = \frac{\mathcal{P}\Delta(\mu s) + \mu_\mathrm{L}\mu_\mathrm{R}\Delta\lambda\Delta s}{\mathcal{P}\Delta\mu}, \tag{1.65}$$

or, equivalently, Eqs. (1.47) and (1.64)

$$\frac{\Delta(\mu u) - \Delta p}{\Delta \mu} = \frac{\mu_\mathrm{R} s_\mathrm{R}^{1/\gamma} \lambda_\mathrm{L} - \mu_\mathrm{L} s_\mathrm{L}^{1/\gamma} \lambda_\mathrm{R}}{\Delta(\mu s^{1/\gamma})}, \tag{1.66}$$

the jump conditions can be enforced while pressure is held constant across the contact wave. If the nonlinear wave speeds are assumed to be of the form $\lambda_\mathrm{L} = u_\mathrm{L} - \hat{a}$ and $\lambda_\mathrm{R} = u_\mathrm{R} + \hat{a}$, $\hat{a}$ can be solved for from either of the two preceding equations to yield

$$\hat{a} = -\frac{\Delta u \Delta(\rho p^{1/\gamma})}{2(\rho_\mathrm{L} + \rho_\mathrm{R})\Delta p^{1/\gamma}} + \sqrt{\left[\frac{\Delta u \Delta(\rho p^{1/\gamma})}{2(\rho_\mathrm{L} + \rho_\mathrm{R})\Delta p^{1/\gamma}}\right]^2 + \frac{\Delta p \Delta p^{2/\gamma}}{(\rho_\mathrm{L} + \rho_\mathrm{R})(\Delta p^{1/\gamma})^2}}. \tag{1.67}$$

Distribution Statement A: Approved for Public Release; Distribution is Unlimited. AFRL-2021-4182

This form of $\hat{a}$ leads to wave speeds which guarantee positivity as well as guaranteeing that the Eigenvalues are increasing according to $\lambda_{\text{L}} < u_* < \lambda_{\text{R}}$. Note that the second term in the radicand is related to the sound speed which will become more obvious in the following sections. The advantage of this form is that for symmetrical expanding flows, the star state velocity is zero.

Homentropic case $\Delta s = 0$

When the specific entropy of both the left and right states of the Riemann problem are equal, the equations reduce to the homentropic form. In this limit, as Δs approaches 0, the Eigensystem simplifies significantly. Special attention must be paid to this case since it can greatly affect the conditioning of the linearization. This is an important case as much of the flowfield can be in such a state. In the absence of contacts, this is certainly the case. When the entropy gradient vanishes at a cell interface, the contact wave collapses, making the system over defined. However, there is an interesting caveat; without the contact wave, p_* is unconditionally constant in the intermediate region. For the case $\Delta s \to 0$, $s_{\text{L}} = s_{\text{R}} = s$, the contact wave vanishes and the entropy equation becomes irrelevant. Since the majority of flows will be contact free, this is the dominant case for solutions with smooth flows. In this limit, the partial derivative in Eq. (1.63) simplifies to

$$\frac{\partial S}{\partial \rho}_* = \lim_{\Delta s \to 0} \frac{s_{\text{R}}^{1/\gamma} s_{\text{L}} - s_{\text{L}}^{1/\gamma} s_{\text{R}}}{\Delta s^{1/\gamma}} \tag{1.68}$$

$$= -(\gamma - 1)s \tag{1.69}$$

which is equivalent to the derivative in Eq. (1.9). Thus the determinant of the matrix of right Eigenvectors is well defined,

$$|R| = -\gamma s \Delta\lambda \tag{1.70}$$

which takes the form

$$\vec{r}^{(1)} = \begin{pmatrix} 1 \\ \lambda_{\text{L}} \\ s \end{pmatrix}, \quad \vec{r}^{(2)} = \begin{pmatrix} 1 \\ u_* \\ -(\gamma - 1)s \end{pmatrix}, \quad \vec{r}^{(3)} = \begin{pmatrix} 1 \\ \lambda_{\text{R}} \\ s \end{pmatrix}, \tag{1.71}$$

with the star state velocity,

$$u_* = \frac{\rho_{\text{R}}(\lambda_{\text{R}} - u_{\text{R}})\lambda_{\text{L}} - \rho_{\text{L}}(\lambda_{\text{L}} - u_{\text{L}})\lambda_{\text{R}}}{\rho_{\text{R}}(\lambda_{\text{R}} - u_{\text{R}}) - \rho_{\text{L}}(\lambda_{\text{L}} - u_{\text{L}})}. \tag{1.72}$$

The star state mass density also reduces to

$$\rho_* = \rho \frac{\Delta\lambda - \Delta u}{\Delta\lambda}, \tag{1.73}$$

and with $\lambda_{\text{L}} = u_{\text{L}} - \hat{a}$ and $\lambda_{\text{R}} = u_{\text{R}} + \hat{a}$, $\hat{a}$ takes the form

$$\hat{a} = -\frac{\Delta u}{2} + \sqrt{\left[\frac{\Delta u}{2}\right]^2 + s\frac{\Delta \rho^\gamma}{\Delta \rho}} \tag{1.74}$$

which satisfies the positivity condition given from Eq. (1.73)

$$\hat{a} > -\frac{\Delta u}{2}. \tag{1.75}$$

Distribution Statement A: Approved for Public Release; Distribution is Unlimited. AFRL-2021-4182

Note that the form of $\hat{a}$ given by Eq. (1.74) is not necessary to satisfy the jump conditions. The necessary jump condition is satisfied by $\lambda_{\text{L}} = -\lambda_{\text{R}}$.

Homentropic and Isobaric case $\Delta s = 0$ and $\Delta \rho = 0$

In the limit of both vanishing $\Delta s \to 0$ and $\Delta \rho \to 0$, such as the case for uniform flow conditions or a symmetry boundary condition (solid wall), $\Delta p \to 0$. The star state velocity reduces to

$$u_* = \frac{\lambda_{\text{L}} u_{\text{R}} - \lambda_{\text{R}} u_{\text{L}}}{\Delta u - \Delta \lambda} \quad \left(= \frac{1}{2}(u_{\text{L}} + u_{\text{R}}) \right) \tag{1.76}$$

with mass density

$$\rho_* = \rho \frac{\Delta \lambda - \Delta u}{\Delta \lambda} \quad \left(= \frac{2\rho a}{2a + \Delta u} \to \hat{a} > -\frac{\Delta u}{2} \right) \tag{1.77}$$

The speed of sound quantity in Eq. (1.74) takes the form

$$\lim_{\Delta \rho \to 0} s \frac{\Delta \rho^\gamma}{\Delta \rho} = a^2 \tag{1.78}$$

where $a = a_{\text{L}} = a_{\text{R}}$ is the speed of sound. This can be coded as

$$\hat{a} = -\frac{\Delta u}{2} + \sqrt{\left[\frac{\Delta u}{2}\right]^2 + s \frac{(\rho_{\text{R}} + \varepsilon)^\gamma - \rho_{\text{L}}^\gamma}{\Delta \rho + \varepsilon}} \tag{1.79}$$

where

$$\varepsilon = 10^{-10} \min[\rho_{\text{L}}, \rho_{\text{R}}] \tag{1.80}$$

to provide a seemless implementation with the homentropic case.

1.4.4 On the choice of wave speeds

The wave speeds presented in the previous sections are but just one choice of several options. It is possible to obtain an intermediate region which matches the exact solution to the Riemann problem. This is achieved by including the second Riemann invariant, namely

$$u_{\text{L}} + \frac{2a_{\text{L}}}{\gamma - 1} = u_* + \frac{2a_{*,\text{L}}}{\gamma - 1} \tag{1.81}$$

with our previous derivation of the jump conditions and intermediate state. Although we do not go through the exercise here, the result for isentropic expansions is well known, the details of which can be found in [Toro, 1999] for example. The star pressure and velocity are given by (equations 9.35, 9.32, 4.46, and 9.37 from Toro) with the exact 2-rarefaction pressure given by

$$p_* = \left(\frac{a_{\text{L}} + a_{\text{R}} - \frac{\gamma - 1}{2} \Delta u}{\frac{a_{\text{L}}}{p_{\text{L}}^z} + \frac{a_{\text{R}}}{p_{\text{R}}^z}} \right)^{1/z}. \tag{1.82}$$

Distribution Statement A: Approved for Public Release; Distribution is Unlimited. AFRL-2021-4182

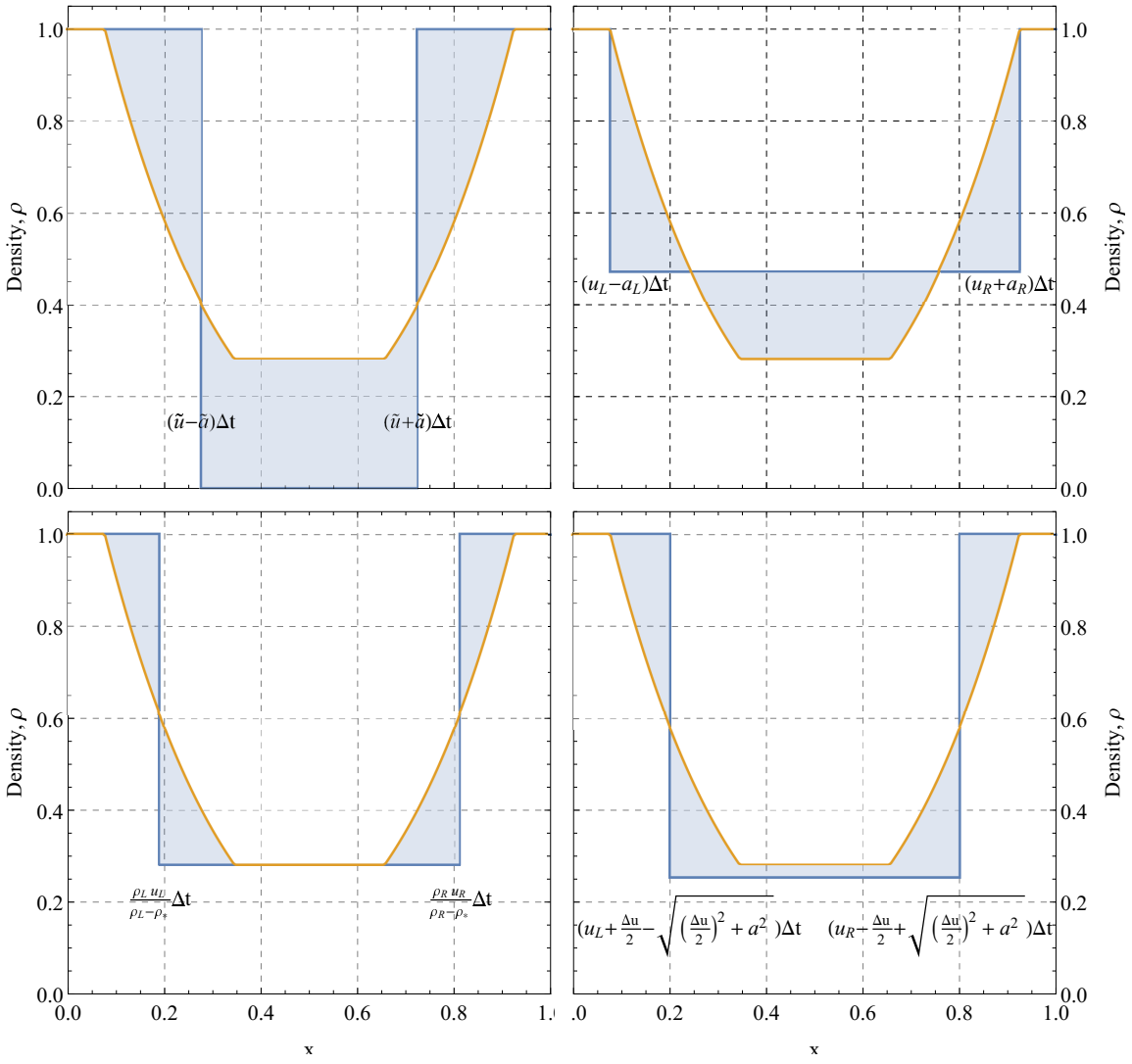

Figure 1.4: Comparison of various numerical approximations for the nonlinear wave speeds for symmetrical expanding waves. The exact solution is given by the solid yellow line while the linear approximation is given in blue. The distance which the vertical blue lines travel is given by the numerical wave speed multiplied by the expansion time. Roe's linearization provides the slowest numerical wave speeds while the HLLE scheme provides the fastest. With the waves expanding at Mach 1.118, Roe's linearization produces an intermediate density of 0 as can be seen in the top left plot. The HLLE linearizes with wave speed estimates taken as the head of the rarefaction waves leading to the highest intermediate density as can be seen in the top right plot. The bottom left shows the numerical wave speeds which generate the exact values in the intermediate star region. The plot in the bottom right is obtained using numerical wave speeds resulting from Eq. (1.79). Note that the area shaded below the exact solution must equal the shaded area above to satisfy the jump conditions and hence conservation. For its simplicity, Eq. (1.79) is surprisingly accurate, and despite its slight underprediction of the density for these conditions, it is always positvivity conservative.

Distribution Statement A: Approved for Public Release; Distribution is Unlimited. AFRL-2021-4182

The intermediate mass densities and sound speeds are given by

$$\rho_{*,\text{L}} = \rho_\text{L}\left(\frac{p_*}{p_\text{L}}\right)^{1/\gamma} \quad \text{and} \quad \rho_{*,\text{R}} = \rho_\text{R}\left(\frac{p_*}{p_\text{R}}\right)^{1/\gamma} \tag{1.83}$$

$$a_{*,\text{L}} = \sqrt{\frac{\gamma p_*}{\rho_{*,\text{L}}}} \quad \text{and} \quad a_{*,\text{R}} = \sqrt{\frac{\gamma p_*}{\rho_{*,\text{R}}}} \tag{1.84}$$

respectively. The star state densities in combination with the star velocity

$$u_* = \frac{\left(\frac{p_\text{L}}{p_\text{R}}\right)^z \frac{u_\text{L}}{a_\text{L}} + \frac{u_\text{R}}{a_\text{R}} + 2\frac{\left(\frac{p_\text{L}}{p_\text{R}}\right)^z - 1}{\gamma - 1}}{\frac{\frac{p_\text{L}}{p_\text{R}}}{a_\text{L}} + \frac{1}{a_\text{L}}}, \quad \text{where} \quad z = \frac{\gamma - 1}{2\gamma} \tag{1.85}$$

are used to compute the wave speeds

$$\lambda_\text{L} = \frac{\rho_1 u_* - \rho_\text{L} u_\text{L}}{\rho_1 - \rho_\text{L}} \quad \text{and} \quad \lambda_\text{R} = \frac{\rho_\text{R} u_\text{R} - \rho_2 u_*}{\rho_\text{R} - \rho_2}. \tag{1.86}$$

Note that these wave speeds result in the exact intermediate state when applied in an approximate Riemann solver. This is illustrated in Fig. 1.4 along with the numerical wave speeds resulting from Roes' scheme, the HLLE scheme, and the current scheme.

As an alternative to the numerical wave speeds resulting from Eq. (1.67), the left numerical wave speed can be expressed in terms of the right wave speed and vice- versa. This gives the option to assign one of the waves speeds and allow the other to follow from conservation. For the general case, the left wave speed can be expressed in terms of the right wave speed as

$$\lambda_\text{L} = u_\text{L} - \frac{c_2 - \text{sgn}(\Delta s)\sqrt{c_2^2 - 2c_1 c_3}}{c_1} \quad \text{for} \quad \Delta s \neq 0 \tag{1.87}$$

where

$$c_1 = 2\rho_\text{L}(\mu_\text{R} s_\text{R}^{1/\gamma} - \rho_\text{L}(\lambda_\text{R} - u_\text{L}) s_\text{L}^{1/\gamma}) \tag{1.88}$$

$$c_2 = \rho_\text{L} s_\text{L}^{1/\gamma} \Delta(\rho^\gamma s) - \mu_\text{R}(\lambda_\text{R} - u_\text{R})\Delta(\rho s^{1/\gamma}) \tag{1.89}$$

$$c_3 = \mu_\text{R} s_\text{R}^{1/\gamma}(\mu_\text{R}\Delta u - \Delta(\rho^\gamma s)) \tag{1.90}$$

The coefficients for the right wave speed can be found by reversing the indices of the left and right states:

$$\lambda_\text{R} = u_\text{R} + \frac{c_2 + \text{sgn}(\Delta s)\sqrt{c_2^2 + 2c_1 c_3}}{c_1} \quad \text{for} \quad \Delta s \neq 0 \tag{1.91}$$

where

$$c_1 = 2\rho_\text{R}(\mu_\text{L} s_\text{L}^{1/\gamma} - \rho_\text{R}(\lambda_\text{L} - u_\text{R}) s_\text{R}^{1/\gamma}) \tag{1.92}$$

$$c_2 = \rho_\text{R} s_\text{R}^{1/\gamma} \Delta(\rho^\gamma s) - \mu_\text{L}(\lambda_\text{L} - u_\text{L})\Delta(\rho s^{1/\gamma}) \tag{1.93}$$

$$c_3 = \mu_\text{L} s_\text{L}^{1/\gamma}(\mu_\text{L}\Delta u - \Delta(\rho^\gamma s)) \tag{1.94}$$

Distribution Statement A: Approved for Public Release; Distribution is Unlimited. AFRL-2021-4182

These choices wave speeds have not been examined in great detail due to their introduced complexity but may prove to be useful if constant pressure is an absolute requirement across the contact wave in the intermediate state. It is unknown whether they provide a more accurate interface flux.

Similar expressions can be computed for the homentropic case, $\Delta s \to 0$, The resulting numerical wave speeds from the jump conditions take the form

$$\lambda_{\text{L}} = u_{\text{L}} + \frac{\mu_{\text{R}}\Delta u - s\Delta\rho^{\gamma}}{\lambda_{\text{R}}\Delta\rho - \Delta\rho u}, \tag{1.95}$$

$$\lambda_{\text{R}} = u_{\text{R}} + \frac{\mu_{\text{L}}\Delta u - s\Delta\rho^{\gamma}}{\lambda_{\text{L}}\Delta\rho - \Delta\rho u}. \tag{1.96}$$

This form of the numerical wave speeds has been used quite extensively, typically by computing first either $\lambda_{\text{L}} = u_{\text{L}} - a_{\text{L}}$ or $\lambda_{\text{R}} = u_{\text{R}} - a_{\text{R}}$ and then using either Eq. (1.95) or Eq. (1.96) as appropriate. This can be quite beneficial when one of the nonlinear waves strongly dominates the other and it may be desirable to include extra diffusion with the HLLE wave speeds.

1.4.5 Updating the energy component

The methods discussed thusfar are purely for entropy conservation and are for isentropic flows only. In order to solve for flows with shocks, the isentropic system must be combined or hybridized with the energy conservation form of the Euler equations. For the flux-difference splitting scheme, this can only be accomplished through the characteristic decomposition from the resulting Riemann problem. Revisiting the finite-difference formulation, Eq. (1.19) becomes

$$\tilde{F}(Q_{L,i+1/2}, Q_{R,i+1/2}) = \frac{1}{2}(F(\mathbf{Q}_{\text{L}}) + F(\mathbf{Q}_{\text{R}})) - \frac{1}{2}\sum_{k=1}^{N} |\lambda^{k}_{i+1/2}|(\mathbf{Q}^{k+1} - \mathbf{Q}^{k}) \tag{1.97}$$

since

$$\tilde{A}(\mathbf{Q}_{\text{L}}, \mathbf{Q}_{\text{R}})(\mathbf{Q}_{\text{R}} - \mathbf{Q}_{\text{L}}) = \sum_{k=1}^{N} |\lambda^{k}_{i+1/2}|\alpha^{k}_{i+1/2}\bar{r}^{k}_{i+1/2} \tag{1.98}$$

$$= \sum_{k=1}^{N} |\lambda^{k}_{i+1/2}|(\mathbf{Q}^{k+1} - \mathbf{Q}^{k}). \tag{1.99}$$

Once the intermediate states for mass, momentum, and entropy are computed, the energy states can be computed. The numerical flux can therefore simply be obtained from

$$|\lambda_{\text{L}}|(E_{*,\text{L}} - E_{\text{L}}) + |u_{*}|(E_{*,\text{R}} - E_{*,\text{L}}) + |\lambda_{\text{R}}|(E_{\text{R}} - E_{*,\text{R}}) \tag{1.100}$$

where

$$E_{*,\text{L}} = \frac{p_{*,\text{L}}}{\gamma - 1} + \frac{1}{2}\rho_{*,\text{L}}u^{2}_{*,\text{L}} \quad \text{and} \quad E_{*,\text{R}} = \frac{p_{*,\text{R}}}{\gamma - 1} + \frac{1}{2}\rho_{*,\text{R}}u^{2}_{*,\text{R}} \tag{1.101}$$

where $p_{*,\text{L}}$ and $p_{*,\text{R}}$ as well as $u_{*,\text{L}}$ and $u_{*,\text{R}}$ have been differentiated from one another since the scheme does not always guarantee $p_{*,\text{L}} = p_{*,\text{R}}$ or $u_{*,\text{L}} = u_{*,\text{R}}$ across the contact.

Distribution Statement A: Approved for Public Release; Distribution is Unlimited. AFRL-2021-4182

Each finite volume cell requires values for both the entropy and energy quantities since either quantity can be required based on whether an isentropic or energy conservation scheme is utilized. Therefore our system of equations is augmented to include both entropy and energy,

$$\mathbf{Q} = \begin{pmatrix} \rho \\ \rho u \\ S \\ E \end{pmatrix} \quad \text{and} \quad \mathbf{F} = \begin{pmatrix} \rho u \\ \rho u^2 + p \\ uS \\ u(\frac{\gamma p}{\gamma - 1} + \frac{1}{2}\rho u^2) \end{pmatrix} \tag{1.102}$$

where as before $p = \rho^{\gamma-1} S$.

1.4.6 Extension to multiple dimensions

Extension to multiple dimensions is essentially a matter of including the shear waves in the system. For Roe's scheme, the averaging procedure introduces a cross dependency of the waves on each other which produces unphysical jumps and reduces the positivity limit. Of great importance is the fact that the shear waves do not influence the density or pressure in the star region and hence the positivity preserving property of the scheme. The three-dimensional Eigenvectors in the x-direction take the form,

$$\vec{r}^{(1)} = \begin{pmatrix} 1 \\ u_* \\ v_* \\ w_* \\ \frac{\partial S}{\partial \rho}_* \end{pmatrix}, \quad \vec{r}^{(2)} = \begin{pmatrix} 1 \\ \lambda_{\text{L}} \\ v_{\text{L}} \\ w_{\text{L}} \\ s_{\text{L}} \end{pmatrix}, \quad \vec{r}^{(3)} = \begin{pmatrix} 0 \\ 0 \\ 1 \\ 0 \\ 0 \end{pmatrix}, \quad \vec{r}^{(4)} = \begin{pmatrix} 0 \\ 0 \\ 0 \\ 1 \\ 0 \end{pmatrix}, \quad \vec{r}^{(5)} = \begin{pmatrix} 1 \\ \lambda_{\text{R}} \\ v_{\text{R}} \\ w_{\text{R}} \\ s_{\text{R}} \end{pmatrix}. \tag{1.103}$$

Since the contact wave has no tangential velocity components, v_* and w_* are equal to zero. Furthermore, there is no jump in the shear velocities across the nonlinear waves, allowing great simplification of the nonlinear Eigenvectors. The choice of v_{L} and w_{L} in the left-running nonlinear Eigenvector as well as v_{R} and w_{R} in the right-running nonlinear Eigenvector ensures there is no jump in the shear velocities across the linear waves. For sake of completeness, the linearization is extended here to three dimensions for an arbitrary surface normal vector, $\hat{n} = [n_x, n_y, n_z]$ and tangential components $\hat{t} = [t_x, t_y, t_z]$ and $\hat{s} = [s_x, s_y, s_z]$. here arranged by contact, left nonlinear, shear, and right nonlinear waves, respectively, can be aligned with the normal vector to obtain,

$$\vec{r}^{(1)} = \begin{pmatrix} 1 \\ n_x \hat{u}_* \\ n_y \hat{u}_* \\ n_z \hat{u}_* \\ \frac{\partial S}{\partial \rho}_* \end{pmatrix}, \quad \vec{r}^{(2)} = \begin{pmatrix} 1 \\ n_x \hat{\lambda}_{\text{L}} + t_x \hat{v}_{\text{L}} + s_x \hat{v}_{\text{L}} \\ n_y \hat{\lambda}_{\text{L}} + t_y \hat{v}_{\text{L}} + s_y \hat{v}_{\text{L}} \\ n_z \hat{\lambda}_{\text{L}} + t_z \hat{v}_{\text{L}} + s_z \hat{v}_{\text{L}} \\ s_{\text{L}} \end{pmatrix}, \quad \vec{r}^{(3)} = \begin{pmatrix} 0 \\ t_x \\ t_y \\ t_z \\ 0 \end{pmatrix}, \quad \vec{r}^{(4)} = \begin{pmatrix} 0 \\ s_x \\ s_y \\ s_z \\ 0 \end{pmatrix}. \tag{1.104}$$

$$\vec{r}^{(5)} = \begin{pmatrix} 1 \\ n_x \hat{\lambda}_{\text{R}} + t_x \hat{v}_{\text{R}} + s_x \hat{v}_{\text{R}} \\ n_y \hat{\lambda}_{\text{R}} + t_y \hat{v}_{\text{R}} + s_y \hat{v}_{\text{R}} \\ n_z \hat{\lambda}_{\text{R}} + t_z \hat{v}_{\text{R}} + s_z \hat{v}_{\text{R}} \\ s_{\text{R}} \end{pmatrix}. \tag{1.105}$$

Distribution Statement A: Approved for Public Release; Distribution is Unlimited. AFRL-2021-4182

The determinant of R is given by

$$|\hat{R}| = s_{\mathrm{R}}(\hat{u}_* - \hat{\lambda}_{\mathrm{L}}) + s_{\mathrm{L}}(\hat{\lambda}_{\mathrm{R}} - \hat{u}_*) + \frac{\partial S}{\partial \rho}_* (\hat{\lambda}_{\mathrm{L}} - \hat{\lambda}_{\mathrm{R}}) \tag{1.106}$$

where $\frac{\partial S}{\partial \rho}_*$ remains the same as Eq. (1.48) except with the rotated quantities, $\hat{\mu}$, $\hat{u}$, and $\hat{\lambda}$.
The left Eigenvectors are similarly found by right multiplying with the rotation matrix, T

$$\vec{l}^{(1)} = \frac{1}{|\hat{R}|} \begin{pmatrix} s_{\mathrm{L}}\hat{\lambda}_{\mathrm{R}} - s_{\mathrm{R}}\hat{\lambda}_{\mathrm{L}} \\ n_x(s_{\mathrm{R}} - s_{\mathrm{L}}) \\ n_y(s_{\mathrm{R}} - s_{\mathrm{L}}) \\ n_z(s_{\mathrm{R}} - s_{\mathrm{L}}) \\ \hat{\lambda}_{\mathrm{L}} - \hat{\lambda}_{\mathrm{R}} \end{pmatrix}^T, \quad \vec{l}^{(2)} = \frac{1}{|\hat{R}|} \begin{pmatrix} \hat{u}_* s_{\mathrm{R}} - \hat{\lambda}_{\mathrm{R}} \frac{\partial S}{\partial \rho}_* \\ n_x(\frac{\partial S}{\partial \rho}_* - s_{\mathrm{R}}) \\ n_y(\frac{\partial S}{\partial \rho}_* - s_{\mathrm{R}}) \\ n_z(\frac{\partial S}{\partial \rho}_* - s_{\mathrm{R}}) \\ \hat{\lambda}_{\mathrm{R}} - \hat{u}_* \end{pmatrix}^T, \tag{1.107}$$

$$\vec{l}^{(3)} = \frac{1}{|\hat{R}|} \begin{pmatrix} \hat{u}_*(s_{\mathrm{L}}\hat{v}_{\mathrm{R}} - s_{\mathrm{R}}\hat{v}_{\mathrm{L}}) + \frac{\partial S}{\partial \rho}_*(\hat{v}_{\mathrm{L}}\hat{\lambda}_{\mathrm{R}} - \hat{v}_{\mathrm{R}}\hat{\lambda}_{\mathrm{L}}) \\ n_x(s_{\mathrm{R}}\hat{v}_{\mathrm{L}} - s_{\mathrm{L}}\hat{v}_{\mathrm{R}} + \frac{\partial S}{\partial \rho}_*(\hat{v}_{\mathrm{R}} - \hat{v}_{\mathrm{L}})) + t_x|\hat{R}| \\ n_y(s_{\mathrm{R}}\hat{v}_{\mathrm{L}} - s_{\mathrm{L}}\hat{v}_{\mathrm{R}} + \frac{\partial S}{\partial \rho}_*(\hat{v}_{\mathrm{R}} - \hat{v}_{\mathrm{L}})) + t_y|\hat{R}| \\ n_z(s_{\mathrm{R}}\hat{v}_{\mathrm{L}} - s_{\mathrm{L}}\hat{v}_{\mathrm{R}} + \frac{\partial S}{\partial \rho}_*(\hat{v}_{\mathrm{R}} - \hat{v}_{\mathrm{L}})) + t_z|\hat{R}| \\ \hat{u}_*(\hat{v}_{\mathrm{L}} - \hat{v}_{\mathrm{R}}) + \hat{v}_{\mathrm{R}}\hat{\lambda}_{\mathrm{L}} - \hat{v}_{\mathrm{L}}\hat{\lambda}_{\mathrm{R}} \end{pmatrix}^T, \tag{1.108}$$

$$\vec{l}^{(4)} = \frac{1}{|\hat{R}|} \begin{pmatrix} \hat{u}_*(s_{\mathrm{L}}\hat{w}_{\mathrm{R}} - s_{\mathrm{R}}\hat{w}_{\mathrm{L}}) + \frac{\partial S}{\partial \rho}_*(\hat{w}_{\mathrm{L}}\hat{\lambda}_{\mathrm{R}} - \hat{w}_{\mathrm{R}}\hat{\lambda}_{\mathrm{L}}) \\ n_x(s_{\mathrm{R}}\hat{w}_{\mathrm{L}} - s_{\mathrm{L}}\hat{w}_{\mathrm{R}} + \frac{\partial S}{\partial \rho}_*(\hat{w}_{\mathrm{R}} - \hat{w}_{\mathrm{L}})) + s_x|\hat{R}| \\ n_y(s_{\mathrm{R}}\hat{w}_{\mathrm{L}} - s_{\mathrm{L}}\hat{w}_{\mathrm{R}} + \frac{\partial S}{\partial \rho}_*(\hat{w}_{\mathrm{R}} - \hat{w}_{\mathrm{L}})) + s_y|\hat{R}| \\ n_z(s_{\mathrm{R}}\hat{w}_{\mathrm{L}} - s_{\mathrm{L}}\hat{w}_{\mathrm{R}} + \frac{\partial S}{\partial \rho}_*(\hat{w}_{\mathrm{R}} - \hat{w}_{\mathrm{L}})) + s_z|\hat{R}| \\ \hat{u}_*(\hat{w}_{\mathrm{L}} - \hat{w}_{\mathrm{R}}) + \hat{w}_{\mathrm{R}}\hat{\lambda}_{\mathrm{L}} - \hat{w}_{\mathrm{L}}\hat{\lambda}_{\mathrm{R}} \end{pmatrix}^T, \tag{1.109}$$

$$\vec{l}^{(5)} = \frac{1}{|\hat{R}|} \begin{pmatrix} \hat{\lambda}_{\mathrm{L}} \frac{\partial S}{\partial \rho}_* - \hat{u}_* s_{\mathrm{L}} \\ n_x(s_{\mathrm{L}} - \frac{\partial S}{\partial \rho}_*) \\ n_y(s_{\mathrm{L}} - \frac{\partial S}{\partial \rho}_*) \\ n_z(s_{\mathrm{L}} - \frac{\partial S}{\partial \rho}_*) \\ \hat{u}_* - \hat{\lambda}_{\mathrm{L}} \end{pmatrix}^T, \tag{1.110}$$

It is important that all rotated velocities be constructed with the appropriate rotated components.

$$\hat{\lambda}_{\mathrm{L}} = \hat{u}_{\mathrm{L}} - a_{\mathrm{L}}, \quad \hat{\lambda}_{\mathrm{R}} = \hat{u}_{\mathrm{R}} + a_{\mathrm{R}} \tag{1.111}$$

The rotated velocities are computed via

$$\hat{u} = n_x u + n_y v + n_z w \tag{1.112}$$

$$\hat{v} = t_x u + t_y v + t_z w \tag{1.113}$$

$$\hat{w} = s_x u + s_y v + s_z w \tag{1.114}$$

Distribution Statement A: Approved for Public Release; Distribution is Unlimited. AFRL-2021-4182

yielding the normal and tangential components, respectively.

The resulting wave strengths take the form

$$\alpha^{(1)}|R| = (s_{\text{L}}\hat{\lambda}_{\text{R}} - s_{\text{R}}\hat{\lambda}_{\text{L}})\Delta\rho + \Delta s\Delta\rho\hat{u} + (\hat{\lambda}_{\text{L}} - \hat{\lambda}_{\text{R}})\Delta S \tag{1.115}$$

$$\alpha^{(2)}|R| = \left(\hat{u}_* s_{\text{R}} - \hat{\lambda}_{\text{R}}\frac{\partial S}{\partial \rho}_*\right)\Delta\rho + \left(\frac{\partial S}{\partial \rho}_* - s_{\text{R}}\right)\Delta\rho\hat{u} + (\hat{\lambda}_{\text{R}} - \hat{u}_*)\Delta S \tag{1.116}$$

$$\alpha^{(3)}|R| = \left(\hat{u}_*(s_{\text{L}}\hat{v}_{\text{R}} - s_{\text{R}}\hat{v}_{\text{L}}) + \frac{\partial S}{\partial \rho}_*(\hat{v}_{\text{L}}\hat{\lambda}_{\text{R}} - \hat{v}_{\text{R}}\hat{\lambda}_{\text{L}})\right)\Delta\rho + \left(s_{\text{R}}\hat{v}_{\text{L}} - s_{\text{L}}\hat{v}_{\text{R}} + \frac{\partial S}{\partial \rho}_*(\hat{v}_{\text{R}} - \hat{v}_{\text{L}})\right)\Delta\rho\hat{u} + |R|\Delta\rho\hat{v} + (\hat{u}_*(\hat{v}_{\text{L}} - \hat{v}_{\text{R}}) + \hat{v}_{\text{R}}\hat{\lambda}_{\text{L}} - \hat{v}_{\text{L}}\hat{\lambda}_{\text{R}})\Delta S \tag{1.117}$$

$$\alpha^{(4)}|R| = \left(\hat{u}_*(s_{\text{L}}\hat{w}_{\text{R}} - s_{\text{R}}\hat{w}_{\text{L}}) + \frac{\partial S}{\partial \rho}_*(\hat{w}_{\text{L}}\hat{\lambda}_{\text{R}} - \hat{w}_{\text{R}}\hat{\lambda}_{\text{L}})\right)\Delta\rho + \left(s_{\text{R}}\hat{w}_{\text{L}} - s_{\text{L}}\hat{w}_{\text{R}} + \frac{\partial S}{\partial \rho}_*(\hat{w}_{\text{R}} - \hat{w}_{\text{L}})\right)\Delta\rho\hat{u} + |R|\Delta\rho\hat{w} + (\hat{u}_*(\hat{w}_{\text{L}} - \hat{w}_{\text{R}}) + \hat{w}_{\text{R}}\hat{\lambda}_{\text{L}} - \hat{w}_{\text{L}}\hat{\lambda}_{\text{R}})\Delta S \tag{1.118}$$

$$\alpha^{(5)}|R| = \left(\hat{\lambda}_{\text{L}}\frac{\partial S}{\partial \rho}_* - \hat{u}_* s_{\text{L}}\right)\Delta\rho + \left(\frac{\partial S}{\partial \rho}_* - s_{\text{R}}\right)\Delta\rho\hat{u} + (\hat{\lambda}_{\text{R}} - \hat{u}_*)\Delta S \tag{1.119}$$

An advantage of this system is that the nonlinear and contact waves are completely independent of the shear wave, just as the HLLE method.

The resulting Riemann invariants take the form

1.5 Hybridization

The isentropic equations are applied to expanding flows while applying standard conservation of energy to shocks. There are several criteria that can be chosen to function in a switching mechanism. We extend the wave strengths at the cell faces to apply to the whole control cell volume. If the divergence in a cell is negative, $\nabla \cdot \vec{u} > 0$, the nonlinear wave strength is computed as

$$\alpha = \frac{|\nabla p| - \rho a \nabla \cdot \vec{u}}{2a^2} \tag{1.120}$$

Otherwise, the wave strength is computed as

$$\alpha = \frac{|\nabla p| + \rho a \nabla \cdot \vec{u}}{2a^2} \tag{1.121}$$

We compute a cell-local velocity divergence which is then used to determine if the gas in a cell is under compression. We compute an average velocity at each cell from the interpolation scheme, $\tilde{u} = (u_{\text{L,ex}} + u_{\text{R,ex}})$ which is used in the divergence equation

$$\nabla \cdot \vec{u} = \int_S \vec{u} \cdot \hat{n} dS \tag{1.122}$$

Distribution Statement A: Approved for Public Release; Distribution is Unlimited. AFRL-2021-4182

we make the determination if pressure will be recovered from the total energy or entropy variables. Note that a cell can experience both severe rarefactions or shocks at its interfaces, but the divergence will determine its compressibility and hence whether the flow is isentropic or not.

At a cell interface, where the flow is detected to be compressive, Roe's scheme is untilized. If Roe's scheme is used to compute an interface flux, the star region is computed from the comservative variables with energy, converted to entropy, and it's corresponding flux for the entropy variable.

1.6 Time marching

The solution is marched in time via the the 2nd-order Adams-Bashforth multi-step scheme:

$$Q^{n+1} = Q^n + \frac{t_{n+1} - t_n}{2(t_n - t_{n-1})} L\left[(t_n + t_{n+1} - 2t_{n-1})Q^n - (t_{n+1} - t_n)Q^{n-1}\right] \tag{1.123}$$

The 2nd-order TVD Runge-Kutta scheme also works for the proposed scheme:

$$\tilde{Q}^{n+1} = Q^n + \Delta t L(Q^n) \tag{1.124}$$

$$Q^{n+1} = \frac{1}{2}Q^n + \frac{1}{2}\tilde{Q}^n + \frac{1}{2}\Delta t L(\tilde{Q}^{n+1}) \tag{1.125}$$

Both schemes are stable for the proposed scheme at similar CFL numbers. The AB2 scheme has the advantage requiring only one flux evaluation per iterative step and one less boundary exchange for parallelized implementations.

1.7 1D implementation with 3rd order reconstruction

An example of how to implement the new linearization is presented here. For existing approximate Riemann solver implementation, the vector of conserved quantites and corresponding fluxes is augmented by 1 to include entropy:

$$Q = \begin{pmatrix} \rho \\ \rho u \\ E \\ S \end{pmatrix}, \quad F = \begin{pmatrix} \rho u \\ \rho u^2 + p \\ u H_\circ \\ uS \end{pmatrix}. \tag{1.126}$$

At the start of each iterative time step, the equation of state is used to compute the primitive variables for each cell using either $p = \rho^\gamma s$ or $p = (\gamma - 1)\rho\varepsilon$. Typically, the choice is determined based on how the conserved quantities were updated in the previous time iteration. From the primitive quantities, it is then determined if there is fluid expansion or compression at the cell interface by means of $\Delta u/a$. If an expansion is detected and the condition $u_{\text{L}} - a_{\text{L}} < u_{\text{R}} + a_{\text{R}}$ holds, the isentropic Eigensystem is utilized,

$$L = \frac{1}{|R|}\begin{pmatrix} \frac{\partial S}{\partial \rho}_* \lambda_{\text{R}} - s_{\text{R}} u_* & s_{\text{R}} - \frac{\partial S}{\partial \rho}_* & 0 & u_* - \lambda_{\text{R}} \\ s_{\text{R}}\lambda_{\text{L}} - s_{\text{L}}\lambda_{\text{R}} & s_{\text{L}} - s_{\text{R}} & 0 & \lambda_{\text{R}} - \lambda_{\text{L}} \\ 0 & 0 & 0 & 0 \\ s_{\text{L}} u_* - \lambda_{\text{L}} \frac{\partial S}{\partial \rho}_* & \frac{\partial S}{\partial \rho}_* - s_{\text{L}} & 0 & \lambda_{\text{L}} - u_* \end{pmatrix} \tag{1.127}$$

Distribution Statement A: Approved for Public Release; Distribution is Unlimited. AFRL-2021-4182

where

$$|R| = s_{\text{R}}(\lambda_{\text{L}} - u_*) - s_{\text{L}}(\lambda_{\text{R}} - u_*) + \frac{\partial S}{\partial \rho}_* (\lambda_{\text{R}} - \lambda_{\text{L}}) \tag{1.128}$$

otherwise

$$L = -\frac{1}{2\tilde{a}\tilde{h}} \begin{pmatrix} \tilde{a}(\tilde{u}^2 - 2\tilde{h}) & -2\tilde{a}\tilde{u} & 2\tilde{a} & 0 \\ -\tilde{u}\left(\frac{1}{2}\tilde{a}\tilde{u} + \tilde{h}\right) & \tilde{a}\tilde{u} + \tilde{h} & -\tilde{a} & 0 \\ -\tilde{u}\left(\frac{1}{2}\tilde{a}\tilde{u} - \tilde{h}\right) & \tilde{a}\tilde{u} - \tilde{h} & -\tilde{a} & 0 \\ 0 & 0 & 0 & 0 \end{pmatrix} \tag{1.129}$$

is utilized to compute the characteristic variables for each cell in the stencil for the given interface:

$$W_i = L_{1/2} Q_i, \quad i = -1, 0, 1, 2 \tag{1.130}$$

These characteristic variables are then interpolated to obtain 3rd-order upwind and downwind biased point values at the cell interface via

$$w_L = \frac{1}{6}(2\bar{w}_{j-1} + 5\bar{w}_j - \bar{w}_{j+1}), \tag{1.131}$$

$$w_R = \frac{1}{6}(2\bar{w}_{j+1} + 5\bar{w}_j - \bar{w}_{j-1}). \tag{1.132}$$

To ensure monotonicity, the MP limiters of (Colella and Woodward, Suresh and Huynh) are applied as follows

$$w_{\text{L}} \leftarrow \text{median}(w_{\text{L}},\ \bar{w}_i,\ w^{\text{MP}}) \tag{1.133}$$

$$w^{\text{MP}} = \bar{w}_i + \text{minmod}[\bar{w}_{i+1} - \bar{w}_i,\ \alpha(\bar{w}_i - \bar{w}_{i-1})] \tag{1.134}$$

$$w_{\text{R}} \leftarrow \text{median}(w_{\text{R}},\ \bar{w}_i,\ w^{\text{MP}}) \tag{1.135}$$

$$w^{\text{MP}} = \bar{w}_i + \text{minmod}[\bar{w}_{i-1} - \bar{w}_i,\ \alpha(\bar{w}_i - \bar{w}_{i+1})] \tag{1.136}$$

Once W_{L} and W_{R} are computed, they are transformed back to physical space via the matrix of right Eigenvectors R, such that $Q_{\text{L}} = R_{1/2} W_{\text{L}}$ and $Q_{\text{R}} = R_{1/2} W_{\text{R}}$. Note that either the energy or the entropy components have yet to be computed. The appropriate reconstructed components are obtained from either

$$E_{\text{L}} = \frac{p_{\text{L}}}{\gamma - 1} + \frac{1}{2}\rho_{\text{L}} u_{\text{L}}^2 \quad \text{and} \quad E_{\text{R}} = \frac{p_{\text{R}}}{\gamma - 1} + \frac{1}{2}\rho_{\text{R}} u_{\text{R}}^2 \tag{1.137}$$

or

$$S_{\text{L}} = \rho_{\text{L}} s_{\text{L}} \quad \text{and} \quad S_{\text{R}} = \rho_{\text{R}} s_{\text{R}} \tag{1.138}$$

Note that this requires the primitive variables to be computed once again from the equation of state. With the entire reconstructed state vector known, the numerical flux at the cell interface is obtained from

$$F_{i+1/2} = \frac{1}{2}(F_L + F_R) - \sum_{k=1}^{N} |\lambda^k_{i+1/2}| \alpha^k_{i+1/2} \vec{r}^k_{i+1/2} \tag{1.139}$$

Distribution Statement A: Approved for Public Release; Distribution is Unlimited. AFRL-2021-4182

where

$$R = \begin{pmatrix} 1 & 1 & 0 & 1 \\ u_* & \lambda_{\mathrm{L}} & 0 & \lambda_{\mathrm{R}} \\ 0 & 0 & 0 & 0 \\ \frac{\partial S}{\partial \rho}_* & s_{\mathrm{L}} & 0 & s_{\mathrm{R}} \end{pmatrix} \tag{1.140}$$

for the isentropic case or otherwise

$$R = \begin{pmatrix} 1 & 1 & 1 & 0 \\ \tilde{u} & \tilde{u} - \tilde{a} & \tilde{u} + \tilde{a} & 0 \\ \frac{1}{2}\tilde{u}^2 & \tilde{h}_\circ - \tilde{a}\tilde{u} & \tilde{h}_\circ + \tilde{a}\tilde{u} & 0 \\ 0 & 0 & 0 & 0 \end{pmatrix} \tag{1.141}$$

With all numerical interface fluxes computed, a loop is performed over all cells to integrate forward in time. A switch based on the velocity divergence in the cell is used to determine if the cell is updated via energy or entropy conservation.

1.8 Extension to MHD

In magnetohydrodynamic flows, there can exist conditions in which not only the kinetic component becomes the dominant energy, but also the energy from the magnetic pressure. As a consequence, all linearization deficiencies and solutions presented for the Euler equations are applicable to the MHD equations as well. The MHD system in isentropic form is given by

$$Q = \begin{pmatrix} \rho \\ \rho u \\ \rho v \\ \rho w \\ B_y \\ B_z \\ S \end{pmatrix}, \quad F = \begin{pmatrix} \rho u \\ \rho u^2 + p_\circ - B_x^2/\mu_\circ \\ \rho uv - B_x B_y/\mu_\circ \\ \rho uw - B_x B_y/\mu_\circ \\ uB_y - vB_x \\ uB_z - wB_x \\ uS \end{pmatrix}. \tag{1.142}$$

where $p_\circ$ is the sum of the thermal and magnetic pressures,

$$p_\circ = p + \frac{B^2}{2\mu_\circ}, \tag{1.143}$$

and the entropy density S is the same as for the Euler equations. The right Eigenvectors have the form

$$\vec{r}^{(1)} = \begin{pmatrix} 1 \\ u \\ v \\ w \\ 0 \\ 0 \\ \frac{\partial S}{\partial \rho}_* \end{pmatrix}, \quad \vec{r}^{(2)} = \begin{pmatrix} 1 \\ u - c_s \\ v - \frac{a^2}{c_s(c_f^2 - a^2)} \frac{B_x B_y}{\mu_\circ \rho} \\ w - \frac{a^2}{c_s(c_f^2 - a^2)} \frac{B_x B_z}{\mu_\circ \rho} \\ -\frac{a^2}{c_f^2 - a^2} \frac{B_y}{\rho} \\ -\frac{a^2}{c_f^2 - a^2} \frac{B_z}{\rho} \\ s \end{pmatrix}, \quad \vec{r}^{(3)} = \begin{pmatrix} 1 \\ u + c_s \\ v + \frac{a^2}{c_s(c_f^2 - a^2)} \frac{B_x B_y}{\mu_\circ \rho} \\ w + \frac{a^2}{c_s(c_f^2 - a^2)} \frac{B_x B_z}{\mu_\circ \rho} \\ -\frac{a^2}{c_f^2 - a^2} \frac{B_y}{\rho} \\ -\frac{a^2}{c_f^2 - a^2} \frac{B_z}{\rho} \\ s \end{pmatrix}. \tag{1.144}$$

Distribution Statement A: Approved for Public Release; Distribution is Unlimited. AFRL-2021-4182

$$\vec{r}^{(4)} = \begin{pmatrix} 1 \\ u - c_f \\ v - \frac{a^2}{c_f(c_s^2 - a^2)} \frac{B_x B_y}{\mu_\circ \rho} \\ w - \frac{a^2}{c_f(c_s^2 - a^2)} \frac{B_x B_z}{\mu_\circ \rho} \\ -\frac{a^2}{c_s^2 - a^2} \frac{B_y}{\rho} \\ -\frac{a^2}{c_s^2 - a^2} \frac{B_z}{\rho} \\ s \end{pmatrix}, \quad \vec{r}^{(5)} = \begin{pmatrix} 1 \\ u + c_f \\ v + \frac{a^2}{c_f(c_s^2 - a^2)} \frac{B_x B_y}{\mu_\circ \rho} \\ w + \frac{a^2}{c_f(c_s^2 - a^2)} \frac{B_x B_z}{\mu_\circ \rho} \\ -\frac{a^2}{c_s^2 - a^2} \frac{B_y}{\rho} \\ -\frac{a^2}{c_s^2 - a^2} \frac{B_z}{\rho} \\ s \end{pmatrix}. \tag{1.145}$$

$$\vec{r}^{(6)} = \begin{pmatrix} 0 \\ 0 \\ B_z \\ -B_y \\ B_z \sqrt{\frac{\mu_\circ}{\rho}} \\ -B_y \sqrt{\frac{\mu_\circ}{\rho}} \\ 0 \end{pmatrix}, \quad \vec{r}^{(7)} = \begin{pmatrix} 0 \\ 0 \\ B_z \\ -B_y \\ -B_z \sqrt{\frac{\mu_\circ}{\rho}} \\ B_y \sqrt{\frac{\mu_\circ}{\rho}} \\ 0 \end{pmatrix}. \tag{1.146}$$

In order to derive a similar linearization as for the isentropic Euler equations, appropriate forms for the slow, fast, and Alfven waves must be assumed to not only give an accurate approximation, but also to allow inversion of the right Eigenvectors to achieve the wave strengths in closed form. This has been so far elusive but not detrimental to an isentropic MHD solver. The HLLE solver is used for MHD flows where strong expansions persist with dominating kinetic and magnetic pressures. The isentropic MHD equations are hybridized with the standard MHD equations in exactly the same way as discussed for the Euler equations.

1.9 Numerical results

1.9.1 Einfeldt 1-1-5

Einfeldt's 1-1-5 problem is a symmetric expansion wave problem, producing rarefactions of moderate strength. The initial conditions for the Riemann problem are given by

$$\begin{pmatrix} \rho_{\text{L}} \\ u_{\text{L}} \\ p_{\text{L}} \\ T_{\text{L}} \end{pmatrix} = \begin{pmatrix} 1 \\ -1 \\ 1.8 \\ 1.8 \end{pmatrix} \quad \text{and} \quad \begin{pmatrix} \rho_{\text{R}} \\ u_{\text{R}} \\ p_{\text{R}} \\ T_{\text{R}} \end{pmatrix} = \begin{pmatrix} 1 \\ 1 \\ 1.8 \\ 1.8 \end{pmatrix} \tag{1.147}$$

It was chosen as a test case since Roe's method produces a valid linearization, with the wave speeds being Mach 0.63 which is under the linearization limit of Mach 0.94 where the scheme fails. The plots in Fig. 1.5 show the results for the temperature using 4 different solution techniques. The solution on the left was obtained solving the Euler equations in energy conservation form. The blue data set results from using the linearization of Roe while the red is the new linearization. Both schemes produce nearly identical results. The solution on the right was obtained solving the Euler equations in entropy conservation form and shows excellent agreement with the exact solution given by the gray line. Similar solutions were first given in Kapper [2009].

Distribution Statement A: Approved for Public Release; Distribution is Unlimited. AFRL-2021-4182

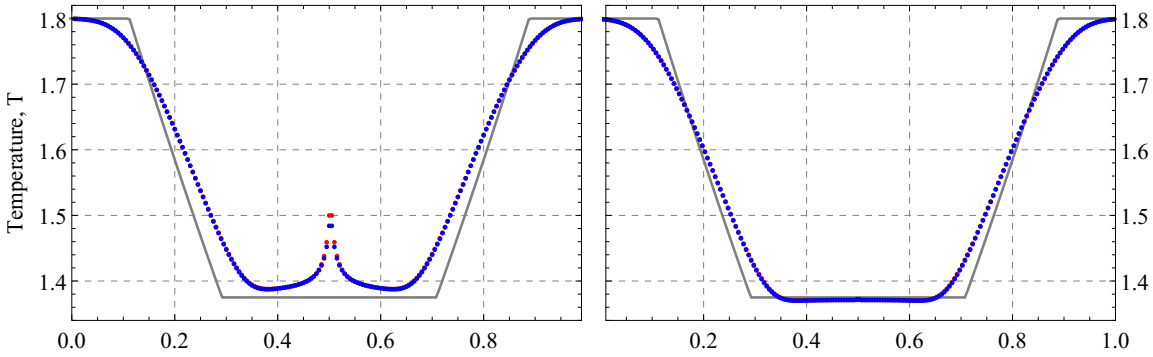

Figure 1.5: Einfeldt 1-1-5 rarefaction problem. Both the current and Roe's schemes produce very similar 1^{st}-order results. The overshoot in temperature with energy conservation (*left*) is eliminated when entropy conservation is utilized (*right*).

1.9.2 Einfeldt 1-2-3

Einfeldt's 1-2-3 problem increases the rarefaction strength from Mach 0.63 to 1.3 which is beyond the limit for which Roe's scheme is linearizable. As a result, we have no comparison for Roe's scheme. We instead compare both 1^{st}- and 3^{rd}-order variants of the proposed scheme as shown in Fig. 1.6. The initial conditions for the Riemann problem are given by

$$\begin{pmatrix} \rho_{\text{L}} \\ u_{\text{L}} \\ p_{\text{L}} \\ T_{\text{L}} \end{pmatrix} = \begin{pmatrix} 1 \\ -2 \\ 0.4 \\ 0.4 \end{pmatrix} \quad \text{and} \quad \begin{pmatrix} \rho_{\text{R}} \\ u_{\text{R}} \\ p_{\text{R}} \\ T_{\text{R}} \end{pmatrix} = \begin{pmatrix} 1 \\ 2 \\ 0.4 \\ 0.4 \end{pmatrix} \tag{1.148}$$

There are small undershoots in both the density and temperature as the result of start-up effects. These effects are greatly minimized with the 3^{rd}-order reconstruction which produces highly accurate temperature profiles for this problem.

1.9.3 Asymmetric 1-2-3

An axi-symmetric variant of the 1-2-3 problem in which a density jump is introduced at the interface of the two rarefaction waves is used to test the contact-capturing capabilites of the current scheme. The initial conditions for the Riemann problem are given by

$$\begin{pmatrix} \rho_{\text{L}} \\ u_{\text{L}} \\ p_{\text{L}} \\ T_{\text{L}} \end{pmatrix} = \begin{pmatrix} 1 \\ -2 \\ 0.4 \\ 0.4 \end{pmatrix} \quad \text{and} \quad \begin{pmatrix} \rho_{\text{R}} \\ u_{\text{R}} \\ p_{\text{R}} \\ T_{\text{R}} \end{pmatrix} = \begin{pmatrix} 1 \\ 2 \\ 2 \\ 2 \end{pmatrix} \tag{1.149}$$

This test is significant because the conditions are such that Roe's linearization fails but if the HLLE scheme is used, it greatly smears the contact. Furthermore, since Roe's linearization fails, there was previously no way to perform a characteristic trnasformation since Roe's linearization

Distribution Statement A: Approved for Public Release; Distribution is Unlimited. AFRL-2021-4182

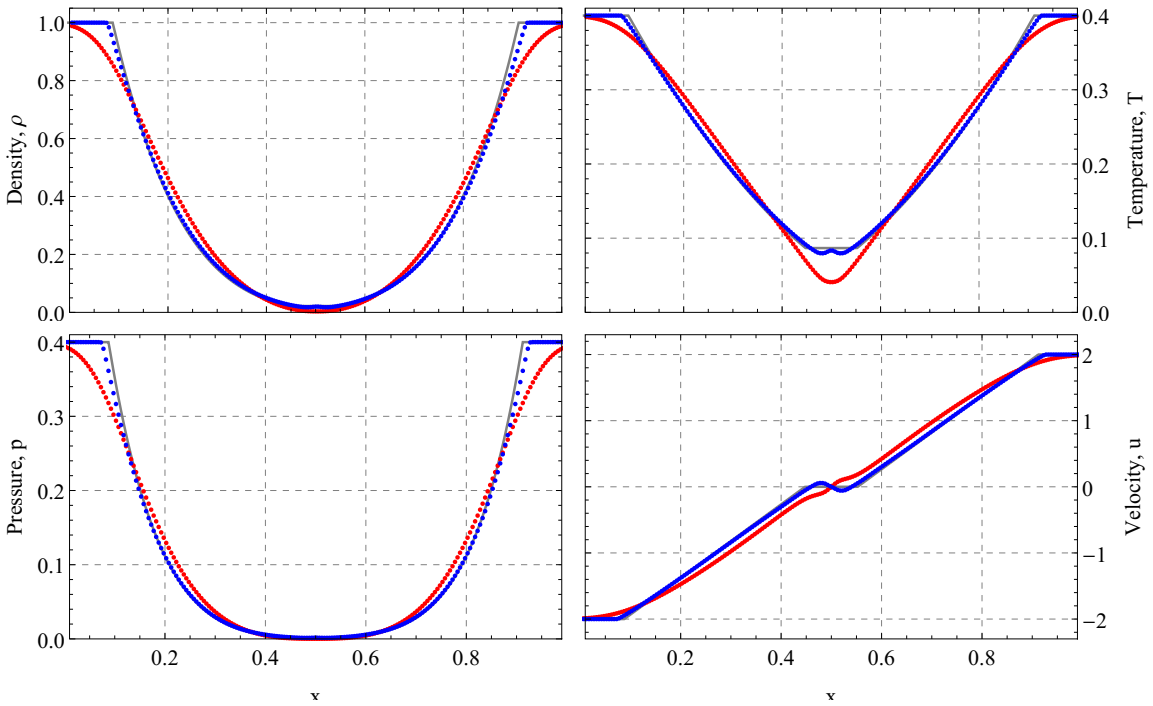

Figure 1.6: Einfeldt 1-2-3 rarefaction problem. Denisty, pressure, temperature, and velocity are plotted for the 1st-order linearization scheme (*red*) as well as the 3rd-order extension (*blue*) obtained with 200 cells.

Distribution Statement A: Approved for Public Release; Distribution is Unlimited. AFRL-2021-4182

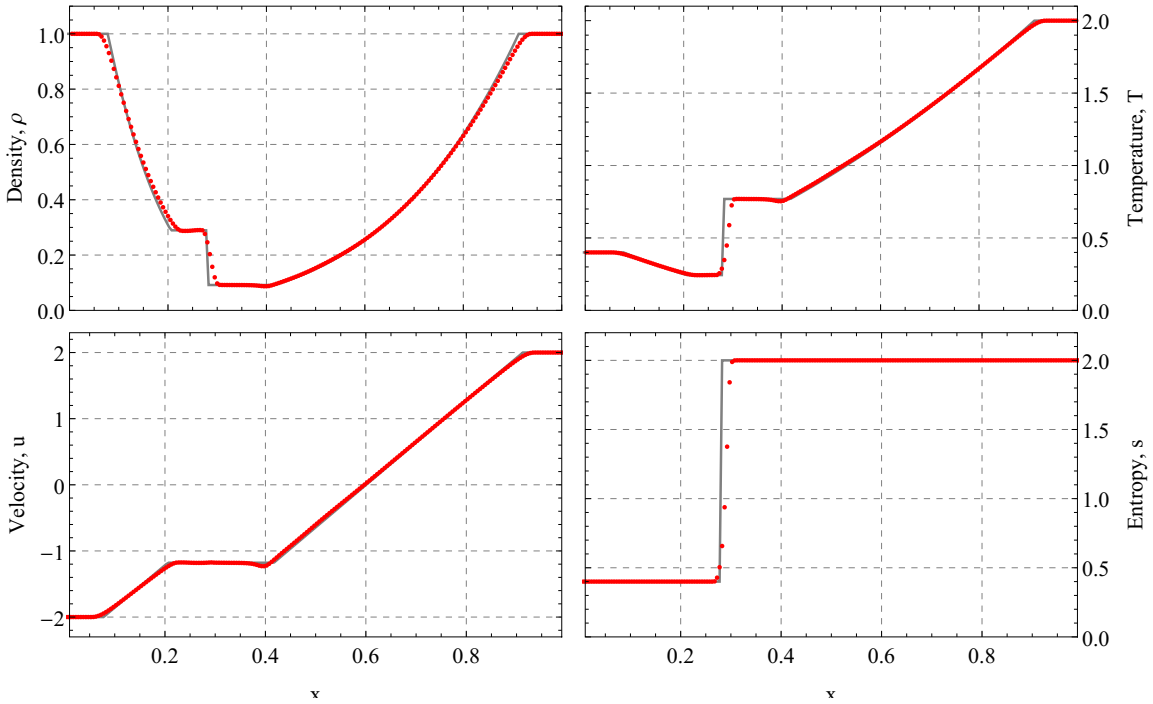

Figure 1.7: Einfeldt asymmetric 1-2-3 rarefaction problem. Denisty, pressure, temperature, and velocity are plotted for the current linearization scheme with 3rd-order reconstruction with 200 cells.

Distribution Statement A: Approved for Public Release; Distribution is Unlimited. AFRL-2021-4182

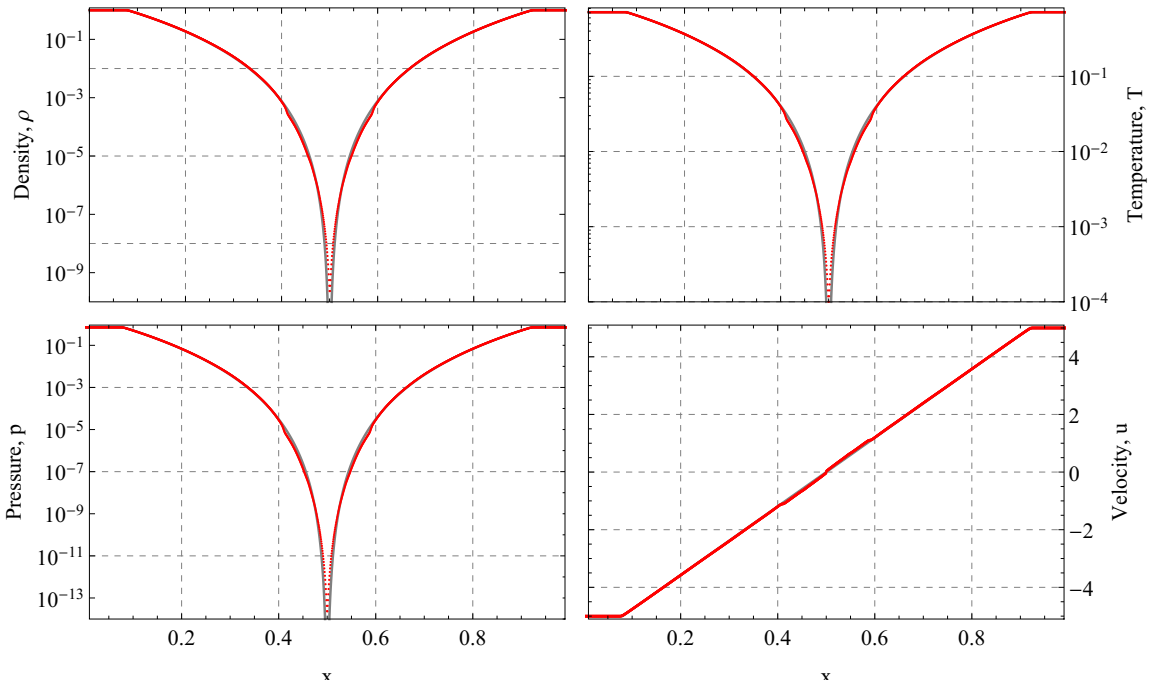

Figure 1.8: Einfeldt vacuum rarefaction problem. Denisty, pressure, temperature, and velocity are plotted for the current linearization scheme with 3rd-order reconstruction with 1600 cells.

fails and the HLLE scheme does not provide for one. This means higher-order schemes cannot operate on the characteristic values, and in such a highly-nonlinear regime, this is likely to not be positivity-conserving. With the 3rd-order reconstruction scheme and the hybrid conservation of entropy scheme, the results of the current scheme compare very favorably with the exact solution in Fig. 1.7.

1.9.4 Vacuum

If the rarefaction speed surpasses the cavitation speed, then a vacuum will result [Jeffrey 2003]. The limit here being achieved with Mach 5 for $\gamma = 7/5$. The initial conditions for the Riemann problem are given by

$$\begin{pmatrix} \rho_{\text{L}} \\ u_{\text{L}} \\ p_{\text{L}} \\ T_{\text{L}} \end{pmatrix} = \begin{pmatrix} 1 \\ -5 \\ 5/7 \\ 5/7 \end{pmatrix} \quad \text{and} \quad \begin{pmatrix} \rho_{\text{R}} \\ u_{\text{R}} \\ p_{\text{R}} \\ T_{\text{R}} \end{pmatrix} = \begin{pmatrix} 1 \\ 5 \\ 5/7 \\ 5/7 \end{pmatrix} \tag{1.150}$$

The proposed scheme achieves unprecedented accuracy with the exact solution. For a simulation with 1600 cells, temperatures as low as 10^{-4}, densities below 10^{-9}, and pressure below 10^{-13} are achieved. The smoothest results have been found when a transition from the 3rd-order scheme is

Distribution Statement A: Approved for Public Release; Distribution is Unlimited. AFRL-2021-4182

made to 1st-order if

$$\frac{\Delta u}{\min(a_{\text{L}}, a_{\text{R}})} > 0.7 \tag{1.151}$$

This is due to an over-expansion in which the flow pulls too hard away and the collapses back in on itself, resulting in a compression of the flow. As a result, this switch is used in all further test cases.

1.9.5 Linde-Roe corner expansion

Linde and Roe introduced a severe corner expansion problem to prove the robustness of the HLLE solver as applied to two-dimensional expansion problems. The initial conditions of flow past a backward-facing step were chosen such that near-vacuum conditions are reached at the corner according to Prandtl-Meyer theory. Thus Roe's scheme fails to provide a linearization and standard energy-conservation schemes produce large overheating effects. Here we compare a hybridization of the current scheme for flows where

$$\frac{\Delta u}{\min(a_{\text{L}}, a_{\text{R}})} > 0 \tag{1.152}$$

at cell interfaces with Roe's scheme. Plots in Fig. 1.9 compare solutions obtained with conservation of energy, entropy, and a hybridization of the two. The switch between energy and entropy conservation is determined by the compression of the gas within each cell. If the gas in a cell experiences an expansion,

$$\frac{\nabla \cdot \vec{u}}{a} > 0, \tag{1.153}$$

the cell is solved via entropy conservation, otherwise via energy conservation. The switch as implemented for the hybrid solution is shown by the black cells in the bottom right plot. The white cells show where energy conservation is applied. The temperature at the cells closet to the wall have been extracted for comparing the energy conservation scheme with the hybrid scheme. As expected, the energy conservation scheme over predicts the temperature at the lowest value at the wall by two orders of magnitude. The exact solution of the expansion wave emanating in the x-direction from the base of the wall is given by the dashed black line in Fig. 1.10. The current solver matches this value very accurately. This overheating is also very pronounced in the the energy conservation solution in the shear wave which initiates and develops too far below the corner.

1.9.6 Mach 10.2 axi-symmetric flow past a cylinder

Axi-symmetric flow past a cylinder is obtained with a source term eqivalent to

$$\dot{\Omega} = Ad\theta \begin{pmatrix} 0 \\ 0 \\ \rho v_\theta^2 + p \\ \rho v_r v_\theta \\ 0 \\ 0 \end{pmatrix}. \tag{1.154}$$

Distribution Statement A: Approved for Public Release; Distribution is Unlimited. AFRL-2021-4182

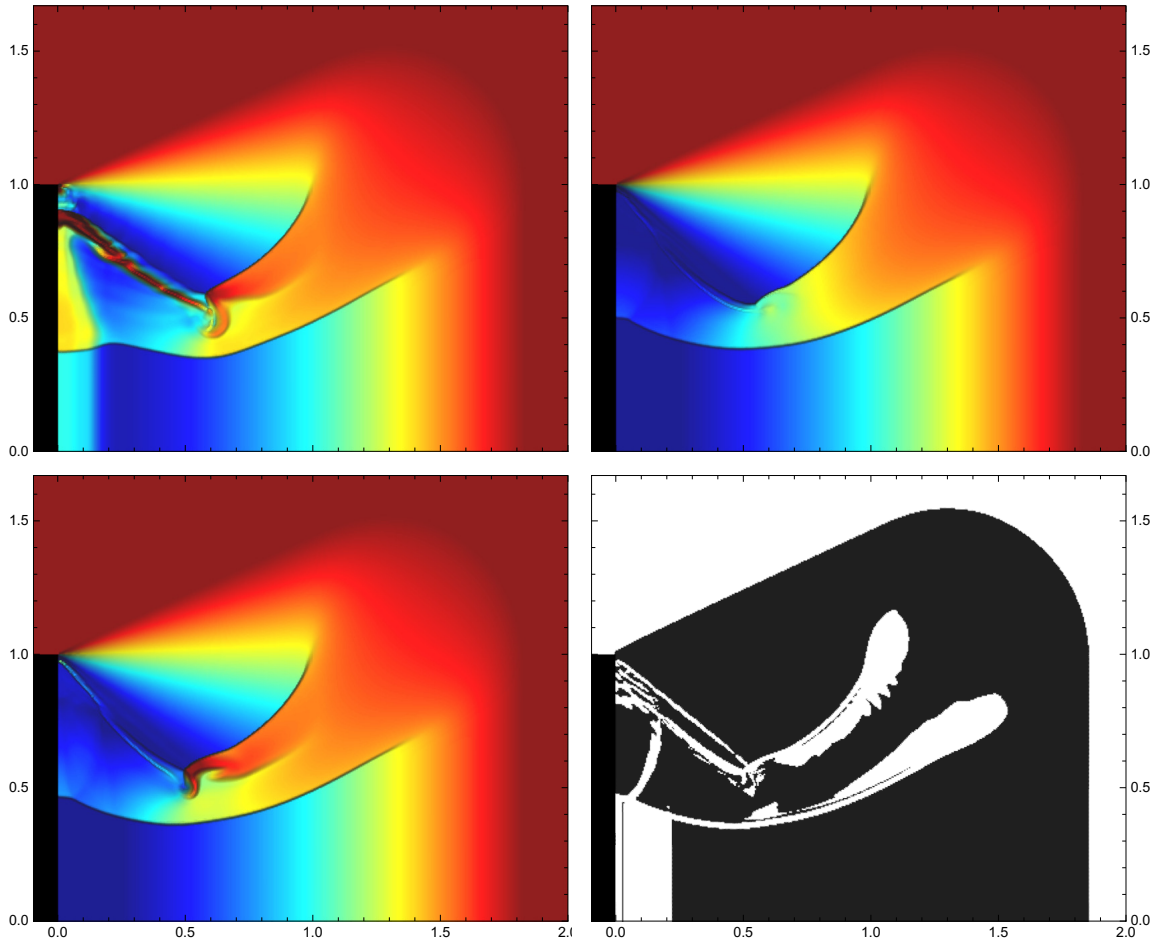

Figure 1.9: Temperature plots for the Linde-Roe corner expansion problem. The top left solution was obtained with energy conservation while the top right was obtained with entropy conservation. The bottom left was obtained with a hybridization of enery and entropy conservation with the switch indicated in the the bottom right plot. The energy conservation solution shows overheating near the wall and in the shear wave emanating from the corner flow. Furthermore, the shear wave location and shock detail appears different than in the hybrid solution, including the emergence of a Mach stem and incorrect location of the shear wave. The numerical fluxes for all plots were obtained from a hybridization with the current scheme and Roe's scheme, based on the fluid compression of each cell.

Distribution Statement A: Approved for Public Release; Distribution is Unlimited. AFRL-2021-4182

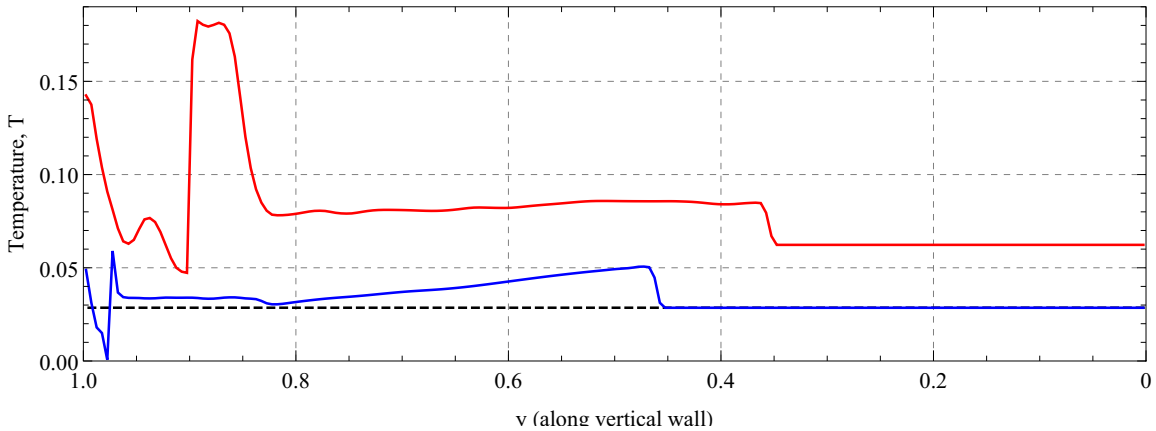

Figure 1.10: Wall temperature for Linde-Roe corner expansion problem. The solution obtained with energy conservation is given in red and shows an over estimation of the temperature at the cells nearest the wall. The results obtained with the hybrid scheme are much more favorable, matching very well with the exact solution indicated by the black dashed line.

The upper half of the plot in Fig. 1.11 gives the mass density while the lower half indicates the switch between energy and entropy conservation. Energy conservation cells are given in white while entropy conservation was used to compute cells in black.

1.9.7 Supersonic jet

The simulation of a Mach 1.5 under-expanded jet has also been included to demonstrate the robustness of the hybridization in two dimensions on practical applications. The upper half of the plot in Fig. 1.12 gives the Mach number while the lower half indicates the switch between energy and entropy conservation. Energy conservation cells are given in white while entropy conservation was used to compute cells in black. All structures are well resolved including the expansion of the jet and Mach disc. The flow is highly unsteady as evident by the fluctuating jet boundary and shear layers.

1.10 Conclusions

A novel flux difference splitting scheme for the isentropic Euler equations has been introduced. It can be used to obtain linearizations to the Riemann problem where Roe's linearization fails. It can be fully intergrated into existing numerical codes where Roe's approximate linearization is utilized. It can be fused with existing approximate Riemann solvers with minimal effort. Results show unparalleled results when compared with previous solution techniques and the accuracy of many approximate Riemann solvers can be improved when hybridized with the new linearization.

Distribution Statement A: Approved for Public Release; Distribution is Unlimited. AFRL-2021-4182

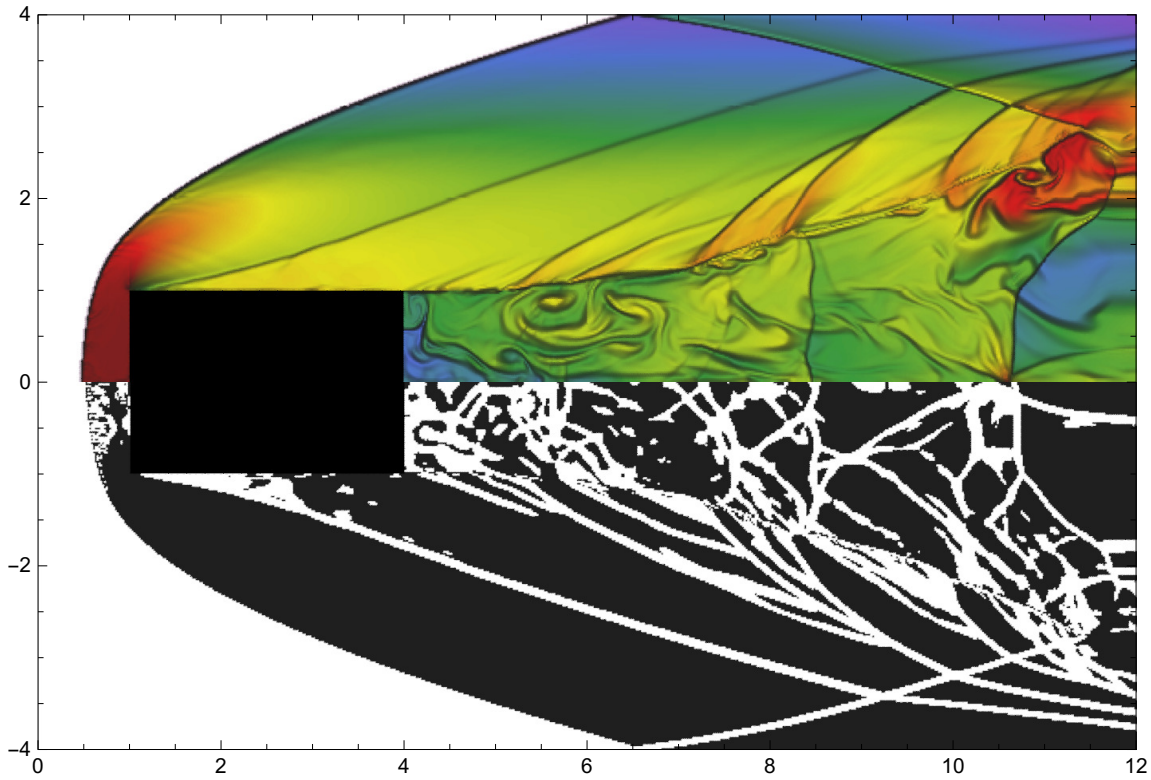

Figure 1.11: Mach 10.2 axi-symmetric flow past cylinder: a simulated Schlieren image colormapped to $\log T$ is plotted above the switching function which indicates entropy-conservation cells in black and energy-conservation cells in white.

Distribution Statement A: Approved for Public Release; Distribution is Unlimited. AFRL-2021-4182

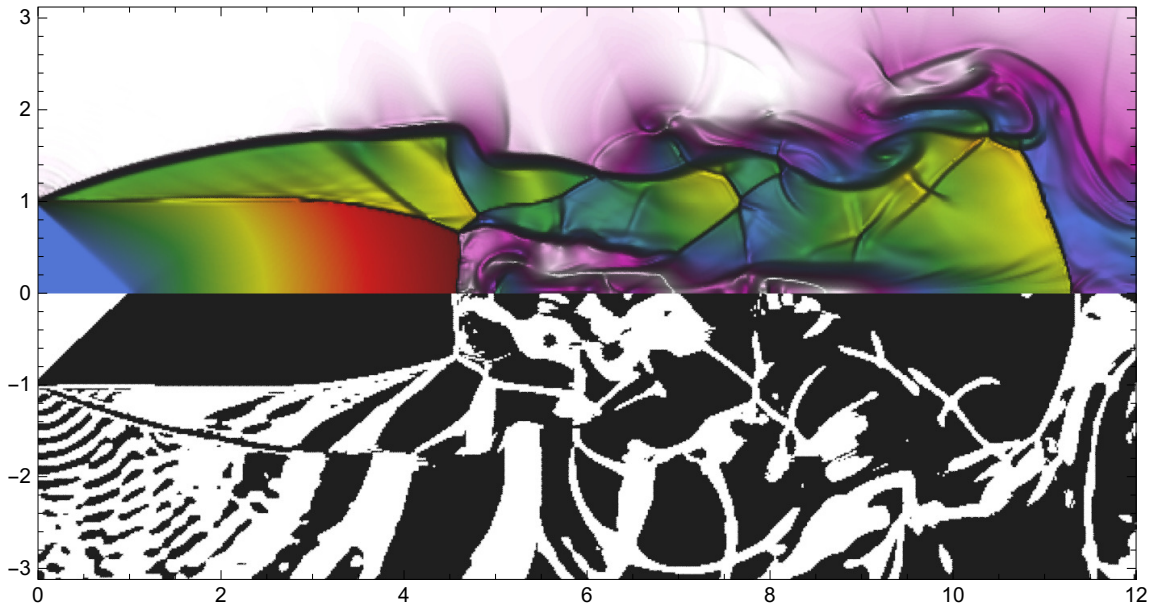

Figure 1.12: Mach 1.5 under-expanded axi-symmetric jet: a simulated Schlieren image colormapped to the Mach number is plotted above the switching function which indicates entropy-conservation cells in black and energy-conservation cells in white.

Distribution Statement A: Approved for Public Release; Distribution is Unlimited. AFRL-2021-4182

B Enhanced Non-Equilibrium Plasma Models **B-1**

B.1 Effects of Collisional-Radiative Processes with Relative Drift in Electric Propulsion Devices B-2

B.2 Potential Energy and Angular Momentum Conservation in Particle Merging and Collision Models B-13

Distribution Statement A: Approved for Public Release; Distribution is Unlimited. AFRL-2021-4182

Effects of Collisional-Radiative Processes with Relative Drift in Electric Propulsion Devices

IEPC-2019-A191

Presented at the 36th International Electric Propulsion Conference
University of Vienna, Austria
September 15-20, 2019

Richard J. E. Abrantes*
National Research Council Research Associateship, Washington, D.C., 20001, USA

Robert Lilly†
ERC Inc., Edwards AFB, California, 93524, USA

Robert Martin‡
Air Force Research Laboratory, Edwards AFB, California, 93524, USA

Abstract: As future spacecraft missions begin to demand higher performance characteristics from its electric propulsion systems, the complexity of new thruster systems and operations will increase to meet these objectives. However, the arrival of these new potential thrusters will involve greater challenges to overcome such as new plasma physics phenomena under the context of electric propulsion. In this work, the Field-Reversed-Configuration thruster is presented as one such device with strong multifluid effects that are necessarily part of the thruster's operation. These multifluid effects are important not only for the ionization of the plasma, but for the formation of the plasmoid that will lead to thrust. Therefore, the reaction kinetics involving multifluid effects will be the focus of discussion and analysis in this study to convey its significance for such thrusters. Steady-state and time-dependent simulations incorporating the multifluid rate coefficients were performed showing the multifluid effect's impact on the plasma parameters relevant to new, forthcoming propulsion devices.

I. Introduction

As the complexity of new electric propulsion (EP) systems increases, there is a growing need to understand the multiphysics and multiscale nature of the plasma dynamics within these devices. One such device that exemplifies the increasing complexity of these forthcoming propulsion devices is the Field-Reversed Configuration (FRC) thruster.[1,2] The FRC thruster is an EP device that employs a two-step process to generate thrust. Each thrust cycle begins with the formation of the plasmoid through the induced magnetic field generated by the azimuthally-driven electron stream. This plasmoid is formed once the induced magnetic field encloses upon itself, hence "Field-Reversed Configuration", after which a set of external coils are modulated to eject the plasmoid out of the thruster channel. In comparison with current EP technology, this device presents greater challenges as this electromagnetic device operates through highly-transient conditions, requiring thorough plasma ionization, plasmoid formation configured through the magnetic field's reversal, and proper modulation of the coils for plasmoid ejection.[3]

Since the operation of the FRC thruster is highly dependent on the efficacy of plasmoid ejection, the formation of the plasmoid is an important, foundational phase that must be realized for each thrust cycle. The intricacies of FRC formation requires resolving as many physical processes as possible that contribute towards

*NRC Postdoctoral Research Associate, AFRL/RQRS (In-Space Propulsion Branch), richard_june.abrantes.ctr@us.af.mil
†Research Engineer, AFRL/RQRS (In-Space Propulsion Branch), robert.lilly.3.ctr@us.af.mil
‡Computational Scientist, AFRL/RQRS (In-Space Propulsion Branch), robert.martin.101@us.af.mil

Distribution Statement A: Approved for Public Release; Distribution is Unlimited. PA# 19458

Distribution Statement A: Approved for Public Release; Distribution is Unlimited. AFRL-2021-4182

each plasmoid ejection sequence. Recently, multifluid codes have been developed simply to investigate the influence of electromagnetic fields on the plasmoid formation process.[4] The goal of these initial simulations is to study the likelihood of plasmoid formation due to the interactions between the plasma fluids and the electromagnetic field. But, the study of electromagnetic coupling within FRC plasmoids is only one important facet of the entire formation sequence; a more realistic simulation of the plasmoid's formation requires coupling the plasma reaction kinetics within this multifluid environment.

In this work, a collisional-radiative model was employed to capture the reaction kinetics within an FRC simulation. The collisional-radiative model monitors the variations in the atomic state distribution (ASD) as well as other impacted properties like temperature due to the collisional and radiative processes occurring within the plasma system. The rate coefficients that are calculated and used in collisional-radiative models conventionally assume non-streaming heavy species (atomic) and electron energy distributions. By contrast, the FRC operation is characterized by a strong toroidal electron current flow moving perpendicular to the axially streaming ions. Therefore, any CR model that is coupled to an FRC simulation, or any device with strong multifluid characteristics, should account for relative streaming corrections in the collisional rate calculations. Rate coefficients modified for relative streaming effects will be incorporated into the CR model to show the impact of the multifluid phenomena on the reaction kinetics.[5,6] These modified reaction kinetics are crucial as the inelastic processes couple to the multifluid FRC formation.

This paper is organized as follows: Section II will discuss the appropriate modifications to the rates as derived from a previous work, after which rate maps and steady-state simulation results using the modified rates will be discussed. The calculated rates will also be utilized in Section III where computational results of a time-dependent simulation will be analyzed. This section will briefly address the parameters used for the prototypical, in-house FRC thruster as well as their scalability. This work will then be concluded in Section IV.

II. Atomic Data and Modification of the Rate Equations

In a multiphysics plasma simulation, the collisional-radiative model captures the changes in the atomic state distribution due to the inelastic processes occurring in the plasma. The inelastic processes modeled in this work include electron-impact excitation and deexcitation, electron-impact ionization and its inverse three-body recombination, along with the radiative processes of radiative recombination and spontaneous emission. These processes enter the CR model in the form of rates dictating how quickly each transition occurs from one atomic state to another. However, a sufficiently complete set of atomic and transition data is necessary to generate the rates that are needed in a CR simulation. For this study, cFAC, the C++ variant of the Flexible Atomic Code (FAC), was employed to generate all of the necessary atomic and transition data for the CR calculations.[7] While there is the well-known caveat that these atomic codes based on perturbative methods are inaccurate for near-neutral/low-Z applications, this code is much more complete in its ability to generate data for many different types of transitions. Therefore, the self-consistency associated with generating copious transition data amongst the computed atomic states makes cFAC a viable candidate to study since the entire set of reaction kinetics is coherently modified due to multifluid effects. Although this particular atomic code was used in this study, one should note that this CR model is capable of accommodating more accurate data sets should they become available.

As mentioned, cFAC was used to produce atomic and transition data for this study. While the FRC thruster is capable of utilizing a variety of propellant species, xenon was the element chosen in this work due to its prevalence in many electric propulsion systems. 53 levels of Xe^{+0}, 117 levels of Xe^{+1}, and only 5 levels of Xe^{+2} were included in the simulation to display the code's multistage ionization capabilities. The number of levels chosen for each ion stage was based on the continuum threshold from NIST along with the decision to limit the computational expenses associated with generating the rate coefficient maps.[8] These levels produced a total of 8166 electron-impact excitation channels, 4150 electron-impact ionization channels, and 4150 radiative recombination channels, each bearing cross-sectional data to be integrated within the CR model's rate calculation routine. Lastly, 2600 spontaneous emission transitions generated Einstein A rate coefficients to be used in the model, which obviously do not require any modification for the multifluid effect. The multifluid rate equations used to generate the rate coefficient maps are described in the following subsections.

Distribution Statement A: Approved for Public Release; Distribution is Unlimited. PA# 19458

Distribution Statement A: Approved for Public Release; Distribution is Unlimited. AFRL-2021-4182

A. Electron-Impact Excitation and Deexcitation

The first set of processes which will be discussed is electron-impact excitation and deexcitation. The corresponding multifluid rates were derived by Le and Cambier and are shown in Eqs. (2) and (3).[5] These rates were derived by accounting for the properties of both fluids, e.g. temperature and fluid velocity, and performing the integrations over the non-dimensionalized energy space, x, under a center-of-mass (COM) frame. As a result, the excitation and deexcitation rates are augmented by the exponential and $\zeta^{(0)}$ factors that account for the non-dimensionalized multifluid drift energy, λ. The $\zeta^{(0)}$ factor takes the form below:

$$\zeta^{(0)} = \frac{1}{2}\int_{-1}^{+1} dy e^{2\xi y} = \frac{\sinh(2\xi)}{2\xi} \quad \text{s.t.} \quad \lim_{\xi\to 0}\zeta^{(0)} = 1 \tag{1}$$

In addition, the deexcitation rate coefficient may be rewritten in terms of the forward excitation cross section by enforcing detailed balance through the Klein-Rosseland relation. Note as well for both equations that the equations converge to the well-known rate coefficient equations when the multifluid effect embodied in λ approaches 0.

$$\Gamma_{sl}^{ex} = N_s N_l \overline{g}_{\tilde{T}} e^{-\lambda} \int_{x=x^*}^{\infty} dx\ x e^{-x} \overline{\sigma}_{sl}^{ex}(x) \zeta^{(0)} \left(\sqrt{\lambda x}\right) \tag{2}$$

$$\Gamma_{su}^{de} = N_s N_u \overline{g}_{\tilde{T}} e^{-\lambda} e^{x^*} \frac{g_l}{g_u} \int_{x=x^*}^{\infty} dx\ x e^{-x} \overline{\sigma}_{sl}^{ex}(x) \zeta^{(0)} \left(\sqrt{\lambda(x-x^*)}\right) \tag{3}$$

Using the cross-sections generated from cFAC and implementing the multifluid rate calculations, 2-dimensional rate coefficient maps as a function of temperature, $\tilde{T}$ (which has been approximated as the electron temperature, T_e), and the COM non-dimensional kinetic energy, λ, were generated for each transition. Two sample sets of transition rate maps are shown below in Figs. 1 and 2.

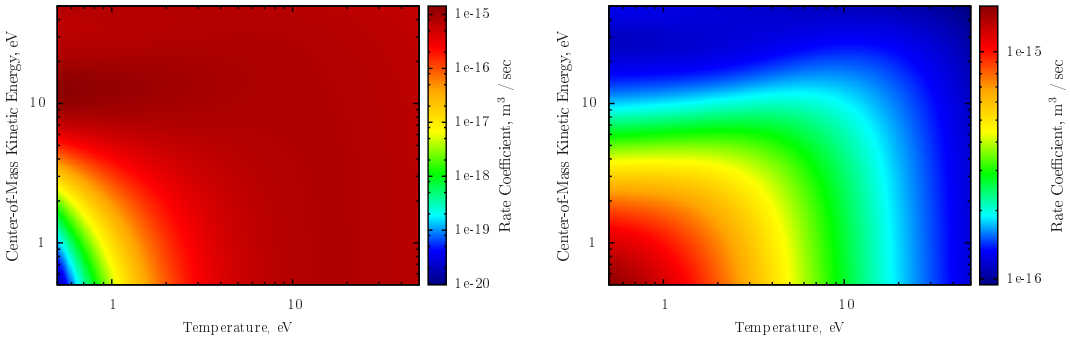

(a) Excitation (b) Deexcitation

Figure 1: Electron-impact excitation and deexcitation multifluid rate coefficients between (lower state) Xe^{+0} $5p^4_{3/2}(J=0)$ and (upper state) Xe^{+0} $[5p^3_{3/2}(J=0)\ 5d^1_{5/2}(J=5/2)]$ $(J=3)$. The energy gap between both states as calculated by cFAC is 9.723 eV.

Figs. 1a and 1b represent the general set of excitation and deexcitation rate coefficient maps that have been tabulated, i.e. most of the rate coefficient maps follow the contour maps shown in these subfigures. As the input parameters approach the abscissa on these maps, the rates are more closely represented by an integration over the thermal distribution, while rates that are much closer to the ordinate correlate to the beam-like rates. In contrast, Figs. 2a and 2b represent the set of excitation and deexcitation rate coefficients for a transition that is spin-forbidden. The allowed transition in 1a requires a threshold energy for the reaction to proceed, hence the eventual rise and peak of the rate coefficient especially closer to the ordinate. However, the strong monotonic dropoff in the forbidden transition's cross-section leads to a profile that is very similar to the deexcitation rate.

Distribution Statement A: Approved for Public Release; Distribution is Unlimited. PA# 19458

Distribution Statement A: Approved for Public Release; Distribution is Unlimited. AFRL-2021-4182

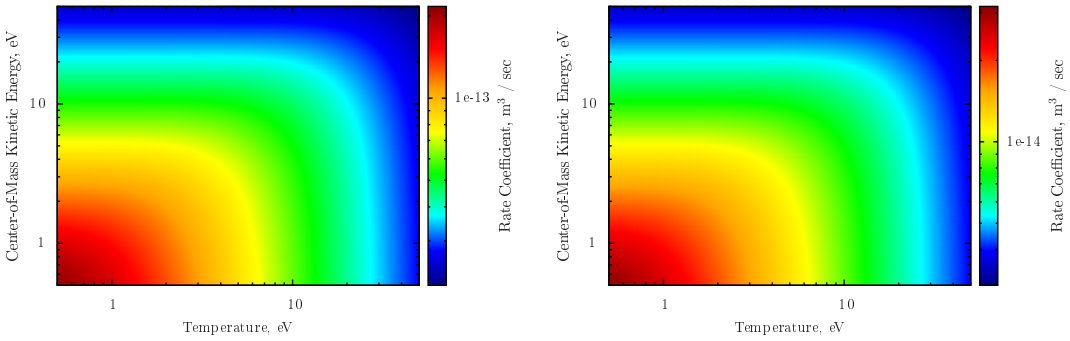

(a) Excitation (b) Deexcitation

Figure 2: Electron-impact excitation and deexcitation multifluid rate coefficients between (lower state) Xe^{+0} $[5p^3_{3/2}(J=3/2)\ 6d^1_{3/2}(J=3/2)]$ $(J=0)$ and (upper state) Xe^{+0} $[5p^3_{3/2}(J=3/2)\ 6d^1_{3/2}(J=3/2)]$ $(J=3)$. The energy gap between both states as calculated by cFAC is 0.0226 eV. Note that these rate coefficient maps are for a spin-forbidden transition.

B. Electron-Impact Ionization and Three-Body Recombination

The next set of inelastic processes to discuss are electron-impact ionization and its inverse three-body recombination process. The rates in Eqs. 4 and 5 were derived in a separate paper by Le and Cambier, but present a heightened challenge due to the third body (electron) entering the inverse collision process.[6] This leads to a familiar formulation in the multifluid ionization rate compared to the two-body processes of excitation and deexcitation, but a more complicated and numerically expensive formula for the three-body recombination process. As one can see, the recombination formula still employs the same exponential and $\zeta^{(0)}$ factors, albeit with an extra $\zeta^{(0)}$ factor due to the introduction of a third body in the process and the use of a differential cross section (DCS) in the integrated cross section's (ICS) stead. Unlike the previous rates, three-body recombination rate coefficient requires the DCS because of the variability in the two electrons' energy difference; this is akin to the incorporation of three-body recombination events in a Vlasov inelastic collision term.

$$\Gamma^{ion}_{sl} = N_s N_l \overline{g}_{\tilde{T}} e^{-\lambda} \int_{x=x^*}^{\infty} dx_0\ x_0 e^{-x_0} \overline{\sigma}^{ion}_{sl}(x_0) \zeta^{(0)} \left(\sqrt{\lambda x_0}\right) \tag{4}$$

$$\Gamma^{rec}_{su} = \frac{g_n}{2 g_i \mathbb{Z}_e} N_u N_s^2 \overline{g}_{\tilde{T}} e^{-2\lambda} e^{x^*} \int_{x^*}^{\infty} dx_0\ x_0\ e^{-x_0} \int_{x^*}^{x_0} \zeta^{(0)} \left(\sqrt{\lambda x_1}\right) \zeta^{(0)} \left(\sqrt{\lambda x_2}\right) \left(\frac{d\sigma^{ion}}{d\nu}\right)\ d\nu \tag{5}$$

Figures 3a and 3b represent the typical rate coefficient maps produced by integrating Eqs. 4 and 5, respectively. Note that the three-body recombination rate uses the ionization cross section in its integration by enforcing detailed balance through the Fowler relation. The map contours are very similar to the "allowed" excitation and deexcitation maps shown previously, where there is a heightened transition likelihood if much of the electron energy lies past beyond the ionization threshold. Likewise with deexcitation, the three-body recombination map decreases as the temperature or COM kinetic energy increases since there is a higher likelihood of inverse processes occurring when the electrons are slow and easily captured by the ionic species.

One side note regarding the differential cross section is that the output generated by the atomic code for ionization are integrated cross sectional values. In order to resolve this issue, the DCS profile used in this work is the hydrogen DCS equation which have been scaled to the cross sections produced by cFAC so that the original ICS is retained in the rate calculation. However, these DCS profiles can be replaced by more appropriate formulations should a complete set of profiles exist in the open.

C. Radiative Recombination

Complementary to the set of collisional events in a CR model are the radiation or photon-driven processes that can also alter the state of a plasma. While these rates were not explicitly derived by Le and Cambier, the

Distribution Statement A: Approved for Public Release; Distribution is Unlimited. PA# 19458

Distribution Statement A: Approved for Public Release; Distribution is Unlimited. AFRL-2021-4182

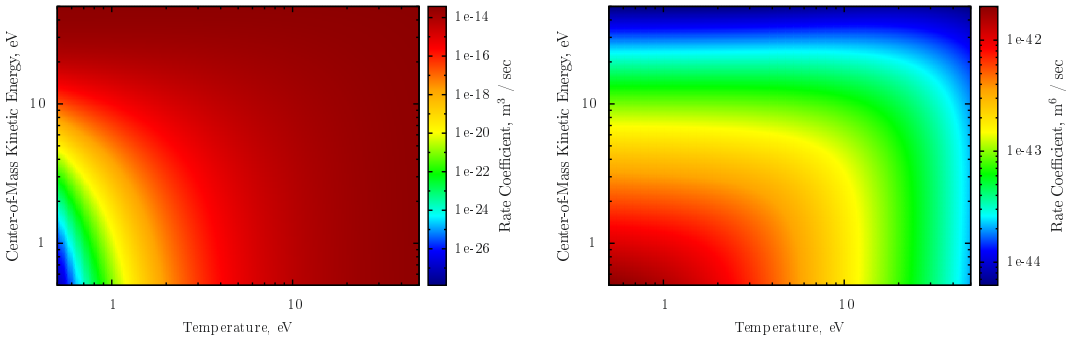

(a) Ionization (b) Recombination

Figure 3: Electron-impact ionization and three-body recombination multifluid rate coefficients between (lower state) Xe^{+1} $5p^3_{3/2}(J = 3/2)$ and (upper state) Xe^{+2} $5p^2_{3/2}(J = 2)$. The energy gap between both states as calculated by cFAC is 20.342 eV.

formulation for radiative recombination is a mere extension of the two-body multifluid rate derivations that were already performed. In this work, the optically-thin assumption has been imposed on the model so that no re/absorption takes place within the plasma whether by photoexcitation or photoionization. However, the multifluid modification clearly only extends to the radiative recombination rate equation because of its collisional nature. The rate of change in atomic state density due to radiative recombination is shown in Eq. 6 where the Milne relation has been applied to recast the equation in terms of the photoionization cross section.

$$\Gamma^{rr}_{su} = N_s N_u \overline{g}_{\tilde{T}} e^{-\lambda} e^{x^*} \left(\frac{k_B \tilde{T}}{m_e c^2} \right) \frac{g_l}{2g_u} \int_{x=x^*}^{\infty} dx \; x^2 e^{-x} \overline{\sigma}^{pi}_{sl}(x) \zeta^{(0)} \left(\sqrt{\lambda(x - x^*)} \right) \tag{6}$$

Accounting for the energy equation's evolution due to radiative recombination is not as trivial when compared to the previous collisional processes' energy loss rates because discrete energy gaps are lost from the total electron energy. In the case of radiative recombination, a broadband loss in electron energy can occur since any excess energy beyond the ionization threshold is lost in the form of radiation during the recombination process. Therefore, an additional energy factor is multiplied within the radiative recombination energy coefficient's integrand to account for the energy loss of the system due to this particular process. This energy rate coefficient is shown in Eq. 7 below.

$$Q^{rr}_{su} = N_s N_u \overline{g}_{\tilde{T}} e^{-\lambda} e^{x^*} \left(\frac{(k_B \tilde{T})^2}{m_e c^2} \right) \frac{g_l}{2g_u} \int_{x=x^*}^{\infty} dx \; x^3 e^{-x} \overline{\sigma}^{pi}_{sl}(x) \zeta^{(0)} \left(\sqrt{\lambda(x - x^*)} \right) \tag{7}$$

A sample set of radiative recombination density and energy rate coefficients are shown in Figs. 4a and 4b, respectively. The map of radiative recombination density rate coefficients shows a very similar contour map to the maps shown in electron-impact deexcitation and three-body recombination. But, the additional energy factor in the radiative recombination energy rate integration creates a different contour map which shows an increase in the rate coefficient as one traverses positively in COM kinetic energy. This is expected since an increase in COM kinetic energy simply means an increased energy loss in the form of radiation should the electrons with an additional streaming component recombine with the ionized species.

D. Elastic Collision

The last set of terms to be incorporated within the CR model are the elastic collision terms. These terms do not directly change the atomic state distribution, but do influence the overall set of reaction kinetics because of variations in temperature induced by elastic collisions. Both electron-neutral and electron-ion elastic collisions are being considered in this work. The form for higher-order moments of the inelastic

Distribution Statement A: Approved for Public Release; Distribution is Unlimited. PA# 19458

Distribution Statement A: Approved for Public Release; Distribution is Unlimited. AFRL-2021-4182

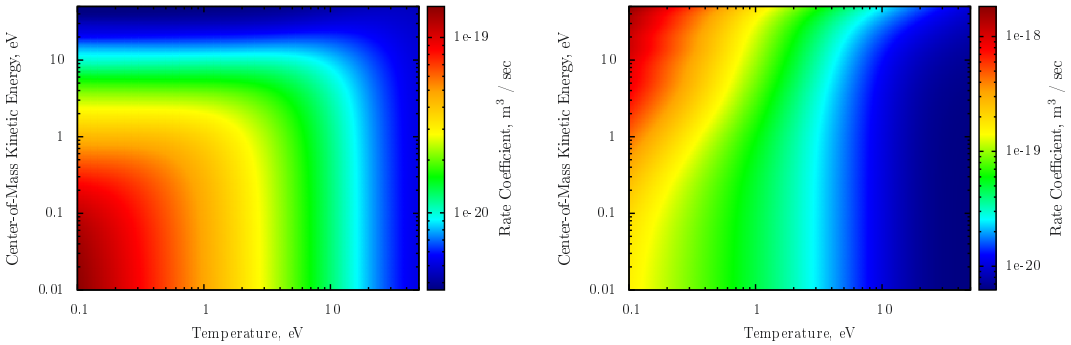

(a) Radiative Recombination

(b) Radiative Recombination Energy

Figure 4: Radiative recombination density and energy multifluid rate coefficients between (lower state) Xe^{+1} $5p^3_{3/2}(J = 3/2)$ and (upper state) Xe^{+2} $5p^2_{3/2}(J = 2)$. The energy gap between both states as calculated by cFAC is 20.342 eV.

collision processes which yield the momentum transfer and thermal relaxation rate coefficient equations, while accounting for the multifluid drift, was derived by Le and Cambier; although the paper solves the equation for a threshold energy gap, taking the energy gap to be 0 eV allows the equation to be solved for elastic collisions. The momentum transfer and thermal relaxation rates are shown below in Eqs. 8 and 9.

$$K^{en} = m_e N_e N^{+0} \frac{2}{3} \overline{g}_{\tilde{T}} e^{-\lambda} \int_{x=x^*}^{\infty} dx\; x^2 e^{-x} \overline{\sigma}^{en}(x) \left(1 - \langle \cos\chi \rangle_{\Omega'}\right) \zeta^{(1)} \left(\sqrt{\lambda x}\right) \tag{8}$$

$$J^{en} = N_e N^{+0} \overline{g}_{\tilde{T}} e^{-\lambda} \int_{x=x^*}^{\infty} dx\; x^2 e^{-x} \overline{\sigma}^{en}(x) \left(1 - \langle \cos\chi \rangle_{\Omega'}\right) \left[\zeta^{(0)} \left(\sqrt{\lambda x}\right) - \frac{2\lambda}{3} \zeta^{(1)} \left(\sqrt{\lambda x}\right)\right] \tag{9}$$

Integration of higher-order inelastic collision rate coefficients leads to the additional $\zeta^{(1)}$ factor elaborated below:

$$\zeta^{(1)} = \frac{3}{4\xi} \int_{-1}^{+1} dy e^{2\xi y} = \frac{3}{4\xi^2} \left[\cosh(2\xi) - \frac{\sinh(2\xi)}{2\xi}\right] \quad \text{s.t.} \quad \lim_{\xi \to 0} \zeta^{(1)} = 1 \tag{10}$$

Another aspect of the electron-neutral elastic collision rates is the $1 - \langle \cos\chi \rangle_{\Omega'}$ modifier, which when multiplied to the total elastic collision cross section yields the momentum transfer cross section. For electron-neutral Xe collisions, these cross sections were found in McEachran and Stauffer's elastic collision studies.[9] As before, rate coefficient maps were generated as a function of temperature and COM kinetic energy for the momentum transfer and thermal relaxation rate coefficients shown in Figs. 5a and 5b, respectively. A unique feature of these maps is the presence of multiple maxima as one traverses along the COM kinetic energy axis at low temperatures. This results from the Ramsauer-Townsend effect where the electron's wavelike interaction with each of the atom's electron shells results in a decreased collision cross section.[10,11]

Finally, the momentum transfer and thermal relaxation rate coefficients for the electron-ion elastic collisions can be determined by using Rutherford's scattering analytical DCS with a cut-off impact parameter based on the Debye length.[12] The integrated cross section is provided via Eq. 11:

$$\sigma^{ei,m} = \frac{e^4}{16\pi\varepsilon_0^2\epsilon^2} \ln\Lambda \tag{11}$$

Using the integrated cross section, closed form, analytical equations can be obtained for the electron-ion momentum transfer and thermal relaxation rate coefficients. These rate coefficients are still functions of both temperature and COM kinetic energy and are calculated through the course of the simulation instead of being tabulated like the previous collision rates.

Distribution Statement A: Approved for Public Release; Distribution is Unlimited. PA# 19458

Distribution Statement A: Approved for Public Release; Distribution is Unlimited. AFRL-2021-4182

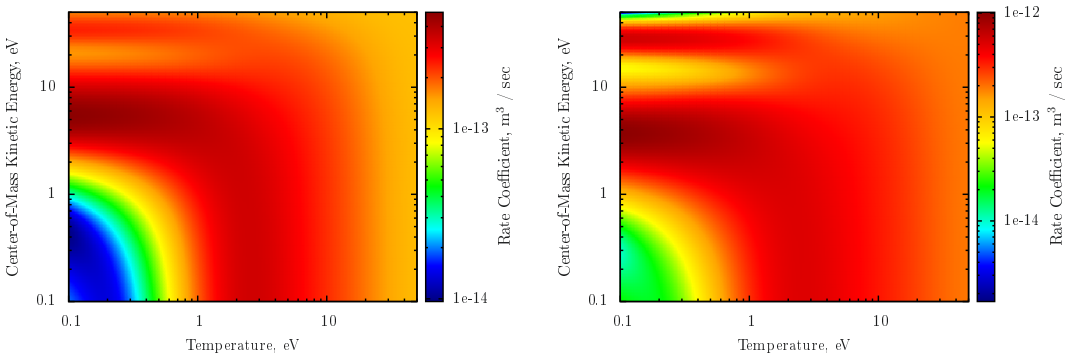

(a) Momentum Transfer

(b) Thermal Relaxation

Figure 5: Elastic collision multifluid rate coefficients for Xe^{+0}. Subfigures 5a and 5bcorresponds to the momentum transfer and thermal relaxation rate coefficients, respectively.

$$K^{ei} = m_e N_e N^{+i} \frac{16\sqrt{\pi}}{3} \frac{q_i^2 e^2}{\mu^2 \alpha^3} \ln\Lambda \left[\frac{3\sqrt{\pi}}{4\lambda^{3/2}} \mathrm{erf}\left(\sqrt{\lambda}\right) - \frac{3}{2\lambda} \exp\left(-\lambda\right) \right] \tag{12}$$

$$J^{ei} = N_e N^{+i} 8\sqrt{\pi} \frac{q_i^2 e^2}{\mu^2 \alpha^3} \ln\Lambda \, \exp\left(-\lambda\right) \tag{13}$$

E. Steady-State Simulations

Steady-state Xe simulations were performed using the collisional-radiative model to determine the impact of the multifluid effect on the plasma. This was performed by observing the average charge of the xenon plasma as the electron temperature and center-of-mass kinetic energy are varied. By imposing a center-of-mass kinetic energy, one can imagine streaming electrons relative to stationary heavy species. For these steady-state simulations, the terms considered in the model include electron-impact excitation and deexcitation, electron-impact ionization and three-body recombination, along with the radiative processes of radiative recombination and spontaneous emission. All of the processes listed above, with the exception of spontaneous emission, use modified rates that account for the multifluid effect. The solution to this system was obtained by performing a linear solve of the atomic state distribution's master equations with no density rate-of-change and replacing one of the equations with the charge neutrality constraint. The results are shown in Fig. 6.

Figure 6 shows the average charge of the Xe heavy species as a function of temperature for 4 different center-of-mass kinetic energy differentials labeled as 'dKE' on the figure: 0 eV, 0.1 eV, 0.5 eV, and 0.75 eV. These simulations were conducted assuming an electron density of 1×10^{19} m^{-3}. The impact can be clearly observed as one increases the COM kinetic energy that the average charge correspondingly increases. For instance, a comparison of the 0.75 eV stream with the case of no bulk streaming shows that there is a 0.25 eV temperature difference for both cases to achieve the same heavy species charge. The difference is also readily visible for the 0.1 eV case as well. The streaming effect clearly impacts the steady-state kinetics and allows the excitation and ionization multifluid effect to produce higher average charge values in comparison to the non-streaming scenario.

III. Time-Dependent Evolution of Collisional-Radiative Equations

The last simulation performed in this work is a time-dependent investigation of the streaming electrons' effect on the evolution of the plasma. This simulation is intended to be a representation of the reaction kinetics during the formation of the plasmoid in a Field-Reversed-Configuration thruster. If one pictures an infinitesimal cell within the FRC channel where the weakly-ionized stationary Xe gas is bombarded by azimuthally-streaming electrons, this scenario would be captured by the temporal evolution of the CR model.

Distribution Statement A: Approved for Public Release; Distribution is Unlimited. PA# 19458

Distribution Statement A: Approved for Public Release; Distribution is Unlimited. AFRL-2021-4182

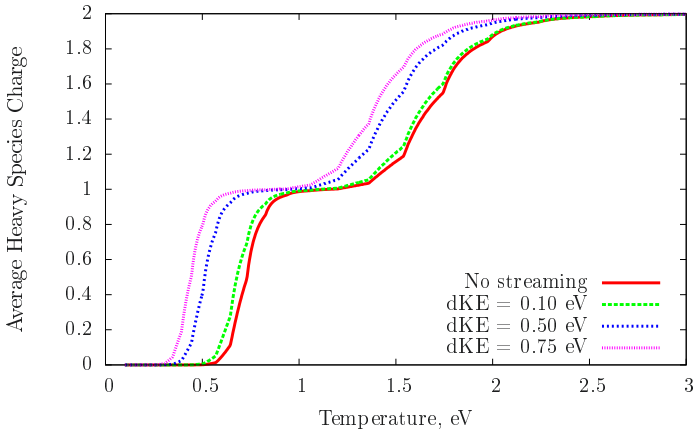

Figure 6: Steady State Ionization Fraction

The master equations corresponding to this model is described below.

A. Time-Dependent Master Equations

The time-dependent set of equations used to evolve the atomic state distribution function are shown below. The first equation shown in Eq. 14 represents the time rate of change of each atomic state density that is being modeled in the collisional-radiative model. The source on the RHS represents all of the collisional-radiative processes being considered for the atomic state's evolution. The additional equations, Eqs. 15 and 16 respectively, model the momentum and energy changes for both the electron and heavy species fluids.

$$\frac{dN_i^{+k}}{dt} = \Gamma_{+k,i}^{(inelas)} \qquad \text{for all ions, } +k\text{, and all respective states, } i \tag{14}$$

$$\frac{d(m_{\frac{e}{h}} N_{\frac{e}{h}} \mathbf{u}_{\frac{e}{h}})}{dt} = \mp \cancel{(\mathbf{u}_e - \mathbf{u}_h)\left(K^{(ec,neu)} + K^{(ec,ion)} + K^{(inelas)}\right)} \tag{15}$$

$$\begin{aligned} \frac{d\varepsilon_{\frac{e}{h}}}{dt} &= \mp \left(\overline{\mathbf{u}} - \mathbf{u}_{\frac{e}{h}}\right) \cdot (\mathbf{u}_e - \mathbf{u}_h) \left(K^{(ec,neu)} + K^{(ec,ion)} + \cancel{K^{(inelas)}}\right) \\ &\quad \mp 2\frac{m_e}{m_h} k \left(T_e - T_h\right) \left(J^{(ec,neu)} + J^{(ec,ion)} + \cancel{J^{(inelas)}}\right) - \left[\Xi^{(inelas)}\right]_{(e^- \text{ Eqn})} \end{aligned} \tag{16}$$

The momentum equations consists of the momentum transfer effects due to elastic electron-neutral and electron-ion elastic collisions, as well as inelastic collision processes which lead to changes in the ASD. In this study, however, these terms are being neglected in addition to the spatial considerations that come with solving the momentum equations. This was enforced so that the studies will be focused towards the formation of the plasma without the added complexity of a changing COM kinetic energy. Therefore, the streaming electron energy will be a constant throughout the course of the simulation, while the heavy species are assumed to be motionless in the bulk velocity.

Finally, the energy equations for both electron and heavy species are included, allowing for the evolution of the electron and heavy species temperatures. In this equation set, not only do the energy changes due to momentum transfer exist from the elastic collisions, but the variations caused by the thermal relaxation process from elastic collisions are also included. Since inelastic collisions also alter the energies of both fluids, there are corresponding momentum transfer and thermal relaxation rates due to these processes; the inclusion of these rates will be the subject of future CR studies. Lastly, the loss or gain of energy due to changes in the atomic state distribution, i.e. transition energy gap, must be incorporated in the electron equation.

Distribution Statement A: Approved for Public Release; Distribution is Unlimited. PA# 19458

Distribution Statement A: Approved for Public Release; Distribution is Unlimited. AFRL-2021-4182

B. Simulation Results

The simulation performed in this work is intended to capture the plasma generation process which takes place within a Field-Reversed-Configuration thruster. As such, the electron streaming energy has been fixed to 0.01 eV; this corresponds to prototypical parameters of electrons revolving at a frequency of 1 MHz around the thruster channel with a radius of approximately 6 cm. There certainly are no defined or standardized FRC thruster parameters as the thruster can be scaled for optimal performance parameters. The choice of dKE = 0.01 eV does not take a large advantage of the ionization rate as it approaches the thermal, non-streaming limit of the rate coefficients. But, slight increases in the thruster dimension or revolution frequency can more quickly lead to more variations in plasma characteristics. Using Backward Euler with Newtonian iterations to temporally evolve the system, the results generated from the simulation are shown in Figs. 7a to 8.

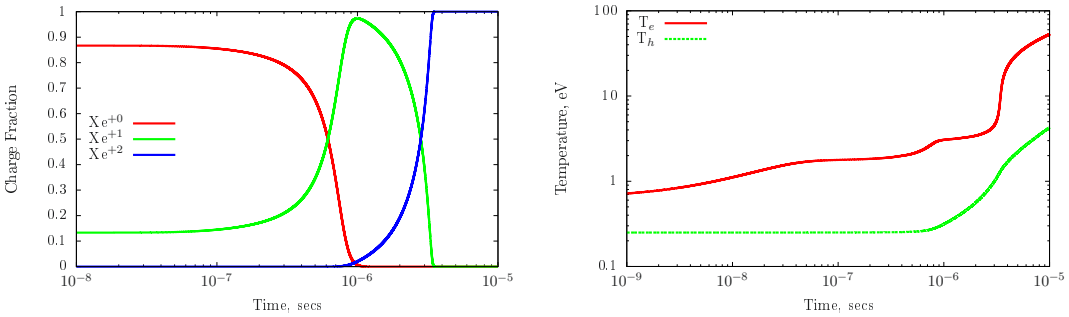

(a) Charge Fraction Evolution

(b) Temperature Evolution

(c) Evolution of several parameters of the xenon plasma. To simulate the Field-Reversed-Configuration thruster's plasma generation, a constant electron streaming energy source has been assumed for the simulation.

Figure 7a shows the charge fraction evolution of each ionization stage of Xe considered in the model. From the simulation, an initial ionization fraction of 0.133 was assumed with a total heavy species density 1 $\times$ 10^{21} m^{-3}. The electron density was determined based on the quasineutral assumption. The results show that a majority of the neutral population has depleted at 1 μs, at which point the growth of Xe^{+2} begins as the Xe^{+1} population depletes. By the end of the simulation at 10 μs, most of the plasma consists of Xe^{+2} ions. The rapid rise in Xe^{+2} can be explained from the temperatures plot shown in Fig. 7b.

The initial electron temperature assumed for the simulation was 0.65 eV while the heavy species temperature was initialized at 0.25 eV. One can see that the constant streaming electron energy source leads to a continual rise in electron temperature. As each ionization stage peaks during the evolution of the plasma, sudden increases in electron temperature can be observed in the plot of the fluid temperatures. As the system continues to siphon energy from the constant electron energy stream, the electron temperature grows into the 10s of eV. The heavy species temperature eventually begins to equilibrate with the electron temperature at the μs timescale. It should be reiterated that these results are ideal with respect to the presence of a constant electron energy source, i.e. a true evolution of the electron momentum would have no constant electron energy source. A full simulation of the FRC formation would also require solving the fluids' momentum equations, accounting for the problem's spatial dimensionality, and incorporating other collisional terms which were not included in this simulation.

Figure 8 shows the rate of energy transfer due to the collisional processes involved in the simulation. The amount of energy provided by electrons led to larger electron energy losses due to electron-impact excitation and ionization as opposed to the gains provided the inverse processes. For the case of momentum transfer energy and thermal relaxation rates, the plot shows a larger energy exchange process through thermal relaxation in comparison to the momentum transfer rates. In the momentum transfer energy rate, it should also be noted that the energy increase due to the electrons' constant streaming energy is not factored into this term as shown in the plot. The last set of energy losses stem from the radiative processes which shows that spontaneous emission has the largest radiative sink term for most of the simulation's run.

Distribution Statement A: Approved for Public Release; Distribution is Unlimited. PA# 19458

Distribution Statement A: Approved for Public Release; Distribution is Unlimited. AFRL-2021-4182

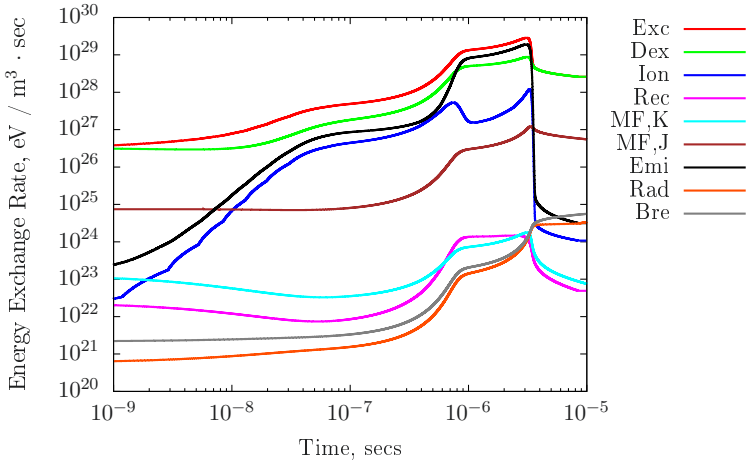

Figure 8: Evolution of the energy gain and loss rates due to multiple elastic and inelastic collision processes. The table lists energy variations caused by electron-impact excitation (Exc), deexcitation (Dex), ionization (Ion), three-body recombination (Rec), momentum transfer collisions (MF,K), thermal relaxation collisions (MF,J), spontaneous emissions (Emi), radiative recombination (Rad), and bremsstrahlung (Bre).

IV. Conclusion

The direction of future electric propulsion devices presents many challenges born out of these systems' increasing complexity as pursuits for better performance characteristics are sought. The Field-Reversed-Configuration thruster represents one such thruster at the forefront of propulsion research which has strong multifluid aspects that lead to the formation of the plasmoid. The multifluid reaction kinetics was presented as a contributing factor to the formation of the plasmoid, thereby leading to the implementation of multifluid rate coefficient calculations generalized for any atomic species. In this work, Xe^{+0} to Xe^{+2} were used to generate steady-state and time-dependent simulation results to determine the importance of multifluid effects in next generation of EP devices that may exhibit such characteristics.

In the steady-state simulations, average charge values of the Xe species were calculated for a range of electron temperatures and multiple center-of-mass kinetic energy values. It was shown that for values as small as tenths and even hundredths of eV, the difference in average charge states can be observed in the system. On the other hand, the objective of the time-dependent simulation is to show the contribution of the relative multifluid streaming effect through several plasma parameters. Although the transience of the simulation does not capture the effects as immediately as the steady-state simulation, the impact of the streaming electrons as an energy source term is visible in the growth of the ionizing plasma.

These simulations helped elucidate the importance of multifluid reaction kinetics within the FRC thruster. But, a more thorough simulation incorporating additional energy terms and spatial/fluid effects are needed to capture the FRC thruster's plasmoid formation and ejection physics. Multifluid reaction rate kinetics may also be significant for more exotic electric propulsion concepts and other physical devices beyond the electric propulsion community. As such, much work involving these multifluid effects and their impact on many plasma physics devices will continue to be pursued in the future.

Acknowledgments

The authors would like to thank Hai P. Le (LLNL) for stimulating discussions.

This research was performed while R. J. E. Abrantes held an NRC Research Associateship award at the Air Force Research Laboratory (AFRL, Edwards AFB) under grant No. FA9550-18-D-0002.

The authors would also like to acknowledge support provided by the Air Force Office of Scientific Research

Distribution Statement A: Approved for Public Release; Distribution is Unlimited. PA# 19458

Distribution Statement A: Approved for Public Release; Distribution is Unlimited. AFRL-2021-4182

(AFOSR) grant No. FA9550-17RQCOR465 (PO: Dr. Mitat Birkan).

References

[1]Hugrass, W., and Grimm, R. *A numerical study of the generation of an azimuthal current in a plasma cylinder using a transverse rotating magnetic field*, Journal of Plasma Physics, 26(3), 455-464, 1981.

[2]Slough, J., Kirtley, D., and Weber, T. *Pulsed plasmoid propulsion: The ELF thruster*, 31th International Electric Propulsion Conference, 20-24, 2009.

[3]Boeuf, J.-P. *Tutorial: Physics and modeling of Hall thrusters*, Journal of Applied Physics, 121, 011101, 2017.

[4]Sousa, É. M. *A Blended Finite Element Method for Multi-Fluid Plasma Modeling*, Ph.D. thesis. University of Washington, 2014.

[5]Le, H. P., and Cambier, J. L. *Modeling of inelastic collisions in a multifluid plasma: Excitation and deexcitation*, Physics of Plasmas, 22(9), 093512, 2015.

[6]Le, H. P., and Cambier, J. L. *Modeling of inelastic collisions in a multifluid plasma: Ionization and recombination*, Physics of Plasmas, 23(6), 063505, 2016.

[7]Stambulchik, E. *cFAC*, https://github.com/fnevgeny/cfac.

[8]Kramida, A., Ralchenko, Y., Reader, J., and NIST ASD Team (2018). *NIST Atomic Spectra Database* (ver. 5.6.1), [Online]. Available: https://physics.nist.gov/asd [2019, August 5]. National Institute of Standards and Technology, Gaithersburg, MD.

[9]McEachran, R. P., and Stauffer, A. D. *Momentum transfer cross sections for the heavy noble gases*, The European Physical Journal D, 68(6), 153, 2014.

[10]Ramsauer, C. *Über den Wirkungsquerschnitt der Gasmoleküle gegenüber langsamen Elektronen*, Annalen der Physik, 6(64), 513-540, 1921.

[11]Townsend, J. S., and Bailey, V. A., *XCVII. The motion of electrons in gases*, The London, Edinburgh, and Dublin Philosophical Magazine and Journal of Science, 42(252), 873-891, 1921.

[12]Burgers, J. M., *Flow equations for composite gases*, Maryland Univ College Park Inst for Fluid Dynamics and Applied Mathematics, 1969.

Distribution Statement A: Approved for Public Release; Distribution is Unlimited. PA# 19458

Distribution Statement A: Approved for Public Release; Distribution is Unlimited. AFRL-2021-4182

Potential Energy and Angular Momentum Conservation in Particle Merging and Collision Models

ROBERT MARTIN
AEROSPACE SYSTEMS DIRECTORATE, 9/24/2019

THE AIR FORCE RESEARCH LABORATORY

Distribution Statement A: Approved for Public Release; Distribution is Unlimited. PA# 19485

Distribution Statement A: Approved for Public Release; Distribution is Unlimited. AFRL-2021-4182

Outline

Hall Thruster Transport Modeling

Conservation in Particle Merging

DSMC & Angular Momentum

Conclusion and Future Work

Distribution Statement A: Approved for Public Release; Distribution is Unlimited. PA# 19485

Distribution Statement A: Approved for Public Release; Distribution is Unlimited. AFRL-2021-4182

Hall Effect Thrusters

Particle-in-Cell (PIC) Simulations:

- Traditionally Modeled in R-Z
- Named for Hall Current in θ
- Uses Quasi-1D Electron Fluid Solve
- Ohm's Law $\rightarrow$ No e^--momentum

RZ-Plane Simulation

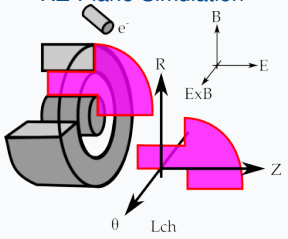

Distribution Statement A: Approved for Public Release; Distribution is Unlimited. PA# 19485

Distribution Statement A: Approved for Public Release; Distribution is Unlimited. AFRL-2021-4182

Hall Effect Thrusters

Particle-in-Cell (PIC) Simulations:

- Traditionally Modeled in R-Z
- Named for Hall Current in θ
- Uses Quasi-1D Electron Fluid Solve
- Ohm's Law $\rightarrow$ No e^--momentum
- Zθ Unrolled to YZ

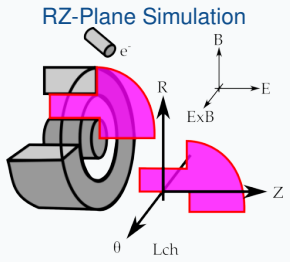

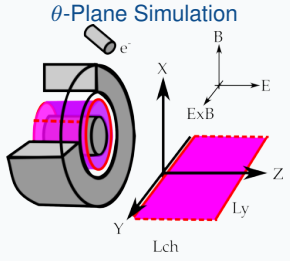

Distribution Statement A: Approved for Public Release; Distribution is Unlimited. PA# 19485

Distribution Statement A: Approved for Public Release; Distribution is Unlimited. AFRL-2021-4182

Hall Effect Thrusters

Particle-in-Cell (PIC) Simulations:

- Traditionally Modeled in R-Z
- Named for Hall Current in θ
- Uses Quasi-1D Electron Fluid Solve
- Ohm's Law $\rightarrow$ No e^--momentum
- Zθ Unrolled to YZ
- Electron ExB Drift
- Unmagnetized Ions
- Results in Hall Current (Namesake)

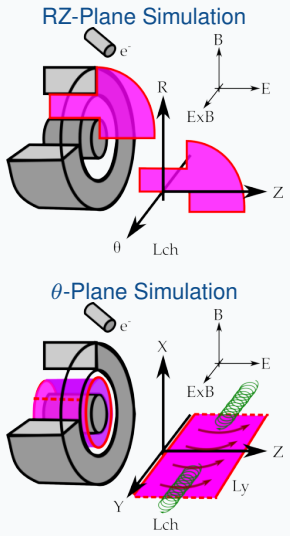

Distribution Statement A: Approved for Public Release; Distribution is Unlimited. PA# 19485

Distribution Statement A: Approved for Public Release; Distribution is Unlimited. AFRL-2021-4182

Hall Effect Thrusters

Particle-in-Cell (PIC) Simulations:

- Traditionally Modeled in R-Z
- Named for Hall Current in θ
- Uses Quasi-1D Electron Fluid Solve
- Ohm's Law $\rightarrow$ No e^--momentum
- Zθ Unrolled to YZ
- Electron ExB Drift
- Unmagnetized Ions
- Results in Hall Current (Namesake)
- Classic Mobility: e^--Neutral Collision
- Electrons Mobility Required for Current

RZ-Plane Simulation

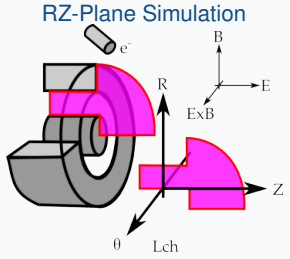

θ-Plane Simulation

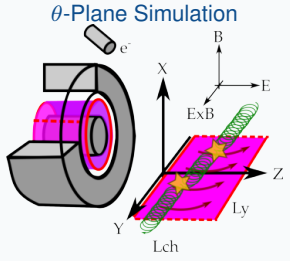

Distribution Statement A: Approved for Public Release; Distribution is Unlimited. PA# 19485

Distribution Statement A: Approved for Public Release; Distribution is Unlimited. AFRL-2021-4182

Hall Effect Thrusters

Particle-in-Cell (PIC) Simulations:

- Traditionally Modeled in R-Z
- Named for Hall Current in θ
- Uses Quasi-1D Electron Fluid Solve
- Ohm's Law $\rightarrow$ No e^--momentum
- Zθ Unrolled to YZ
- Electron ExB Drift
- Unmagnetized Ions
- Results in Hall Current (Namesake)
- Classic Mobility: e^--Neutral Collision
- Electrons Mobility Required for Current
- Ion-Acoustic Waves: Collisionless Mobility?

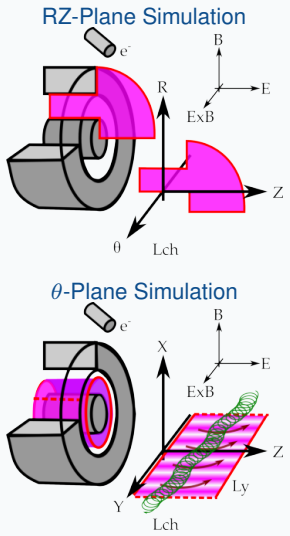

Distribution Statement A: Approved for Public Release; Distribution is Unlimited. PA# 19485

Distribution Statement A: Approved for Public Release; Distribution is Unlimited. AFRL-2021-4182

Impact of Mobility

Model Predictions Sensitive to Mobility:

- Classical Mobility Insufficient in Near Plume

From LaFleur,Phys Plasmas 23, 053503 (2016)

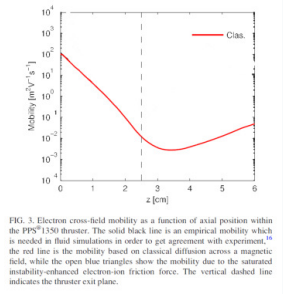

FIG. 3. Electron cross-field mobility as a function of axial position within the PPS®1350 thruster. The solid black line is an empirical mobility which is needed in fluid simulations in order to get agreement with experiment,[16] the red line is the mobility based on classical diffusion across a magnetic field, while the open blue triangles show the mobility due to the saturated instability-enhanced electron-ion friction force. The vertical dashed line indicates the thruster exit plane.

(Thruster Simulation will not “Light”)

Distribution Statement A: Approved for Public Release; Distribution is Unlimited. PA# 19485

Distribution Statement A: Approved for Public Release; Distribution is Unlimited. AFRL-2021-4182

AFRL

Impact of Mobility

Model Predictions Sensitive to Mobility:

- Classical Mobility Insufficient in Near Plume
- Enhanced Emperical “Bohm” (1/B) Mobility
- Also Needs Coefficient by “Zone” (i.e. Anode/Channel/Plume Regions)

From LaFleur,Phys Plasmas 23, 053503 (2016)

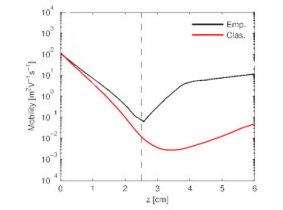

FIG. 3. Electron cross-field mobility as a function of axial position within the PPS®1350 thruster. The solid black line is an empirical mobility which is needed in fluid simulations in order to get agreement with experiment,[16] the red line is the mobility based on classical diffusion across a magnetic field, while the open blue triangles show the mobility due to the saturated instability-enhanced electron-ion friction force. The vertical dashed line indicates the thruster exit plane.

Impact of Mobility on Discharge Profile

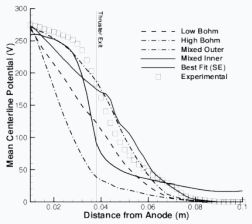

(Koo, PhD Dissertation)

THE AIR FORCE RESEARCH LABORATORY

Distribution Statement A: Approved for Public Release; Distribution is Unlimited. PA# 19485

Distribution Statement A: Approved for Public Release; Distribution is Unlimited. AFRL-2021-4182

Impact of Mobility

Model Predictions Sensitive to Mobility:

- Classical Mobility Insufficient in Near Plume
- Enhanced Emperical “Bohm” (1/B) Mobility
- Also Needs Coefficient by “Zone”
  (i.e. Anode/Channel/Plume Regions)
- Behavior Sensitive to Plume Coefficient

Critical Near Mode Changes

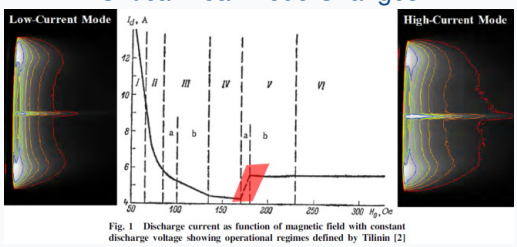

Fig. 1 Discharge current as function of magnetic field with constant discharge voltage showing operational regimes defined by Tilinin [2]

Sekerak, Gallimore, Brown, Hofer, and Polk, JPP 2016

Brown, Lobbia, and Blakely, JPC 2014

Impact of Mobility on Discharge Profile

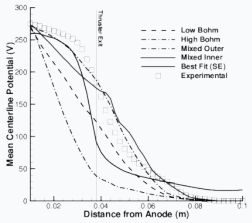

(Koo, PhD Dissertation)

Distribution Statement A: Approved for Public Release; Distribution is Unlimited. PA# 19485

Distribution Statement A: Approved for Public Release; Distribution is Unlimited. AFRL-2021-4182

Impact of Mobility

Model Predictions Sensitive to Mobility:

- Classical Mobility Insufficient in Near Plume
- Enhanced Emperical “Bohm” (1/B) Mobility
- Also Needs Coefficient by “Zone”
  (i.e. Anode/Channel/Plume Regions)
- Behavior Sensitive to Plume Coefficient

Thruster Predictions Currently Depend on
Emperically Tuned Parameters

Critical Near Mode Changes

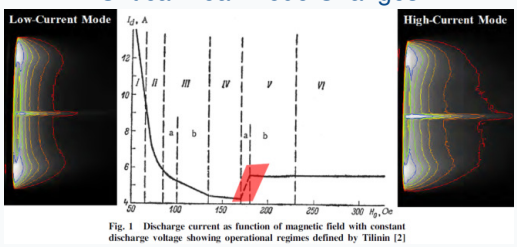

Fig. 1 Discharge current as function of magnetic field with constant discharge voltage showing operational regimes defined by Tilinin [2]

Sekerak, Gallimore, Brown, Hofer, and Polk, JPP 2016

Brown, Lobbia, and Blakely, JPC 2014

Impact of Mobility on Discharge Profile

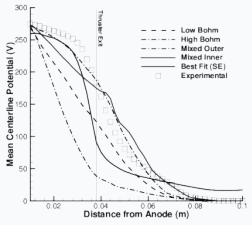

(Koo, PhD Dissertation)

Distribution Statement A: Approved for Public Release; Distribution is Unlimited. PA# 19485

Distribution Statement A: Approved for Public Release; Distribution is Unlimited. AFRL-2021-4182

Impact of Mobility

Model Predictions Sensitive to Mobility:

- Classical Mobility Insufficient in Near Plume
- Enhanced Emperical “Bohm” (1/B) Mobility
- Also Needs Coefficient by “Zone”
  (i.e. Anode/Channel/Plume Regions)
- Behavior Sensitive to Plume Coefficient

Thruster Predictions Currently Depend on
Emperically Tuned Parameters

Goal: Develop Predictive Physical Models for Anomalous Transport

Critical Near Mode Changes

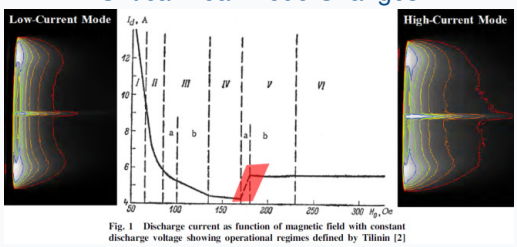

Fig. 1 Discharge current as function of magnetic field with constant discharge voltage showing operational regimes defined by Tilinin [2]

Sekerak, Gallimore, Brown, Hofer, and Polk, JPP 2016

Brown, Lobbia, and Blakely, JPC 2014

Impact of Mobility on Discharge Profile

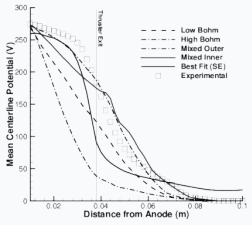

(Koo, PhD Dissertation)

Distribution Statement A: Approved for Public Release; Distribution is Unlimited. PA# 19485

Distribution Statement A: Approved for Public Release; Distribution is Unlimited. AFRL-2021-4182

AFRL

Collisionless Instability and Transport

Current Driven Instability:

- HET Ion-Acoustic Instability
  -Driven by j_θ Hall Current
  -Anomalous e-Transport? (LaFleur)
  -Focus of 1D/2D Full-PIC Studies

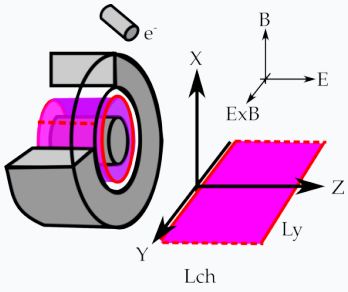

Distribution Statement A: Approved for Public Release; Distribution is Unlimited. PA# 19485

Distribution Statement A: Approved for Public Release; Distribution is Unlimited. AFRL-2021-4182

Collisionless Instability and Transport

Current Driven Instability:

- HET Ion-Acoustic Instability
  -Driven by j_θ Hall Current
  -Anomalous e-Transport? (LaFleur)
  -Focus of 1D/2D Full-PIC Studies
- $\langle \Delta n_e, \Delta E_\theta \rangle \rightarrow$ Axial Transport
  Initial Exponential Growth Saturates

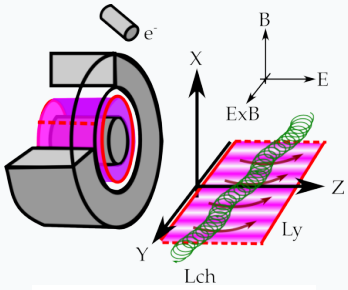

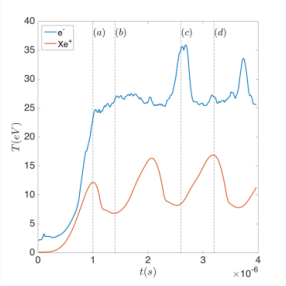

Distribution Statement A: Approved for Public Release; Distribution is Unlimited. PA# 19485

Distribution Statement A: Approved for Public Release; Distribution is Unlimited. AFRL-2021-4182

Collisionless Instability and Transport

Current Driven Instability:

- HET Ion-Acoustic Instability
  -Driven by j_θ Hall Current
  -Anomalous e-Transport? (LaFleur)
  -Focus of 1D/2D Full-PIC Studies
- $\langle \Delta n_e, \Delta E_\theta \rangle \rightarrow$ Axial Transport
  Initial Exponential Growth Saturates
- Electrons Heat & Ions Steepen/Trap

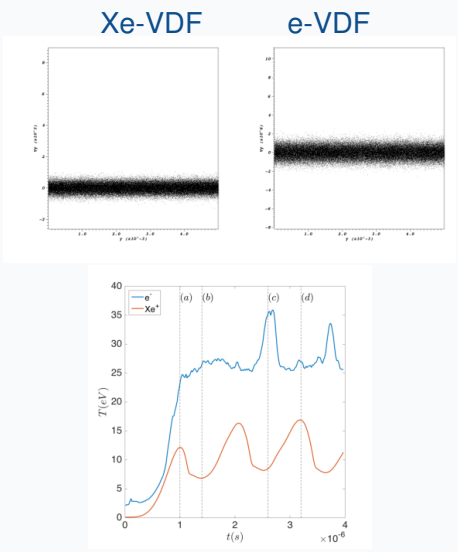

Distribution Statement A: Approved for Public Release; Distribution is Unlimited. PA# 19485

Distribution Statement A: Approved for Public Release; Distribution is Unlimited. AFRL-2021-4182

Collisionless Instability and Transport

Current Driven Instability:

- HET Ion-Acoustic Instability
  -Driven by j_θ Hall Current
  -Anomalous e-Transport? (LaFleur)
  -Focus of 1D/2D Full-PIC Studies
- $\langle \Delta n_e, \Delta E_\theta \rangle \rightarrow$ Axial Transport
  Initial Exponential Growth Saturates
- Electrons Heat & Ions Steepen/Trap
- Ion Wave breaks above C_s

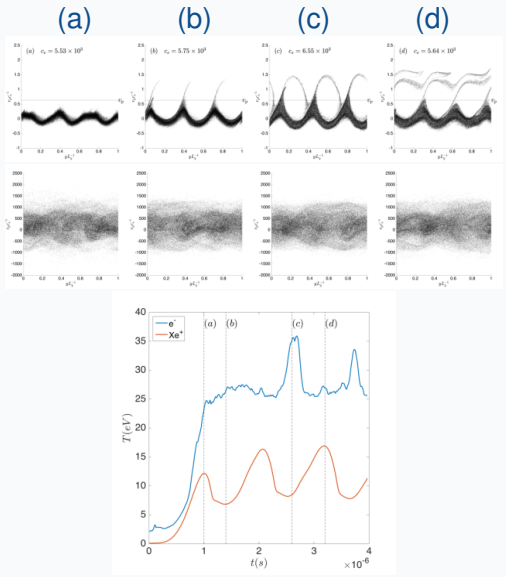

Distribution Statement A: Approved for Public Release; Distribution is Unlimited. PA# 19485

Distribution Statement A: Approved for Public Release; Distribution is Unlimited. AFRL-2021-4182

Collisionless Instability and Transport

Current Driven Instability:

- HET Ion-Acoustic Instability
  -Driven by j_θ Hall Current
  -Anomalous e-Transport? (LaFleur)
  -Focus of 1D/2D Full-PIC Studies
- $\langle \Delta n_e, \Delta E_\theta \rangle \rightarrow$ Axial Transport
  Initial Exponential Growth Saturates
- Electrons Heat & Ions Steepen/Trap
- Ion Wave breaks above C_s
- Waves not “Turbulence”?...

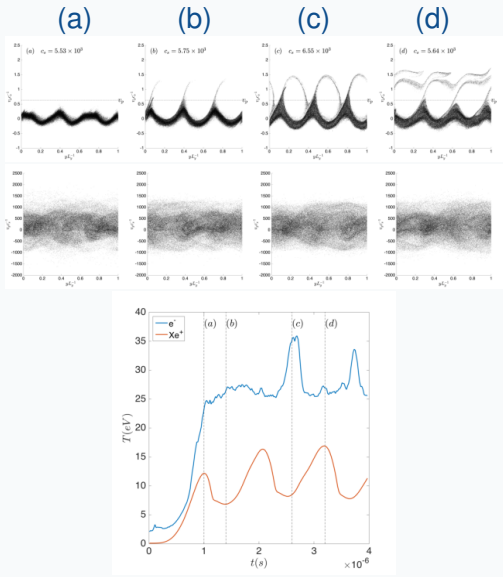

Distribution Statement A: Approved for Public Release; Distribution is Unlimited. PA# 19485

Distribution Statement A: Approved for Public Release; Distribution is Unlimited. AFRL-2021-4182

AFRL

Collisionless Instability and Transport

Current Driven Instability:

- HET Ion-Acoustic Instability
  -Driven by j_θ Hall Current
  -Anomalous e-Transport? (LaFleur)
  -Focus of 1D/2D Full-PIC Studies
- $\langle \Delta n_e, \Delta E_\theta \rangle \rightarrow$ Axial Transport
  Initial Exponential Growth Saturates
- Electrons Heat & Ions Steepen/Trap
- Ion Wave breaks above C_s
- Waves not “Turbulence”?...
- Kinetic Ions, but Electrons Near Fluid?

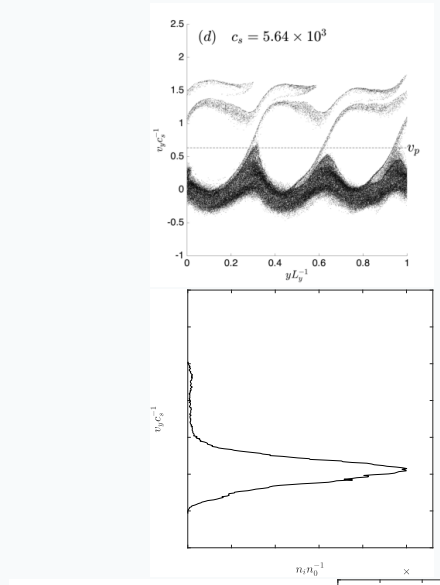

THE AIR FORCE RESEARCH LABORATORY

Distribution Statement A: Approved for Public Release; Distribution is Unlimited. PA# 19485

Distribution Statement A: Approved for Public Release; Distribution is Unlimited. AFRL-2021-4182

AFRL

Collisionless Instability and Transport

Current Driven Instability:

- HET Ion-Acoustic Instability
  -Driven by j_θ Hall Current
  -Anomalous e-Transport? (LaFleur)
  -Focus of 1D/2D Full-PIC Studies
- $\langle \Delta n_e, \Delta E_\theta \rangle \rightarrow$ Axial Transport
  Initial Exponential Growth Saturates
- Electrons Heat & Ions Steepen/Trap
- Ion Wave breaks above C_s
- Waves not “Turbulence”?...
- Kinetic Ions, but Electrons Near Fluid?

Goal: Find Impact of Coulomb Collisions on Anomalous Transport

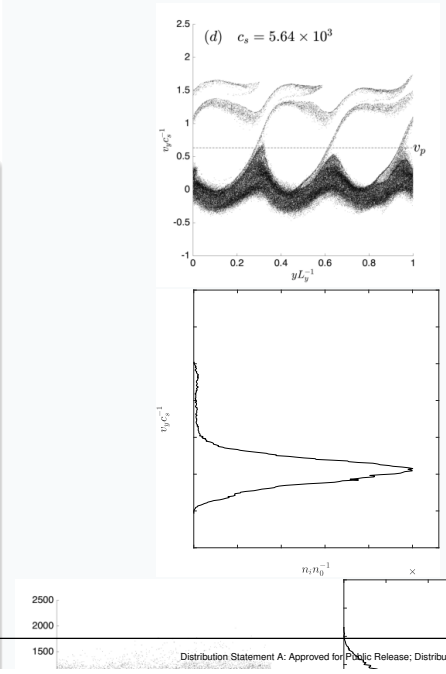

Distribution Statement A: Approved for Public Release; Distribution is Unlimited. PA# 19485

Distribution Statement A: Approved for Public Release; Distribution is Unlimited. AFRL-2021-4182

AFRL

Collisionless Instability and Transport

Current Driven Instability:

- HET Ion-Acoustic Instability
  -Driven by j_θ Hall Current
  -Anomalous e-Transport? (LaFleur)
  -Focus of 1D/2D Full-PIC Studies
- $\langle \Delta n_e, \Delta E_\theta \rangle \rightarrow$ Axial Transport
  Initial Exponential Growth Saturates
- Electrons Heat & Ions Steepen/Trap
- Ion Wave breaks above C_s
- Waves not "Turbulence"?...
- Kinetic Ions, but Electrons Near Fluid?

Goal: Find Impact of Coulomb Collisions on Anomalous Transport
Challenge: Nanbu DSMC Coulomb Collisions $\rightarrow$ Rapid Heating
High $T_e > T_e^{exp}$ makes $\lambda_{Debye} > L_y$ & Suppresses Ion-Wave

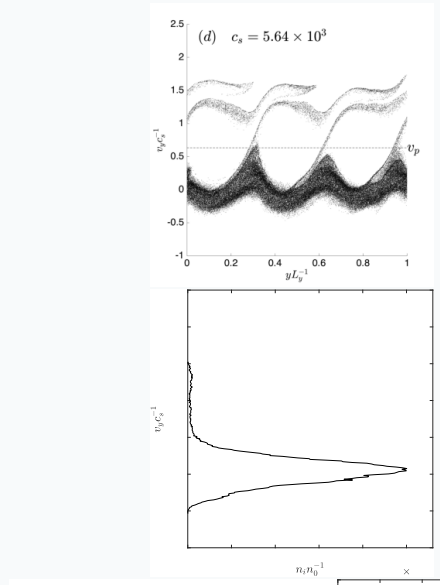

Distribution Statement A: Approved for Public Release; Distribution is Unlimited. PA# 19485

Distribution Statement A: Approved for Public Release; Distribution is Unlimited. AFRL-2021-4182

Numerical Heating

Impact of Collisions on PIC Heating

- Explicit PIC Simulations Naturally Heat
  Stochastic Noise $\rightarrow$ Field Energy $\rightarrow$ Heating

Distribution Statement A: Approved for Public Release; Distribution is Unlimited. PA# 19485

Distribution Statement A: Approved for Public Release; Distribution is Unlimited. AFRL-2021-4182

Numerical Heating

Impact of Collisions on PIC Heating

- Explicit PIC Simulations Naturally Heat
  Stochastic Noise $\rightarrow$ Field Energy $\rightarrow$ Heating
- Collision Models Can Further Exacerbate this Issue

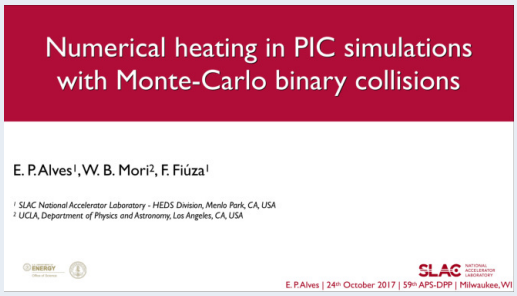

Distribution Statement A: Approved for Public Release; Distribution is Unlimited. PA# 19485

Distribution Statement A: Approved for Public Release; Distribution is Unlimited. AFRL-2021-4182

Numerical Heating

Impact of Collisions on PIC Heating

- Explicit PIC Simulations Naturally Heat
  Stochastic Noise → Field Energy → Heating
- Collision Models Can Further Exacerbate this Issue
- Issue Highlighted at 2017 APS DPP Talk by Alves et. al.

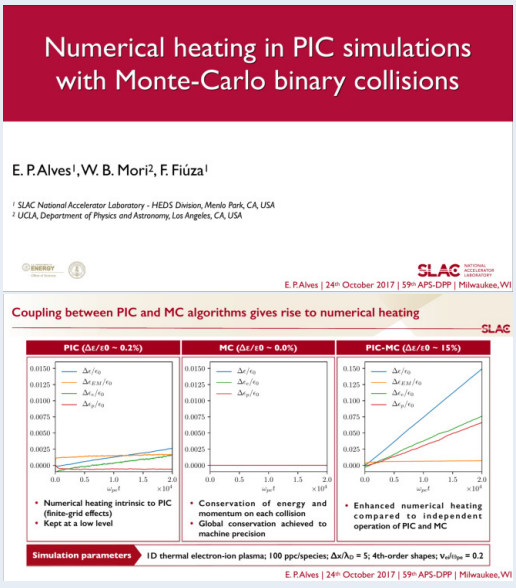

Distribution Statement A: Approved for Public Release; Distribution is Unlimited. PA# 19485

Distribution Statement A: Approved for Public Release; Distribution is Unlimited. AFRL-2021-4182

Numerical Heating

Impact of Collisions on PIC Heating

- Explicit PIC Simulations Naturally Heat
  Stochastic Noise → Field Energy → Heating
- Collision Models Can Further Exacerbate this Issue
- Issue Highlighted at 2017 APS DPP Talk by Alves et. al.
- Binary Collisions Dramatically Enhanced Numerical Heating
  Final Analysis of Scaling and Mitigation Currently still Pending

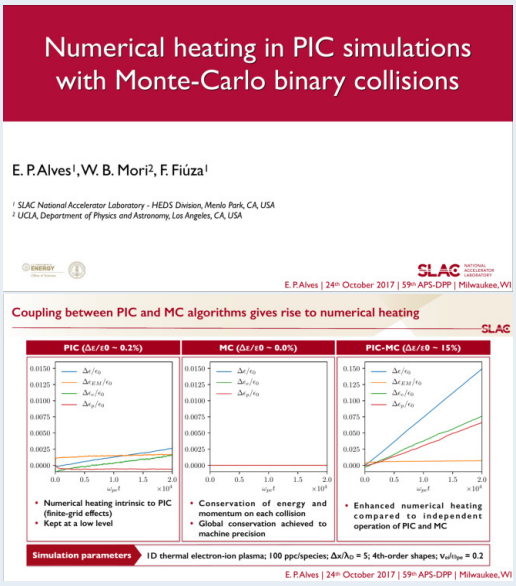

Distribution Statement A: Approved for Public Release; Distribution is Unlimited. PA# 19485

Distribution Statement A: Approved for Public Release; Distribution is Unlimited. AFRL-2021-4182

Numerical Heating

Impact of Collisions on PIC Heating

- Explicit PIC Simulations Naturally Heat
  Stochastic Noise $\rightarrow$ Field Energy $\rightarrow$ Heating
- Collision Models Can Further Exacerbate this Issue
- Issue Highlighted at 2017 APS DPP Talk by Alves et. al.
- Binary Collisions Dramatically Enhanced Numerical Heating
  Final Analysis of Scaling and Mitigation Currently still Pending
- Reminded of DSMC13 Presentation on Conservative Merging

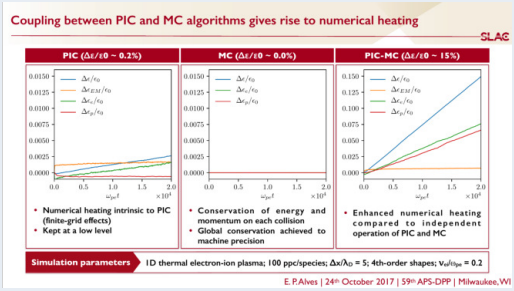

Distribution Statement A: Approved for Public Release; Distribution is Unlimited. PA# 19485

Distribution Statement A: Approved for Public Release; Distribution is Unlimited. AFRL-2021-4182

Numerical Heating

Impact of Collisions on PIC Heating

- Explicit PIC Simulations Naturally Heat
  Stochastic Noise $\rightarrow$ Field Energy $\rightarrow$ Heating
- Collision Models Can Further Exacerbate this Issue
- Issue Highlighted at 2017 APS DPP Talk by Alves et. al.
- Binary Collisions Dramatically Enhanced Numerical Heating
  Final Analysis of Scaling and Mitigation Currently still Pending
- Reminded of DSMC13 Presentation on Conservative Merging
- Particularly with Respect to High-Order Potential/Particle Shape

VS.

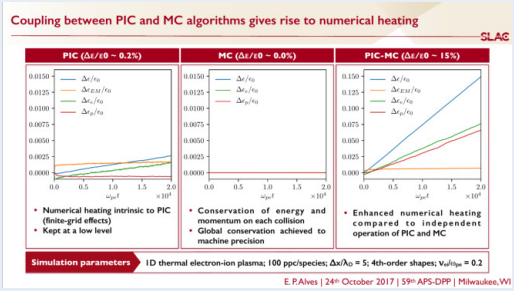

Distribution Statement A: Approved for Public Release; Distribution is Unlimited. PA# 19485

Distribution Statement A: Approved for Public Release; Distribution is Unlimited. AFRL-2021-4182

Numerical Heating

Impact of Collisions on PIC Heating

- Explicit PIC Simulations Naturally Heat
  Stochastic Noise $\rightarrow$ Field Energy $\rightarrow$ Heating
- Collision Models Can Further Exacerbate this Issue
- Issue Highlighted at 2017 APS DPP Talk by Alves et. al.
- Binary Collisions Dramatically Enhanced Numerical Heating
  Final Analysis of Scaling and Mitigation Currently still Pending
- Reminded of DSMC13 Presentation on Conservative Merging
- Particularly with Respect to High-Order Potential/Particle Shape

Next: Recap on Conservation Analysis for Particle Merge

VS.

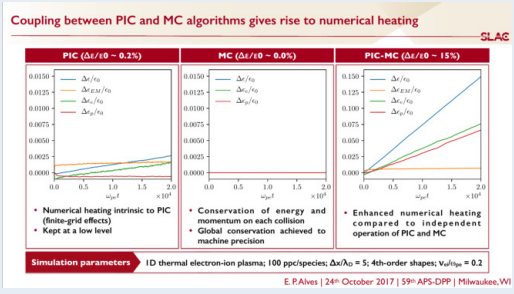

Distribution Statement A: Approved for Public Release; Distribution is Unlimited. PA# 19485

Distribution Statement A: Approved for Public Release; Distribution is Unlimited. AFRL-2021-4182

AFRL

Motivation for Merge Spherical Test Case

Parabolic Test is Insufficient

- Conserving $\mathrm{tr}(v^2)$ important due to collisional invariance
- Original Scheme also Conserved $\mathrm{tr}(x^2)$... Important?

Distribution Statement A: Approved for Public Release; Distribution is Unlimited. PA# 19485

Distribution Statement A: Approved for Public Release; Distribution is Unlimited. AFRL-2021-4182

Motivation for Merge Spherical Test Case

Parabolic Test is Insufficient

- Conserving $\mathrm{tr}(v^2)$ important due to collisional invariance
- Original Scheme also Conserved $\mathrm{tr}(x^2)$... Important?
- Potential Energy Conservation via Taylor Expansion

$$\overline{\Phi} = \frac{\sum_p^k w^{(p)} \left[\Phi(\overline{x_i}) + \left.\frac{\partial \Phi}{\partial x_i}\right|_{\overline{x_i}} (x_i^{(p)} - \overline{x_i}) + \frac{1}{2} \left.\frac{\partial^2 \Phi}{\partial x_i \partial x_j}\right|_{\overline{x_i}} (x_i^{(p)} - \overline{x_i})(x_j^{(p)} - \overline{x_j}) \right]}{\sum_p^k w^{(p)}} + O\left(\Delta x^3 \Big|_{\max} \right)$$

$$= \Phi(\overline{x_i}) + \left.\frac{\partial^2 \Phi}{\partial x_i \partial x_j}\right|_{\overline{x_i}} \frac{\sum_p^k w^{(p)} \left[(x_i^{(p)} - \overline{x_i})(x_j^{(p)} - \overline{x_j}) \right]}{\sum_p^k w^{(p)}} + O\left(\Delta x^3 \Big|_{\max} \right)$$

Distribution Statement A: Approved for Public Release; Distribution is Unlimited. PA# 19485

Distribution Statement A: Approved for Public Release; Distribution is Unlimited. AFRL-2021-4182

Motivation for Merge Spherical Test Case

Parabolic Test is Insufficient

- Conserving $\mathrm{tr}(v^2)$ important due to collisional invariance
- Original Scheme also Conserved $\mathrm{tr}(x^2)$... Important?
- Potential Energy Conservation via Taylor Expansion
- $O\left(\Delta x^2\big|_{\max}\right)$ Energy Conservation Requires Center of Mass, $\overline{x_i}$, Only

$$\overline{\Phi} = \frac{\sum_p^k w^{(p)}\left[\Phi(\overline{x_i}) + \frac{\partial \Phi}{\partial x_i}\Big|_{\overline{x_i}}(x_i^{(p)} - \overline{x_i}) + \frac{1}{2}\frac{\partial^2 \Phi}{\partial x_i \partial x_j}\Big|_{\overline{x_i}}(x_i^{(p)} - \overline{x_i})(x_j^{(p)} - \overline{x_j})\right]}{\sum_p^k w^{(p)}} + O\left(\Delta x^3\big|_{\max}\right)$$

$$= \Phi(\overline{x_i}) + \frac{\partial^2 \Phi}{\partial x_i \partial x_j}\Big|_{\overline{x_i}} \frac{\sum_p^k w^{(p)}\left[(x_i^{(p)} - \overline{x_i})(x_j^{(p)} - \overline{x_j})\right]}{\sum_p^k w^{(p)}} + O\left(\Delta x^3\big|_{\max}\right)$$

Distribution Statement A: Approved for Public Release; Distribution is Unlimited. PA# 19485

Distribution Statement A: Approved for Public Release; Distribution is Unlimited. AFRL-2021-4182

AFRL

Motivation for Merge Spherical Test Case

Parabolic Test is Insufficient

- Conserving $\mathrm{tr}(v^2)$ important due to collisional invariance
- Original Scheme also Conserved $\mathrm{tr}(x^2)$... Important?
- Potential Energy Conservation via Taylor Expansion
- $O\left(\Delta x^2\big|_{\max}\right)$ Energy Conservation Requires Center of Mass, $\overline{x_i}$, Only
- Next Order? Requires Full $(x_i^{(p)}-\overline{x_i})(x_j^{(p)}-\overline{x_j})$ Tensor for Arbitrary Φ

$$\overline{\Phi} = \frac{\sum_p^k w^{(p)}\left[\Phi(\overline{x_i})+\left.\frac{\partial\Phi}{\partial x_i}\right|_{\overline{x_i}}(x_i^{(p)}-\overline{x_i})+\frac{1}{2}\left.\frac{\partial^2\Phi}{\partial x_i\partial x_j}\right|_{\overline{x_i}}(x_i^{(p)}-\overline{x_i})(x_j^{(p)}-\overline{x_j})\right]}{\sum_p^k w^{(p)}}+O\left(\Delta x^3\big|_{\max}\right)$$

$$= \Phi(\overline{x_i})+\left.\frac{\partial^2\Phi}{\partial x_i\partial x_j}\right|_{\overline{x_i}}\frac{\sum_p^k w^{(p)}\left[(x_i^{(p)}-\overline{x_i})(x_j^{(p)}-\overline{x_j})\right]}{\sum_p^k w^{(p)}}+O\left(\Delta x^3\big|_{\max}\right)$$

Distribution Statement A: Approved for Public Release; Distribution is Unlimited. PA# 19485

Distribution Statement A: Approved for Public Release; Distribution is Unlimited. AFRL-2021-4182

Motivation for Merge Spherical Test Case

Parabolic Test is Insufficient

- Conserving $\mathrm{tr}(v^2)$ important due to collisional invariance
- Original Scheme also Conserved $\mathrm{tr}(x^2)$... Important?
- Potential Energy Conservation via Taylor Expansion
- $O\left(\Delta x^2\big|_{\max}\right)$ Energy Conservation Requires Center of Mass, $\overline{x_i}$, Only
- Next Order? Requires Full $(x_i^{(p)}-\overline{x_i})(x_j^{(p)}-\overline{x_j})$ Tensor for Arbitrary Φ
- But Parabolic Potential $\rightarrow$ Diagonal Hessian!
- $\therefore$ Accidental Exact Potential Conservation via Diagonal 2^{nd} Moment Cons.

$$\overline{\Phi} = \frac{\sum_p^k w^{(p)}\left[\Phi(\overline{x_i})+\left.\frac{\partial\Phi}{\partial x_i}\right|_{\overline{x_i}}(x_i^{(p)}-\overline{x_i})+\frac{1}{2}\left.\frac{\partial^2\Phi}{\partial x_i\partial x_j}\right|_{\overline{x_i}}(x_i^{(p)}-\overline{x_i})(x_j^{(p)}-\overline{x_j})\right]}{\sum_p^k w^{(p)}}+O\left(\Delta x^3\big|_{\max}\right)$$

$$= \Phi(\overline{x_i})+\left.\frac{\partial^2\Phi}{\partial x_i\partial x_j}\right|_{\overline{x_i}}\frac{\sum_p^k w^{(p)}\left[(x_i^{(p)}-\overline{x_i})(x_j^{(p)}-\overline{x_j})\right]}{\sum_p^k w^{(p)}}+O\left(\Delta x^3\big|_{\max}\right)$$

Distribution Statement A: Approved for Public Release; Distribution is Unlimited. PA# 19485

Distribution Statement A: Approved for Public Release; Distribution is Unlimited. AFRL-2021-4182

AFRL

Spherical Test Case

Increased Complexity of Spherical Potential

- Spherical Potential: $\Phi \propto 1/r$

Without Merge & Split

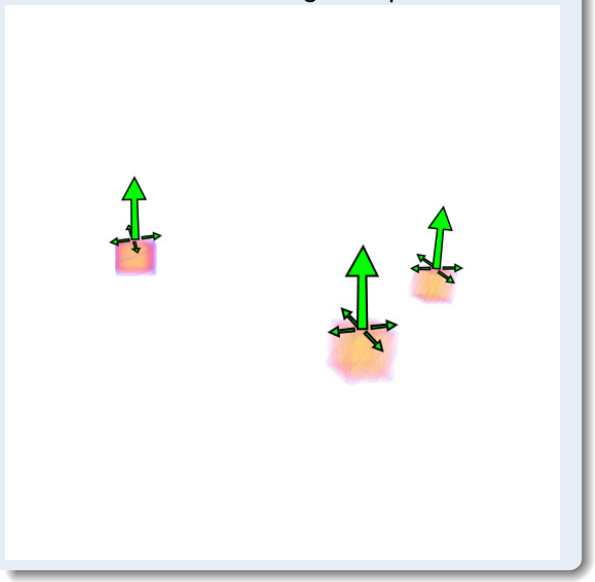

Distribution Statement A: Approved for Public Release; Distribution is Unlimited. PA# 19485

Distribution Statement A: Approved for Public Release; Distribution is Unlimited. AFRL-2021-4182

Spherical Test Case

Increased Complexity of Spherical Potential

- Spherical Potential: $\Phi \propto 1/r$
- Slight $\Delta X \rightarrow$ Orbits Unsynchronized

Without Merge & Split

Distribution Statement A: Approved for Public Release; Distribution is Unlimited. PA# 19485

Distribution Statement A: Approved for Public Release; Distribution is Unlimited. AFRL-2021-4182

Spherical Test Case

Increased Complexity of Spherical Potential

- Spherical Potential: $\Phi \propto 1/r$
- Slight $\Delta X \rightarrow$ Orbits Unsynchronized
- Periods Synched via Orbital Mechanics

Without Merge & Split

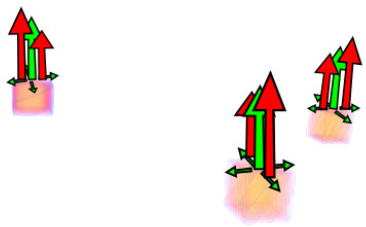

Distribution Statement A: Approved for Public Release; Distribution is Unlimited. PA# 19485

Distribution Statement A: Approved for Public Release; Distribution is Unlimited. AFRL-2021-4182

AFRL

Spherical Test Case

Increased Complexity of Spherical Potential

- Spherical Potential: $\Phi \propto 1/r$
- Slight $\Delta X \rightarrow$ Orbits Unsynchronized
- Periods Synched via Orbital Mechanics
- Periodic with Full Nonlinear-C.N. Push

Without Merge & Split

Distribution Statement A: Approved for Public Release; Distribution is Unlimited. PA# 19485

Distribution Statement A: Approved for Public Release; Distribution is Unlimited. AFRL-2021-4182

AFRL

Spherical Test Case

Increased Complexity of Spherical Potential

- Spherical Potential: $\Phi \propto 1/r$
- Slight $\Delta X \rightarrow$ Orbits Unsynchronized
- Periods Synched via Orbital Mechanics
- Periodic with Full Nonlinear-C.N. Push
- Adding Merge & Split:
  Energy Conservation OK
  Accuracy: Scatter + Dispersion?

Including Merge & Split

Distribution Statement A: Approved for Public Release; Distribution is Unlimited. PA# 19485

Distribution Statement A: Approved for Public Release; Distribution is Unlimited. AFRL-2021-4182

Spherical Test Case

Increased Complexity of Spherical Potential

- Spherical Potential: $\Phi \propto 1/r$
- Slight $\Delta X \rightarrow$ Orbits Unsynchronized
- Periods Synched via Orbital Mechanics
- Periodic with Full Nonlinear-C.N. Push
- Adding Merge & Split:
  Energy Conservation OK
  Accuracy: Scatter + Dispersion?

Source of Dispersion?

Including Merge & Split

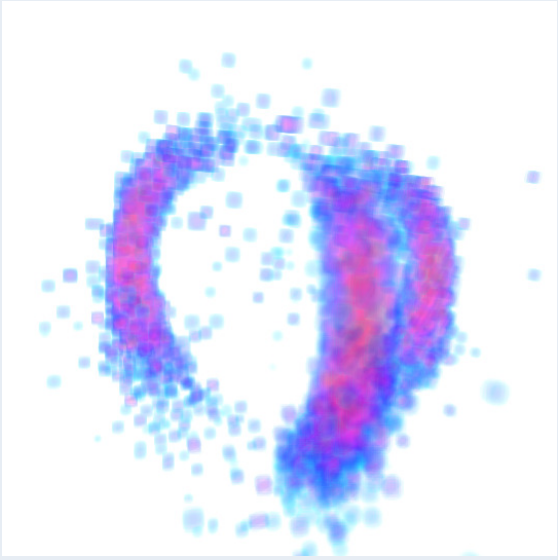

Distribution Statement A: Approved for Public Release; Distribution is Unlimited. PA# 19485

Distribution Statement A: Approved for Public Release; Distribution is Unlimited. AFRL-2021-4182

AFRL

Dispersion from Incomplete 2^{nd} Moment?

$O(\Delta x_{cell}^3)$ Potential Conservation:

- Remap must Preserve Identical Contraction, $\partial_i \partial_j \Phi : \overline{\Delta x_i \Delta x_j}$

$$\begin{bmatrix} \Phi_{xx} & \Phi_{xy} & \Phi_{xz} \\ \Phi_{yx} & \Phi_{yy} & \Phi_{yz} \\ \Phi_{zx} & \Phi_{zy} & \Phi_{zz} \end{bmatrix} : \begin{bmatrix} \overline{\Delta x \Delta x} & \overline{\Delta x \Delta y} & \overline{\Delta x \Delta z} \\ \overline{\Delta y \Delta x} & \overline{\Delta y \Delta y} & \overline{\Delta y \Delta z} \\ \overline{\Delta z \Delta x} & \overline{\Delta z \Delta y} & \overline{\Delta z \Delta z} \end{bmatrix}$$

Distribution Statement A: Approved for Public Release; Distribution is Unlimited. PA# 19485

Distribution Statement A: Approved for Public Release; Distribution is Unlimited. AFRL-2021-4182

Dispersion from Incomplete 2^{nd} Moment?

$O(\Delta x_{cell}^3)$ Potential Conservation:

- Remap must Preserve Identical Contraction, $\partial_i \partial_j \Phi : \overline{\Delta x_i \Delta x_j}$
- 2-Particle Only Reproduces Diagonal with $x_i^{(a/b)} = \overline{x_i} \pm \epsilon_i$ if $\epsilon_i = \overline{\Delta x_i^2}^{1/2}$

$$\begin{bmatrix} \overline{\Delta x \Delta x} & \overline{\Delta x \Delta y} & \overline{\Delta x \Delta z} \\ \overline{\Delta y \Delta x} & \overline{\Delta y \Delta y} & \overline{\Delta y \Delta z} \\ \overline{\Delta z \Delta x} & \overline{\Delta z \Delta y} & \overline{\Delta z \Delta z} \end{bmatrix} \neq \begin{bmatrix} \epsilon_x \epsilon_x & \epsilon_x \epsilon_y & \epsilon_x \epsilon_z \\ \epsilon_y \epsilon_x & \epsilon_y \epsilon_y & \epsilon_y \epsilon_z \\ \epsilon_z \epsilon_x & \epsilon_z \epsilon_y & \epsilon_z \epsilon_z \end{bmatrix}$$

Distribution Statement A: Approved for Public Release; Distribution is Unlimited. PA# 19485

Distribution Statement A: Approved for Public Release; Distribution is Unlimited. AFRL-2021-4182

Dispersion from Incomplete 2^{nd} Moment?

$O(\Delta x_{cell}^3)$ Potential Conservation:

- Remap must Preserve Identical Contraction, $\partial_i \partial_j \Phi : \overline{\Delta x_i \Delta x_j}$
- 2-Particle Only Reproduces Diagonal with $x_i^{(a/b)} = \overline{x_i} \pm \epsilon_i$ if $\epsilon_i = \overline{\Delta x_i^2}^{1/2}$
- Non-Degenerate $\overline{\Delta x_i \Delta x_j} \rightarrow$ 3-Eigenvalues

$$\begin{bmatrix} \overline{\Delta x \Delta x} & \overline{\Delta x \Delta y} & \overline{\Delta x \Delta z} \\ \overline{\Delta y \Delta x} & \overline{\Delta y \Delta y} & \overline{\Delta y \Delta z} \\ \overline{\Delta z \Delta x} & \overline{\Delta z \Delta y} & \overline{\Delta z \Delta z} \end{bmatrix} =$$

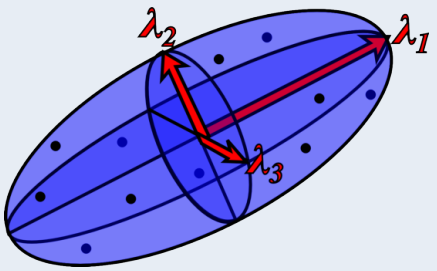

Distribution Statement A: Approved for Public Release; Distribution is Unlimited. PA# 19485

Distribution Statement A: Approved for Public Release; Distribution is Unlimited. AFRL-2021-4182

Dispersion from Incomplete 2^{nd} Moment?

$O(\Delta x_{cell}^3)$ Potential Conservation:

- Remap must Preserve Identical Contraction, $\partial_i \partial_j \Phi : \overline{\Delta x_i \Delta x_j}$
- 2-Particle Only Reproduces Diagonal with $x_i^{(a/b)} = \overline{x_i} \pm \epsilon_i$ if $\epsilon_i = \overline{\Delta x_i^2}^{1/2}$
- Non-Degenerate $\overline{\Delta x_i \Delta x_j} \rightarrow$ 3-Eigenvalues
- Non-Degenerate $\rightarrow$ 4+ Non-Coplanar Particles
  (3-Particles = Plane & $\lambda_3 = 0$; 2-Particles = Line & $\lambda_2, \lambda_3 = 0$)

$$\begin{bmatrix} \overline{\Delta x \Delta x} & \overline{\Delta x \Delta y} & \overline{\Delta x \Delta z} \\ \overline{\Delta y \Delta x} & \overline{\Delta y \Delta y} & \overline{\Delta y \Delta z} \\ \overline{\Delta z \Delta x} & \overline{\Delta z \Delta y} & \overline{\Delta z \Delta z} \end{bmatrix} =$$

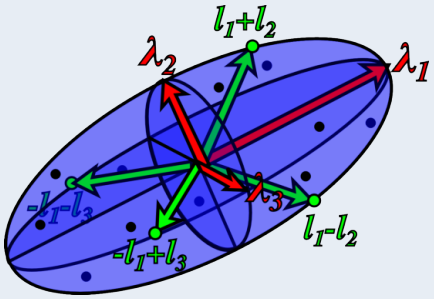

Distribution Statement A: Approved for Public Release; Distribution is Unlimited. PA# 19485

Distribution Statement A: Approved for Public Release; Distribution is Unlimited. AFRL-2021-4182

Dispersion from Incomplete 2^{nd} Moment?

$O(\Delta x_{cell}^3)$ Potential Conservation:

- Remap must Preserve Identical Contraction, $\partial_i \partial_j \Phi : \overline{\Delta x_i \Delta x_j}$
- 2-Particle Only Reproduces Diagonal with $x_i^{(a/b)} = \overline{x_i} \pm \epsilon_i$ if $\epsilon_i = \overline{\Delta x_i^2}^{1/2}$
- Non-Degenerate $\overline{\Delta x_i \Delta x_j} \rightarrow$ 3-Eigenvalues
- Non-Degenerate $\rightarrow$ 4+ Non-Coplanar Particles (3-Particles = Plane & $\lambda_3 = 0$; 2-Particles = Line & $\lambda_2, \lambda_3 = 0$)
- Same $\rightarrow$ 4 Merge for 2^{nd}-Vel. Moment
- "Principal Component Analysis"

$$\begin{bmatrix} \overline{\Delta x \Delta x} & \overline{\Delta x \Delta y} & \overline{\Delta x \Delta z} \\ \overline{\Delta y \Delta x} & \overline{\Delta y \Delta y} & \overline{\Delta y \Delta z} \\ \overline{\Delta z \Delta x} & \overline{\Delta z \Delta y} & \overline{\Delta z \Delta z} \end{bmatrix} =$$

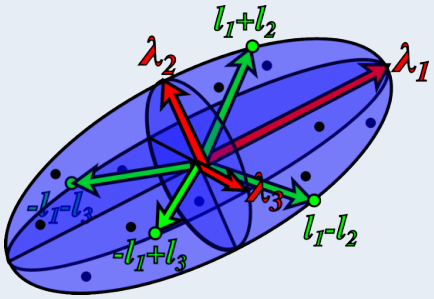

Distribution Statement A: Approved for Public Release; Distribution is Unlimited. PA# 19485

Distribution Statement A: Approved for Public Release; Distribution is Unlimited. AFRL-2021-4182

AFRL

Dispersion from Incomplete 2^{nd} Moment?

$O(\Delta x_{cell}^3)$ Potential Conservation:

- Remap must Preserve Identical Contraction, $\partial_i \partial_j \Phi : \overline{\Delta x_i \Delta x_j}$
- 2-Particle Only Reproduces Diagonal with $x_i^{(a/b)} = \overline{x_i} \pm \epsilon_i$ if $\epsilon_i = \overline{\Delta x_i^2}^{1/2}$
- Non-Degenerate $\overline{\Delta x_i \Delta x_j} \rightarrow$ 3-Eigenvalues
- Non-Degenerate $\rightarrow$ 4+ Non-Coplanar Particles (3-Particles = Plane & $\lambda_3 = 0$; 2-Particles = Line & $\lambda_2, \lambda_3 = 0$)
- Same $\rightarrow$ 4 Merge for 2^{nd}-Vel. Moment
- "Principal Component Analysis"
- Improved but Non-Negligible Scatter and Dispersion

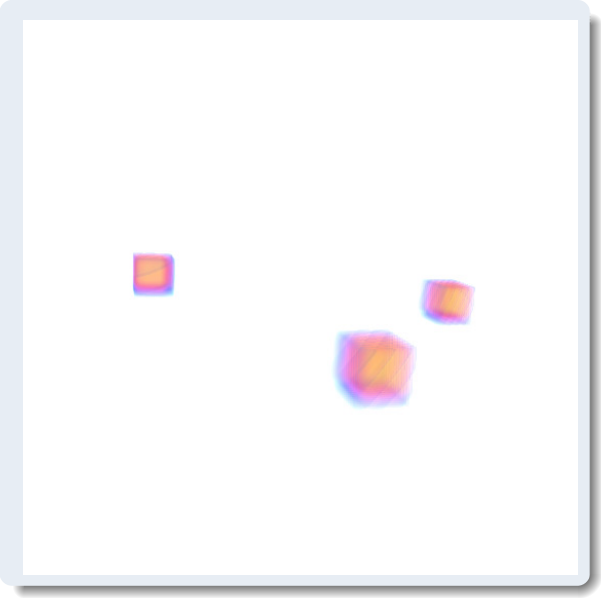

Distribution Statement A: Approved for Public Release; Distribution is Unlimited. PA# 19485

Distribution Statement A: Approved for Public Release; Distribution is Unlimited. AFRL-2021-4182

Dispersion from XV Scatter?

Kinetic Potential Energy Scatter:

- A Closer look at Merge $\rightarrow$ 2
- $\approx$ Match $Sgn\left(\epsilon_i^{(v)}\right)$ to $Sgn(\Delta v_i \Delta v_j)$ Moments
- Select $Sgn\left(\epsilon_i^{(x)}\right)$ to Match $Sgn(\Delta x_i \Delta v_i)$

$$\begin{bmatrix} - & Sgn\left(\epsilon_x^{(v)}\epsilon_y^{(v)}\right) & Sgn\left(\epsilon_x^{(v)}\epsilon_z^{(v)}\right) \\ Sgn\left(\epsilon_y^{(v)}\epsilon_x^{(v)}\right) & - & Sgn\left(\epsilon_y^{(v)}\epsilon_z^{(v)}\right) \\ Sgn\left(\epsilon_z^{(v)}\epsilon_x^{(v)}\right) & Sgn\left(\epsilon_z^{(v)}\epsilon_y^{(v)}\right) & - \end{bmatrix} \approx$$

$$\begin{bmatrix} - & Sgn\left(\overline{\Delta v_x \Delta v_y}\right) & Sgn\left(\overline{\Delta v_x \Delta v_z}\right) \\ Sgn\left(\overline{\Delta v_y \Delta v_x}\right) & - & Sgn\left(\overline{\Delta v_y \Delta v_z}\right) \\ Sgn\left(\overline{\Delta v_z \Delta v_x}\right) & Sgn\left(\overline{\Delta v_z \Delta v_y}\right) & - \end{bmatrix}$$

Distribution Statement A: Approved for Public Release; Distribution is Unlimited. PA# 19485

Distribution Statement A: Approved for Public Release; Distribution is Unlimited. AFRL-2021-4182

Dispersion from XV Scatter?

Kinetic Potential Energy Scatter:

- A Closer look at Merge $\rightarrow 2$
- $\approx$ Match $Sgn\left(\epsilon_i^{(v)}\right)$ to $Sgn(\Delta v_i \Delta v_j)$ Moments
- Select $Sgn\left(\epsilon_i^{(x)}\right)$ to Match $Sgn(\Delta x_i \Delta v_i)$
- Some Improvement Scatter & Dispersion

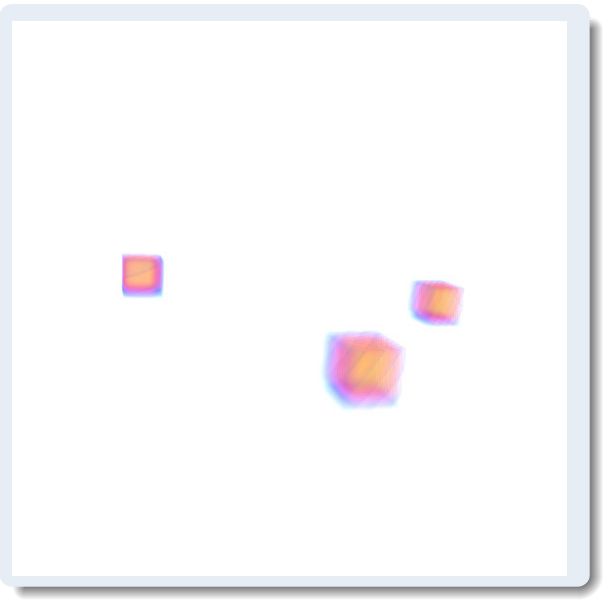

Distribution Statement A: Approved for Public Release; Distribution is Unlimited. PA# 19485

Distribution Statement A: Approved for Public Release; Distribution is Unlimited. AFRL-2021-4182

Dispersion from XV Scatter?

Kinetic Potential Energy Scatter:

- A Closer look at Merge $\rightarrow 2$
- $\approx$ Match $Sgn\left(\epsilon_i^{(v)}\right)$ to $Sgn(\Delta v_i \Delta v_j)$ Moments
- Select $Sgn\left(\epsilon_i^{(x)}\right)$ to Match $Sgn(\Delta x_i \Delta v_i)$
- Some Improvement Scatter & Dispersion
- Why Stop at just XV Sign?
  $\epsilon_i^{(x)} = \left(\overline{\Delta x_i \Delta v_i}\right) / \epsilon_i^{(v)}$

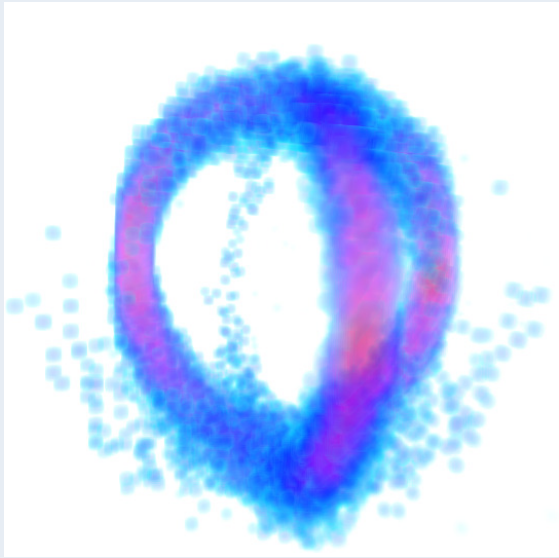

Distribution Statement A: Approved for Public Release; Distribution is Unlimited. PA# 19485

Distribution Statement A: Approved for Public Release; Distribution is Unlimited. AFRL-2021-4182

Dispersion from XV Scatter?

Kinetic Potential Energy Scatter:

- A Closer look at Merge $\rightarrow 2$
- $\approx$ Match $Sgn\left(\epsilon_i^{(v)}\right)$ to $Sgn(\Delta v_i \Delta v_j)$ Moments
- Select $Sgn\left(\epsilon_i^{(x)}\right)$ to Match $Sgn(\Delta x_i \Delta v_i)$
- Some Improvement Scatter & Dispersion
- Why Stop at just XV Sign?
  $\epsilon_i^{(x)} = \left(\overline{\Delta x_i \Delta v_i}\right) / \epsilon_i^{(v)}$
- Much Improved Scatter & Dispersion

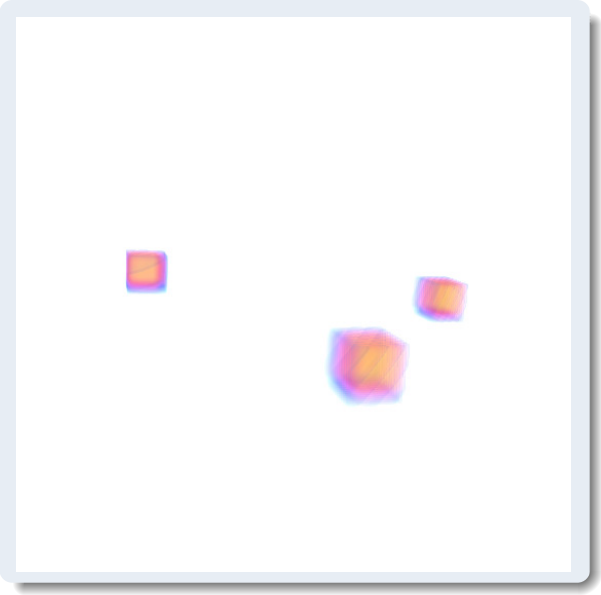

Distribution Statement A: Approved for Public Release; Distribution is Unlimited. PA# 19485

Distribution Statement A: Approved for Public Release; Distribution is Unlimited. AFRL-2021-4182

Dispersion from XV Scatter?

Kinetic Potential Energy Scatter:

- A Closer look at Merge $\rightarrow$ 2
- $\approx$ Match $Sgn\left(\epsilon_i^{(v)}\right)$ to $Sgn(\Delta v_i \Delta v_j)$ Moments
- Select $Sgn\left(\epsilon_i^{(x)}\right)$ to Match $Sgn(\Delta x_i \Delta v_i)$
- Some Improvement Scatter & Dispersion
- Why Stop at just XV Sign?
  $\epsilon_i^{(x)} = \left(\overline{\Delta x_i \Delta v_i}\right) / \epsilon_i^{(v)}$
- Much Improved Scatter & Dispersion
- Sphere Sensitive: Kinetic $\leftrightarrow$ Potential

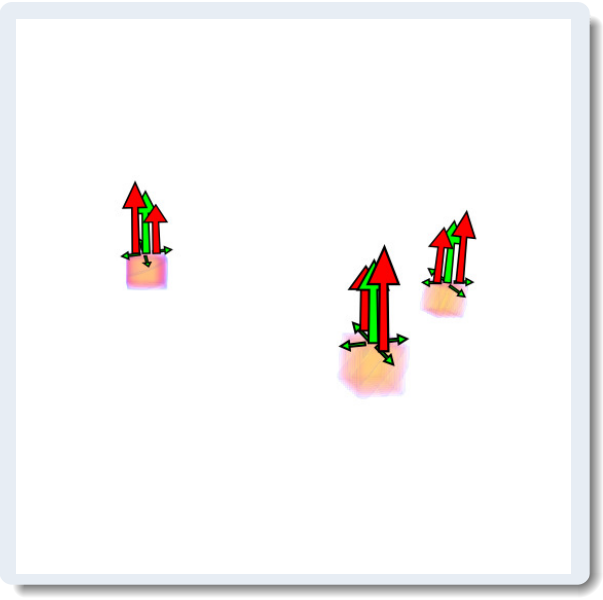

Distribution Statement A: Approved for Public Release; Distribution is Unlimited. PA# 19485

Distribution Statement A: Approved for Public Release; Distribution is Unlimited. AFRL-2021-4182

AFRL

Dispersion from XV Scatter?

Kinetic Potential Energy Scatter:

- A Closer look at Merge $\rightarrow$ 2
- $\approx$ Match $Sgn\left(\epsilon_i^{(v)}\right)$ to $Sgn(\Delta v_i \Delta v_j)$ Moments
- Select $Sgn\left(\epsilon_i^{(x)}\right)$ to Match $Sgn(\Delta x_i \Delta v_i)$
- Some Improvement Scatter & Dispersion
- Why Stop at just XV Sign?
  $\epsilon_i^{(x)} = \left(\overline{\Delta x_i \Delta v_i}\right) / \epsilon_i^{(v)}$
- Much Improved Scatter & Dispersion
- Sphere Sensitive: Kinetic $\leftrightarrow$ Potential
- K.E. & P.E. Conserved Independently...
  XV-Moment $\rightarrow$ Better Combination

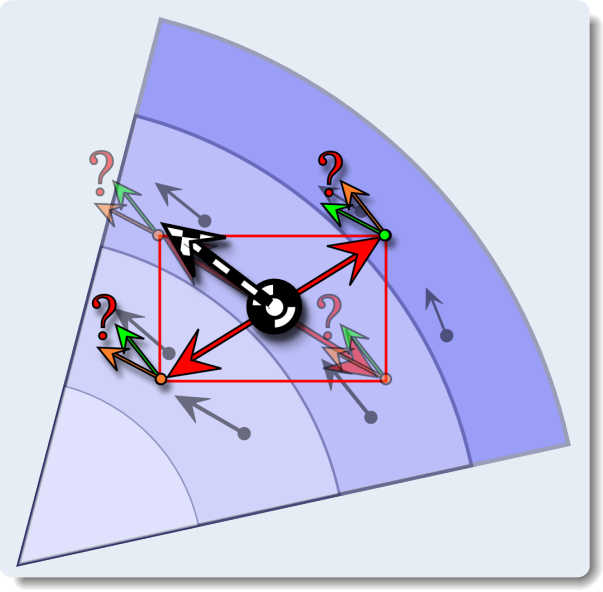

Distribution Statement A: Approved for Public Release; Distribution is Unlimited. PA# 19485

Distribution Statement A: Approved for Public Release; Distribution is Unlimited. AFRL-2021-4182

AFRL

Review Sphere Merge & Split Results

Merge Results after 1-Cycle

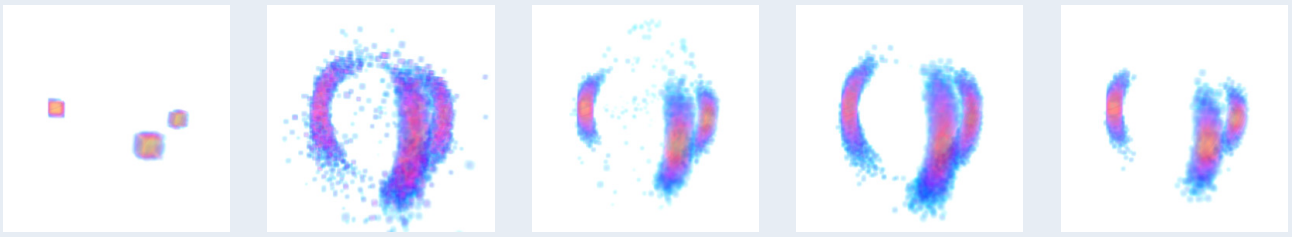

No Merge | Random Sign | PCA | *XV*-Sign | *XV*-Full

Note: Results are Due to Extreme Case Sensitivity
C.N. Push Required for Stability
Period Synchronization Required for Initial Conditions

Distribution Statement A: Approved for Public Release; Distribution is Unlimited. PA# 19485

Distribution Statement A: Approved for Public Release; Distribution is Unlimited. AFRL-2021-4182

AFRL

Review Sphere Merge & Split Results

Merge Results after 1-Cycle

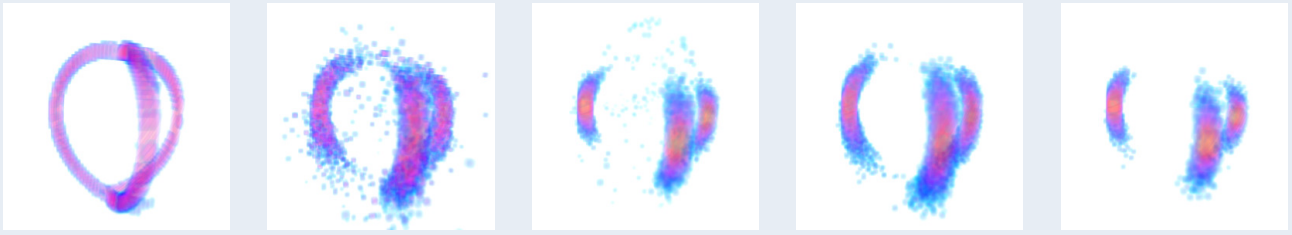

Not Synched | Random Sign | PCA | *XV*-Sign | *XV*-Full

Note: Results are Due to Extreme Case Sensitivity
C.N. Push Required for Stability
Period Synchronization Required for Initial Conditions

Distribution Statement A: Approved for Public Release; Distribution is Unlimited. PA# 19485

Distribution Statement A: Approved for Public Release; Distribution is Unlimited. AFRL-2021-4182

AFRL

Review Sphere Merge & Split Results

Merge Results after 1-Cycle

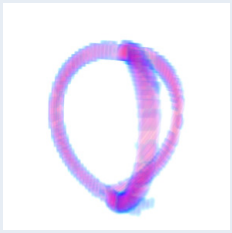
Not Synched

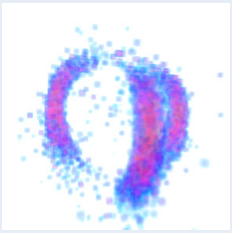
Random Sign

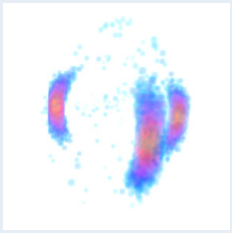
PCA

XV-Sign

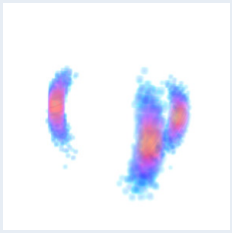
XV-Full

Note: Results are Due to Extreme Case Sensitivity
C.N. Push Required for Stability
Period Synchronization Required for Initial Conditions
Result of Minor Velocity Difference Across IC Box

Distribution Statement A: Approved for Public Release; Distribution is Unlimited. PA# 19485

Distribution Statement A: Approved for Public Release; Distribution is Unlimited. AFRL-2021-4182

AFRL

Review Sphere Merge & Split Results

Merge Results after 1-Cycle

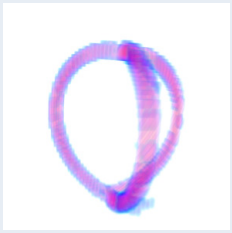
Not Synched

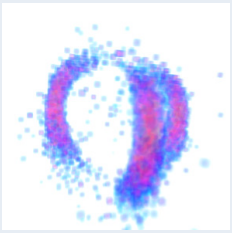
Random Sign

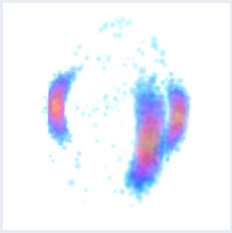
PCA

XV-Sign

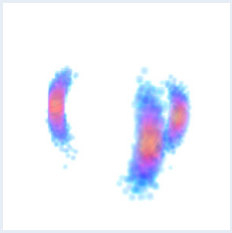
XV-Full

Note: Results are Due to Extreme Case Sensitivity
C.N. Push Required for Stability
Period Synchronization Required for Initial Conditions
Result of Minor Velocity Difference Across IC Box
Merge Scatter in Cells $<$ Synch ΔV

Distribution Statement A: Approved for Public Release; Distribution is Unlimited. PA# 19485

Distribution Statement A: Approved for Public Release; Distribution is Unlimited. AFRL-2021-4182

AFRL

Review Sphere Merge & Split Results

Merge Results after 1-Cycle

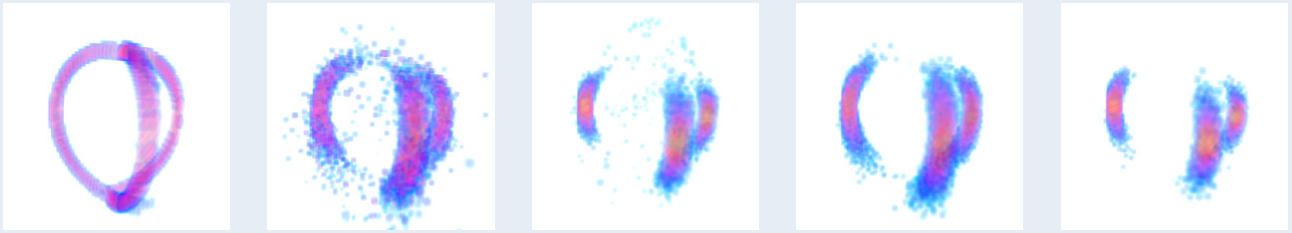

Not Synched | Random Sign | PCA | *XV*-Sign | *XV*-Full

Note: Results are Due to Extreme Case Sensitivity
C.N. Push Required for Stability
Period Synchronization Required for Initial Conditions
Result of Minor Velocity Difference Across IC Box
Merge Scatter in Cells $<$ Synch ΔV

During Q&A of DSMC13, asked by Professor Garcia about Angular Momentum Conservation
I'd assumed that was Orbital Mechanics Specific, but now realize Angular Momentum is a Collisional Invariant...

Distribution Statement A: Approved for Public Release; Distribution is Unlimited. PA# 19485

Distribution Statement A: Approved for Public Release; Distribution is Unlimited. AFRL-2021-4182

Angular Momentum Conservation with DSMC

The Debate over Angular Momentum Conservation

- Meiburg First Questioned DSMC for High Vorticity Flow (1986)
  - Compares Vortex Structure for MD and DSMC in Driven Cavity
  - Suggests Failure Result of Unconserved Angular Momentum

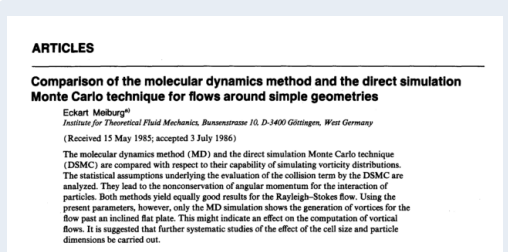

ARTICLES

Comparison of the molecular dynamics method and the direct simulation Monte Carlo technique for flows around simple geometries

Eckart Meiburg[a)]
Institute for Theoretical Fluid Mechanics, Bunsenstrasse 10, D-3400 Göttingen, West Germany

(Received 15 May 1985; accepted 3 July 1986)

The molecular dynamics method (MD) and the direct simulation Monte Carlo technique (DSMC) are compared with respect to their capability of simulating vorticity distributions. The statistical assumptions underlying the evaluation of the collision term by the DSMC are analyzed. They lead to the nonconservation of angular momentum for the interaction of particles. Both methods yield equally good results for the Rayleigh–Stokes flow. Using the present parameters, however, only the MD simulation shows the generation of vortices for the flow past an inclined flat plate. This might indicate an effect on the computation of vortical flows. It is suggested that further systematic studies of the effect of the cell size and particle dimensions be carried out.

Distribution Statement A: Approved for Public Release; Distribution is Unlimited. PA# 19485

Distribution Statement A: Approved for Public Release; Distribution is Unlimited. AFRL-2021-4182

Angular Momentum Conservation with DSMC

The Debate over Angular Momentum Conservation

- Meiburg First Questioned DSMC for High Vorticity Flow (1986)
  - Compares Vortex Structure for MD and DSMC in Driven Cavity
  - Suggests Failure Result of Unconserved Angular Momentum
- Bird Questions Meiburg's Demonstration (1987)
  - MD Conditions Violate Dilute Gas Assumption (3+Body)
  - Demonstrates Angular Momentum Conserving DSMC

  ...but Concludes is is Not Particularly Helpful
  - Shows Subcells Help and $\Delta x < \lambda_{mfp}$ Important

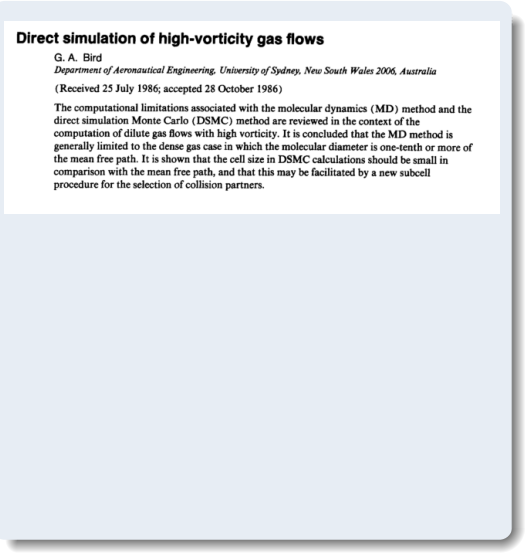

Direct simulation of high-vorticity gas flows

G. A. Bird

Department of Aeronautical Engineering, University of Sydney, New South Wales 2006, Australia

(Received 25 July 1986; accepted 28 October 1986)

The computational limitations associated with the molecular dynamics (MD) method and the direct simulation Monte Carlo (DSMC) method are reviewed in the context of the computation of dilute gas flows with high vorticity. It is concluded that the MD method is generally limited to the dense gas case in which the molecular diameter is one-tenth or more of the mean free path. It is shown that the cell size in DSMC calculations should be small in comparison with the mean free path, and that this may be facilitated by a new subcell procedure for the selection of collision partners.

Distribution Statement A: Approved for Public Release; Distribution is Unlimited. PA# 19485

Distribution Statement A: Approved for Public Release; Distribution is Unlimited. AFRL-2021-4182

Angular Momentum Conservation with DSMC

The Debate over Angular Momentum Conservation

- Meiburg First Questioned DSMC for High Vorticity Flow (1986)
  - Compares Vortex Structure for MD and DSMC in Driven Cavity
  - Suggests Failure Result of Unconserved Angular Momentum
- Bird Questions Meiburg's Demonstration (1987)
  - MD Conditions Violate Dilute Gas Assumption (3+Body)
  - Demonstrates Angular Momentum Conserving DSMC

  ...but Concludes is is Not Particularly Helpful
  - Shows Subcells Help and $\Delta x < \lambda_{mfp}$ Important
- Nanbu Further Settles Debate
  - Shows Vorticity is actually Independent of Angular Momentum (i.e. Vorticity only Requires Linear Momentum Conservation)
  - Shows that Expectation of Angular Momentum is Conserved
  - Shows Variance of Angular Momentum Propotional to Δx

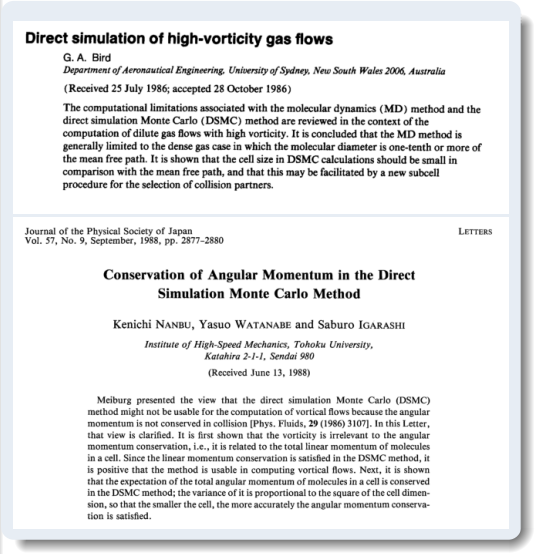

Direct simulation of high-vorticity gas flows

G. A. Bird

Department of Aeronautical Engineering, University of Sydney, New South Wales 2006, Australia

(Received 25 July 1986; accepted 28 October 1986)

The computational limitations associated with the molecular dynamics (MD) method and the direct simulation Monte Carlo (DSMC) method are reviewed in the context of the computation of dilute gas flows with high vorticity. It is concluded that the MD method is generally limited to the dense gas case in which the molecular diameter is one-tenth or more of the mean free path. It is shown that the cell size in DSMC calculations should be small in comparison with the mean free path, and that this may be facilitated by a new subcell procedure for the selection of collision partners.

Journal of the Physical Society of Japan
Vol. 57, No. 9, September, 1988, pp. 2877–2880

LETTERS

Conservation of Angular Momentum in the Direct Simulation Monte Carlo Method

Kenichi NANBU, Yasuo WATANABE and Saburo IGARASHI

Institute of High-Speed Mechanics, Tohoku University, Katahira 2-1-1, Sendai 980

(Received June 13, 1988)

Meiburg presented the view that the direct simulation Monte Carlo (DSMC) method might not be usable for the computation of vortical flows because the angular momentum is not conserved in collision [Phys. Fluids, **29** (1986) 3107]. In this Letter, that view is clarified. It is first shown that the vorticity is irrelevant to the angular momentum conservation, i.e., it is related to the total linear momentum of molecules in a cell. Since the linear momentum conservation is satisfied in the DSMC method, it is positive that the method is usable in computing vortical flows. Next, it is shown that the expectation of the total angular momentum of molecules in a cell is conserved in the DSMC method; the variance of it is proportional to the square of the cell dimension, so that the smaller the cell, the more accurately the angular momentum conservation is satisfied.

Distribution Statement A: Approved for Public Release; Distribution is Unlimited. PA# 19485

Distribution Statement A: Approved for Public Release; Distribution is Unlimited. AFRL-2021-4182

Angular Momentum Conservation with DSMC

The Debate over Angular Momentum Conservation

- Meiburg First Questioned DSMC for High Vorticity Flow (1986)
  - Compares Vortex Structure for MD and DSMC in Driven Cavity
  - Suggests Failure Result of Unconserved Angular Momentum
- Bird Questions Meiburg's Demonstration (1987)
  - MD Conditions Violate Dilute Gas Assumption (3+Body)
  - Demonstrates Angular Momentum Conserving DSMC

  ...but Concludes is is Not Particularly Helpful
  - Shows Subcells Help and $\Delta x < \lambda_{mfp}$ Important
- Nanbu Further Settles Debate
  - Shows Vorticity is actually Independent of Angular Momentum

  (i.e. Vorticity only Requires Linear Momentum Conservation)
  - Shows that Expectation of Angular Momentum is Conserved
  - Shows Variance of Angular Momentum Propotional to Δx
- DSMC Conserves Angular Momentum in $\Delta x \rightarrow 0$ Limit

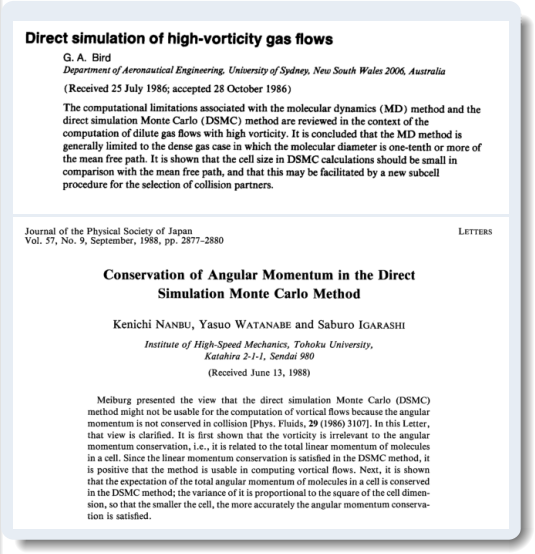

Direct simulation of high-vorticity gas flows

G. A. Bird

Department of Aeronautical Engineering, University of Sydney, New South Wales 2006, Australia

(Received 25 July 1986; accepted 28 October 1986)

The computational limitations associated with the molecular dynamics (MD) method and the direct simulation Monte Carlo (DSMC) method are reviewed in the context of the computation of dilute gas flows with high vorticity. It is concluded that the MD method is generally limited to the dense gas case in which the molecular diameter is one-tenth or more of the mean free path. It is shown that the cell size in DSMC calculations should be small in comparison with the mean free path, and that this may be facilitated by a new subcell procedure for the selection of collision partners.

Journal of the Physical Society of Japan
Vol. 57, No. 9, September, 1988, pp. 2877–2880

LETTERS

Conservation of Angular Momentum in the Direct Simulation Monte Carlo Method

Kenichi NANBU, Yasuo WATANABE and Saburo IGARASHI

Institute of High-Speed Mechanics, Tohoku University, Katahira 2-1-1, Sendai 980

(Received June 13, 1988)

Meiburg presented the view that the direct simulation Monte Carlo (DSMC) method might not be usable for the computation of vortical flows because the angular momentum is not conserved in collision [Phys. Fluids, **29** (1986) 3107]. In this Letter, that view is clarified. It is first shown that the vorticity is irrelevant to the angular momentum conservation, i.e., it is related to the total linear momentum of molecules in a cell. Since the linear momentum conservation is satisfied in the DSMC method, it is positive that the method is usable in computing vortical flows. Next, it is shown that the expectation of the total angular momentum of molecules in a cell is conserved in the DSMC method; the variance of it is proportional to the square of the cell dimension, so that the smaller the cell, the more accurately the angular momentum conservation is satisfied.

Distribution Statement A: Approved for Public Release; Distribution is Unlimited. PA# 19485

Distribution Statement A: Approved for Public Release; Distribution is Unlimited. AFRL-2021-4182

Angular Momentum Conservation with DSMC

The Debate over Angular Momentum Conservation

- Meiburg First Questioned DSMC for High Vorticity Flow (1986)
  - Compares Vortex Structure for MD and DSMC in Driven Cavity
  - Suggests Failure Result of Unconserved Angular Momentum
- Bird Questions Meiburg's Demonstration (1987)
  - MD Conditions Violate Dilute Gas Assumption (3+Body)
  - Demonstrates Angular Momentum Conserving DSMC

  ...but Concludes is is Not Particularly Helpful
  - Shows Subcells Help and $\Delta x < \lambda_{mfp}$ Important
- Nanbu Further Settles Debate
  - Shows Vorticity is actually Independent of Angular Momentum

  (i.e. Vorticity only Requires Linear Momentum Conservation)
  - Shows that Expectation of Angular Momentum is Conserved
  - Shows Variance of Angular Momentum Propotional to Δx
- DSMC Conserves Angular Momentum in $\Delta x \to 0$ Limit

  As Graeme was sure to let everyone know from then on...

Bird Wins!

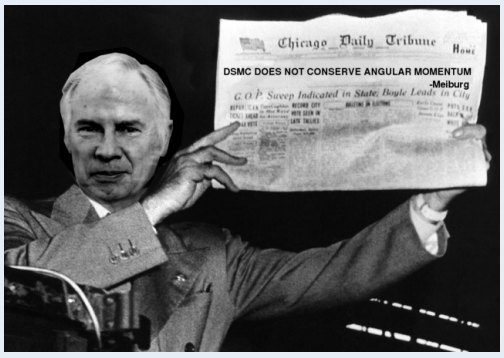

Distribution Statement A: Approved for Public Release; Distribution is Unlimited. PA# 19485

Distribution Statement A: Approved for Public Release; Distribution is Unlimited. AFRL-2021-4182

AFRL

Angular Momentum Conservation with DSMC

The Debate over Angular Momentum Conservation

- Meiburg First Questioned DSMC for High Vorticity Flow (1986)
  - Compares Vortex Structure for MD and DSMC in Driven Cavity
  - Suggests Failure Result of Unconserved Angular Momentum
- Bird Questions Meiburg's Demonstration (1987)
  - MD Conditions Violate Dilute Gas Assumption (3+Body)
  - Demonstrates Angular Momentum Conserving DSMC
  ...but Concludes is is Not Particularly Helpful
  - Shows Subcells Help and $\Delta x < \lambda_{mfp}$ Important
- Nanbu Further Settles Debate
  - Shows Vorticity is actually Independent of Angular Momentum
  (i.e. Vorticity only Requires Linear Momentum Conservation)
  - Shows that Expectation of Angular Momentum is Conserved
  - Shows Variance of Angular Momentum Propotional to Δx
- DSMC Conserves Angular Momentum in $\Delta x \to 0$ Limit
  As Graeme was sure to let everyone know from then on...

Average Angular Momentum seems enough for Rarefied Flow...
But what if Random Walks Couple to Field Energies?

Bird Wins!

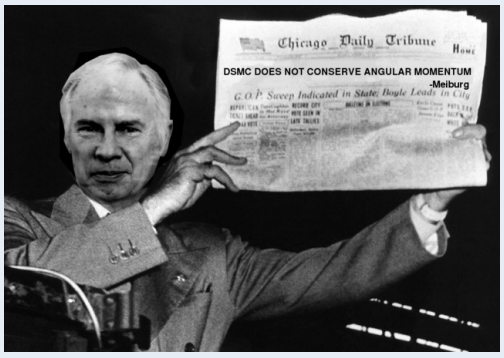

Distribution Statement A: Approved for Public Release; Distribution is Unlimited. PA# 19485

Distribution Statement A: Approved for Public Release; Distribution is Unlimited. AFRL-2021-4182

AFRL

Angular Momentum Conservation with DSMC

The Debate over Angular Momentum Conservation

- Meiburg First Questioned DSMC for High Vorticity Flow (1986)
  - Compares Vortex Structure for MD and DSMC in Driven Cavity
  - Suggests Failure Result of Unconserved Angular Momentum
- Bird Questions Meiburg's Demonstration (1987)
  - MD Conditions Violate Dilute Gas Assumption (3+Body)
  - Demonstrates Angular Momentum Conserving DSMC
  ...but Concludes is is Not Particularly Helpful
  - Shows Subcells Help and $\Delta x < \lambda_{mfp}$ Important
- Nanbu Further Settles Debate
  - Shows Vorticity is actually Independent of Angular Momentum
  (i.e. Vorticity only Requires Linear Momentum Conservation)
  - Shows that Expectation of Angular Momentum is Conserved
  - Shows Variance of Angular Momentum Propotional to Δx
- DSMC Conserves Angular Momentum in $\Delta x \to 0$ Limit
  As Graeme was sure to let everyone know from then on...

Average Angular Momentum seems enough for Rarefied Flow...
But what if Random Walks Couple to Field Energies?
Are $\Delta x \to 0$ collision Cells actually Practical?
And Where is Bird's Angular Momentum Conserving DSMC?

Bird Wins!

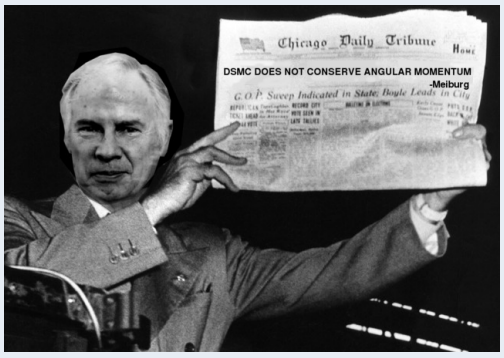

Distribution Statement A: Approved for Public Release; Distribution is Unlimited. PA# 19485

Distribution Statement A: Approved for Public Release; Distribution is Unlimited. AFRL-2021-4182

Angular Momentum Conservation with DSMC

Implementation of Angular Momentum Conservation

- Angular Momentum Conservation Direct Consequence of Boltzmann Equation:
  $\frac{\partial f}{\partial t}+\vec{v}\cdot\nabla_x f+\frac{q}{m}(\vec{E}+\vec{v}\times\vec{B})\cdot\nabla_v f=\int g_{ij}\sigma_{ij}(g_{ij},\Omega)(f_i' f_j'-f_i f_j)d\Omega d^3\vec{v}'$
  (i.e. Collisions happen at Points in x-Space)

Discrete Form

$$\begin{aligned}\omega^{total} &= \vec{x}_i\times\vec{v}_i+\vec{x}_j\times\vec{v}_j\\ &= (\bar{x}+\Delta\vec{x})\times(\bar{v}+\Delta\vec{v})+(\bar{x}-\Delta\vec{x})\times(\bar{v}-\Delta\vec{v})\\ &= 2(\bar{x}\times\bar{v}+\Delta\vec{x}\times\Delta\vec{v})\\ &= 2(\bar{x}\times\vec{v})|_{\lim\Delta\vec{x}\to 0}\end{aligned}$$

Distribution Statement A: Approved for Public Release; Distribution is Unlimited. PA# 19485

Distribution Statement A: Approved for Public Release; Distribution is Unlimited. AFRL-2021-4182

Angular Momentum Conservation with DSMC

Implementation of Angular Momentum Conservation

- Angular Momentum Conservation Direct Consequence of Boltzmann Equation:
  $\frac{\partial f}{\partial t}+\vec{v}\cdot\nabla_x f+\frac{q}{m}(\vec{E}+\vec{v}\times\vec{B})\cdot\nabla_v f=\int g_{ij}\sigma_{ij}(g_{ij},\Omega)(f_i' f_j'-f_i f_j)d\Omega d^3\vec{v}'$
  (i.e. Collisions happen at Points in x-Space)
- However: DSMC only Approximates $\lim \Delta\vec{x}\to 0$

Discrete Form

$$\begin{aligned}\omega^{total} &= \vec{x}_i\times\vec{v}_i+\vec{x}_j\times\vec{v}_j\\ &= (\bar{x}+\Delta\vec{x})\times(\bar{v}+\Delta\vec{v})+(\bar{x}-\Delta\vec{x})\times(\bar{v}-\Delta\vec{v})\\ &= 2(\bar{x}\times\bar{v}+\Delta\vec{x}\times\Delta\vec{v})\\ &= 2(\bar{x}\times\vec{v})|_{\lim\Delta\vec{x}\to 0}\end{aligned}$$

Distribution Statement A: Approved for Public Release; Distribution is Unlimited. PA# 19485

Distribution Statement A: Approved for Public Release; Distribution is Unlimited. AFRL-2021-4182

Angular Momentum Conservation with DSMC

Implementation of Angular Momentum Conservation

- Angular Momentum Conservation Direct Consequence of Boltzmann Equation:
  $\frac{\partial f}{\partial t}+\vec{v}\cdot\nabla_x f+\frac{q}{m}(\vec{E}+\vec{v}\times\vec{B})\cdot\nabla_v f=\int g_{ij}\sigma_{ij}(g_{ij},\Omega)(f_i' f_j'-f_i f_j)d\Omega d^3\vec{v}'$
  (i.e. Collisions happen at Points in x-Space)
- However: DSMC only Approximates $\lim \Delta\vec{x}\to 0$
- Bird's Conservation Implementation Description is Unhelpful

Discrete Form

$$\begin{aligned}\omega^{total} &= \vec{x}_i\times\vec{v}_i+\vec{x}_j\times\vec{v}_j\\ &= (\bar{x}+\Delta\vec{x})\times(\bar{v}+\Delta\vec{v})+(\bar{x}-\Delta\vec{x})\times(\bar{v}-\Delta\vec{v})\\ &= 2(\bar{x}\times\bar{v}+\Delta\vec{x}\times\Delta\vec{v})\\ &= 2(\bar{x}\times\vec{v})|_{\lim\Delta\vec{x}\to 0}\end{aligned}$$

The introduction of subcells minimizes the destruction of vorticity caused by the nonconservation of the angular momentum of the collision pairs. As noted above, the loss of vorticity occurs because the inpact parameters are chosen at random, independently of the relative locations of the two molecules in the cell. In order to assess the effects of this approximation, the relative locations of the molecules after the collision can be adjusted so that the angular momentum in the collisions is exactly conserved. The molecules are moved along the apse line of the collision in the center of mass frame of reference without moving the center of mass itself.

Distribution Statement A: Approved for Public Release; Distribution is Unlimited. PA# 19485

Distribution Statement A: Approved for Public Release; Distribution is Unlimited. AFRL-2021-4182

Angular Momentum Conservation with DSMC

Implementation of Angular Momentum Conservation

- Angular Momentum Conservation Direct Consequence of Boltzmann Equation:
  $\frac{\partial f}{\partial t}+\vec{v}\cdot\nabla_x f+\frac{q}{m}(\vec{E}+\vec{v}\times\vec{B})\cdot\nabla_v f=\int g_{ij}\sigma_{ij}(g_{ij},\Omega)(f_i' f_j'-f_i f_j)d\Omega d^3\vec{v}'$
  (i.e. Collisions happen at Points in x-Space)
- However: DSMC only Approximates $\lim \Delta\vec{x}\to 0$
- Bird's Conservation Implementation Description is Unhelpful
- Easier to Explain in terms of $\Delta\vec{x}$ and $\Delta\vec{v}$

Discrete Form

$$\begin{aligned}\omega^{total} &= \vec{x}_i\times\vec{v}_i+\vec{x}_j\times\vec{v}_j\\ &= (\bar{x}+\Delta\vec{x})\times(\bar{v}+\Delta\vec{v})+(\bar{x}-\Delta\vec{x})\times(\bar{v}-\Delta\vec{v})\\ &= 2(\bar{x}\times\bar{v}+\Delta\vec{x}\times\Delta\vec{v})\\ &= 2(\bar{x}\times\bar{v})|_{\lim\Delta\vec{x}\to 0}\end{aligned}$$

Angular Momentum Conserving Binary Collisions

Given $\vec{v}_i$ and $\vec{v}_j$:

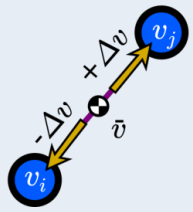

Distribution Statement A: Approved for Public Release; Distribution is Unlimited. PA# 19485

Distribution Statement A: Approved for Public Release; Distribution is Unlimited. AFRL-2021-4182

AFRL

Angular Momentum Conservation with DSMC

Implementation of Angular Momentum Conservation

- Angular Momentum Conservation Direct Consequence of Boltzmann Equation:
  $\frac{\partial f}{\partial t}+\vec{v}\cdot\nabla_x f+\frac{q}{m}(\vec{E}+\vec{v}\times\vec{B})\cdot\nabla_v f=\int g_{ij}\sigma_{ij}(g_{ij},\Omega)(f_i' f_j'-f_i f_j)d\Omega d^3\vec{v}'$
  (i.e. Collisions happen at Points in x-Space)
- However: DSMC only Approximates $\lim \Delta\vec{x}\to 0$
- Bird's Conservation Implementation Description is Unhelpful
- Easier to Explain in terms of $\Delta\vec{x}$ and $\Delta\vec{v}$

Discrete Form

$$\begin{aligned}\omega^{total} &= \vec{x}_i\times\vec{v}_i+\vec{x}_j\times\vec{v}_j\\ &= (\bar{x}+\Delta\vec{x})\times(\bar{v}+\Delta\vec{v})+(\bar{x}-\Delta\vec{x})\times(\bar{v}-\Delta\vec{v})\\ &= 2(\bar{x}\times\bar{v}+\Delta\vec{x}\times\Delta\vec{v})\\ &= 2(\bar{x}\times\bar{v})|_{\lim\Delta\vec{x}\to 0}\end{aligned}$$

Angular Momentum Conserving Binary Collisions

Given $\vec{v}_i$ and $\vec{v}_j$:

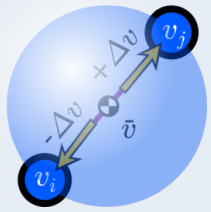

Energy Conservation if
v_i' and v_j' on Line through $\bar{v}$

Distribution Statement A: Approved for Public Release; Distribution is Unlimited. PA# 19485

Distribution Statement A: Approved for Public Release; Distribution is Unlimited. AFRL-2021-4182

Angular Momentum Conservation with DSMC

Implementation of Angular Momentum Conservation

- Angular Momentum Conservation Direct Consequence of Boltzmann Equation:
  $\frac{\partial f}{\partial t}+\vec{v}\cdot\nabla_x f+\frac{q}{m}(\vec{E}+\vec{v}\times\vec{B})\cdot\nabla_v f=\int g_{ij}\sigma_{ij}(g_{ij},\Omega)(f_i' f_j'-f_i f_j)d\Omega d^3\vec{v}'$
  (i.e. Collisions happen at Points in x-Space)
- However: DSMC only Approximates $\lim \Delta\vec{x}\to 0$
- Bird's Conservation Implementation Description is Unhelpful
- Easier to Explain in terms of $\Delta\vec{x}$ and $\Delta\vec{v}$

Discrete Form

$$\begin{aligned}\omega^{total} &= \vec{x}_i\times\vec{v}_i+\vec{x}_j\times\vec{v}_j\\ &= (\bar{x}+\Delta\vec{x})\times(\bar{v}+\Delta\vec{v})+(\bar{x}-\Delta\vec{x})\times(\bar{v}-\Delta\vec{v})\\ &= 2(\bar{x}\times\bar{v}+\Delta\vec{x}\times\Delta\vec{v})\\ &= 2(\bar{x}\times\bar{v})|_{\lim\Delta\vec{x}\to 0}\end{aligned}$$

Angular Momentum Conserving Binary Collisions

Given $\vec{v}_i$ and $\vec{v}_j$:

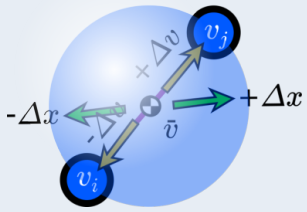

Including Δx

Distribution Statement A: Approved for Public Release; Distribution is Unlimited. PA# 19485

Distribution Statement A: Approved for Public Release; Distribution is Unlimited. AFRL-2021-4182

Angular Momentum Conservation with DSMC

Implementation of Angular Momentum Conservation

- Angular Momentum Conservation Direct Consequence of Boltzmann Equation:
  $\frac{\partial f}{\partial t}+\vec{v}\cdot\nabla_x f+\frac{q}{m}(\vec{E}+\vec{v}\times\vec{B})\cdot\nabla_v f=\int g_{ij}\sigma_{ij}(g_{ij},\Omega)(f_i' f_j'-f_i f_j)d\Omega d^3\vec{v}'$
  (i.e. Collisions happen at Points in x-Space)
- However: DSMC only Approximates $\lim \Delta\vec{x}\to 0$
- Bird's Conservation Implementation Description is Unhelpful
- Easier to Explain in terms of $\Delta\vec{x}$ and $\Delta\vec{v}$

Discrete Form

$$\begin{aligned}\omega^{total} &= \vec{x}_i\times\vec{v}_i+\vec{x}_j\times\vec{v}_j\\ &= (\bar{x}+\Delta\vec{x})\times(\bar{v}+\Delta\vec{v})+(\bar{x}-\Delta\vec{x})\times(\bar{v}-\Delta\vec{v})\\ &= 2(\bar{x}\times\bar{v}+\Delta\vec{x}\times\Delta\vec{v})\\ &= 2(\bar{x}\times\vec{v})|_{\lim\Delta\vec{x}\to 0}\end{aligned}$$

Angular Momentum Conserving Binary Collisions

Given $\vec{v}_i$ and $\vec{v}_j$:

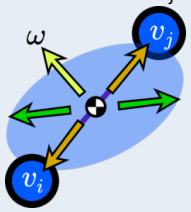

Including Δx
Defines Plane and Non-zero $\vec{\omega}$

Distribution Statement A: Approved for Public Release; Distribution is Unlimited. PA# 19485

Distribution Statement A: Approved for Public Release; Distribution is Unlimited. AFRL-2021-4182

Angular Momentum Conservation with DSMC

Implementation of Angular Momentum Conservation

- Angular Momentum Conservation Direct Consequence of Boltzmann Equation:
  $\frac{\partial f}{\partial t}+\vec{v}\cdot\nabla_x f+\frac{q}{m}(\vec{E}+\vec{v}\times\vec{B})\cdot\nabla_v f=\int g_{ij}\sigma_{ij}(g_{ij},\Omega)(f_i' f_j'-f_i f_j)d\Omega d^3\vec{v}'$
  (i.e. Collisions happen at Points in x-Space)
- However: DSMC only Approximates $\lim \Delta\vec{x}\to 0$
- Bird's Conservation Implementation Description is Unhelpful
- Easier to Explain in terms of $\Delta\vec{x}$ and $\Delta\vec{v}$
- In-Plane Scatter Required for $\hat{\omega}=\hat{\omega}'$

Discrete Form

$$\begin{aligned}\omega^{total} &= \vec{x}_i\times\vec{v}_i+\vec{x}_j\times\vec{v}_j\\ &= (\bar{x}+\Delta\vec{x})\times(\bar{v}+\Delta\vec{v})+(\bar{x}-\Delta\vec{x})\times(\bar{v}-\Delta\vec{v})\\ &= 2(\bar{x}\times\bar{v}+\Delta\vec{x}\times\Delta\vec{v})\\ &= 2(\bar{x}\times\vec{v})|_{\lim\Delta\vec{x}\to 0}\end{aligned}$$

Angular Momentum Conserving Binary Collisions

Given $\vec{v}_i$ and $\vec{v}_j$:

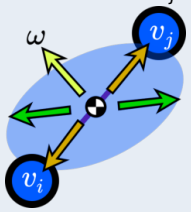

Including Δx
Defines Plane and Non-zero $\vec{\omega}$

Distribution Statement A: Approved for Public Release; Distribution is Unlimited. PA# 19485

Distribution Statement A: Approved for Public Release; Distribution is Unlimited. AFRL-2021-4182

Angular Momentum Conservation with DSMC

Implementation of Angular Momentum Conservation

- Angular Momentum Conservation Direct Consequence of Boltzmann Equation:
  $\frac{\partial f}{\partial t}+\vec{v}\cdot\nabla_x f+\frac{q}{m}(\vec{E}+\vec{v}\times\vec{B})\cdot\nabla_v f=\int g_{ij}\sigma_{ij}(g_{ij},\Omega)(f_i'f_j'-f_if_j)d\Omega d^3\vec{v}'$
  (i.e. Collisions happen at Points in x-Space)
- However: DSMC only Approximates $\lim \Delta\vec{x}\rightarrow 0$
- Bird's Conservation Implementation Description is Unhelpful
- Easier to Explain in terms of $\Delta\vec{x}$ and $\Delta\vec{v}$
- In-Plane Scatter Required for $\hat{\omega}=\hat{\omega}'$
- Angular Momentum Conserved if $\Delta\vec{x}$ Rotated with $\Delta\vec{v}$

Discrete Form

$$\begin{aligned}\omega^{total} &= \vec{x}_i\times\vec{v}_i+\vec{x}_j\times\vec{v}_j\\ &= (\bar{x}+\Delta\vec{x})\times(\bar{v}+\Delta\vec{v})+(\bar{x}-\Delta\vec{x})\times(\bar{v}-\Delta\vec{v})\\ &= 2(\bar{x}\times\bar{v}+\Delta\vec{x}\times\Delta\vec{v})\\ &= 2(\bar{x}\times\vec{v})|_{\lim\Delta\vec{x}\rightarrow 0}\end{aligned}$$

Angular Momentum Conserving Binary Collisions

Given $\vec{v}_i$ and $\vec{v}_j$:

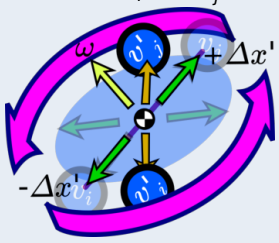

Distribution Statement A: Approved for Public Release; Distribution is Unlimited. PA# 19485

Distribution Statement A: Approved for Public Release; Distribution is Unlimited. AFRL-2021-4182

AFRL

Angular Momentum Conservation with DSMC

Implementation of Angular Momentum Conservation

- Angular Momentum Conservation Direct Consequence of Boltzmann Equation:
  $\frac{\partial f}{\partial t}+\vec{v}\cdot\nabla_x f+\frac{q}{m}(\vec{E}+\vec{v}\times\vec{B})\cdot\nabla_v f=\int g_{ij}\sigma_{ij}(g_{ij},\Omega)(f_i' f_j'-f_i f_j)d\Omega d^3\vec{v}'$
  (i.e. Collisions happen at Points in x-Space)
- However: DSMC only Approximates $\lim \Delta\vec{x}\rightarrow 0$
- Bird's Conservation Implementation Description is Unhelpful
- Easier to Explain in terms of $\Delta\vec{x}$ and $\Delta\vec{v}$
- In-Plane Scatter Required for $\hat{\omega}=\hat{\omega}'$
- Angular Momentum Conserved if $\Delta\vec{x}$ Rotated with $\Delta\vec{v}$
- Modifies DSMC Random Ψ Angle to One Defined by $\Delta\vec{x}$ Plane

Discrete Form

$$\begin{aligned}\omega^{total} &= \vec{x}_i\times\vec{v}_i+\vec{x}_j\times\vec{v}_j\\ &= (\bar{x}+\Delta\vec{x})\times(\bar{v}+\Delta\vec{v})+(\bar{x}-\Delta\vec{x})\times(\bar{v}-\Delta\vec{v})\\ &= 2(\bar{x}\times\bar{v}+\Delta\vec{x}\times\Delta\vec{v})\\ &= 2(\bar{x}\times\vec{v})|_{\lim\Delta\vec{x}\rightarrow 0}\end{aligned}$$

Angular Momentum Conserving Binary Collisions

Given $\vec{v}_i$ and $\vec{v}_j$:

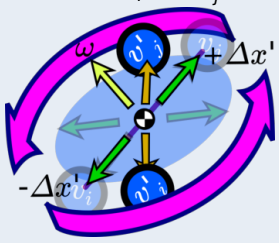

Distribution Statement A: Approved for Public Release; Distribution is Unlimited. PA# 19485

Distribution Statement A: Approved for Public Release; Distribution is Unlimited. AFRL-2021-4182

Angular Momentum Conservation with DSMC

Implementation of Angular Momentum Conservation

- Angular Momentum Conservation Direct Consequence of Boltzmann Equation:
  $\frac{\partial f}{\partial t}+\vec{v}\cdot\nabla_x f+\frac{q}{m}(\vec{E}+\vec{v}\times\vec{B})\cdot\nabla_v f=\int g_{ij}\sigma_{ij}(g_{ij},\Omega)(f_i' f_j'-f_i f_j)d\Omega d^3\vec{v}'$
  (i.e. Collisions happen at Points in x-Space)
- However: DSMC only Approximates $\lim \Delta\vec{x}\to 0$
- Bird's Conservation Implementation Description is Unhelpful
- Easier to Explain in terms of $\Delta\vec{x}$ and $\Delta\vec{v}$
- In-Plane Scatter Required for $\hat{\omega}=\hat{\omega}'$
- Angular Momentum Conserved if $\Delta\vec{x}$ Rotated with $\Delta\vec{v}$
- Modifies DSMC Random Ψ Angle to One Defined by $\Delta\vec{x}$ Plane
- $\Delta\vec{x}$ Random w.r.t. $\Delta\vec{v}$ as $\Delta\vec{x}\to 0$? (Assuming Smooth ρ?)
  i.e. Reverts to Standard DSMC as $\Delta\vec{x}\to 0$

Discrete Form

$$\begin{aligned}\omega^{total} &= \vec{x}_i\times\vec{v}_i+\vec{x}_j\times\vec{v}_j\\ &= (\bar{x}+\Delta\vec{x})\times(\bar{v}+\Delta\vec{v})+(\bar{x}-\Delta\vec{x})\times(\bar{v}-\Delta\vec{v})\\ &= 2(\bar{x}\times\bar{v}+\Delta\vec{x}\times\Delta\vec{v})\\ &= 2(\bar{x}\times\vec{v})|_{\lim\Delta\vec{x}\to 0}\end{aligned}$$

Angular Momentum Conserving Binary Collisions

Given $\vec{v}_i$ and $\vec{v}_j$:

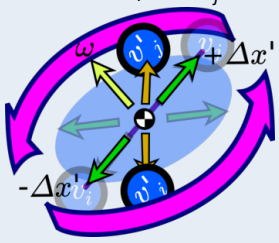

Distribution Statement A: Approved for Public Release; Distribution is Unlimited. PA# 19485

Distribution Statement A: Approved for Public Release; Distribution is Unlimited. AFRL-2021-4182

Angular Momentum Conservation with DSMC

Implementation of Angular Momentum Conservation

- Angular Momentum Conservation Direct Consequence of Boltzmann Equation:
  $\frac{\partial f}{\partial t}+\vec{v}\cdot\nabla_x f+\frac{q}{m}(\vec{E}+\vec{v}\times\vec{B})\cdot\nabla_v f=\int g_{ij}\sigma_{ij}(g_{ij},\Omega)(f_i' f_j'-f_i f_j)d\Omega d^3\vec{v}'$
  (i.e. Collisions happen at Points in x-Space)
- However: DSMC only Approximates $\lim \Delta\vec{x}\to 0$
- Bird's Conservation Implementation Description is Unhelpful
- Easier to Explain in terms of $\Delta\vec{x}$ and $\Delta\vec{v}$
- In-Plane Scatter Required for $\hat{\omega}=\hat{\omega}'$
- Angular Momentum Conserved if $\Delta\vec{x}$ Rotated with $\Delta\vec{v}$
- Modifies DSMC Random Ψ Angle to One Defined by $\Delta\vec{x}$ Plane
- $\Delta\vec{x}$ Random w.r.t. $\Delta\vec{v}$ as $\Delta\vec{x}\to 0$? (Assuming Smooth ρ?)
  i.e. Reverts to Standard DSMC as $\Delta\vec{x}\to 0$
- Potentially Induces $\Delta\vec{x}$ - $\Delta\vec{v}$ Correlations for Finite $\Delta\vec{x}$?

Discrete Form

$$\begin{aligned}\omega^{total} &= \vec{x}_i\times\vec{v}_i+\vec{x}_j\times\vec{v}_j\\ &= (\bar{x}+\Delta\vec{x})\times(\bar{v}+\Delta\vec{v})+(\bar{x}-\Delta\vec{x})\times(\bar{v}-\Delta\vec{v})\\ &= 2(\bar{x}\times\bar{v}+\Delta\vec{x}\times\Delta\vec{v})\\ &= 2(\bar{x}\times\vec{v})|_{\lim\Delta\vec{x}\to 0}\end{aligned}$$

Angular Momentum Conserving Binary Collisions

Given $\vec{v}_i$ and $\vec{v}_j$:

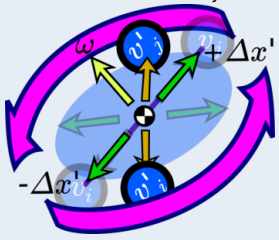

Distribution Statement A: Approved for Public Release; Distribution is Unlimited. PA# 19485

Distribution Statement A: Approved for Public Release; Distribution is Unlimited. AFRL-2021-4182

Angular Momentum Conservation with DSMC

Implementation of Angular Momentum Conservation

- Angular Momentum Conservation Direct Consequence of Boltzmann Equation:
  $\frac{\partial f}{\partial t}+\vec{v}\cdot\nabla_x f+\frac{q}{m}(\vec{E}+\vec{v}\times\vec{B})\cdot\nabla_v f=\int g_{ij}\sigma_{ij}(g_{ij},\Omega)(f_i' f_j'-f_i f_j)d\Omega d^3\vec{v}'$
  (i.e. Collisions happen at Points in x-Space)
- However: DSMC only Approximates $\lim \Delta\vec{x}\to 0$
- Bird's Conservation Implementation Description is Unhelpful
- Easier to Explain in terms of $\Delta\vec{x}$ and $\Delta\vec{v}$
- In-Plane Scatter Required for $\hat{\omega}=\hat{\omega}'$
- Angular Momentum Conserved if $\Delta\vec{x}$ Rotated with $\Delta\vec{v}$
- Modifies DSMC Random Ψ Angle to One Defined by $\Delta\vec{x}$ Plane
- $\Delta\vec{x}$ Random w.r.t. $\Delta\vec{v}$ as $\Delta\vec{x}\to 0$? (Assuming Smooth ρ?)
  i.e. Reverts to Standard DSMC as $\Delta\vec{x}\to 0$
- Potentially Induces $\Delta\vec{x}$ - $\Delta\vec{v}$ Correlations for Finite $\Delta\vec{x}$?

Enforces Discrete Conservation of Angular Momentum
But Potentially Induces Correlations with Density Gradients...

Discrete Form

$$\begin{aligned}\omega^{total} &= \vec{x}_i\times\vec{v}_i+\vec{x}_j\times\vec{v}_j\\ &= (\bar{x}+\Delta\vec{x})\times(\bar{v}+\Delta\vec{v})+(\bar{x}-\Delta\vec{x})\times(\bar{v}-\Delta\vec{v})\\ &= 2(\bar{x}\times\bar{v}+\Delta\vec{x}\times\Delta\vec{v})\\ &= 2(\bar{x}\times\bar{v})|_{\lim\Delta\vec{x}\to 0}\end{aligned}$$

Angular Momentum Conserving Binary Collisions

Given $\vec{v}_i$ and $\vec{v}_j$:

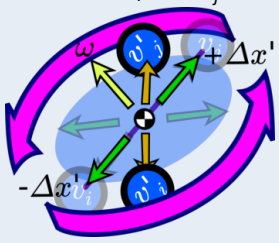

Distribution Statement A: Approved for Public Release; Distribution is Unlimited. PA# 19485

Distribution Statement A: Approved for Public Release; Distribution is Unlimited. AFRL-2021-4182

Angular Momentum Conservation with DSMC

Implementation of Angular Momentum Conservation

- Angular Momentum Conservation Direct Consequence of Boltzmann Equation:
  $\frac{\partial f}{\partial t}+\vec{v}\cdot\nabla_x f+\frac{q}{m}(\vec{E}+\vec{v}\times\vec{B})\cdot\nabla_v f=\int g_{ij}\sigma_{ij}(g_{ij},\Omega)(f_i' f_j'-f_i f_j)d\Omega d^3\vec{v}'$
  (i.e. Collisions happen at Points in x-Space)
- However: DSMC only Approximates $\lim \Delta\vec{x}\to 0$
- Bird's Conservation Implementation Description is Unhelpful
- Easier to Explain in terms of $\Delta\vec{x}$ and $\Delta\vec{v}$
- In-Plane Scatter Required for $\hat{\omega}=\hat{\omega}'$
- Angular Momentum Conserved if $\Delta\vec{x}$ Rotated with $\Delta\vec{v}$
- Modifies DSMC Random Ψ Angle to One Defined by $\Delta\vec{x}$ Plane
- $\Delta\vec{x}$ Random w.r.t. $\Delta\vec{v}$ as $\Delta\vec{x}\to 0$? (Assuming Smooth ρ?)
  i.e. Reverts to Standard DSMC as $\Delta\vec{x}\to 0$
- Potentially Induces $\Delta\vec{x}$ - $\Delta\vec{v}$ Correlations for Finite $\Delta\vec{x}$?

Enforces Discrete Conservation of Angular Momentum
But Potentially Induces Correlations with Density Gradients...

Good Idea?

Discrete Form

$$\begin{aligned}\omega^{total} &= \vec{x}_i\times\vec{v}_i+\vec{x}_j\times\vec{v}_j\\ &= (\bar{x}+\Delta\vec{x})\times(\bar{v}+\Delta\vec{v})+(\bar{x}-\Delta\vec{x})\times(\bar{v}-\Delta\vec{v})\\ &= 2(\bar{x}\times\bar{v}+\Delta\vec{x}\times\Delta\vec{v})\\ &= 2(\bar{x}\times\vec{v})|_{\lim\Delta\vec{x}\to 0}\end{aligned}$$

Angular Momentum Conserving Binary Collisions

Given $\vec{v}_i$ and $\vec{v}_j$:

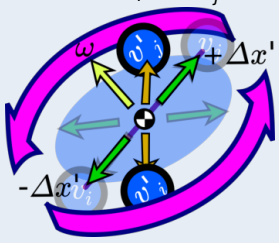

Distribution Statement A: Approved for Public Release; Distribution is Unlimited. PA# 19485

Distribution Statement A: Approved for Public Release; Distribution is Unlimited. AFRL-2021-4182

AFRL

Collisional Spherical Test Case

Spherical Potential Revisited with Coulomb Collisions

- Spherical Potential: $\Phi \propto 1/r$ on 50^3 mesh
- 2x Argon+ Ion Cubes at n_0 =1e18/m^3 in v_y and v_z Orbits

Initial Condition

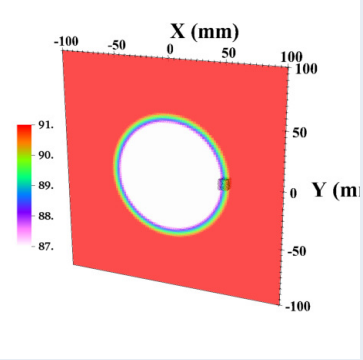

Distribution Statement A: Approved for Public Release; Distribution is Unlimited. PA# 19485

Distribution Statement A: Approved for Public Release; Distribution is Unlimited. AFRL-2021-4182

Collisional Spherical Test Case

Spherical Potential Revisited with Coulomb Collisions

- Spherical Potential: $\Phi \propto 1/r$ on 50^3 mesh
- 2x Argon+ Ion Cubes at n_0 =1e18/m^3 in v_y and v_z Orbits
- Non-Conservation of ω_y from Particle Push?

Collisionless Orbit

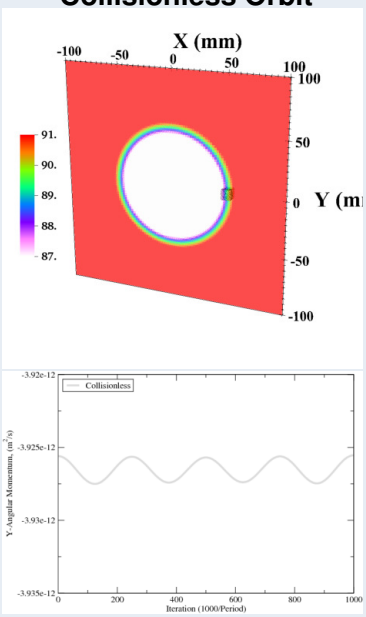

Distribution Statement A: Approved for Public Release; Distribution is Unlimited. PA# 19485

Distribution Statement A: Approved for Public Release; Distribution is Unlimited. AFRL-2021-4182

Collisional Spherical Test Case

Spherical Potential Revisited with Coulomb Collisions

- Spherical Potential: $\Phi \propto 1/r$ on 50^3 mesh
- 2x Argon+ Ion Cubes at n_0 =1e18/m^3 in v_y and v_z Orbits
- Non-Conservation of ω_y from Particle Push?
- Coulomb Collisions Included (Nanbu, Phys. Rev. E, 4642-4652, 1997)

Collisional Orbit

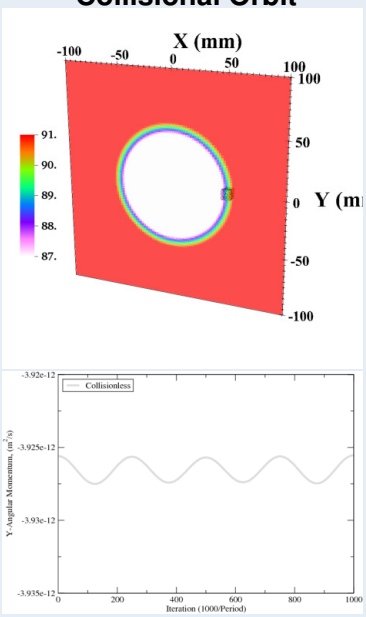

Distribution Statement A: Approved for Public Release; Distribution is Unlimited. PA# 19485

Distribution Statement A: Approved for Public Release; Distribution is Unlimited. AFRL-2021-4182

Collisional Spherical Test Case

Spherical Potential Revisited with Coulomb Collisions

- Spherical Potential: $\Phi \propto 1/r$ on 50^3 mesh
- 2x Argon+ Ion Cubes at n_0 =1e18/m^3 in v_y and v_z Orbits
- Non-Conservation of ω_y from Particle Push?
- Coulomb Collisions Included (Nanbu, Phys. Rev. E, 4642-4652, 1997)
- Significant Dispersion on 50^3 Mesh
- Rapid Deviation of ω_y from Collisionless Case (Note: Lost Particle at ≈700)

Collisional Orbit

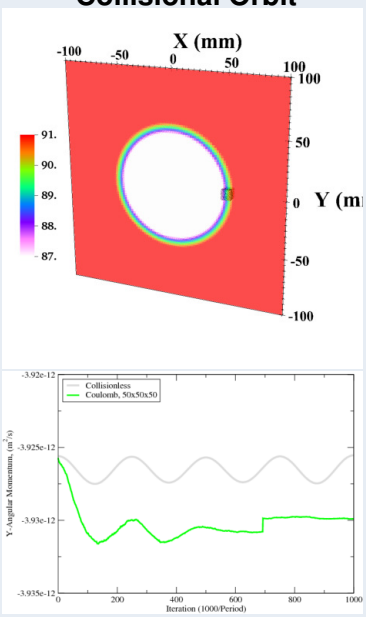

Distribution Statement A: Approved for Public Release; Distribution is Unlimited. PA# 19485

Distribution Statement A: Approved for Public Release; Distribution is Unlimited. AFRL-2021-4182

AFRL

Collisional Spherical Test Case

Spherical Potential Revisited with Coulomb Collisions

- Spherical Potential: $\Phi \propto 1/r$ on 50^3 mesh
- 2x Argon+ Ion Cubes at n_0 =1e18/m^3 in v_y and v_z Orbits
- Non-Conservation of ω_y from Particle Push?
- Coulomb Collisions Included (Nanbu, Phys. Rev. E, 4642-4652, 1997)
- Significant Dispersion on 50^3 Mesh
- Rapid Deviation of ω_y from Collisionless Case (Note: Lost Particle at ≈700)
- Physical or Numerical? Collision Cell Refinement (1,1,1)→(4,4,4)

Collisional Orbit: 50^3 Cells

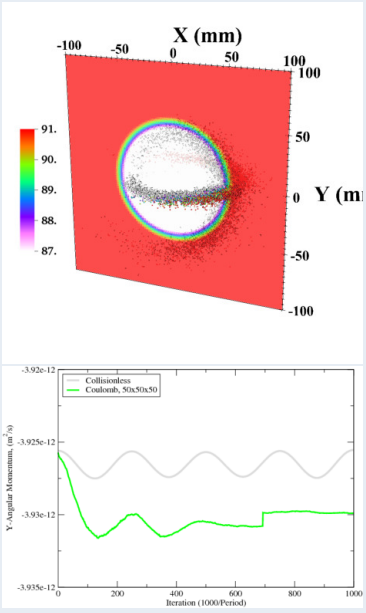

Distribution Statement A: Approved for Public Release; Distribution is Unlimited. PA# 19485

Distribution Statement A: Approved for Public Release; Distribution is Unlimited. AFRL-2021-4182

AFRL

Collisional Spherical Test Case

Spherical Potential Revisited with Coulomb Collisions

- Spherical Potential: $\Phi \propto 1/r$ on 50^3 mesh
- 2x Argon+ Ion Cubes at n_0 =1e18/m^3 in v_y and v_z Orbits
- Non-Conservation of ω_y from Particle Push?
- Coulomb Collisions Included (Nanbu, Phys. Rev. E, 4642-4652, 1997)
- Significant Dispersion on 50^3 Mesh
- Rapid Deviation of ω_y from Collisionless Case (Note: Lost Particle at ≈700)
- Physical or Numerical? Collision Cell Refinement (1,1,1)→(4,4,4)

Collisional Orbit: 100^3 Cells

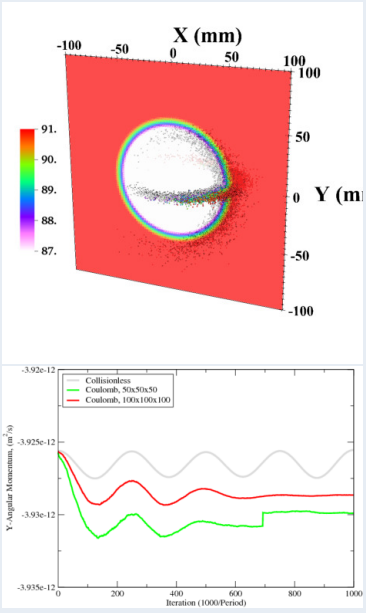

Distribution Statement A: Approved for Public Release; Distribution is Unlimited. PA# 19485

Distribution Statement A: Approved for Public Release; Distribution is Unlimited. AFRL-2021-4182

Collisional Spherical Test Case

Spherical Potential Revisited with Coulomb Collisions

- Spherical Potential: $\Phi \propto 1/r$ on 50^3 mesh
- 2x Argon+ Ion Cubes at n_0 =1e18/m^3 in v_y and v_z Orbits
- Non-Conservation of ω_y from Particle Push?
- Coulomb Collisions Included (Nanbu, Phys. Rev. E, 4642-4652, 1997)
- Significant Dispersion on 50^3 Mesh
- Rapid Deviation of ω_y from Collisionless Case (Note: Lost Particle at ≈700)
- Physical or Numerical? Collision Cell Refinement (1,1,1)→(4,4,4)
- Still not Converged? Damped, but also Mean < Collisionless Average

Collisional Orbit: 200^3 Cells

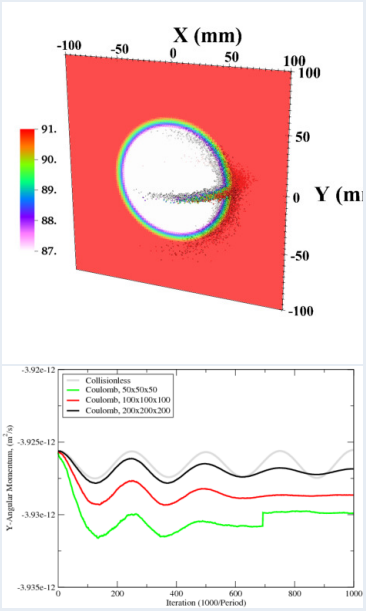

Distribution Statement A: Approved for Public Release; Distribution is Unlimited. PA# 19485

Distribution Statement A: Approved for Public Release; Distribution is Unlimited. AFRL-2021-4182

Collisional Spherical Test Case

Spherical Potential Revisited with Coulomb Collisions

- Spherical Potential: $\Phi \propto 1/r$ on 50^3 mesh
- 2x Argon+ Ion Cubes at n_0 =1e18/m^3 in v_y and v_z Orbits
- Non-Conservation of ω_y from Particle Push?
- Coulomb Collisions Included (Nanbu, Phys. Rev. E, 4642-4652, 1997)
- Significant Dispersion on 50^3 Mesh
- Rapid Deviation of ω_y from Collisionless Case (Note: Lost Particle at ≈700)
- Physical or Numerical? Collision Cell Refinement (1,1,1)→(4,4,4)
- Still not Converged? Damped, but also Mean < Collisionless Average
- Angular Momentum Conserving Collision better Initial Conservation

Conserved Collisions

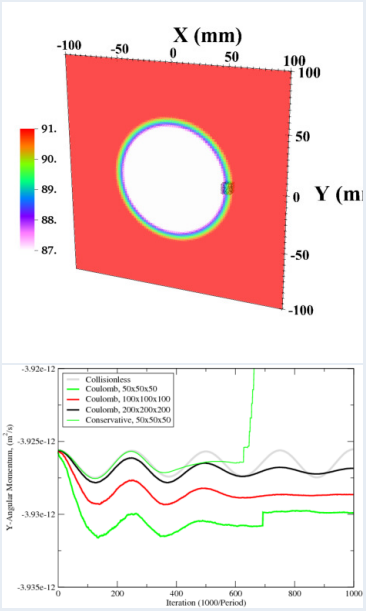

Distribution Statement A: Approved for Public Release; Distribution is Unlimited. PA# 19485

Distribution Statement A: Approved for Public Release; Distribution is Unlimited. AFRL-2021-4182

Collisional Spherical Test Case

Spherical Potential Revisited with Coulomb Collisions

- Spherical Potential: $\Phi \propto 1/r$ on 50^3 mesh
- 2x Argon+ Ion Cubes at n_0 =1e18/m^3 in v_y and v_z Orbits
- Non-Conservation of ω_y from Particle Push?
- Coulomb Collisions Included (Nanbu, Phys. Rev. E, 4642-4652, 1997)
- Significant Dispersion on 50^3 Mesh
- Rapid Deviation of ω_y from Collisionless Case (Note: Lost Particle at ≈700)
- Physical or Numerical? Collision Cell Refinement (1,1,1)→(4,4,4)
- Still not Converged? Damped, but also Mean < Collisionless Average
- Angular Momentum Conserving Collision better Initial Conservation
- More Particles Scattered Out of Domain?
- Potential Conserved only in Constant $\vec{E}$... Rotated Out of Cell?

Conserved: 50^3 Cells

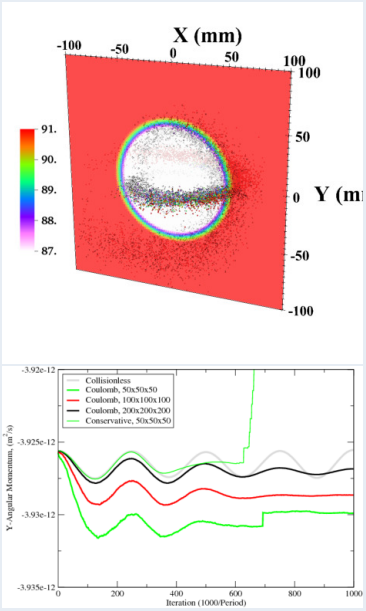

Distribution Statement A: Approved for Public Release; Distribution is Unlimited. PA# 19485

Distribution Statement A: Approved for Public Release; Distribution is Unlimited. AFRL-2021-4182

Collisional Spherical Test Case

Spherical Potential Revisited with Coulomb Collisions

- Spherical Potential: $\Phi \propto 1/r$ on 50^3 mesh
- 2x Argon+ Ion Cubes at n_0 =1e18/m^3 in v_y and v_z Orbits
- Non-Conservation of ω_y from Particle Push?
- Coulomb Collisions Included (Nanbu, Phys. Rev. E, 4642-4652, 1997)
- Significant Dispersion on 50^3 Mesh
- Rapid Deviation of ω_y from Collisionless Case (Note: Lost Particle at $\approx$700)
- Physical or Numerical? Collision Cell Refinement (1,1,1)$\rightarrow$(4,4,4)
- Still not Converged? Damped, but also Mean $<$ Collisionless Average
- Angular Momentum Conserving Collision better Initial Conservation
- More Particles Scattered Out of Domain?
- Potential Conserved only in Constant $\vec{E}$... Rotated Out of Cell?
- Better Convergence with Subcells $\rightarrow$ Mean matches Mean of Collisionless
- Dissipation Underresolved with $N_p/cell$?

Conserved: 100^3 **Cells**

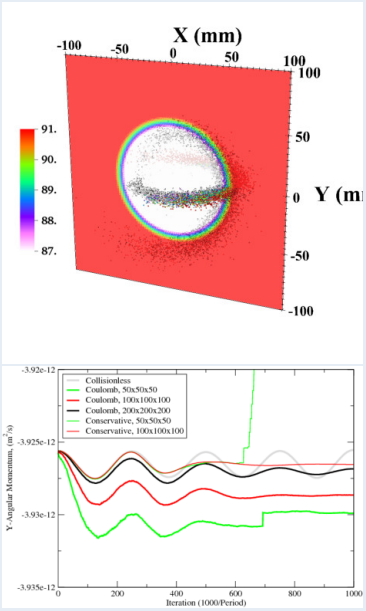

Distribution Statement A: Approved for Public Release; Distribution is Unlimited. PA# 19485

Distribution Statement A: Approved for Public Release; Distribution is Unlimited. AFRL-2021-4182

Collisional Spherical Test Case

Spherical Potential Revisited with Coulomb Collisions

- Spherical Potential: $\Phi \propto 1/r$ on 50^3 mesh
- 2x Argon+ Ion Cubes at n_0 =1e18/m^3 in v_y and v_z Orbits
- Non-Conservation of ω_y from Particle Push?
- Coulomb Collisions Included (Nanbu, Phys. Rev. E, 4642-4652, 1997)
- Significant Dispersion on 50^3 Mesh
- Rapid Deviation of ω_y from Collisionless Case (Note: Lost Particle at $\approx$700)
- Physical or Numerical? Collision Cell Refinement (1,1,1)$\rightarrow$(4,4,4)
- Still not Converged? Damped, but also Mean $<$ Collisionless Average
- Angular Momentum Conserving Collision better Initial Conservation
- More Particles Scattered Out of Domain?
- Potential Conserved only in Constant $\vec{E}$... Rotated Out of Cell?
- Better Convergence with Subcells $\rightarrow$ Mean matches Mean of Collisionless
- Dissipation Underresolved with $N_p/cell$?

Angular Momentum Conserved in Collision

PIC Field Coupling Inhibited? Future Work...

Conserved: 200^3 **Cells**

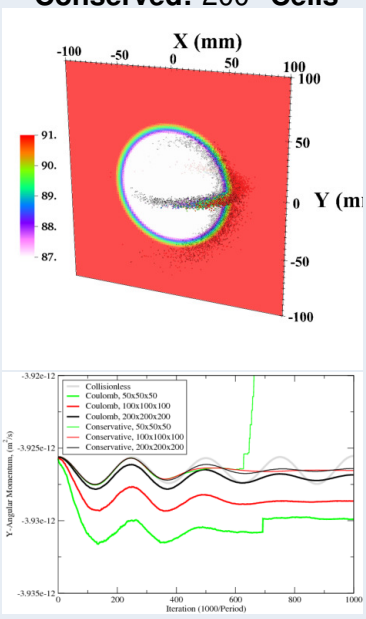

Distribution Statement A: Approved for Public Release; Distribution is Unlimited. PA# 19485

Distribution Statement A: Approved for Public Release; Distribution is Unlimited. AFRL-2021-4182

Conclusions and Future Work

Observations:

- Adding Binary Collisions to PIC May Cause Poor Conservation
- Prior Merge Work Showed 2nd-Order Potential Energy Conservation in General
- Potential Energy Conservation Enhanced with Low-Order Potential Basis
- Previous Options all Still Dispersive... Angular Momentum Instead?
- Need for Angular Momentum Conservation Long Debated in DSMC
- Potentially not Needed in Rarefied Flow and Abandoned?
- Exact Angular Momentum Conservation Possible at Expense of Collisional Randomness. Good Idea?

Future Work:

- Revisit Merge/Split for Angular Momentum Conservation (4-Particles?)
- Impact on Conservation of Angular Momentum Conserving Collision in PIC
- Convergence/Validation of Modified Method (Broken DSMC?)
- Continue Investigations of Anomalous Transport in HET

Angular Momentum

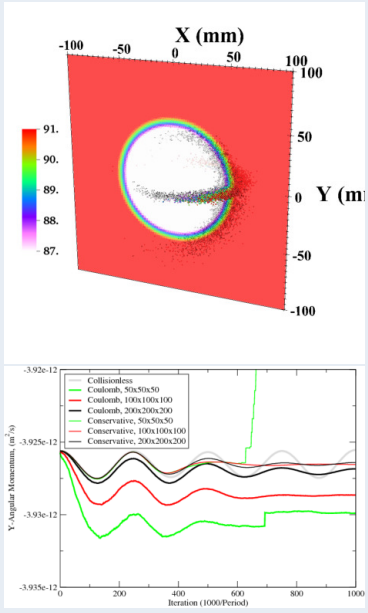

Distribution Statement A: Approved for Public Release; Distribution is Unlimited. PA# 19485

Distribution Statement A: Approved for Public Release; Distribution is Unlimited. AFRL-2021-4182

AFRL

Acknowledgments

Special Thanks:
Samuel J. Araki

This material is based upon work supported by the
Air Force Office of Scientific Research under award number
FA9550-17RQCOR465 (PO: Birkan)

Any opinions, finding, and conclusion or recommendations expressed in this material are those of the author and do not necessarily reflect the views of the United States Air Force.

Questions?

Distribution Statement A: Approved for Public Release; Distribution is Unlimited. PA# 19485

Distribution Statement A: Approved for Public Release; Distribution is Unlimited. AFRL-2021-4182

C Machine Learning for FRC Formation Dynamics **C-1**

C.1 Towards Predictive M&S in the Age of Big Data and Overfitting C-2

C.2 Analyzing the Field Reversed Configuration Formation Stage using Machine Learning Algorithms C-31

C.3 Using Neural Networks to Understand Field Reversed Configuration Formation Stage C-45

C.4 Improved Models and Understanding for Field-Reversed Configuration (FRC) Thrusters (2/2): Learning and Conclusion C-46

Distribution Statement A: Approved for Public Release; Distribution is Unlimited. AFRL-2021-4182

Towards Predictive M&S in the Age of Big Data and Overfitting

Robert Martin

In-space Propulsion Branch, Aerospace Systems Directorate Rocket Propulsion Division (AFRL/RQRS).

Joint work with Dan Eckhardt (AFRL/RQRS), Justin Koo (AFRL/RQRS), Christine Greve (Texas A&M), Timothy Gallagher (AFRL/RQTC), Ken Hara (Texas A&M).

Distribution Statement A: Approved for Public Release; Distribution is Unlimited; PA #19284

Distribution Statement A: Approved for Public Release; Distribution is Unlimited. AFRL-2021-4182

AFRL

M&S Challenge: Predicting Flight from Ground Test

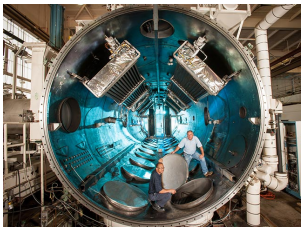

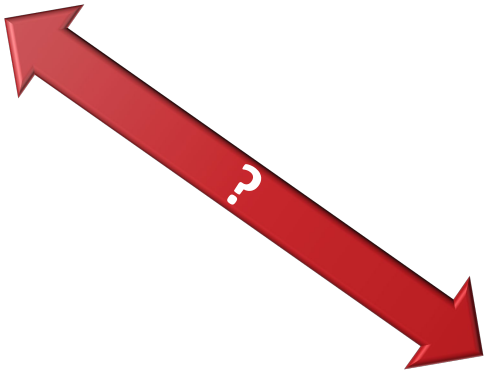

Distribution Statement A: Approved for Public Release; Distribution is Unlimited; PA #19284

Distribution Statement A: Approved for Public Release; Distribution is Unlimited. AFRL-2021-4182

AFRL

M&S Challenge: Predicting Flight from Ground Test

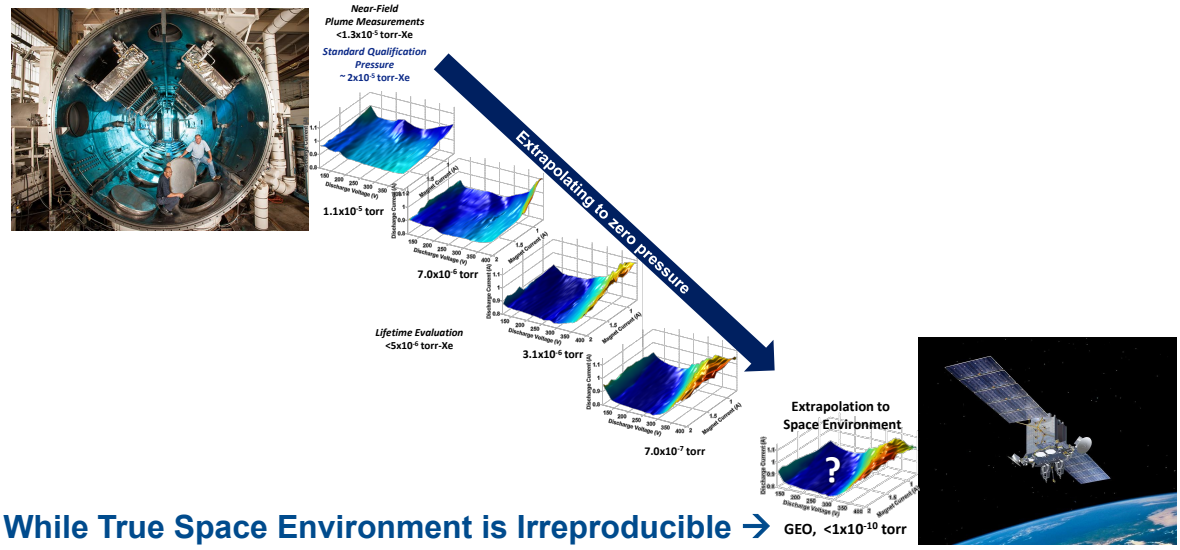

While True Space Environment is Irreproducible →

THE AIR FORCE RESEARCH LABORATORY

Distribution Statement A: Approved for Public Release; Distribution is Unlimited; PA #19284

Distribution Statement A: Approved for Public Release; Distribution is Unlimited. AFRL-2021-4182

AFRL

M&S Challenge: Predicting Flight from Ground Test

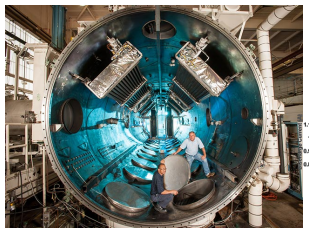

Near-Field Plume Measurements <1.3x10^{-5} torr-Xe

Standard Qualification Pressure ~ 2x10^{-5} torr-Xe

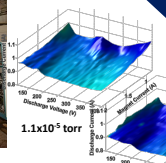

1.1x10^{-5} torr

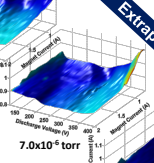

7.0x10^{-6} torr

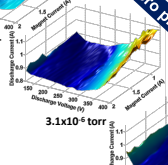

3.1x10^{-6} torr

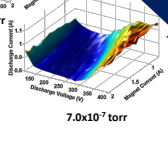

7.0x10^{-7} torr

Extrapolating to zero pressure

Demands Models with Extrapolative Power

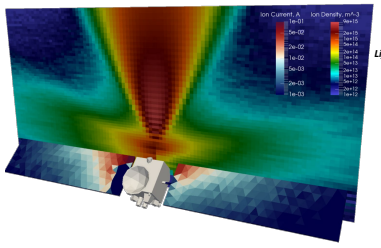

Lifetime Evaluation <5x10^{-6} torr-Xe

Extrapolation to Space Environment

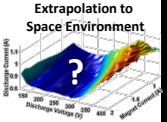

GEO, <1x10^{-10} torr

THE AIR FORCE RESEARCH LABORATORY

Distribution Statement A: Approved for Public Release; Distribution is Unlimited; PA #19284

Distribution Statement A: Approved for Public Release; Distribution is Unlimited. AFRL-2021-4182

Direct Numerical Simulation: Aren't Physics-Based Models Enough?

$$Life = f(thruster, environment, geometry, materials)?$$

Yes, and the Equations are Simple!

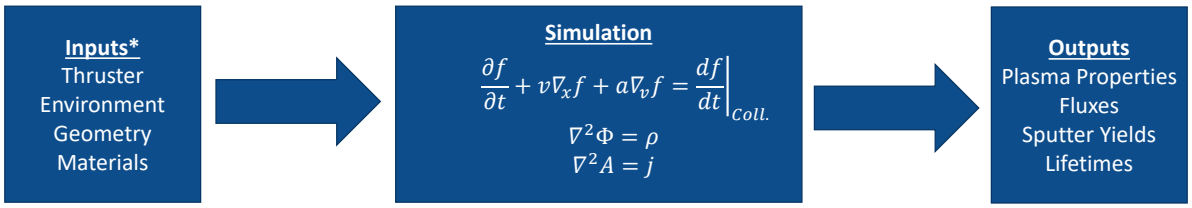

***Note:** Never Known Exactly. In Nonlinear (Chaotic) Systems Solutions May Causally Diverge

Distribution Statement A: Approved for Public Release; Distribution is Unlimited; PA #19284

Distribution Statement A: Approved for Public Release; Distribution is Unlimited. AFRL-2021-4182

AFRL

Direct Numerical Simulation: Aren't Physics-Based Models Enough?

$$Life = f(thruster, environment, geometry, materials)?$$

Yes, and the Equations are Simple*

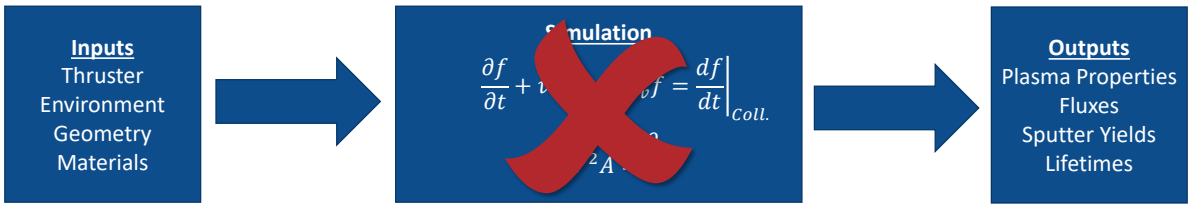

***To Write Down…**
But Completely Computationally Intractable
(Including On Any Conceivable Future Supercomputer)

Distribution Statement A: Approved for Public Release; Distribution is Unlimited; PA #19284

Distribution Statement A: Approved for Public Release; Distribution is Unlimited. AFRL-2021-4182

AFRL

Direct Numerical Simulation: Aren't Physics-Based Models Enough?

$$Life = f(thruster, environment, geometry, materials)?$$

Yes, and the Equations are Simple(r)!

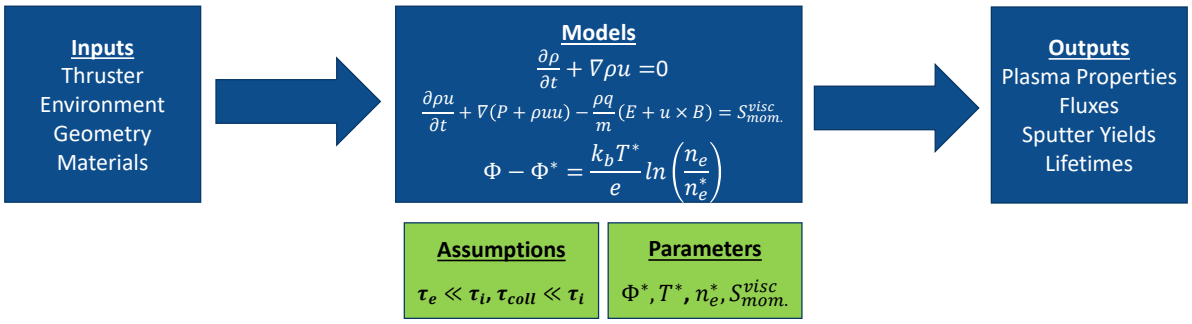

Instead We use Models

Distribution Statement A: Approved for Public Release; Distribution is Unlimited; PA #19284

Distribution Statement A: Approved for Public Release; Distribution is Unlimited. AFRL-2021-4182

AFRL

Direct Numerical Simulation: Aren't Physics-Based Models Enough?

$$Life = f(thruster, environment, geometry, materials)?$$

Yes, and the Equations are Simple(r)!

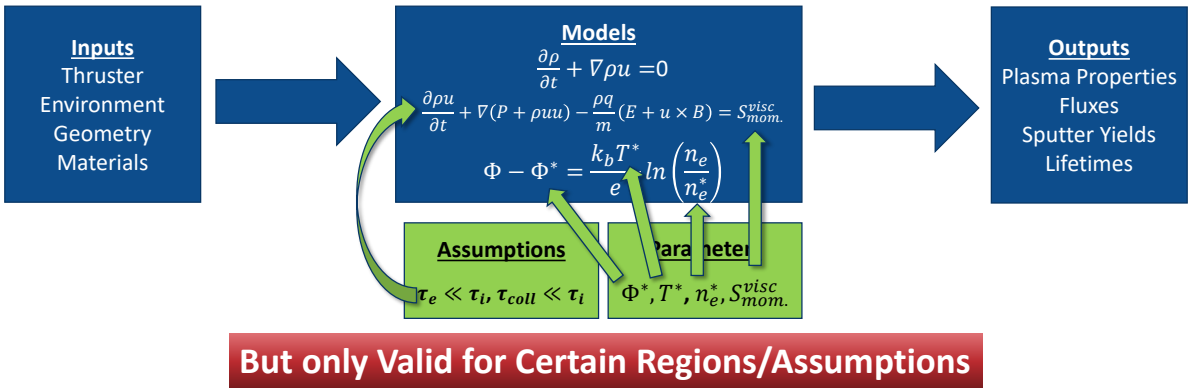

But only Valid for Certain Regions/Assumptions

Distribution Statement A: Approved for Public Release; Distribution is Unlimited; PA #19284

Distribution Statement A: Approved for Public Release; Distribution is Unlimited. AFRL-2021-4182

AFRL

Direct Numerical Simulation: Aren't Physics-Based Models Enough?

$$Life = f(thruster, environment, geometry, materials)?$$

Yes, and the Equations are Simple(r)!

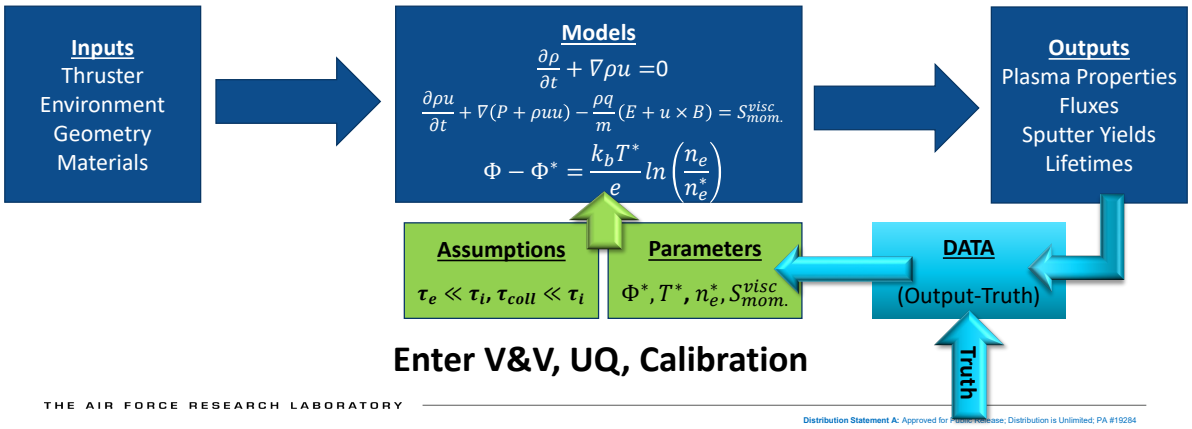

Distribution Statement A: Approved for Public Release; Distribution is Unlimited; PA #19284

Distribution Statement A: Approved for Public Release; Distribution is Unlimited. AFRL-2021-4182

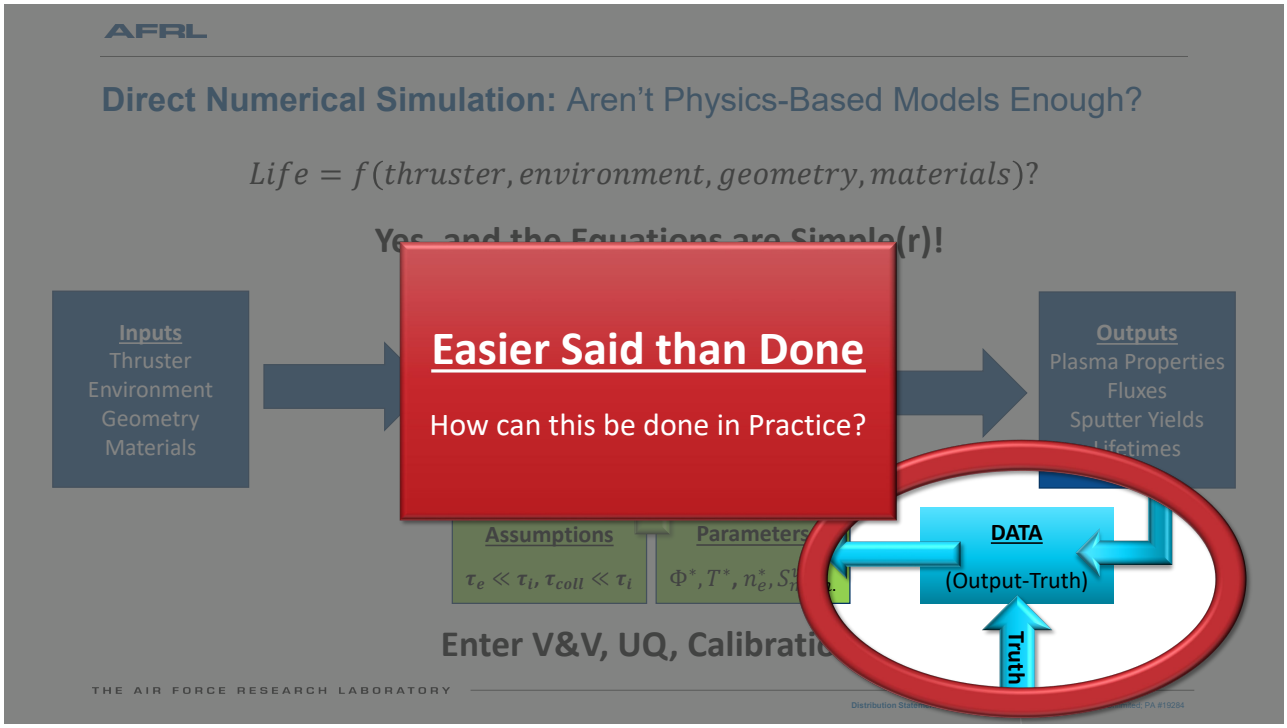

Distribution Statement A: Approved for Public Release; Distribution is Unlimited. AFRL-2021-4182

Solution: Why not just Machine Learn Everything?

- **Machine Learning!**
  Universal Approximation Thm. → Any $f^{arb.}(X^{In}; a_i)$ Possible

Find '<u>Best</u>' $f^{arb.}$ from all possible $f^{arb.}$ s.t.

$$Y^{Out} \cong f^{arb.}(X^{In}; a_i)$$

How? **Lots of Data**!

- **Still Underconstrained for Large Network!**
  But Large Network Required to Span Possibilities

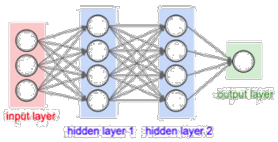

- **Regularization Needed:**
  Success of CNNs more from "C" not "NN"
  Possible for Physical Assumptions/Symmetries?

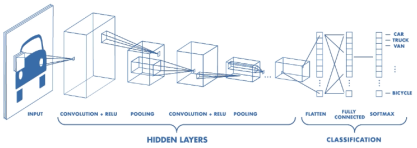

- **Quality of Results Depends on Assumptions**

Distribution Statement A: Approved for Public Release; Distribution is Unlimited; PA #19284

Distribution Statement A: Approved for Public Release; Distribution is Unlimited. AFRL-2021-4182

AFRL

Machine Learning: Who Needs Physics-Based Models?

$$Life = f(thruster, environment, geometry, materials)?$$

Yes, and the Equations ~~are Simple~~ Don't Matter?

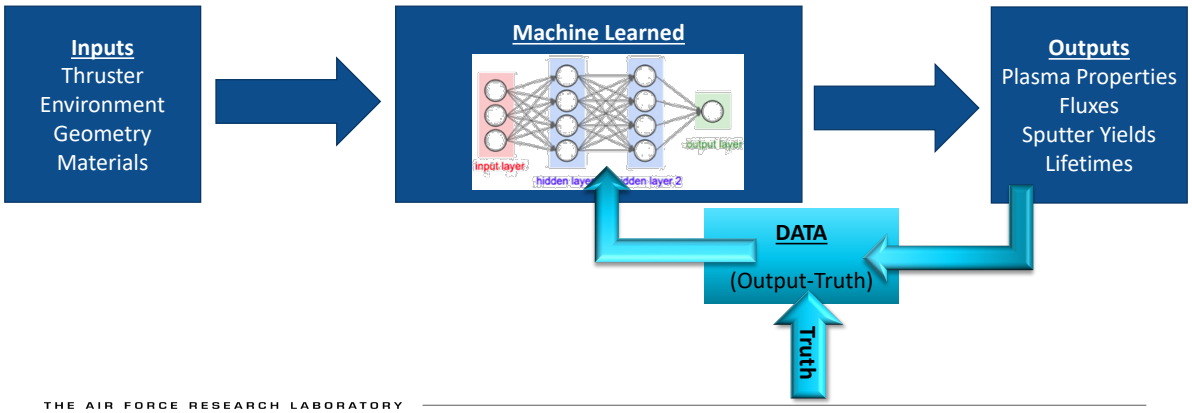

Distribution Statement A: Approved for Public Release; Distribution is Unlimited; PA #19284

Distribution Statement A: Approved for Public Release; Distribution is Unlimited. AFRL-2021-4182

AFRL

Machine Learning: Who Needs Physics-Based Models?

$$Life = f(thruster, environment, geometry, materials)?$$

Yes, and the Equations ~~are Simple~~ Don't Matter?

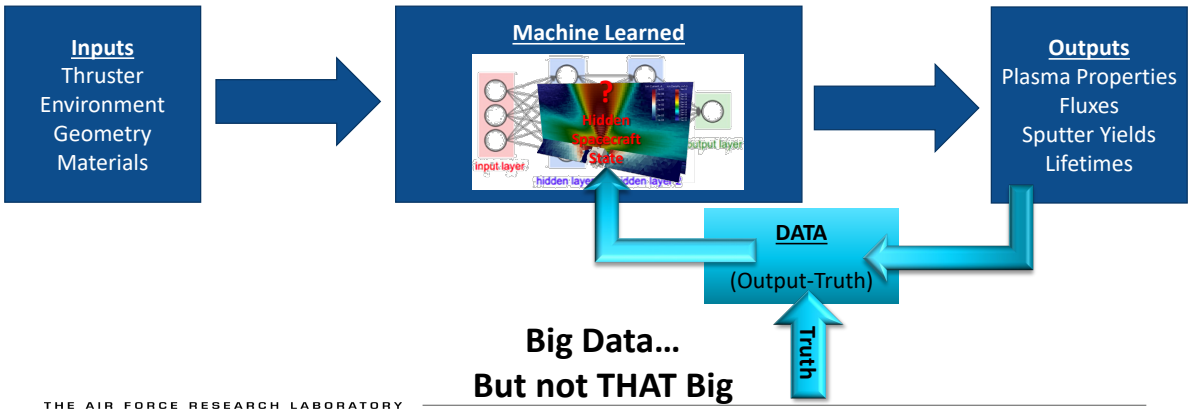

Big Data…
But not THAT Big

THE AIR FORCE RESEARCH LABORATORY

Distribution Statement A: Approved for Public Release; Distribution is Unlimited; PA #19284

Distribution Statement A: Approved for Public Release; Distribution is Unlimited. AFRL-2021-4182

AFRL

Machine Learning: What About Replacing Empirical (Closure) Models?

$$Life = f(thruster, environment, geometry, materials)?$$

Possibly, and the Networks Can be Small(er)!

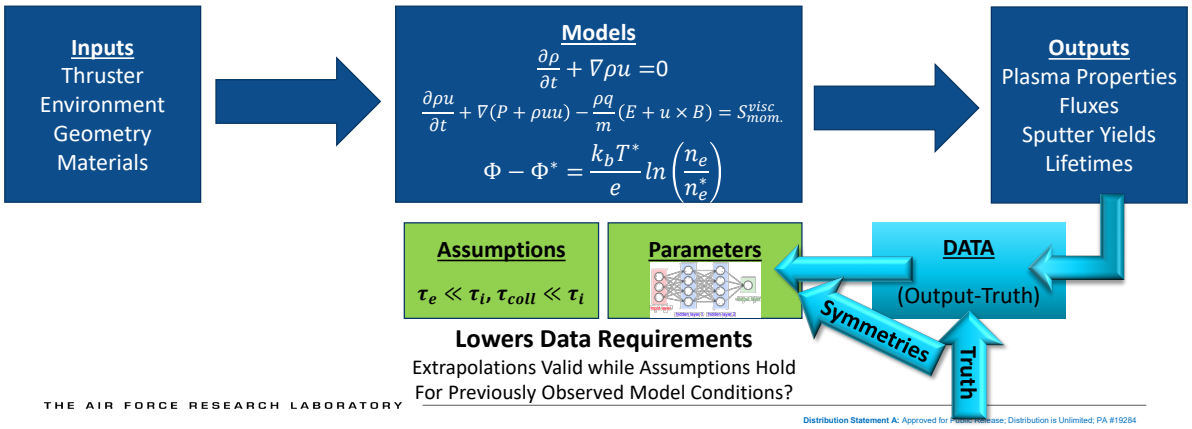

Distribution Statement A: Approved for Public Release; Distribution is Unlimited; PA #19284

Distribution Statement A: Approved for Public Release; Distribution is Unlimited. AFRL-2021-4182

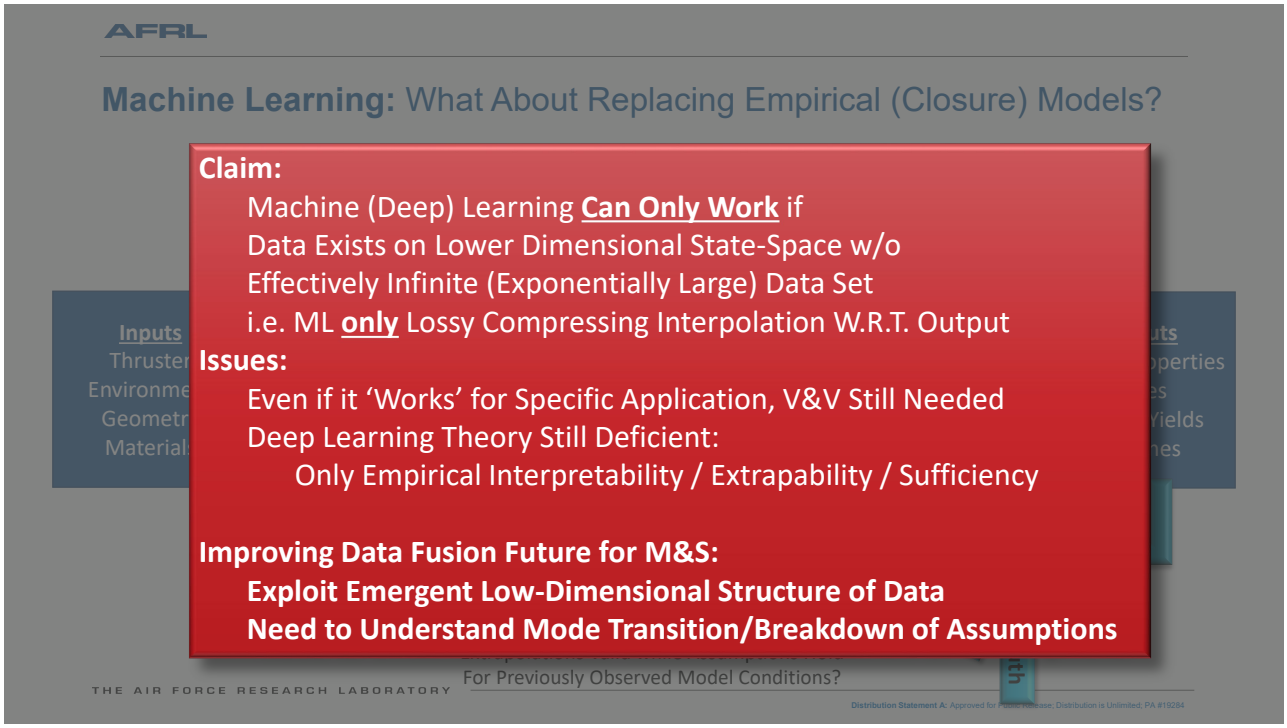

Distribution Statement A: Approved for Public Release; Distribution is Unlimited. AFRL-2021-4182

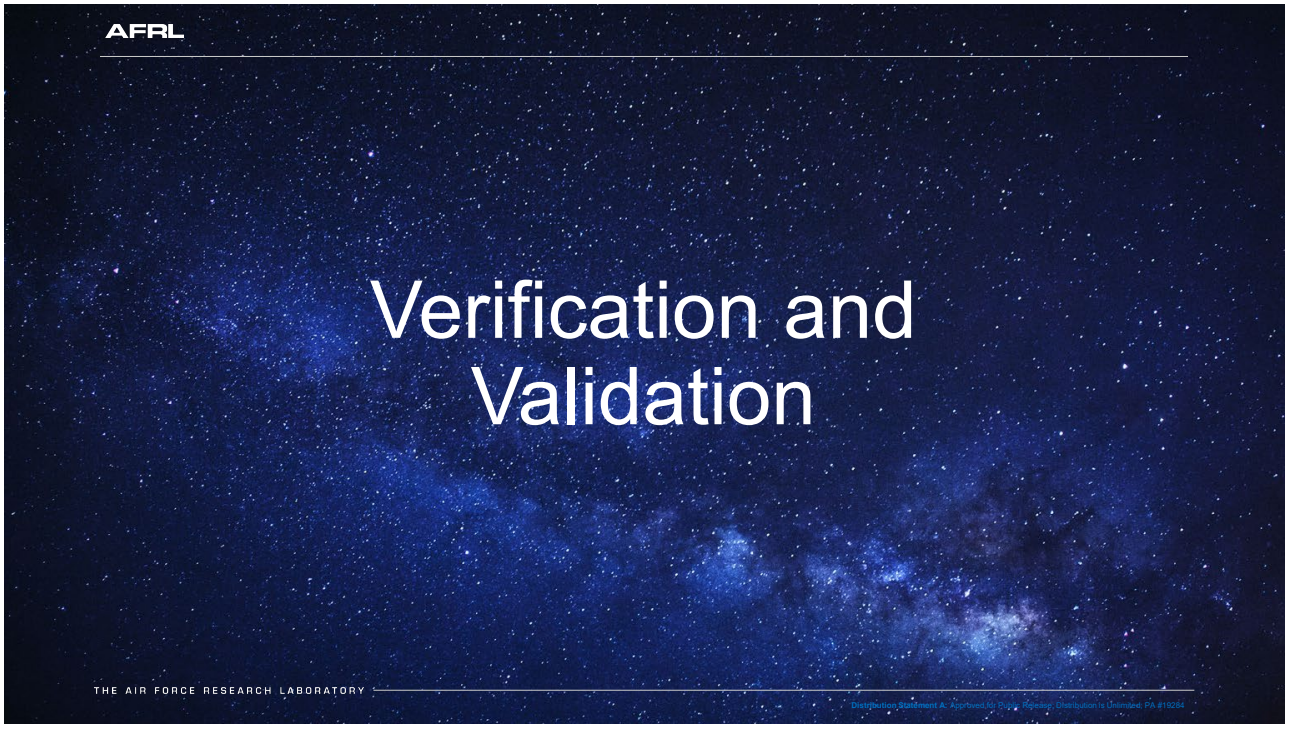

Distribution Statement A: Approved for Public Release; Distribution is Unlimited. AFRL-2021-4182

Verification and Validation

- Often Performed at Asymptotic Limits
  - Asymptotic Limit → Exact Solutions
  - Provides Convergence Tests
  - Irrelevant in Regimes of Interest?
  - Convergence in Limits ≠ V&V

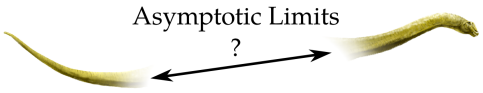

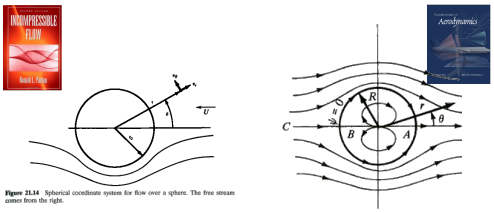

Figure 21.14 Spherical coordinate system for flow over a sphere. The free stream comes from the right.

Flow over a cylinder

$$\psi = V_\infty r \sin\theta - \frac{\kappa}{2\pi}\frac{\sin\theta}{r}$$

Distribution Statement A: Approved for Public Release; Distribution is Unlimited; PA #19284

Distribution Statement A: Approved for Public Release; Distribution is Unlimited. AFRL-2021-4182

Verification and Validation

- Often Performed at Asymptotic Limits
  - Asymptotic Limit → Exact Solutions
  - Provides Convergence Tests
  - Irrelevant in Regimes of Interest?
  - Convergence in Limits ≠ V&V
- Complex Behaviors often Between Limits
  - i.e. Turbulence between Simple Limits
  - Traditional Verification may Fail

From Exact (Asymptotic) Convergence to Statistical Convergence…

Nothing Between?

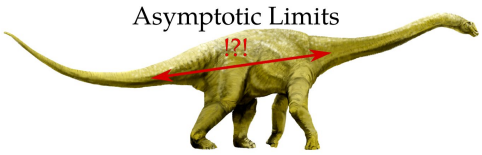

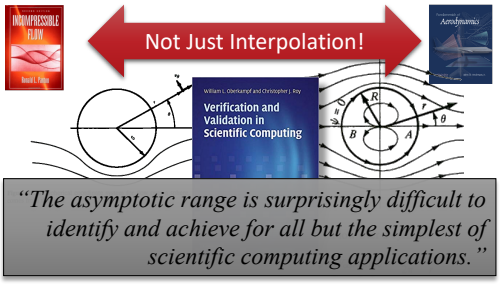

"The asymptotic range is surprisingly difficult to identify and achieve for all but the simplest of scientific computing applications."

Distribution Statement A: Approved for Public Release; Distribution is Unlimited; PA #19284

Distribution Statement A: Approved for Public Release; Distribution is Unlimited. AFRL-2021-4182

The Problem with Underconstrained V&V

- Design Requirements rely on QoIs
  - Performance-Based Designing
  - Is Goal of Simulation to Predict QoIs?
- Many QoIs are Insensitive
  - Initial Designs via Back of Envelope
  - Based on Equilibrium and Efficiency
  - Thrust/Temperature/Etc. Appropriate?
- Goal of High Fidelity Simulation…
  - Understand Deviations from Design?
  - Many DOF + Few QoI → Overfit!
  - Occam's Razor:
    Model Parameter vs. #QoI

Right Answer Probably for Wrong Reason

(∴More Wrong Fits than Right)

Unique Validation Requires Invertability to State

Fundamental Theorem of Linear Algebra

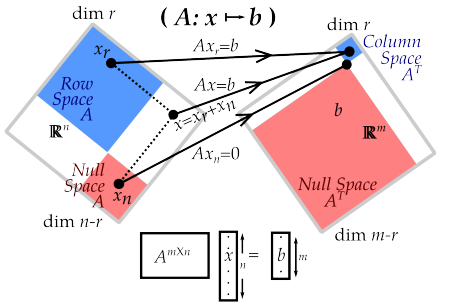

Underconstrained Problems

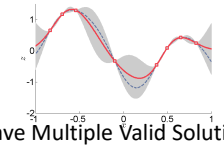

Have Multiple Valid Solutions

Distribution Statement A: Approved for Public Release; Distribution is Unlimited; PA #19284

Distribution Statement A: Approved for Public Release; Distribution is Unlimited. AFRL-2021-4182

Distribution Statement A: Approved for Public Release; Distribution is Unlimited. AFRL-2021-4182

AFRL

Compression of State Space

Removing Irrelevant Information

Reference Signal

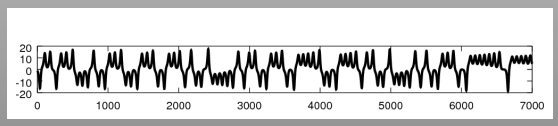

ML as Optimal Lossy Compression

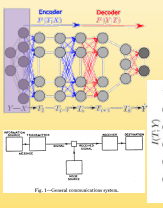

Opening the black box of Deep Neural Networks via Information

Schwartz-Ziv & Tishby

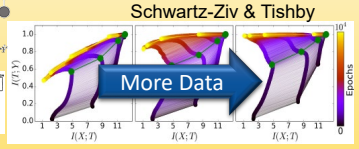

Linear Methods

Moments

Mean: 0.524
Min/Max: -18.75, 18.91
Std. Dev: 7.9221

Power Spectra

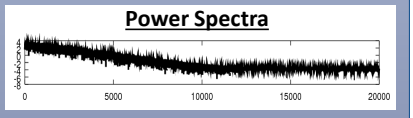

⋮
PDF
Wavelets
SVD

Time-Delay Embedding

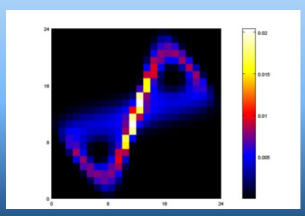

THE AIR FORCE RESEARCH LABORATORY

Distribution Statement A: Approved for Public Release; Distribution is Unlimited; PA #19284

Distribution Statement A: Approved for Public Release; Distribution is Unlimited. AFRL-2021-4182

AFRL

Compression of State Space

Removing Irrelevant Information

Reference Signal

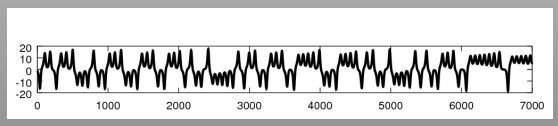

ML as Optimal Lossy Compression

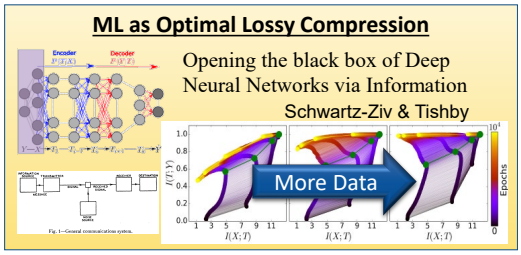

Linear Methods

Moments

Mean: 0.524
Min/Max: -18.75, 18.91
Std. Dev: 7.9221

Power Spectra

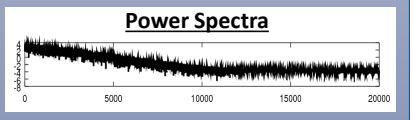

⋮
PDF
Wavelets
SVD

Time-Delay Embedding

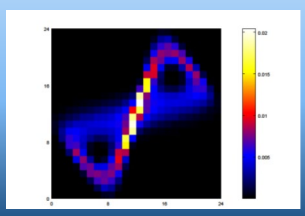

THE AIR FORCE RESEARCH LABORATORY

Distribution Statement A: Approved for Public Release; Distribution is Unlimited; PA #19284

Distribution Statement A: Approved for Public Release; Distribution is Unlimited. AFRL-2021-4182

AFRL

Takens' Theorem

Motivation for Time-Delay Delay Representations

The System State, $\vec{x}(t)$, Defines all Observables, $y(\vec{x})$, for $t \to \infty$

Takens' Theorem: *For General Smooth Observables, $y(\vec{x})$*
The Manifold, M_Y, of the Time-Delay Vectors:
$$\{y(\vec{x}_i), y(\vec{x}_i + \Delta t), \cdots, y(\vec{x}_i + k\Delta t)\}$$
is Diffeomorphic to Original State Space Attractor, M
if $k > 2 \times (Attractor\ Dimension, d_a)$

Time Delay Embedding Encodes Information about State-Space Flow
(Destroyed by Statistical Representations)

Convergent Cross Mapping (CCM)

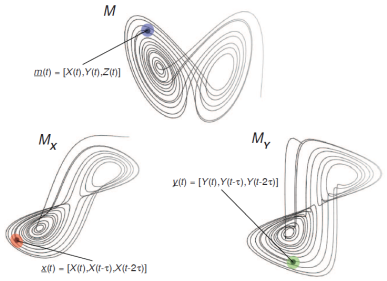

Detecting Causality in Complex Ecosystems –Sugihara et. Al, *Science*, 2012

Synchronized "State+Flow" → Validation for ALL Observables
(i.e. Right Answer for Right Reason)

Distribution Statement A: Approved for Public Release; Distribution is Unlimited; PA #19284

Distribution Statement A: Approved for Public Release; Distribution is Unlimited. AFRL-2021-4182

AFRL

Takens' Theorem

Motivation for Time-Delay Delay Representations

The System State, $\vec{x}(t)$, Defines all Observables, $y(\vec{x})$, for $t \to \infty$

Takens' Theorem: *For General Smooth Observables, $y(\vec{x})$*
The Manifold, M_Y, of the Time-Delay Vectors:
$$\{y(\vec{x}_i), y(\vec{x}_i + \Delta t), \cdots, y(\vec{x}_i + k\Delta t)\}$$
is Diffeomorphic to Original State Space Attractor, M
*if $k > 2 \times$ (**Attractor Dimension, d_a**)*

Time Delay Embedding Encodes Information about State-Space Flow
(Destroyed by Statistical Representations)

Convergent Cross Mapping (CCM)

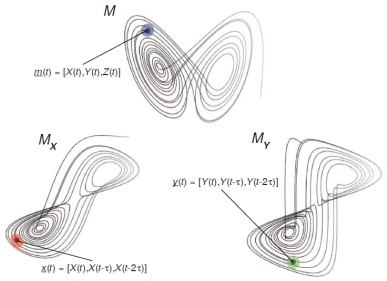

Detecting Causality in Complex Ecosystems –Sugihara et. Al, *Science*, 2012

Synchronized "State+Flow" → Validation for ALL Observables
(i.e. Right Answer for Right Reason)

Distribution Statement A: Approved for Public Release; Distribution is Unlimited; PA #19284

Distribution Statement A: Approved for Public Release; Distribution is Unlimited. AFRL-2021-4182

Evidence for Low-D: Causal Relationships in EP-TEMPEST

Convergent Cross Mapping (CCM)

- Constructs Nonlinear Maps from Data
  X→Y: $\vec{y} = g(\vec{x})$ & Y→X: $\vec{x} = g^{-1}(\vec{y})$
- Supports Chaotic Signal Reconstruction
- Bidirectional High ρ_{ccm} → "Generalized Synchrony"
  Observables nonlinear f of Low-D State!
  NOT Independent Variables
- CCM Identifies Causation: Thruster → Cage
  Despite Very Low SNR in Cage Signal
- Deviation from Low-D Implies **Anomalous Behavior**

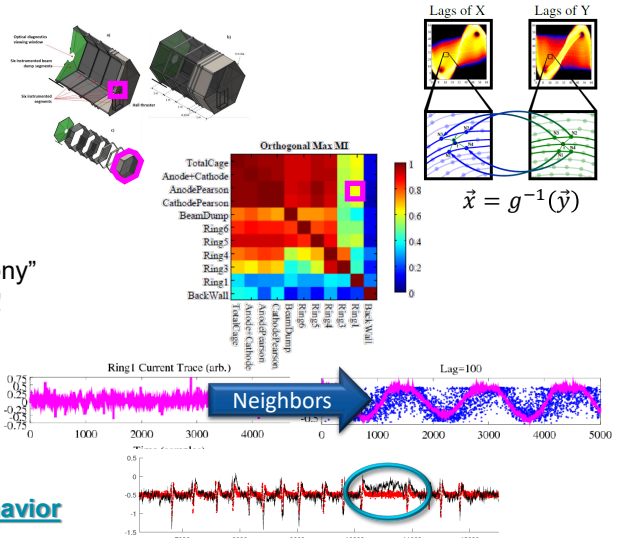

Eckhardt, Koo, Martin, Holmes, Hara, "Spatiotemporal data fusion and manifold reconstruction in Hall thrusters," PSST, April 2019

Figure 16. 3D SNR reconstruction (ThrusterSupportPotential→AnodePearson)

Distribution Statement A: Approved for Public Release; Distribution is Unlimited; PA #19284

Distribution Statement A: Approved for Public Release; Distribution is Unlimited. AFRL-2021-4182

Verification Results[1]: Blackbox Model Calibration of HPHall

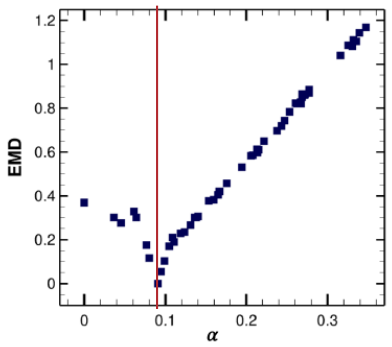

FIG. 11. The EMD response surface of the coefficient for the Bohm mobility model, α, when the reference solution is chosen to be $\alpha_{exact} = 0.0909$.

Simultaneous Convergence of Other Observables

TABLE III. Optimization of α for a HET discharge plasma using HPHall.

	Dynamic	Static	
		Run 1	Run 2
α range	$0.05-0.2$	$0.08-0.1$	$0.085-0.095$
Optimal α	0.089	0.0907	0.0909
(ε_α)	(-2.1%)	(-0.22%)	($<0.01\%$)
EMD (A)	**0.029**	**0.0203**	**0.0201**
Current, I_d	0.777 A	0.792 A	0.791 A
(ε_I)	(-1.74%)	($+0.15\%$)	($+0.05\%$)
Thrust, T	12.4 mN	12.6 mN	12.6 mN
(ε_T)	(-1.25%)	($+0.21\%$)	($+0.15\%$)
Isp	1476.71 s	1498.61 s	1497.74 s
(ε_{Isp})	(-1.3%)	($+0.21\%$)	($+0.15\%$)
η	46.39%	46.88%	46.87%
(ε_η)	(-0.77%)	($+0.26\%$)	($+0.25\%$)

Better than Hand Calibration Directly on Thrust/ISP Data

Synchronized Dynamics = Synchronized Observables

1. Greve, Hara, Martin, Eckhardt, Koo, "Data-Driven Calibration Model for Nonlinear Dynamics of Physical Phenomena," Submitted, J. Appl. Phys.

Distribution Statement A: Approved for Public Release; Distribution is Unlimited; PA #19284

Distribution Statement A: Approved for Public Release; Distribution is Unlimited. AFRL-2021-4182

AFRL

Goal: Synchronize Model to Ground & Validate

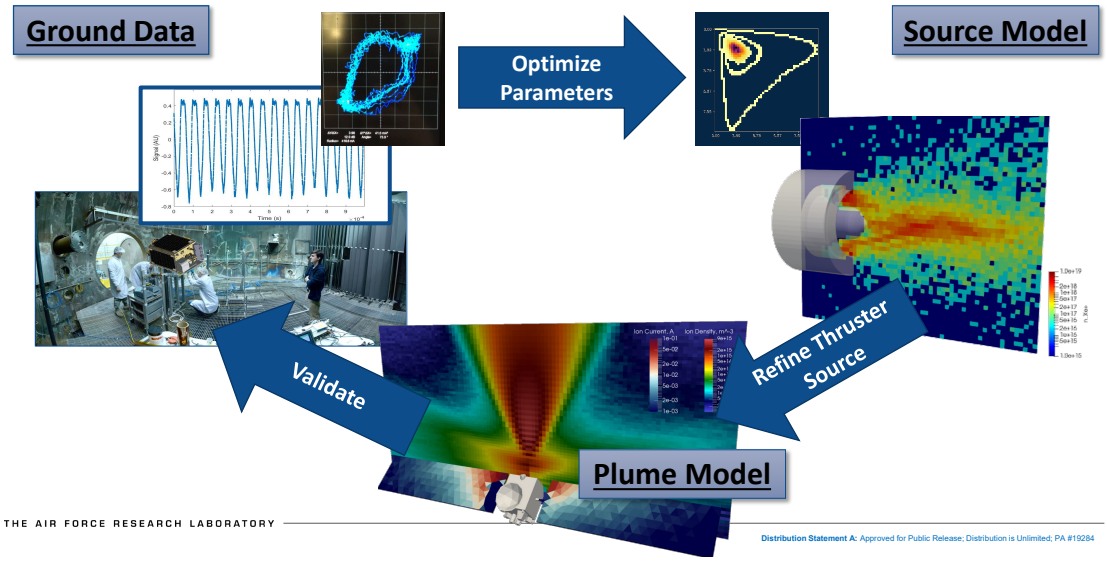

THE AIR FORCE RESEARCH LABORATORY

Distribution Statement A: Approved for Public Release; Distribution is Unlimited; PA #19284

Distribution Statement A: Approved for Public Release; Distribution is Unlimited. AFRL-2021-4182

Acknowledgements

The authors would like to acknowledge the support provided by the Air Force Office of Scientific Research (AFOSR),

Grant No. 17RQCOR465 (PO: Birkan)

Any opinions, finding, and conclusions or recommendations expressed in this material are those of the author and do not necessarily reflect the views of the United States Air Force.

Distribution Statement A: Approved for Public Release; Distribution is Unlimited; PA #19284

Distribution Statement A: Approved for Public Release; Distribution is Unlimited. AFRL-2021-4182

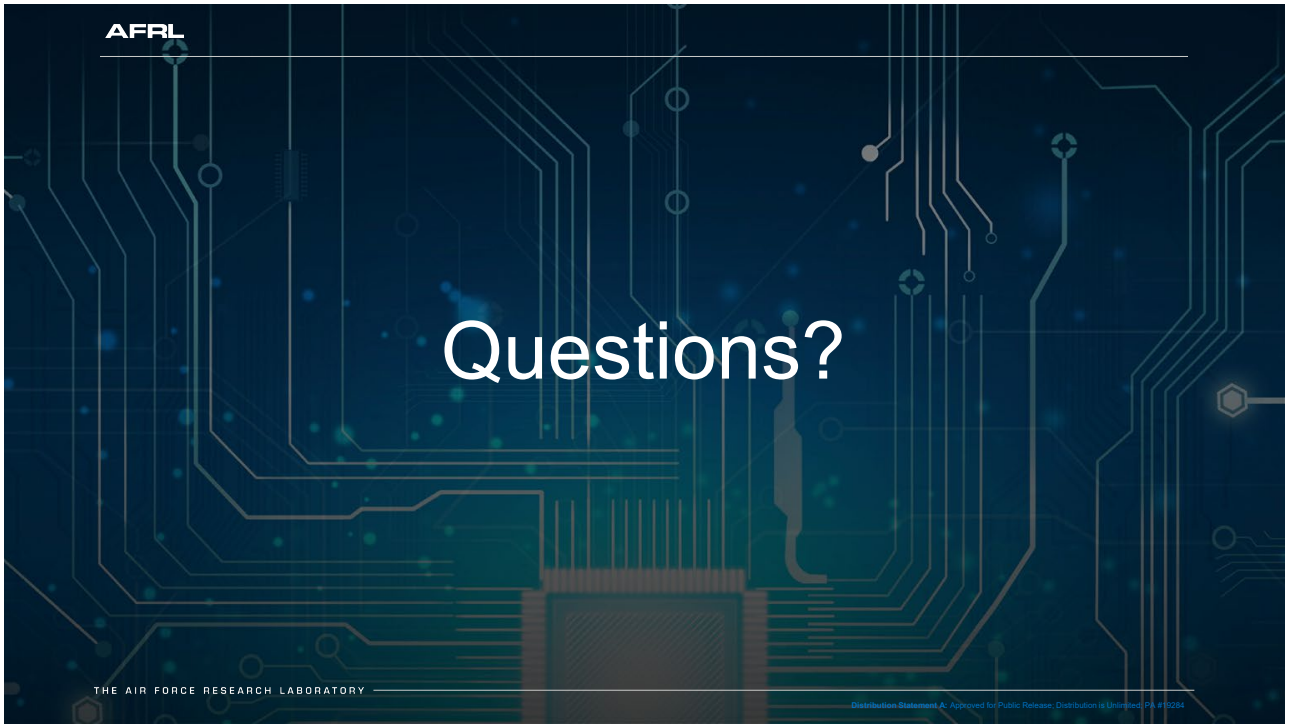

Distribution Statement A: Approved for Public Release; Distribution is Unlimited. AFRL-2021-4182

Analyzing the Field Reversed Configuration Formation Stage using Machine Learning Algorithms

Éder M. Sousa*,[1], Robert C. Lilly[1], Robert S. Martin[2], Richard J. Abrantes[3]
[1]ERC Inc., Edwards AFB, CA
[2]Air Force Research Lab, Edwards AFB, CA
[3]UCLA, Los Angeles, CA

Multi-scale and multi-physics processes dominate the formation stage of an field reversed configuration (FRC), which require a multi-fluid description of the plasma. In addition, FRC formation using rotating magnetic fields (RMF) requires that the RMF penetrate into the plasma. The RMF penetration is governed by the RMF frequency and intensity as well as the plasma resistivity. A theoretical threshold is needed to be achieved for full RMF penetration. In the current research we show that this theoretical limit is a necessary but sufficient condition. We use machine learning (ML) deep neural networks (DNN) to help determine the boundary that separates cases where the RMF leads to an axial field reversal. Of all the ML algorithms that we tried, the highest accuracy score of 0.920 was achieved using DNN.

***Index Terms*—Multi-Fluid Plasma Model, Field Reversed Configuration, Plasma Simulations, Machine Learning, Deep Neural Networks**

I. Introduction

With the development of faster computer and mathematical algorithms, more complex plasma problems can be simulated with a reasonably level of accuracy and in a timely manner. The computational challenges lie in the multi-scale and multi-physics aspects of the problems; approximate models are known to miss important physics, while fully detailed, kinetic simulations are computationally prohibitive.

A good compromise plasma model that balances complexity and computational cost is the multi-fluid plasma (MFP) model. The MFP model describes each os the plasma species as a separate fluid, where the mass, momentum, and energy of each species is evolved separately. The species interact with each other through collisions and electromagnetic fields. [1] The equations for the MFP model are derived by taking velocity moments of the Boltzmann equation. The system is closed with an equation-of-state usually assuming an isotropic pressure. The electromagnetic fields are advanced in time using Maxwell's equations.

The MFP model has a broad range of time-scales because of the different species sound speed, as the characteristic speeds of the model, as well as, the speed-of-light. These speeds differ greatly and can cause simulations to become very stiff by requiring very small time-steps. The model is a generalization of the magnetohydrodynamic [2] (MHD) model and makes no asymptotic approximations about the high frequency oscillations or the electron inertia. As a result, the MFP model captures more waves than MHD, including waves that propagate faster than the magnetosonic speed. [3]

The numerical scheme chosen is the discontinuous Galerkin (DG) finite element method due to its ability to capture shocks, conservation properties, high-order accuracy, and for providing flux/source coupling. This last benefit is particularly useful in multi-physics problems such as out target application. The DG method version implemented is described in Ref. [4].

*esousa@rand.org, Distribution A: Approved for public release; distribution unlimited. PA clearance No. 18549

Distribution Statement A: Approved for Public Release; Distribution is Unlimited. AFRL-2021-4182

The MFP model and the DG method were implemented on a computational framework, APOLLO, developed at the Air Force Research Laboratory. The framework uses the Portable, Extensible Toolkit for Scientific Computation [5] (PETSc), for data management and parallelization. PETSc is designed to simplify the development of large-scale scientific application codes in Fortran, C, C++, and Python.

One of the applications of interest is the Electrodeless Lorentz Force thruster [6], which creates a high-density, magnetized plasmoid known as a Field Reversed Configuration [7] (FRC) employing a Rotating Magnetic Field (RMF). The FRC is a self-organized magnetized plasma configuration in the shape of a highly compact toroid, characterized by the presence of closed magnetic field lines and a high ratio of toroidal to poloidal current. Since FRCs are magnetically insulated from the external field, they can readily detach from the confining external field, and can easily be translated and accelerated by applied magnetic fields.

Previous analysis of the formation of a FRC using a RMF have determined a threshold limit [8] combination of the RMF frequency and intensity required to be exceeded in order to achieve full field penetration. An empirical equations has been determined for the field penetration threshold. Our goal is to determine how computational data compares with said threshold.

Experimental and simulation data are riddled with uncertainty. One way that we address uncertainty quantification is to use machine learning algorithms that are able to detect patterns on the data, learn from them, and make predictions with a specific probability of occurrence. Although four classification algorithms are used, logistic regression [9], K-Nearest Neighbors [10] (KNN), Support Vector Machines [11] (SVM), and Random Forest [11] were used, results are presented only using Deep Neural Networks [12], [13] because it had the best accuracy score. The main objective is to determine parameter regimes where full RMF penetration is possible and axial magnetic field reversal occurs.

The paper is organized as follows, the background of the problem is described in Sec. II. Section III describes the physical model used in the simulations. Section IV shows the framework schematic. The initial results for the FRC formation studies is presented in Sec. V and the machine learning analysis is done in Sec. VI. The paper is summarized in Sec. VII.

II. Background

The FRC formation system with a RMF can be characterized by two dimensionless parameters, $\lambda = R/\delta$ where $\delta = (2\eta/\mu_o\omega)^{1/2}$ is the classical skin depth, and by $\gamma = \omega_{ce}/\nu_{ei}$ where $\nu_{ei} = (ne^2/m_e)$ is the electron-ion collision frequency. These two parameters can be rewritten in terms that are more relevant to the problem,

$$\lambda = R\left(\frac{\mu_o\omega}{2\eta}\right)^{1/2}, \tag{1}$$

which is mainly dependent on the RMF frequency, ω, and

$$\gamma = \frac{1}{e}\left(\frac{B_\omega}{n\eta}\right), \tag{2}$$

mainly dependent on the magnitude of the RMF, B_ω. Where R is the chamber radius, e is the electron charge, n is the number density, and η is the plasma resistivity.

Forming an FRC using an RMF requires that the field is able to penetrate the plasma, overcoming the resistive effect of electron-ion collisions. In the work of Hugrass and Grimm [14] and Milroy [8] it was shown that the magnitude of the externally-driven field must exceed a certain critical value before much of the azimuthal current is generated in the plasma column. They measured the current drive using the parameter α, defined as the ratio of the driven current over the current obtained if all of the electrons rotate synchronously with the RMF,

$$\alpha = \frac{2}{\mu_o neR^2}\left(B_z(r=R) - B_z(r=0)\right). \tag{3}$$

Previous research [14] has shown that the steady-state value of α close to one when γ exceeds a certain threshold. This is because the electrons get tied into the magnetic field lines when the RMF is strong enough to generate a force on the electrons

Distribution Statement A: Approved for Public Release; Distribution is Unlimited. AFRL-2021-4182

that is sufficient to overcome the electron-ion drag (resistivity).

Milroy [8] was able to estimate the critical threshold, γ_c, for full field penetration as a function of λ,

$$\gamma_c = 1.12\lambda, \qquad for \quad \lambda \leq 6.5, \tag{4}$$

$$\gamma_c = 1.12\lambda(1+1.2(\lambda-6.5)^{0.4}), \qquad for \quad \lambda > 6.5. \tag{5}$$

This empirical threshold value of γ_c is investigated in this paper, using simulations with different values of γ and λ. We use the reversal of B_z anywhere in the domain as a proxy for an FRC formation. The description of the physical plasma model and numerical code used are shown below.

III. The Multi-Fluid plasma model

The Multi-Fluid plasma model [15] is obtained by taking velocity moments of the Boltzmann equation for each of the species present in the plasma. The model a is reduction from the kinetic representation of the plasma by assuming a Maxwellian distribution function. Each species is modeled as a separate fluid and its mass, momentum and total energy are described as,

$$\frac{\partial \rho_s}{\partial t} + \nabla \cdot (\rho_s \mathbf{u}_s) = 0,$$

$$\begin{aligned} \frac{\partial \rho_s \mathbf{u}_s}{\partial t} &+ \nabla \cdot \left(\rho_s \mathbf{u}_s \mathbf{u}_s + p_s \overleftrightarrow{\mathbf{I}}\right) \\ &= \frac{\rho_s q_s}{m_s}(\mathbf{E} + \mathbf{u}_s \times \mathbf{B}) + \sum_{r \neq s} \mathbf{R}_{rs}, \end{aligned}$$

$$\begin{aligned} \frac{\partial \varepsilon_s}{\partial t} &+ \nabla \cdot ((\varepsilon_s + p_s)\mathbf{u}_s) \\ &= \left(\frac{\rho_s q_s}{m_s}\mathbf{E} + \sum_{r \neq s} \mathbf{R}_{rs}\right) \cdot \mathbf{u}_s + \sum_{r \neq s} Q_{rs}, \end{aligned}$$

where the subscript s denotes the species, ρ_s is the density, $\mathbf{u}_s$ is the velocity, $\mathbf{E}$ and $\mathbf{B}$ are the electric and magnetic fields, m is the mass, q_s is the charge, $p_s = n_s T_s$ is the pressure, and ε_s is the total energy given as

$$\varepsilon_s = \frac{p_s}{\gamma - 1} + \frac{1}{2}\rho_s |\mathbf{u}_s|^2. \tag{6}$$

The momentum transfer between species s and r is accounted for in $\mathbf{R}_{rs}$, and $\mathbf{R}_{rs} \cdot \mathbf{u}_s$ is Ohmic heating. The momentum transfer term is described as,

$$\mathbf{R}_{ei} = -n_e^2 e^2 (\eta_{\parallel} \mathbf{v}_{\parallel} + \eta_{\perp} \mathbf{v}_{\perp}) \tag{7}$$

where η is the resistivity and $\mathbf{v} = \mathbf{u}_e - \mathbf{u}_i$. The subscripts $\parallel$ and $\perp$ denote the directions parallel and perpendicular to magnetic field.

The Spitzer resistivity is used to calculate the parallel component,

$$\eta_{\parallel} = \frac{\pi e^2 m_e^{1/2} \ln \Lambda}{(4\pi\varepsilon_o)^2 T_e^{3/2}}, \tag{8}$$

where $\ln \Lambda$ is the Coulomb logarithm and the electron temperature, T_e, is in units of energy. The perpendicular component of the resistivity is $\eta_{\perp} = 1.96\eta_{\parallel}$ [16].

In Eq. (6), Q_{rs} is the thermal equilibration term between species, which drives the plasma to reach an equilibrium temperature for all species in the absence of other transport terms. The thermal equilibration is evaluated differently for ions and electrons, respectively

$$Q_{ie} = Q_{\Delta} = \frac{3\eta_{\parallel} n_e^2 e^2}{m_i}(T_e - T_i), \tag{9}$$

$$Q_{ei} = -\mathbf{R}_{ie} \cdot (\mathbf{u}_e - \mathbf{u}_i) - Q_{\Delta}. \tag{10}$$

To close the system, the electromagnetic fields are evolved using the Maxwell's equations in purely hyperbolic form [17],

$$\frac{\partial \mathbf{B}}{\partial t} + \nabla \times \mathbf{E} + \gamma \nabla \Psi = 0,$$

$$\frac{1}{c^2}\frac{\partial \mathbf{E}}{\partial t} - \nabla \times \mathbf{B} + \chi \nabla \Phi = -\mu_o \sum_s \frac{q_s}{m_s}\rho_s \mathbf{u}_s,$$

$$\frac{1}{\chi}\frac{\partial \Phi}{\partial t} + \nabla \cdot \mathbf{E} = \sum_s \frac{q_s}{m_s}\rho_s,$$

$$\frac{1}{\xi c^2}\frac{\partial \Psi}{\partial t} + \nabla \cdot \mathbf{B} = 0.$$

The equations are presented in this form to account for the divergence constraint of the magnetic field and Gauss' law. The divergence errors that arise due to numerical discretization are propagated out

Distribution Statement A: Approved for Public Release; Distribution is Unlimited. AFRL-2021-4182

of the computational domain at speeds ξc and χc, therefore, larger values will result in faster "cleaning" of the computational domain. However, larger values of ξ and χ impose smaller time-steps, and, choosing a value of one is usually sufficient.

The numerical model used is the nodal discontinuous Galerkin [18] finite element method. This method provides good coupling between the sources and flux term and is able to represent the solution with high order of accuracy. The method is also very localized, where each element update only requires information from adjacent element, making the method highly parallelizable.

IV. Code development

The Multi-Fluid plasma framework is implemented using the PETSc [5] library, in particular the DMPlex [19] subclass for unstructured data management. DMPlex stores the connectivity information associated with the mesh as a layered directed acyclic graph (DAG), which allows for dimension free programming, and optimization of not only file I/O but also parallel data distribution using graph partitioning libraries. The mesh used for this application are either gmsh [20] or exodusII grid files. Output files are writen using VTK file format which can be easily read by Visit or Paraview.

PETSc time-stepping (TS) functionality is used to advance the algorithm in time. Currently only explicit time integrators are implemented. The default time integrator is the strong-stability preserving (SSP) second order Runge-Kutta method [21]. The APOLLO code is schematically represented in Fig. 1.

V. Simulating FRC Formation

One of the problems of interest is the FRC formation using a rotating magnetic field (RMF). Simulations of the problem require a good coupling between the ion/electron fluid variables and the electromagnetic fields due to its inherent multi-scale nature with disparate time scales.

In this paper, the RMF is implemented as a boundary condition by defining a magnetic vector potential as $A_z = B_t r \cos(\omega t + \theta)$, where ω is the RMF frequency. It is required that the RMF

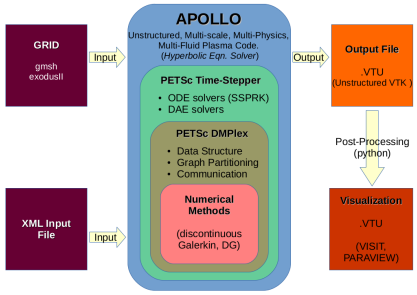

Fig. 1: Schematic of the Apollo code. The framework takes to files as input, a gmsh grid file and a deck with the details of the simulations, equations to be solved, boundary conditions, source terms, and constants. The PETCs time-stepper advances the solution in time which is spatially discretized using a discontinuous Galerkin method. VTU files are output at predefined time intervals. These VTU files are post-processed before they are ready to be visualized in Visit or Paraview.

frequency be bounded by the ion and electron cyclotron frequencies, $\omega_{ci} < \omega < \omega_{ce}$, to freeze the electrons fluid into the magnetic field lines but not the ions. Boundary conditions for the magnetic and electric field can be obtained by taking the curl and the time derivative of the magnetic vector potential, respectively.

For the simulations presented here the θ dependence will be ignored in order to produce a uniform, idealized RMF. Hugrass [22] has shown that the spatial dependence along the θ-direction is important and that spatial harmonics considerably change the RMF effectiveness.

In addition to the RMF (the in plane field), the flux conserving ring produces a current in the θ-direction that keeps the B_z flux constant(out of plane field). The flux conserving ring boundary condition is described in ref. [14], and given as

$$\begin{aligned} B_z(a,t) &= \frac{b^2 B_a(0)}{b^2 - a^2} \\ &- \frac{1}{\pi(b^2 - a^2)} \int_0^a r dr \int_0^{2\pi} d\theta B_z(r,\theta,t) d\theta, \end{aligned}$$

where $r = a$ is the plasma radius, $r = b$ is the radius

Distribution Statement A: Approved for Public Release; Distribution is Unlimited. AFRL-2021-4182

of the flux conserver, $B_a(0)$ is the initial value of B_z at $r = a$. The second term on the right-hand-side represents the calculation of the axial magnetic flux throughout the plasma.

The FRC formation process a current in the azimuthal direction, J_θ, is generated by the RMF causing the axial magnetic field, B_z to reverse at the axis, $r = 0$. In our simulations the plasma is initialized at a number density of $n_i = n_e = 10^{20}m^{-3}$, $T_i = T_e = 50eV$, the RMF has a frequency $\omega = 1MHz$ and peak magnitude of $60G$, while the bias field $B_z = 50G$. The simulations also assume a constant plasma resistivity of $\eta = 50\mu\Omega m$.

In Fig. 2, we plot the magnitude of B_z at different times, and observe that the field reversal initially occurs in small islands spread throughout the domain but eventually coalesce at the center of the computational domain. Notice the shape of the magnetic null (black contour) seen in Fig. 2b. The rectangular shape is not only seen in the multi-fluid simulations but also in the experimental fast camera pictures. Figure 3 shows Imacon fast camera snapshots taken from the MSNW experimental FRC. The results are for an Argon gas injected at 280 m/s, at a pressure of 2 mTorr, and at an RMF phase angle of 30 degrees. The light emission from the plasma shows clearly a thin rectangular cross-section with rounded edges of the plasma. A closer look at the problem initialization sheds some light on the possible reason for a rectangular cross-section. The RMF is initialized perfectly uniform at the boundaries and penetrates the plasma with relative ease tying the electrons to the magnetic field lines. It is also worth noting, from Fig. 4, that the circular symmetry of the problem is broken by the planar geometry of the RMF, the inner radius of the plasma ring has numerous straight edges while the outer radius is circular with plasma "tails".

Very few simulations of the FRC have been done in the r-θ-plane with notable exceptions to the work of Milroy [8] and Hugrass [14], [22] which focused primarily in the RMF field penetration using the MHD model. Here is the first instance of the multi-fluid plasma model begin applied to this problem of FRC formation.

VI. Using Machine Learning to Analyze the FRC Formation

Machine learning algorithms are used to try to understand the problem of field reversal in an FRCs. Equation 5 defines the threshold that needs to be overcome in order to achieve RMF penetration, which is a requirement for formation. The idea is to vary values of λ and γ around the $\lambda_{critical}$ line to numerically validate this threshold and to create regions where field reversal is more likely than others.

The problem is setup as follows: the value of λ is dependent on the RMF frequency ω and the electron temperature, T_e, through the resistivity, η; γ is dependent on the RMF magnitude B_ω along with T_e and the number density n_e. We create simulations where the values of ω, T_e, and B_ω are chosen randomly using an uniform distribution in the limits $2\pi \times 10^5 Hz < \omega < \pi \times 10^6 Hz$, $30eV < T_e < 50eV$, and $5G < B_\omega < 30G$. The number density is held constant at $1 \times 10^{20}m^{-3}$. A total of four hundred parameter sets are chosen by varying the three parameters. The parameter space is shown in Fig. 5. Notice that high and low values of T_e are present above and below the γ_c line, perhaps indicating a weak dependence of the field penetration on the resistivity.

Machine learning classification methods are used where the features are λ and γ, and the target is the categorical question "Does the axial field B_z reverse?". Although four algorithms were used for the classification problem (Logistic regression, K-nearest neighbors, Support Vector Machines, and Random Forest), we only should the results for deep neural networks because they have the highest accuracy score. Only 320 cases are used in the training stage, with the remaining 80 reserved for testing. The dataset could be bigger, which could reduce the uncertainty in the predictions. However, often in computational science the cost of producing new simulations can be considerable, which is why our dataset is this size.

DNN algorithms can be viewed in its simplest form as a fitting process, where multiple nodes are connected to each other and the strength of each of the connections between nodes is adjusted through

Distribution Statement A: Approved for Public Release; Distribution is Unlimited. AFRL-2021-4182

an optimization process to minimize a loss function which quantifies the error in the predictions.

A DNN was implemented using the Keras module in python. The model consists of three hidden layers, where the dimensionless parameters λ and γ are the inputs and the output is the probability that the FRC axial field will reverse. Each of the hidden layers has fifty or one hundred units/neurons, and use dropout as regularization. The hyperparmeters optimized in the models are the number of layers, the number of units per layer, choice of activation function, choice of optimizer, and the dropout percentage. The training runs for 200 epochs and the optimal model has an accuracy score of 0.920, therefore better than the classification methods. Compared to the accuracy of the theoretical line λ_c at only 0.653, which mean that about 44.7% percent of the dataset that did not reverse (red dots in Fig. 6) is above the threshold line.

VII. Summary

In an attempt to solve more complex plasma physics problems of interest to the Air Force, we have developed a multi-fluid plasma model framework that uses the discontinuous Galerkin numerical scheme. The code is able to attain high order accuracy in space and time as well as capture shocks, maintain conservation properties, and provides good flux/source coupling.

The problem of interest is FRC formation using a RMF at low power, for applications in space propulsion. An idealized two-dimensional simulation setup in the $r-\theta$ plane is performed where the RMF and flux conserving ring effects are included through the boundary conditions and drive the boundary-value problem. Starting from an uniform fully ionized Xenon or Argon plasma we evolve the electron and ion fluids coupled with the electromagnetic fields.

During the formation process, we observe that the bias field reversal occurs first in isolated islands throughout the plasma cross-section and eventually coalesce at the center to form a big magnetic island. In addition, the cross-section of the plasma possesses have a rectangular shape due to the uniform and planar configuration of the RMF. This shape seems to agree with experimental results produced by the MSNW FRC experiment seen through fast camera images.

Lastly, machine learning algorithms were used to determine the probability of FRC formation dependent on the dimensionless parameters λ and γ. Classification algorithms logistic regression, K-nearest neighbor, support vector machine, and random forest are trained using a small dataset of 400 simulations. Deep Neural Networks are also used to find the probability of FRC formation, and in this case we were able to achieve an accuracy score of 0.920. In addition the DNN predicts that the formation boundary is different from the theoretical expression derived by Milroy [8]. Note in fig. 6 that all the cases of reversal (cyan dots) are above the theoretical value of λ_c, point to that being a necessary but not sufficient condition for reversal.

Acknowledgment

This work is supported by grant 17RQCOR465 from the United States Air Force Office of Scientific Research.

The authors would like to thank Justin Little and Jordan Neuhoff from MSNW for fast camera images and discussions regarding their experimental results.

References

[1] U. Shumlak, R. Lilly, N. Reddell, E. Sousa, and B. Srinivasan, "Advanced physics calculations using a multi-fluid plasma model," *Comput. Phys. Commun.*, vol. 182, no. 9, pp. 1767–1770, 2011.

[2] J. P. Freidberg, "Ideal magnetohydrodynamic theory of magnetic fusion systems," *Rev. Mod. Phys*, vol. 54, no. 801, 1982.

[3] U. Shumlak and J. Loverich, "Approximate Riemann solver for the two-fluid plasma model," *J. Comput. Phys.*, vol. 187, pp. 620–638, 2003.

[4] J. Hesthaven and T. Warburton, "Nodal High-Order Methods on Unstructured Grids," *J. Comput. Phys.*, vol. 181, no. 1, pp. 186–221, 2002. [Online]. Available: http://www.sciencedirect.com/science/article/pii/S0021999102971184

[5] S. Balay, S. Abhyankar, M. Adams, J. Brown, P. Brune, K. Buschelman, L. Dalcin, V. Eijkhout, W. Gropp, D. Kaushik, M. Knepley, L. C. McInnes, K. Rupp, B. Smith, S. Zampini, and H. Zhang, "PETSc Users Manual," Argonne National Laboratory, Tech. Rep. ANL-95/11 - Revision 3.5, 2014. [Online]. Available: http://www.mcs.anl.gov/petsc

Distribution Statement A: Approved for Public Release; Distribution is Unlimited. AFRL-2021-4182

[6] J. T. Slough, D. E. Kirtley, and T. Weber, "Pulsed Plasmoid Propulsion: The ELF Thruster," in *31 th Int. Electr. Propuls. Conf.*, Ann Arbor, Michigan, 2009, pp. 1–24. [Online]. Available: https://s3-us-west-2.amazonaws.com/pnwmsnw/ELF{_}IEPC-2009-265.pdf

[7] L. C. Steinhauer, "Review of field-reversed configurations," *Phys. Plasmas*, vol. 18, no. 070501, 2011. [Online]. Available: http://dx.doi.org/10.1063/1.3613680

[8] R. Milroy, "A numerical study of rotating magnetic fields as a current drive for field reversed configurations," *Phys. Plasmas*, vol. 6, no. 7, pp. 2771–2780, 1999.

[9] F. Harrell, *Regression Modeling Strategies*. Springer.

[10] S. Raschka and V. Mirjalili, *Python Machine Learning*, 2nd ed. Packt Publishing Ltd.

[11] A. Geron, *Hands-On Machine Learning with Scikit-Learn and TensorFlow*, 1st ed., N. Tache, Ed. O'Reilly Media, Inc.

[12] A. Gulli and S. Pal, *Deep Learning with Keras: Implementing Deep Learning Models and Neural Networks with the Power of Python*. Packt Publishing Ltd.

[13] I. Goodfellow, Y. Bengio, and A. Courville, *Deep Learning*, T. Dietterich, Ed. The MIT Press.

[14] W. N. Hugrass and R. C. Grimm, "A Numerical Study of the Generation of an Azimuthal Current in a Plasma Cylinder using a Transverse Rotating Magnetic Field," *J. Plasma Phys.*, vol. 26, no. 3, pp. 455–464, 1981.

[15] U. Shumlak, R. Lilly, N. Reddell, E. Sousa, and B. Srinivasan, "Advanced {P}hysics {C}alculations using a {M}ulti-{F}luid {P}lasma {M}odel," *Comput. Phys. Commun.*, vol. 18, pp. 1767–1770, 2011.

[16] S. L. Braginskii, "Transport Processes in Plasma," in *Rev. Plasma Phys.*, A. M. A. Leontovich, Ed. Consultants Bureau, 1965, pp. 205–311.

[17] R. S. C. D. Munz P. Omnes, E. Sonnendruer, and U. Voss, "Divergence Correction Techniques for Maxwell Solvers Based n a Hyperbolic Model," *J. Comput. Phys.*, vol. 161, pp. 484–511, 2000.

[18] J. S. Hesthaven and T. Warburton, *Nodal Discontinuous Galerkin Methods: Algorithms, Analysis, and Applications*. Springer, 2008.

[19] M. Lange, M. G. Knepley, and G. J. Gorman, "Flexible, Scalable Mesh and Data Management using PETSc DMPlex," 2015. [Online]. Available: http://arxiv.org/abs/1505.04633

[20] C. Geuzaine and J. F. Remacle, "Gmsh: a three-dimensional finite element mesh generator with build-in pre- and post-processing facilities," *Int. J. Numer. Methods Eng.*, vol. 79, no. 11, pp. 1309–1331, 2009.

[21] S. Gottlieb, D. Ketcheson, and C. W. Shu, *Strong Stability Preserving Runge-Kutta and Multistep Time Discretizations*. World Scientific, 2011.

[22] W. N. Hugrass, "The Influence of the Spacial Harmonics on the Rotating Magnetic Field Current Drive," *Aust. J. Physi.*, vol. 39, pp. 513–527, 1986.

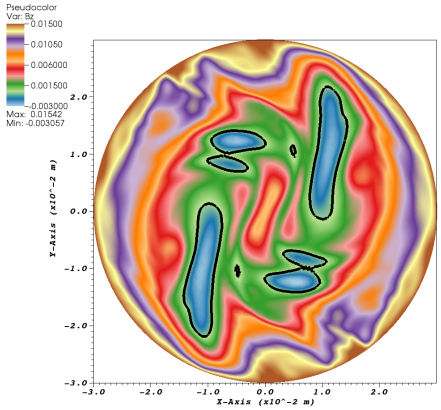

(a) $t = 250ns$

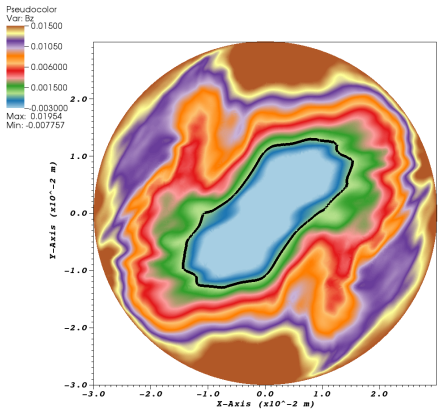

(b) $t = 500ns$

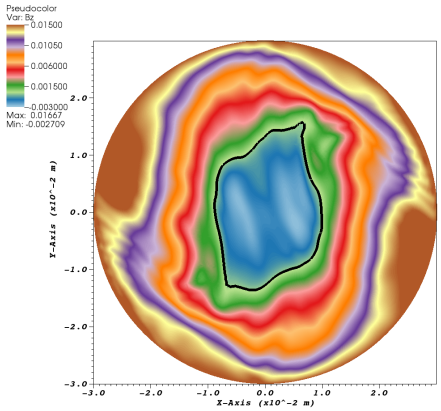

(c) $t = 1500ns$

Fig. 2: Z-component of the magnetic field is plotted over time showing the field reversal is achieved at the center as a result of small magnetic islands coalescence. The Black contours represent represent the magnetic null where B_z=0.

Distribution Statement A: Approved for Public Release; Distribution is Unlimited. AFRL-2021-4182

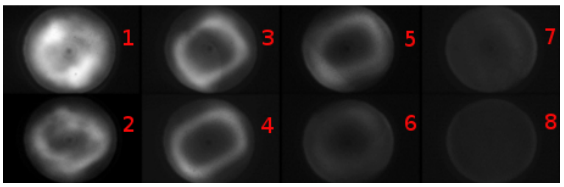

Fig. 3: Fast-camera snapshots of an Argon plasma generated at the FRC experiment at MSNW. The snapshots are at $2\mu s$ intervals. It can be clearly seen that the plasma has a symmetric rectangular shape even though the vacuum chamber has a circular cross-section.

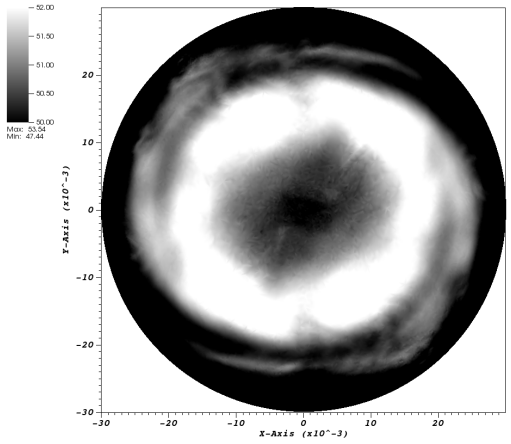

Fig. 4: Electron temperature in eV plotted in a grayscale to approach what would be seen in a fast camera images. The rectangular shape can also be seen in the simulations, resembling the experimental results. A circular cross-section of the plasma is not expected, since the RMF is planar and uniform and not circularly symmetric.

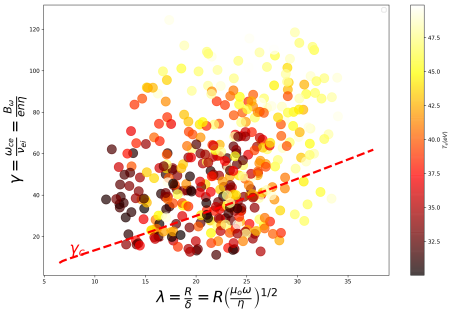

Fig. 5: Randomly selected values of λ, γ, and T_e produce the sample parameter space shown above. The red line is the theoretical value of that γ needs to be for full RMF penetration. The plot shows no discernible separation in the data due to temperature.

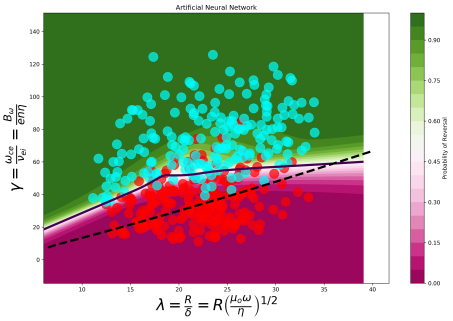

Fig. 6: Probability of axial field reversal is plotted, where the cyan dots represent simulation data where the field actually reversed and the ones in red to when the field did not reverse. The dashed line represent the theoretical threshold of reversal or not, and the solid line is the contour for 50-percent chance of reversal.

Distribution Statement A: Approved for Public Release; Distribution is Unlimited. AFRL-2021-4182

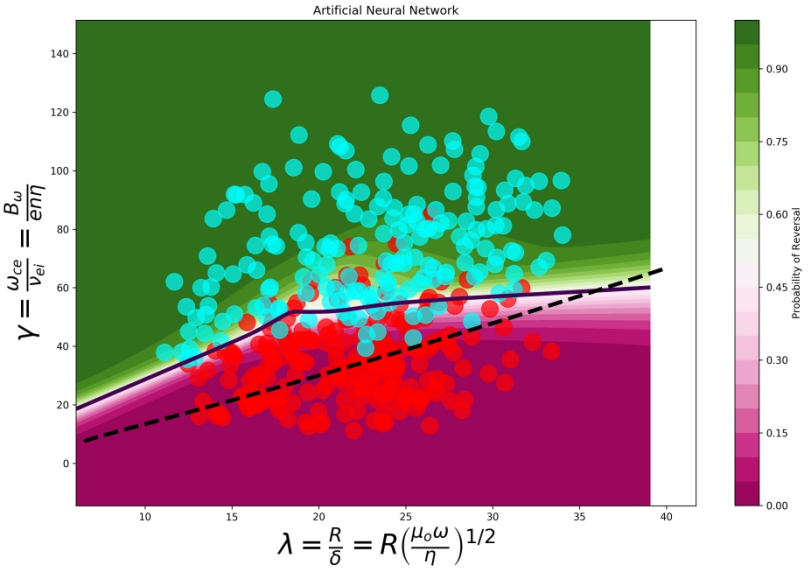

Distribution Statement A: Approved for Public Release; Distribution is Unlimited. AFRL-2021-4182

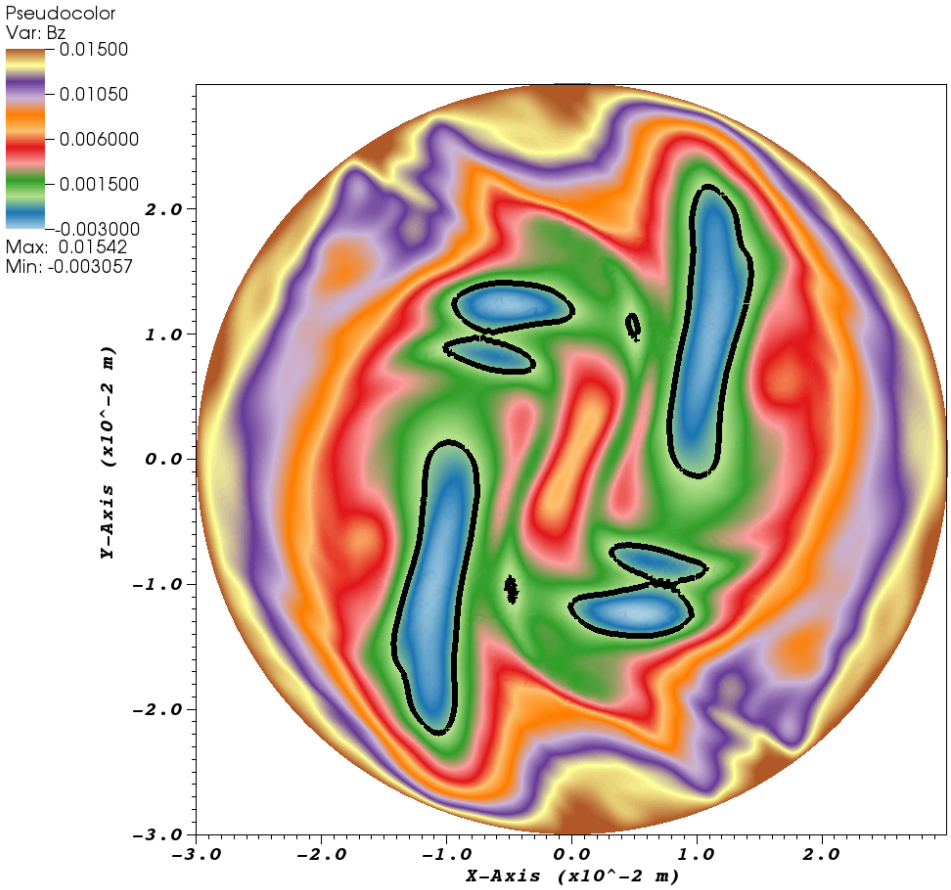

361x374mm (72 x 72 DPI)

Distribution Statement A: Approved for Public Release; Distribution is Unlimited. AFRL-2021-4182

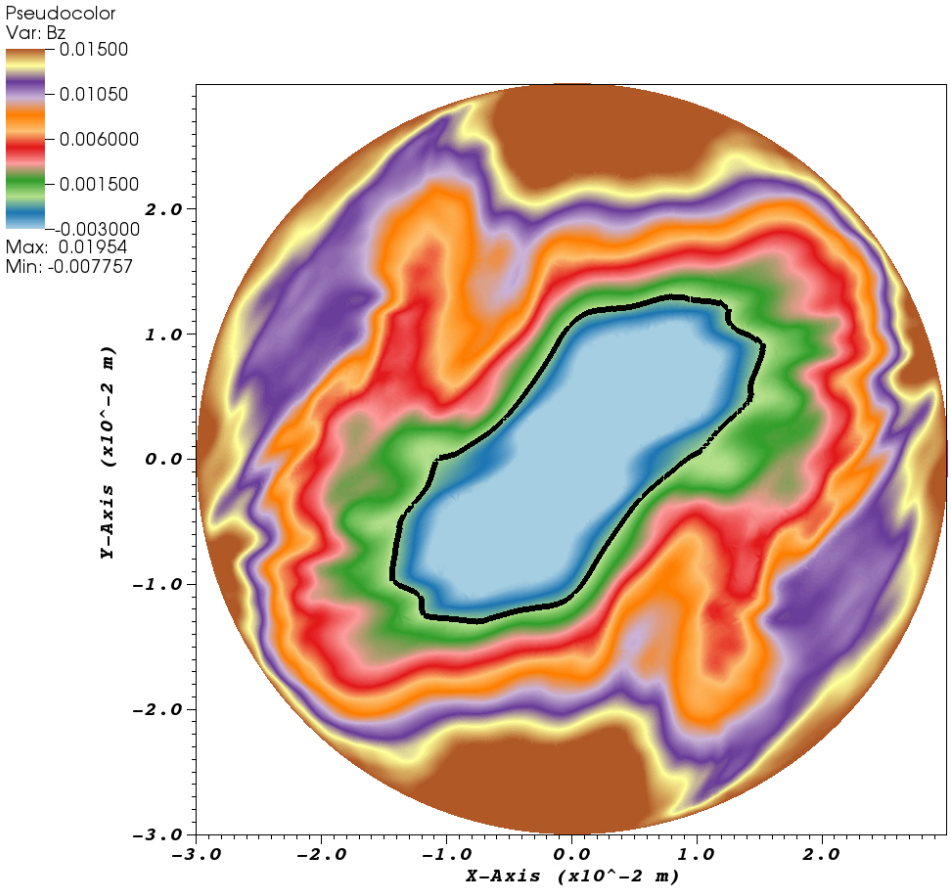

361x374mm (72 x 72 DPI)

Distribution Statement A: Approved for Public Release; Distribution is Unlimited. AFRL-2021-4182

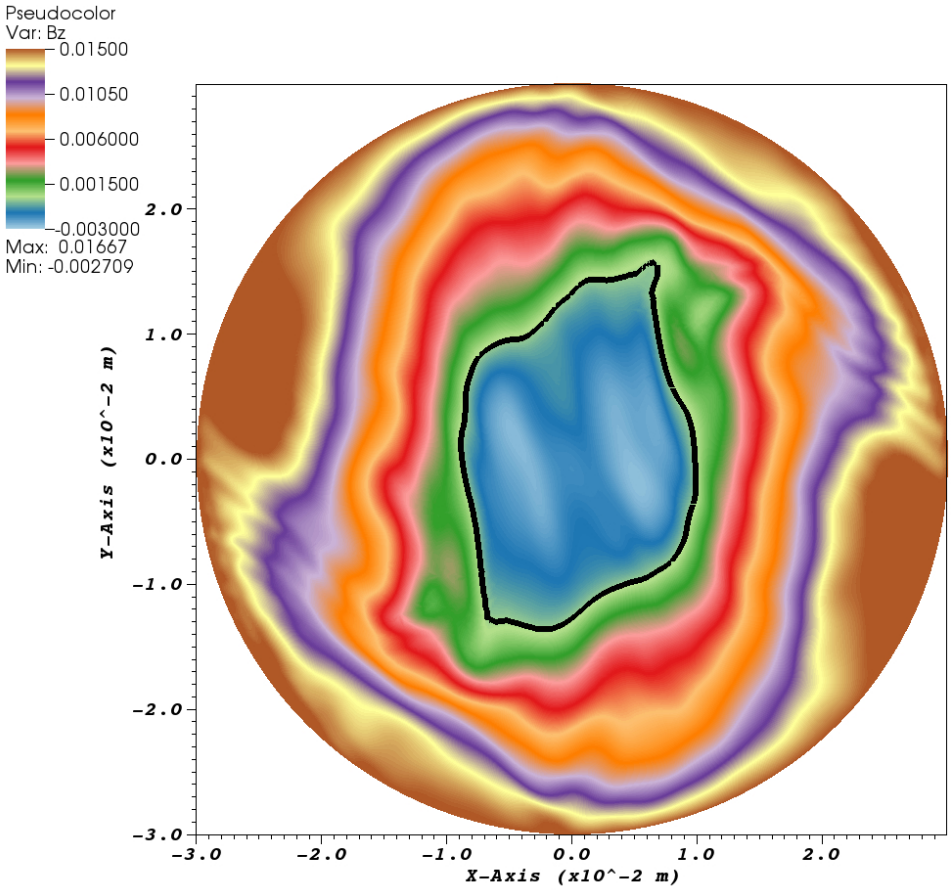

361x374mm (72 x 72 DPI)

Distribution Statement A: Approved for Public Release; Distribution is Unlimited. AFRL-2021-4182

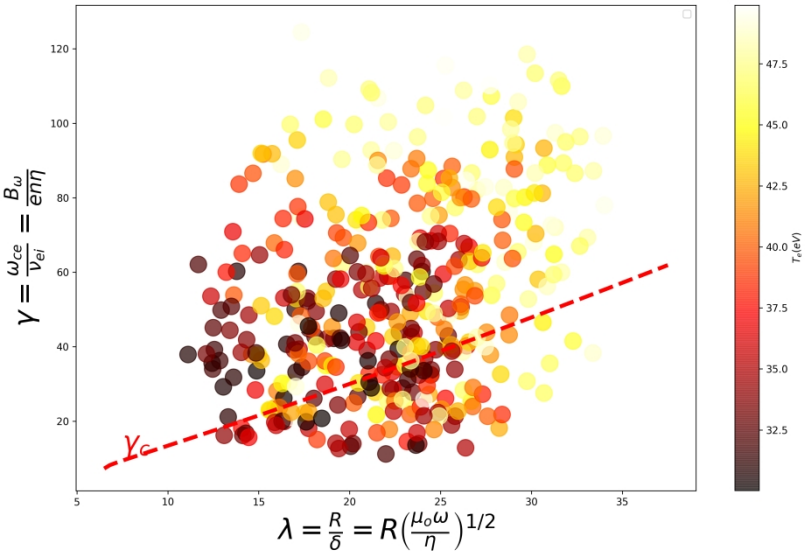

Distribution Statement A: Approved for Public Release; Distribution is Unlimited. AFRL-2021-4182

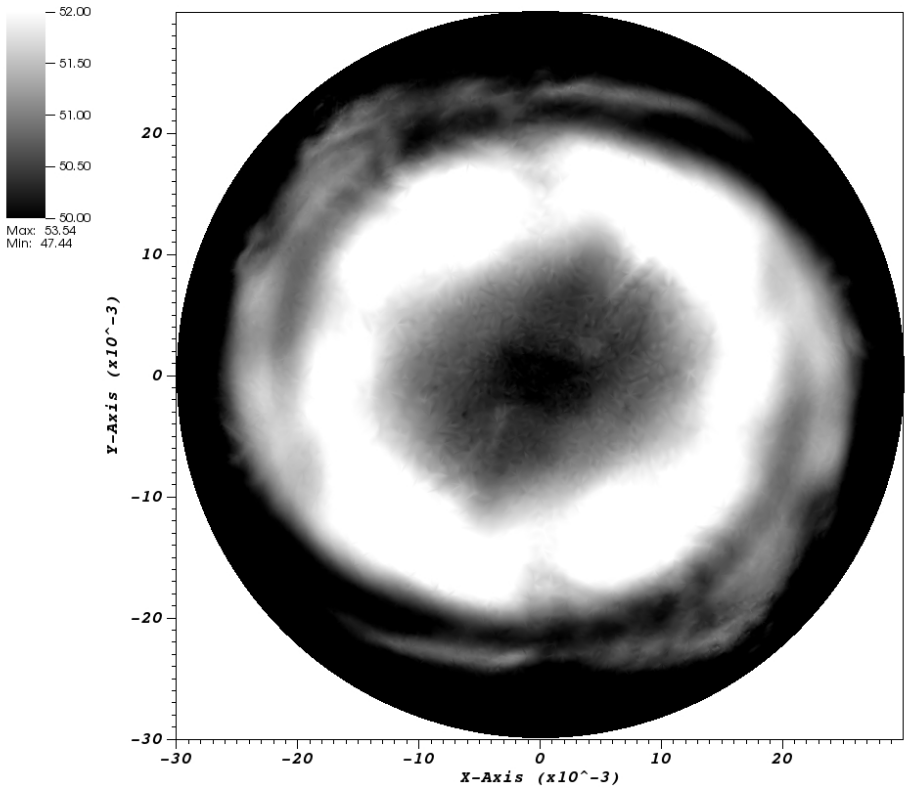

361x328mm (72 x 72 DPI)

Distribution Statement A: Approved for Public Release; Distribution is Unlimited. AFRL-2021-4182

Using Neural Networks to Understand Field Reversed Configuration Formation Stage

Éder M. Sousa[1], Robert C. Lilly[1], Robert S. Martin[2]

Modeling & Simulation Group
In-Space propulsion Branch (RQRS)
[1]ERC Inc.
[2]Air Force Research Lab
Edwards AFB, CA
*eder.sousa.ctr@us.af.mil

This work is supported by grant 17RQCOR465 from the United States Air Force Office of Scientific Research.
Distribution Statement A: Approved for Public Release; Distribution is Unlimited. PA# 18638.

Abstract

The Rotating Magnetic Field (RMF) penetration during the formation stage of a Field Reversed Configuration (FRC) can be characterized by two dimensionless parameters, γ and λ. These two parameters account for the intensity and frequency of the RMF, as well as the plasma resistivity and number density. Work by Milroy, using the magnetohydrodynamics (MHD) model, has shown that in order for the RMF to penetrate a critical threshold has to be achieved. Here we use the multi-fluid plasma model and deep neural networks (DNN) to learn from simulated data the boundary between full field penetration and consequent axial field reversal and non-penetration. The results between the MHD theoretical solution and the simulated multi-fluid one are compared.

The Generic RMF-Based Thruster

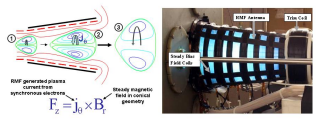

(1) Rotating Magnetic Fields (RMF) form high-density, FRC plasmoid
(2) FRC grows and accelerates driven by RMF generated currents & steady field
(3) FRC expands as ejected, converting any thermal to directed energy

The computational framework uses PETSc unstructured subclass DMPlex and the time-stepping functionality (TS)

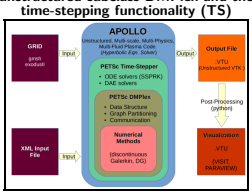

Simulated results and experimental data seem to have the same behavior.

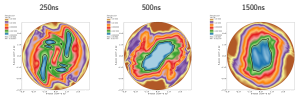

Simulated Brightness.

Experimental fast camera images.

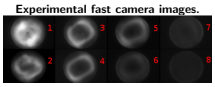

The Rotating Magnetic Field (RMF) penetration can be described by two dimensionless parameters.

- $\lambda = R/\delta$, where $\delta = (2\eta/\mu_0\omega)^{1/2}$ is the classical skin depth;
- $\gamma = \omega_{ce}/\nu_{ei}$, where $\nu_{ei} = \eta(ne^2/m_e)$ is the electron-ion collision frequency;
- These parameters can be expressed in terms of RMF intensity, frequency and the plasma resistivity;

$$\lambda = R\left(\frac{\mu_0\omega}{2\eta}\right)^{1/2}, \qquad \gamma = \frac{1}{e}\left(\frac{B_z}{m_j}\right)$$

- FRC parameters need to be above a critical value of γ_c

$$\gamma > \gamma_c = 1.12\lambda\left[1 + 0.12(\lambda - 6.5)^{0.4}\right]$$

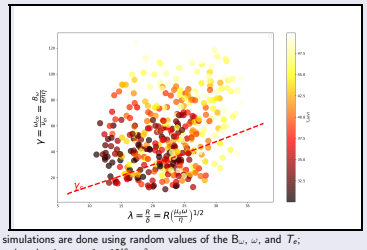

- The simulations are done using random values of the B_z, ω, and T_e;
  - Number density, $n = 1 \times 10^{19} m^{-3}$
  - RMF frequency, $2\pi \times 10^5 Hz < \omega < 10\pi \times 10^5 Hz$
  - RMF field peak intensity, $5G < B_z < 30G$
  - Electron temperature, $30eV < T_e < 50eV$
- We are interested in determining the parameter regime where we will get full RMF penetration as well as consistent B_z field. reversal

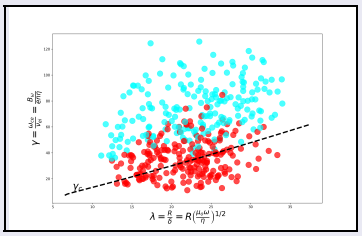

- A question is asked of the data "For each simulation do we get field reversal?" The **No** and **Yes** answers to that question are show above;
- The dashed line is the γ_c theoretical critical value

R. D. Milroy , PoP 7, 10 (2000)

Machine Learning algorithms are used to determine what the threshold for FRC formation should be.

Logistic Regression (LR) Classification

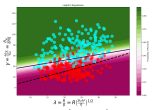

-	Pred No	Pred Yes
Actual No	39	5
Actual Yes	4	32

K-Nearest Neighbors (KNN)

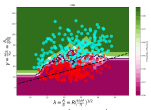

-	Pred No	Pred Yes
Actual No	38	6
Actual Yes	5	31

Random Forest (RF)

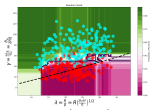

-	Pred No	Pred Yes
Actual No	37	7
Actual Yes	3	34

Python scikit-learn and keras/TensorFlow modules are used to create the models.

- Four hundred simulations were done (320 training/80 test)
- **LR classification**: penalty=L1, accuracy=0.8812
- **KNN**: neighbors=5, accuracy=0.8906
- **RF**: criterion=entropy, max-depth=5, estimators=60, accuracy=0.90
- **ANN**: 3 hidden layers (150, 50, 50 units), using dropout regularization, optimizer=adam, accuracy= 0.9125

Artificial Neural Net (ANN)

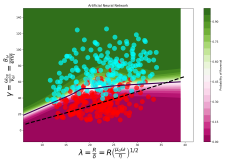

-	Pred No	Pred Yes
Actual No	39	5
Actual Yes	2	34

The algorithms are optimized to decrease bias and over-fitting.

- **LR classification**: Produces a threshold straight line with a different slope. Could be prone to bias.
- **KNN**: This algorithm is more prone to over-fitting. It can be seen that there is an island around $\lambda = 22$.
- **RF**: The algorithm provides a threshold limit that seems to avoid both bias and over-fitting.
- **ANN**: The model produces a "broken" line an avoids both bias and over-fitting while providing the most accurate result.

Using other variables we can see that the FRC formation threshold is more dependent on certain parameters.

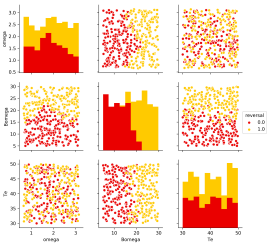

Ongoing & Future Work

- **Development of reduced order and/or multi-fidelity models** to decrease computational cost, increase data points, and quantify the uncertainty in the model
- **Generate high dimensional data**: for each simulation only three variables are randomly generated, increase that number to better understand the FRC formation parameter space
- **Implement physic constrains** to the neural networks to ensure that physical laws are enforced in the predictions
- **Feature and metric engineering**: what parameters should be used to properly characterize the FRC or the "quality" of the formation
- **Apply similar methods to experimental data:** are the simulation and experiments describing the same dynamics (i.e. the same phase space diagram)? What's the FRC threshold limit when only experimental data is used?

Distribution Statement A: Approved for Public Release; Distribution is Unlimited. AFRL-2021-4182

Improved Models and Understanding for Field-Reversed Configuration (FRC) Thrusters

Robert Martin[1], Eder Sousa[2], Robert Lilly[2], Michael Kapper[2]

[1]Air Force Research Laboratory,
[2]ERC Inc.,
Edwards Air Force Base, CA USA

AFOSR Space Propulsion and Power Review, 2018
Distribution A - Approved for public release;
Distribution unlimited.
PA clearance No. 18476

Distribution Statement A: Approved for Public Release; Distribution is Unlimited. AFRL-2021-4182

Outline

1. Introduction & Challenges
2. Model Enhancements
3. Learning in Parameter Space
4. Conclusion & Future Directions

Distribution Statement A: Approved for Public Release; Distribution is Unlimited. AFRL-2021-4182

SECTION: LEARNING IN PARAMETER SPACE

Complex Design Space for Pulsed EM:

- Device Geometry: Length/Diameter/Pitch Angle/etc.
- Gas Flow: Mass Flow/Injection/Mixture/Rate/Density/Pre-Ionization
- Electrical: Energy/Coil Shape/Switching Speed/Frequency/Phase/Bias Field

15+ Dimensional Design Space...
Finding 'Good' Designs like a Needle in a Haystack!

Distribution Statement A: Approved for Public Release; Distribution is Unlimited. AFRL-2021-4182

SECTION: LEARNING IN PARAMETER SPACE

Complex Design Space for Pulsed EM:

- Device Geometry: Length/Diameter/Pitch Angle/etc.
- Gas Flow: Mass Flow/Injection/Mixture/Rate/Density/Pre-Ionization
- Electrical: Energy/Coil Shape/Switching Speed/Frequency/Phase/Bias Field

15+ Dimensional Design Space...
Finding 'Good' Designs like a Needle in a Haystack!

Potential Solutions:

- Theory: Simplified Analysis Bounding Envelope/Reducing Dimension
- Build and Bust: Fix Physical Constraints and Explore
- Simulation: Requires DNS or Model with Extrapolative Power! (Validated)
- Machine Learning: Finding the Curve beyond Theory (Exp. or Sim.)
- Data Fusion: Accelerating Exp. Knowledge $\rightarrow$ Models that Extrapolate (Both)

Distribution Statement A: Approved for Public Release; Distribution is Unlimited. AFRL-2021-4182

Section: Learning in Parameter Space

Complex Design Space for Pulsed EM:

- Device Geometry: Length/Diameter/Pitch Angle/etc.
- Gas Flow: Mass Flow/Injection/Mixture/Rate/Density/Pre-Ionization
- Electrical: Energy/Coil Shape/Switching Speed/Frequency/Phase/Bias Field

15+ Dimensional Design Space...
Finding 'Good' Designs like a Needle in a Haystack!

Potential Solutions:

- Theory: Simplified Analysis Bounding Envelope/Reducing Dimension
- Build and Bust: Fix Physical Constraints and Explore
- Simulation: Requires DNS or Model with Extrapolative Power! (Validated)
- Machine Learning: Finding the Curve beyond Theory (Exp. or Sim.)
- Data Fusion: Accelerating Exp. Knowledge $\rightarrow$ Models that Extrapolate (Both)

Distribution Statement A: Approved for Public Release; Distribution is Unlimited. AFRL-2021-4182

THEORY: RMF PENETRATION

RMF Characterized by Dimensionless Parameters:

- $\lambda = R/\delta$, where $\delta = (2\eta/\mu_o\omega)^{1/2}$ is the classical skin depth
- $\gamma = \omega_{ce}/\nu_{ei}$, where $\nu_{ei} = \eta(ne^2/m_e)$ is the electron-ion collision frequency

These parameter can be expressed in terms of RMF intensity, frequency and the plasma resistivity:

- $\lambda = R\left(\frac{\mu_o\omega}{2\eta}\right)^{1/2}$ $\qquad \gamma = \frac{1}{e}\left(\frac{B_\omega}{n\eta}\right)$

Theory: Hugrass (Aust. J. Phys. 38, 157 1985)
Semi-Emperical: Milroy (PoP 6, 2771 1999)
(RMF penetration in a fixed ion plasma column)

Question: Does this Relationships hold in MFPM?

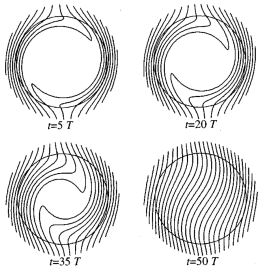

FIG. 1. Evolution of magnetic field lines as the RMF penetrates a plasma column.

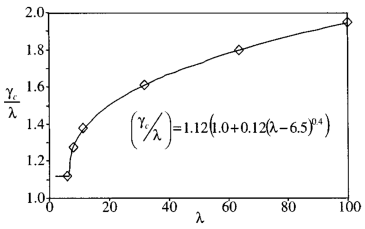

FIG. 4. Critical value of γ vs λ.

Milroy, PoP 6, 2771 (1999)

Distribution Statement A: Approved for Public Release; Distribution is Unlimited. AFRL-2021-4182

THEORY: RMF PENETRATION

RMF Characterized by Dimensionless Parameters:

- $\lambda = R/\delta$, where $\delta = (2\eta/\mu_o\omega)^{1/2}$ is the classical skin depth
- $\gamma = \omega_{ce}/\nu_{ei}$, where $\nu_{ei} = \eta(ne^2/m_e)$ is the electron-ion collision frequency

These parameter can be expressed in terms of RMF intensity, frequency and the plasma resistivity:

- $\lambda = R\left(\frac{\mu_o\omega}{2\eta}\right)^{1/2}$ $\qquad \gamma = \frac{1}{e}\left(\frac{B_\omega}{n\eta}\right)$

Theory: Hugrass (Aust. J. Phys. 38, 157 1985)
Semi-Emperical: Milroy (PoP 6, 2771 1999)
(RMF penetration in a fixed ion plasma column)

Question: Does this Relationships hold in MFPM?

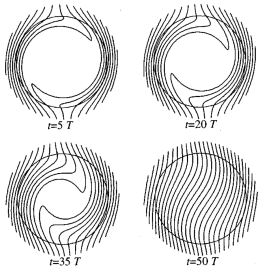

FIG. 1. Evolution of magnetic field lines as the RMF penetrates a plasma column.

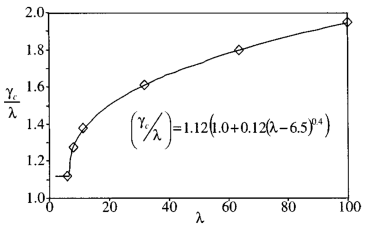

FIG. 4. Critical value of γ vs λ.

Milroy, PoP 6, 2771 (1999)

Distribution Statement A: Approved for Public Release; Distribution is Unlimited. AFRL-2021-4182

LEARNING: RMF PENETRATION

Machine Learning on MFPM Data:

- Randomly Explored (ω, B_ω, T_e) with MFPM
- Points Plotted w.r.t. (λ, γ) from Theory

MFPM Simulated Dataset

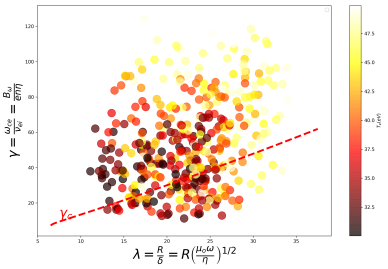

- Density, $n = 1 \times 10^{19} m^{-3}$
- $2\pi \times 10^5 Hz < \omega < 10\pi \times 10^5 Hz$
- $5G < B_\omega < 30G$
- Electron temperature, $30eV < T_e < 50eV$

Distribution Statement A: Approved for Public Release; Distribution is Unlimited. AFRL-2021-4182

Learning: RMF Penetration

Machine Learning on MFPM Data:

- Randomly Explored (ω, B_ω, T_e) with MFPM
- Points Plotted w.r.t. (λ, γ) from Theory
- Theory: Necessary but Not Sufficient

Observed B_z-Reversal

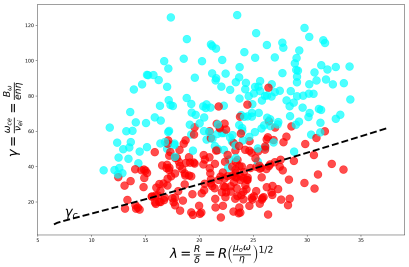

Confusion Matrix

-	Pred No	Pred Yes
Actual No	23	21
Actual Yes	**0**	36

Distribution Statement A: Approved for Public Release; Distribution is Unlimited. AFRL-2021-4182

Learning: RMF Penetration

Machine Learning on MFPM Data:

- Randomly Explored (ω, B_ω, T_e) with MFPM
- Points Plotted w.r.t. (λ, γ) from Theory
- Theory: Necessary but Not Sufficient
- Classical Classifiers Explored
- Fewer False Positives & Higher γ_c

Predicted B_z-Reversal Logistic Regression

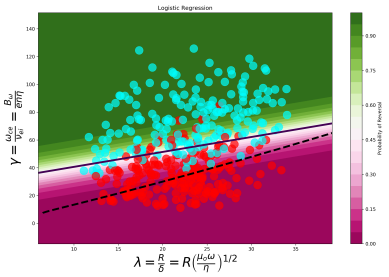

Confusion Matrix

-	Pred No	Pred Yes
Actual No	39	5
Actual Yes	4	32

Distribution Statement A: Approved for Public Release; Distribution is Unlimited. AFRL-2021-4182

Learning: RMF Penetration

Machine Learning on MFPM Data:

- Randomly Explored (ω, B_ω, T_e) with MFPM
- Points Plotted w.r.t. (λ, γ) from Theory
- Theory: Necessary but Not Sufficient
- Classical Classifiers Explored
- Fewer False Positives & Higher γ_c
- Balancing Complexity vs. Accuracy?

Predicted B_z-Reversal K-Nearest Neighbors

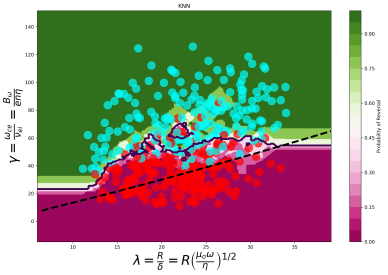

Confusion Matrix

-	Pred No	Pred Yes
Actual No	38	6
Actual Yes	5	31

Distribution Statement A: Approved for Public Release; Distribution is Unlimited. AFRL-2021-4182

Learning: RMF Penetration

Machine Learning on MFPM Data:

- Randomly Explored (ω, B_ω, T_e) with MFPM
- Points Plotted w.r.t. (λ, γ) from Theory
- Theory: Necessary but Not Sufficient
- Classical Classifiers Explored
- Fewer False Positives & Higher γ_c
- Balancing Complexity vs. Accuracy?

Predicted B_z-Reversal Support Vector Machines

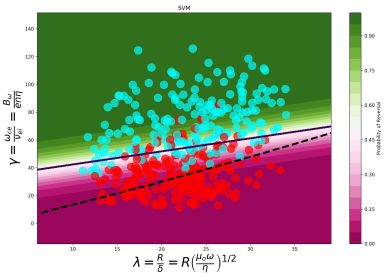

Confusion Matrix

-	Pred No	Pred Yes
Actual No	39	5
Actual Yes	4	32

Distribution Statement A: Approved for Public Release; Distribution is Unlimited. AFRL-2021-4182

Learning: RMF Penetration

Machine Learning on MFPM Data:

- Randomly Explored (ω, B_ω, T_e) with MFPM
- Points Plotted w.r.t. (λ, γ) from Theory
- Theory: Necessary but Not Sufficient
- Classical Classifiers Explored
- Fewer False Positives & Higher γ_c
- Balancing Complexity vs. Accuracy?

Predicted B_z-Reversal Random Forest

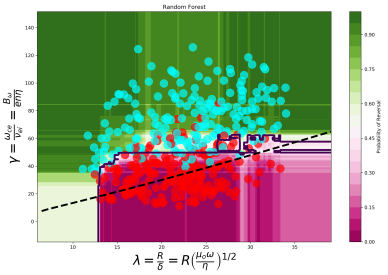

Confusion Matrix

-	Pred No	Pred Yes
Actual No	37	7
Actual Yes	3	33

Distribution Statement A: Approved for Public Release; Distribution is Unlimited. AFRL-2021-4182

Learning: RMF Penetration

Machine Learning on MFPM Data:

- Randomly Explored (ω, B_ω, T_e) with MFPM
- Points Plotted w.r.t. (λ, γ) from Theory
- Theory: Necessary but Not Sufficient
- Classical Classifiers Explored
- Fewer False Positives & Higher γ_c
- Balancing Complexity vs. Accuracy?
- Artificial Neural Network (ANN) with Stochastic Gradient Descent
- Better Classification w/o Extreme Complexity

Predicted B_z-Reversal ANN

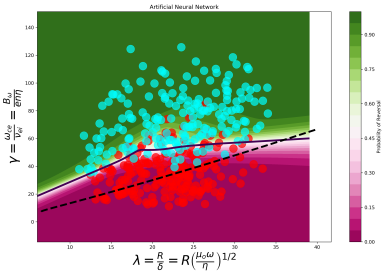

Confusion Matrix

-	Pred No	Pred Yes
Actual No	39	5
Actual Yes	2	34

Distribution Statement A: Approved for Public Release; Distribution is Unlimited. AFRL-2021-4182

Learning: RMF Penetration

Machine Learning on MFPM Data:

- Randomly Explored (ω, B_ω, T_e) with MFPM
- Points Plotted w.r.t. (λ, γ) from Theory
- Theory: Necessary but Not Sufficient
- Classical Classifiers Explored
- Fewer False Positives & Higher γ_c
- Balancing Complexity vs. Accuracy?
- Artificial Neural Network (ANN) with Stochastic Gradient Descent
- Better Classification w/o Extreme Complexity

Open Questions:

- Classification Space (λ, γ) Right for MFPM?
- Relevant Dimensions beyond 2D?
- Data Requirements in 3+D Classification?
- Do Experiments Exhibit Similar Trends?

Predicted B_z-Reversal ANN

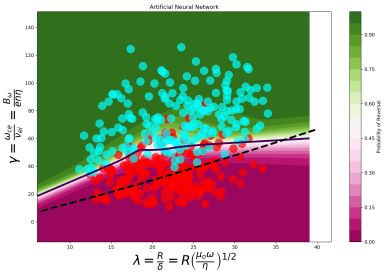

Confusion Matrix

-	Pred No	Pred Yes
Actual No	39	5
Actual Yes	2	34

Distribution Statement A: Approved for Public Release; Distribution is Unlimited. AFRL-2021-4182

Learning: RMF Penetration

Machine Learning on MFPM Data:

- Randomly Explored (ω, B_ω, T_e) with MFPM
- Points Plotted w.r.t. (λ, γ) from Theory
- Theory: Necessary but Not Sufficient
- Classical Classifiers Explored
- Fewer False Positives & Higher γ_c
- Balancing Complexity vs. Accuracy?
- Artificial Neural Network (ANN) with Stochastic Gradient Descent
- Better Classification w/o Extreme Complexity

Open Questions:

- Classification Space (λ, γ) Right for MFPM?
- Relevant Dimensions beyond 2D?
- Data Requirements in 3+D Classification?
- Do Experiments Exhibit Similar Trends?

Predicted B_z-Reversal ANN

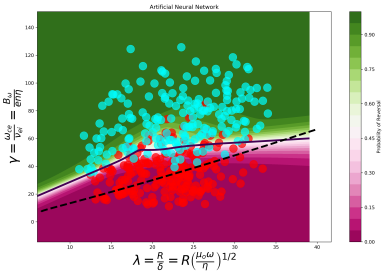

Confusion Matrix

-	Pred No	Pred Yes
Actual No	39	5
Actual Yes	2	34

Distribution Statement A: Approved for Public Release; Distribution is Unlimited. AFRL-2021-4182

Active Subspace for Reversal?

Curse of Dimensionality:

- Optimization Cost Exponential w/ Dim

Distribution Statement A: Approved for Public Release; Distribution is Unlimited. AFRL-2021-4182

Active Subspace for Reversal?

Curse of Dimensionality:

- Optimization Cost Exponential w/ Dim
- Not all Dimensions Created Equal!

Distribution Statement A: Approved for Public Release; Distribution is Unlimited. AFRL-2021-4182

Active Subspace for Reversal?

Curse of Dimensionality:

- Optimization Cost Exponential w/ Dim
- Not all Dimensions Created Equal!

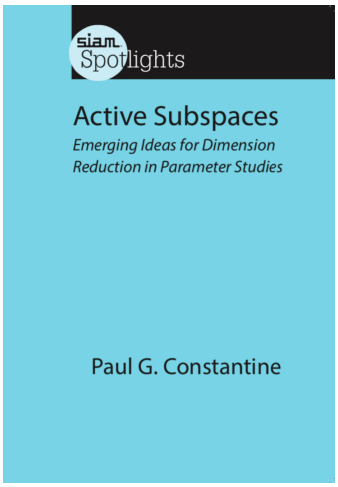

Distribution Statement A: Approved for Public Release; Distribution is Unlimited. AFRL-2021-4182

Active Subspace for Reversal?

Curse of Dimensionality:

- Optimization Cost Exponential w/ Dim
- Not all Dimensions Created Equal!
- First Step: Identify Dominant Dimensions

ACTIVE SUBSPACES

ACTIVE SUBSPACES

GOAL Make intractable high-dimensional parameter studies tractable by discovering and exploiting low-dimensional structure.

DEFINE First $n < m$ eigenvectors of $\int \nabla f \nabla f^T \rho \, d\mathbf{x}$

DISCOVER First $n < m$ eigenvectors of $\frac{1}{N} \sum_{i=1}^{N} \nabla f_i \nabla f_i^T$

APPROXIMATION $f(\mathbf{x}) \approx g(\boldsymbol{W}_1^T \mathbf{x})$

INTEGRATION $\int f(\mathbf{x}) \rho \, d\mathbf{x}$

OPTIMIZATION $\underset{\mathbf{x}}{\text{minimize}} \; f(\mathbf{x})$

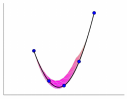

http://activesubspaces.org

Distribution Statement A: Approved for Public Release; Distribution is Unlimited. AFRL-2021-4182

Active Subspace for Reversal?

Curse of Dimensionality:

- Optimization Cost Exponential w/ Dim
- Not all Dimensions Created Equal!
- First Step: Identify Dominant Dimensions
- Often Works in Complex Looking Problems (Dominant Low-D Structure is Common)

ACTIVE SUBSPACES

Active subspaces helped us optimize an expensive scramjet model.

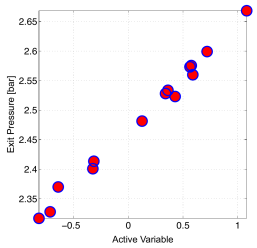

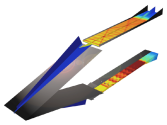

- Multiphysics model of hypersonic scramjet
- 7 input parameters
- No gradients
- Noisy function evaluations
- 2 hours per evaluation

DIMENSION REDUCTION: 7 to 1

http://activesubspaces.org

Distribution Statement A: Approved for Public Release; Distribution is Unlimited. AFRL-2021-4182

Active Subspace for Reversal?

Curse of Dimensionality:

- Optimization Cost Exponential w/ Dim
- Not all Dimensions Created Equal!
- First Step: Identify Dominant Dimensions
- Often Works in Complex Looking Problems (Dominant Low-D Structure is Common)
- Low-D Structure in Random FRC Data?

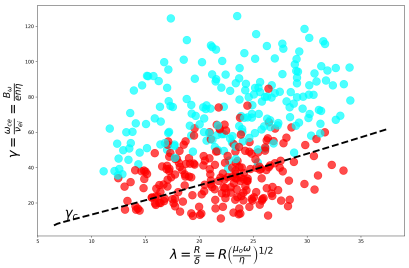

Random Points:

- $2\pi \times 10^5 Hz < \omega < 10\pi \times 10^5 Hz$
- $5G < B_\omega < 30G$
- $30eV < T_e < 50eV$

Distribution Statement A: Approved for Public Release; Distribution is Unlimited. AFRL-2021-4182

Active Subspace for Reversal?

Curse of Dimensionality:

- Optimization Cost Exponential w/ Dim
- Not all Dimensions Created Equal!
- First Step: Identify Dominant Dimensions
- Often Works in Complex Looking Problems (Dominant Low-D Structure is Common)
- Low-D Structure in Random FRC Data?
- Active Subspace for Min(B_z) in (ω, B_ω, T_e)

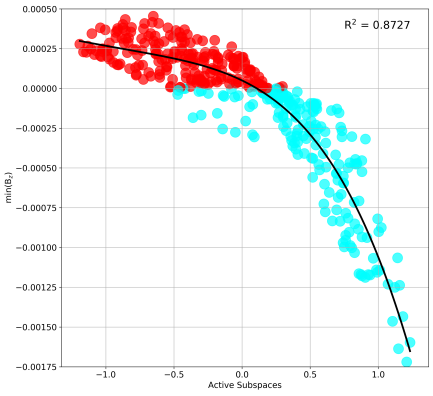

Distribution Statement A: Approved for Public Release; Distribution is Unlimited. AFRL-2021-4182

Active Subspace for Reversal?

Curse of Dimensionality:

- Optimization Cost Exponential w/ Dim
- Not all Dimensions Created Equal!
- First Step: Identify Dominant Dimensions
- Often Works in Complex Looking Problems (Dominant Low-D Structure is Common)
- Low-D Structure in Random FRC Data?
- Active Subspace for Min(B_z) in (ω, B_ω, T_e)
- Needs Experimental Validation
  - Result Model Artifact?
  - Exp. has Many More Dimensions

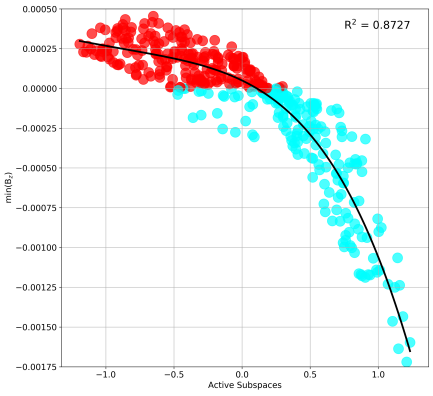

Distribution Statement A: Approved for Public Release; Distribution is Unlimited. AFRL-2021-4182

Active Subspace for Reversal?

Curse of Dimensionality:

- Optimization Cost Exponential w/ Dim
- Not all Dimensions Created Equal!
- First Step: Identify Dominant Dimensions
- Often Works in Complex Looking Problems (Dominant Low-D Structure is Common)
- Low-D Structure in Random FRC Data?
- Active Subspace for Min(B_z) in (ω, B_ω, T_e)
- Needs Experimental Validation
  - Result Model Artifact?
  - Exp. has Many More Dimensions

EP Exp Produce Data Faster than Simulation

Active Subspaces in the Experimental Loop?

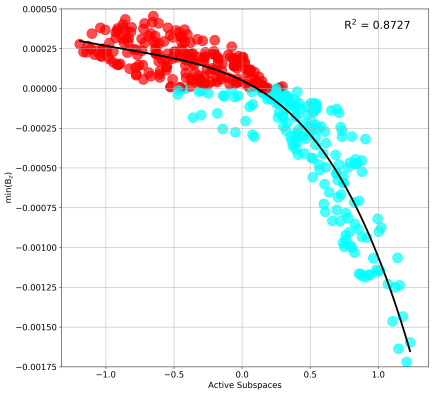

Distribution Statement A: Approved for Public Release; Distribution is Unlimited. AFRL-2021-4182

Section: Conclusion and Future Work

AFRL Pulsed EP Progress:

- Enhanced Models
  - Viscous Multi-Fluid
  - Hybrid Entropy/Energy Conservation
- Improved Understanding
  - Classifiers & Machine Learning
  - Reduced Dimensionality

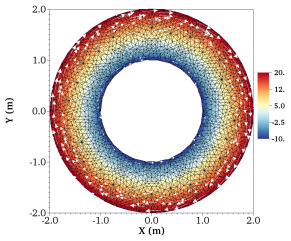

Distribution Statement A: Approved for Public Release; Distribution is Unlimited. AFRL-2021-4182

Section: Conclusion and Future Work

AFRL Pulsed EP Progress:

- Enhanced Models
  - Viscous Multi-Fluid
  - Hybrid Entropy/Energy Conservation
- Improved Understanding
  - Classifiers & Machine Learning
  - Reduced Dimensionality

Near Term Goals:

- Integrate Models
  - Porting DG MFPM to TURF
  - Verify Braginskii Implementation
  - Circuit BCs
  - Radiation Losses
- Re-Engage with Experimental Community

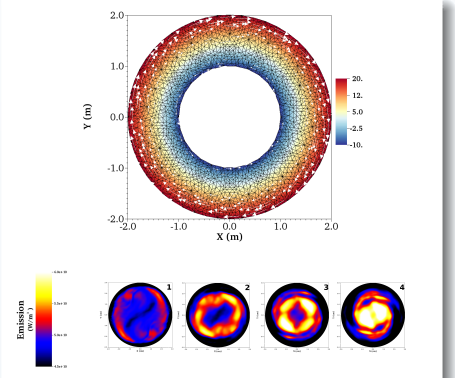

Distribution Statement A: Approved for Public Release; Distribution is Unlimited. AFRL-2021-4182

Section: Conclusion and Future Work

AFRL Pulsed EP Progress:

- Enhanced Models
  - Viscous Multi-Fluid
  - Hybrid Entropy/Energy Conservation
- Improved Understanding
  - Classifiers & Machine Learning
  - Reduced Dimensionality

Near Term Goals:

- Integrate Models
  - Porting DG MFPM to TURF
  - Verify Braginskii Implementation
  - Circuit BCs
  - Radiation Losses
- Re-Engage with Experimental Community

Long Term Goals:

- Cross-Verify MFPM/Kinetic Assumptions
- Quantify Extrapolative Model Power
- Optimize Design of Pulsed EP in High-D
- Actively Control Pulsed EP Systems

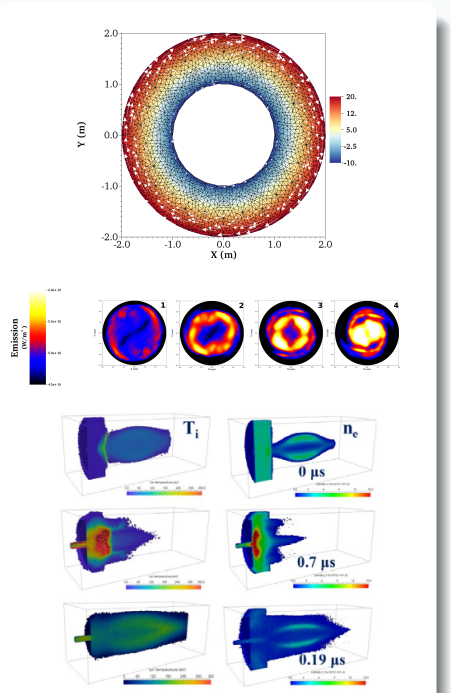

HYPERS Simulation Results for MSX
Omelchenko, *Phys Rev E.* **92**, 023105, 2015

Distribution Statement A: Approved for Public Release; Distribution is Unlimited. AFRL-2021-4182

Acknowledgement

Thank You

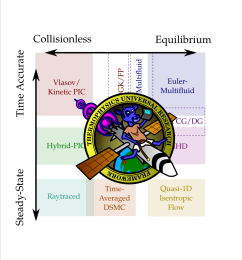

→

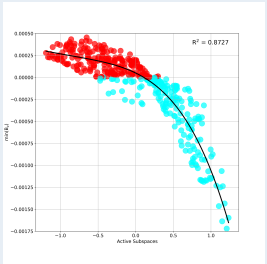

→

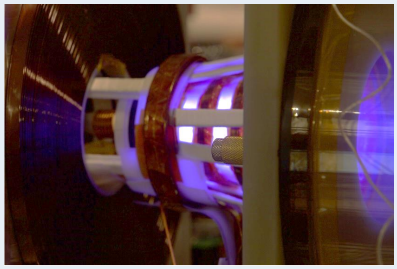

Work Supported through AFOSR Task 17RQCOR465 (PO: Birkan)

Questions?

Distribution Statement A: Approved for Public Release; Distribution is Unlimited. AFRL-2021-4182

AFRL-RQ-ED-TR-2021-0018
Primary Distribution of this Report:

RQR
AFRL R&D Case Files
Completed Interim and Final Tech Reports Repository

AFRL/RQ Technical Library
6 Draco Drive
Edwards AFB, CA 93524-7130

Johns Hopkins University
Whiting School of Engineering
ATTN: Mary T. Gannaway/FSO
10630 Little Patuxent Pkwy, Suite 202
Columbia, MD 21044-3286

Defense Technical Information Center
(1 Electronic Submission via STINT)
Attn: DTIC-ACQS
8725 John J. Kingman Road, Suite 94
Ft. Belvoir, VA 22060-6218